ISSN 1349-1113
JAXA-RR-12-009E

JAXA Research and Development Report

Experimental and Numerical Research on Boundary Layer Transition Analysis at Supersonic Speed: JAXA-ONERA Cooperative Research Project (Part 2)

Kenji YOSHIDA, Yoshine UEDA,
Olivier VERMEERSCH and Daniel ARNAL

March 2013

Japan Aerospace Exploration Agency

Contents

Experimental and Numerical Research on Boundary Layer Transition Analysis at Supersonic Speed: JAXA-ONERA Cooperative Research Project (Part 2)*

Kenji YOSHIDA*1, Yoshine UEDA*1,
Olivier VERMEERSCH*2 and Daniel ARNAL*2

Abstract

Stability analysis on a supersonic natural laminar flow (NLF) wing designed by JAXA was performed at both flight and wind tunnel test conditions as a joint research program between ONERA and JAXA. Both parties validated the NLF wing effect by confirming suppression of crossflow instability at design point, using an e^N method with fixed β strategy proposed by ONERA. Although JAXA's flight test vehicle and wind tunnel test model had almost same averaged roughness height of about 1 μm, it was shown that surface roughness had little influence on measured transition location at both flight and wind tunnel test conditions. Furthermore, JAXA found that the pressure distribution measured in flight test did not completely coincide to the target pressure distribution (Cp_{Target}) for the NLF wing design. It revealed that measured transition location at outer wing region was not delayed in flight test, compared with the transition location predicted with the Cp_{Target} which had large gain to delay the transition. Influence of Reynolds number on transition location was also studied for the target pressure distribution Cp_{Target}. Consequently, chordwise transition location, $(x/c)_{Tr.}$, rapidly moves from mid-chord location to forward location (near leading edge) for increasing Reynolds numbers, according to the change of instability of boundary layer from Tollmien-Schlichting instability to crossflow instability.

Keywords: boundary layer transition, supersonic flow, linear stability analysis, e^N method, natural laminar flow wing, flight test, wind tunnel test

Nomenclature

Cp	:	pressure distribution
Cp_{Target}	:	target pressure distribution
Re	:	Reynolds number
k	:	surface roughness height
R_k	:	Reynolds number based on roughness height
Ra	:	average roughness height
Tu	:	turbulence level
s	:	semi-span
C_L	:	lift coefficient
P_0	:	total pressure
M	:	Mach number
AOA	:	angle of attack
X	:	chorwise direction perpendicular to the leading edge
Y	:	spanwise direction
x_s	:	external streamline direction
y_s	:	crossflow direction
z	:	normal to the surface direction
u,v,w	:	longitudinal, spanwise and normal mean velocity
q'	:	disturbance
$\hat{q}$	:	amplitude function
ω	:	frequency

* Received 7 March, 2013（平成25年3月 7日受付）

*1: Supersonic Transport Team, Aviation Program Group, JAXA
（宇宙航空研究開発機構　航空プログラムグループ　超音速機チーム）

*2: Department of Modeling for Aerodynamics and Energetics (DMAE), ONERA
（フランス航空宇宙研究所　空力／エネルギーモデル部）

$\alpha = \alpha_r + i\alpha_i$	:	complex wave-number in X direction
$\beta = \beta_r + i\beta_i$	:	complex wave-number in Y direction
$\tilde{\alpha} = \tilde{\alpha}_r + i\tilde{\alpha}_i$	:	complex wave-number in x_s direction
$\tilde{\beta} = \tilde{\beta}_r + i\tilde{\beta}_i$	:	complex wave-number in y_s direction
$\vec{k} = (\alpha_r, \beta_r)$	:	wave-number vector
ψ	:	angle between the external streamline and the wave-number vector $\vec{k}$
ϕ	:	angle between the external streamline and X direction
A	:	amplitude of a disturbance
N	:	N factor provided by the integral of imaginary part of longitudinal wave-number

Abbreviations:

TSI	:	Tollmien-Schlichting Instability
CFI	:	CrossFlow Instability
HF	:	Hot Film sensors
DP	:	Dynamic Pressure transducers
Pr	:	Preston tubes
TC	:	ThermoCouples
MAC	:	Mean Aerodynamic Chord
NS	:	Navier-Stokes
LBL	:	Laminar Boundary Layer
TBL	:	Turbulent Boundary Layer
BLE	:	Boundary Layer Edge

Subscripts:

$(\cdot)_{MAC}$	:	relative to the mean aerodynamic chord
$(\cdot)_e$	:	at the boundary layer edge
$(\cdot)_w$	:	at the wall
$(\cdot)_{lam}$	:	relative to the laminar boundary layer region
$(\cdot)_{turb}$	:	relative to the turbulent boundary layer region
$(\cdot)_{env}$	:	relative to stability computation performed using envelope strategy
$(\cdot)_{beta}$	:	relative to stability computation performed using fixed β strategy

1. Introduction

(1) Background

Boundary layer transition prediction is still a challenging subject in both practical engineering field and academic/scientific field[1,17]. ONERA(France) and JAXA(Japan) collaborated to elaborate boundary layer transition prediction methods for three-dimensional wings at supersonic speed in the framework of cooperative research activity[2,5]. This cooperation started on April in 2000 and ended on March in 2008. Both parties obtained good cross-validation for both transition prediction methods and useful information to understand transition phenomenon on the natural laminar flow (NLF) wing of the experimental airplane of JAXA (called "NEXST-1") at flight test condition. It was designed and developed by JAXA in the National EXperimental Supersonic Transport (NEXST) program[3,4]. But both parties also obtained a few issues to be more investigated. After completing a final report[5] of the cooperation, ONERA and JAXA had an opportunity to discuss those remaining challenging subjects, then made new tasks and a research plan. Both parties agreed to continue present research activity to solve the challenging subjects in the cooperative research framework at the 7th ONERA-DLR-JAXA trilateral meeting held in Paris on the 18th of June, 2009. A brief history and principal results of previous cooperative research activity are summarized in Appendix A.

(2) Work tasks

Previous cooperative work on the transition research at supersonic speed conducted from 2000 to 2008 was divided into the following three tasks (see Fig. A-1 and A-2 in Appendix A).

(i) Task 1 : Transition analysis on a sharp cone model at wind tunnel test conditions

(ii) Task 2 : Transition analysis on the nose cone model of the NEXST-1 airplane at wind tunnel test conditions

(iii) Task 3 : Transition analysis on the NLF wing model of the NEXST-1 airplane at wind tunnel and flight test conditions

Through the Task 1 to 3, both parties' transition analysis codes were well validated. Considering the Task 3, good agreement between analysis results and flight test data at inner wing region was obtained. Nonetheless, discrepancy between computations and measurements in the outer wing region highlighted some misunderstanding in transition mechanism analysis. This offered a few subjects to improve and expand previous transition analysis results (see Fig. A-3 in Appendix A).

Furthermore, in order to understand transition mechanism on the NLF wing in detail, we needed to focus on Reynolds number effect and surface roughness influence at the design point condition of the NEXST-1 airplane. As transition phenomenon (in particular, receptivity of freestream disturbances and surface roughness) is generally different for Tollmien-Schlichting (TS) waves and crossflow (CF) disturbances, distinction must be made between these two types of instabilities.

In previous cooperative research, both parties used an approach of stability analysis with "envelope strategy". Although this strategy is convenient for consuming computation time, it cannot always make a clear distinction between TS and CF instabilities. Therefore, another approach based on fixed β strategy has been proposed by ONERA in current e^N method.

Fortunately, one of research members of JAXA had an opportunity of staying at ONERA about 6 weeks from May to June in 2009 under a "short-term stay abroad system" of JAXA. Preliminary, stability characteristics applying the fixed β strategy on the subject of the NEXST-1 NLF wing was investigated, and some new aspects were found by both parties (see Fig. A-4 in Appendix A).

After that, additional tasks were defined in new cooperative research as a follow-up activity to previous cooperation.

(iv) Task 4 : Transition analysis on the NEXST-1 NLF wing model including roughness effect and Reynolds number effect

Present Task 4 consists of the following subtasks.

a) Subtask 4.1: Detailed transition analysis on the NEXST-1 NLF wing model at flight test conditions

As mentioned before, to understand measured transition characteristics at flight test condition more physically, we need to apply fixed β strategy to investigate stability characteristics. This strategy can reveal the most dominant instability of the boundary layer. At the design point condition of the NEXST-1 NLF wing, JAXA controlled growth of crossflow instability to realize that transition due to Tollmien-Schlichting instability (exactly speaking, "oblique" TS wave) was dominant. Previous analysis confirmed that transition due to oblique TS instability occurred at inner wing region by investigating propagation direction of the most amplified disturbance wave. But at outer wing region, we were not able to make it clear. It came from envelope strategy applied to transition analysis. Fixed β strategy, as one of detailed approaches in transition analysis, is well known to be effective and useful for making clear transition mechanism. Therefore, the fixed β strategy was firstly applied in this task.

First of all, we analyzed stability characteristics at the design point condition of NEXST-1 airplane: Mach number 2.0, flight altitude 18 km, angle of attack 1.6 degrees. Then we conducted same analysis at higher Reynolds number condition corresponding to an altitude of 12 km. Comparing them, we confirmed Reynolds number effect and also investigated roughness effect, because practical surface roughness condition kept constant at both Reynolds number conditions.

b) Subtask 4.2: Detailed transition analysis on the NEXST-1 NLF wing model at S2MA wind tunnel test conditions

Before the flight test of the NEXST-1 airplane, JAXA conducted transition measurement in ONERA-S2MA wind tunnel facility to validate JAXA's NLF wing design concept. S2MA wind tunnel has a rather low turbulence level (Tu=0.15%), so that this facility is well adapted to laminar study. In the same way, JAXA made a wing-body configuration model with a great care

devoted to surface polishing and the average surface roughness Ra was measured to study its impact on transition location. During the wind tunnel campaign, the total pressure has been varied from P_0=0.6 to 1.4 bar allowing an investigation of Reynolds number effect on transition location. The experimental pressure distributions were used to conduct stability computations using fixed β strategy. Through detailed analysis of wind tunnel measurements and stability computations, both parties expected to make an effective and useful correlation among transition process, influence of surface roughness and Reynolds number as well as influence of freestream turbulence.

(3) Approach

In the flight test, JAXA observed a slight difference between measured and CFD-computed pressure (Cp) distributions. First of all, that difference should be reduced to improve the discrepancy of transition locations measured in flight test and estimated with e^N method. As one of best ways for it, the Cp distributions for three dimensional laminar boundary layer (3D-LBL) computations were estimated by applying a surface interpolation technique to the measured Cp distributions. Then, both parties applied 3D-LBL code and e^N method with envelope strategy, respectively. By comparing both results with measured transition location data, a useful database for the N factor corresponding to transition was made.

Furthermore, to confirm the nature of transition, the fixed β strategy was applied to stability computations for all cases. Additionally, roughness effect on transition location was evaluated using the Reynolds number $R_k = \frac{U(k) \times k}{\nu(k)}$ based on roughness height k.

(4) Objectives

According to previous sections (“Work tasks“ and “Approach“), main objectives of present cooperative work are to advance previous transition research results on the NEXST-1 airplane, and to confirm the validity of both parties’ transition analysis methods through comparing numerical results with both wind tunnel and flight test measurements at supersonic speed conducted by JAXA. Based on them, present main objectives and approaches are divided into three parts as follows:

(i) Objective 1: To confirm the suppression of crossflow instability (CFI) at the design point of NEXST-1 flight test

→ Approach 1: To conduct stability analysis with fixed β strategy, comparing stability results at off-design points

(ii) Objective 2: To quantify the influence of surface roughness on transition process

→ Approach 2: To compute the roughness Reynolds number based on measured roughness height R_k, using ONERA’s roughness database

(iii) Objective 3: To investigate the Reynolds number effect on the target Cp distribution for the NEXST-1 NLF wing

→ Approach 3: Same as Approach 1

(5) Schedule

Present new cooperative work was achieved within a time span of three years, namely from the end of 2009 to the end of 2012. The first year was mainly devoted to the achievement of the Subtask 4.1 whereas the second year concerned Subtask 4.2. The last year was devoted to achievement of making a final common report and some technical papers for international conferences. Of course, a review meeting was organized each year to discuss, adjust and summarize research results by both parties.

(6) Research plan

Table 1 shows a brief summary of present research subjects.

(7) Contents of present report

The objective of present report is to summarize the results obtained in present cooperative research activity. This report particularly focused on the in-depth comparisons of stability results computed by both parties to experimental results obtained by JAXA.

Present report consists of following three parts: The first part is transition analysis on the NEXST-1

Table 1. Summary of present research activities

		Flowfield	LBL		stability					Rk-study		Re-study	
		Cp(UVW)			Envelope		Fixed β		Database				
		JAXA	ONERA	JAXA	ONERA	JAXA	ONERA	JAXA	ONERA	ONERA	JAXA	ONERA	JAXA
NEXSTI	α_No.4	○	○	○	○	○	○	○	—	—	○	○	○
	α_No.2	○	—	○	—	○	—	○	—	—	—	—	—
	α_No.3	○	—	○	—	○	—	○	—	—	—	—	—
	Re_No.5	○	○	○	○	○	○	○	—	—	○	○	○
S2MA	P0=0.6 bar	○	○	○	○	○	○	○	○	○	○	○	○
	P0=1.0 bar	—	○	○	○	○	○	○	○	—	○	○	○
	P0=1.4 bar	—	○	○	○	○	○	○	○	○	○	○	○

flight test conditions (Chapter 2). Stability analysis is made using fixed β strategy which highlights the most dominant instability of boundary layer leading to the transition for flight test configuration. The second part corresponds to transition analysis on the NEXST-1 wing-body model at S2MA wind tunnel test conditions (Chapter 3). It also describes to make clear the most dominant instability mode. The third part is physical consideration on the influence of roughness and Reynolds number on the NEXST-1 experiments (Chapter 4 and 5). The third part also includes a study of Reynolds number effect on numerical target pressure distribution[1] for the natural laminar flow wing design concept (Chapter 5).

2. Stability computations at NEXST-1 flight test conditions

2.1. Outline of flight test

(1) Design concept

It is very important to control crossflow instability to obtain a significant region of laminar boundary layer on a highly swept wing. JAXA found an ideal pressure distribution to suppress the CFI on supersonic transport (SST) configurations by using a current transition analysis method (e^N method), then developed a CFD-based inverse design method[4] for a natural laminar flow wing design. The procedure of present method is illustrated in Fig. B-1 of Appendix B. The most important part in this procedure is to specify a target pressure coefficient distribution (Cp_{Target}). It consists of (i) an ideal pressure distribution on upper surface to suppress the CFI, and (ii) the difference of Cp distributions on upper and lower surfaces satisfies "warped" wing design condition.

According to this procedure, JAXA firstly prepared an initial configuration designed with three pressure drag reduction concepts based on supersonic linear theory, that is, an arrow planform, a warped wing and an area-ruled body. Then, the difference between the Cp_{Target} and CFD-computed Cp distribution on the initial configuration was estimated. After that, the configuration was modified to reduce the difference of Cp distributions by using supersonic lifting surface theory. Finally, such a step was continued until converging towards the target pressure distribution.

To demonstrate the NLF wing design concept in flight test, JAXA designed and developed an unmanned and scaled supersonic experimental vehicle (called "NEXST-1") shown in Fig. 1, which was manufactured taking account of the elastic deformation at the design point: Mach number M=2.0, lift coefficient C_L=0.1 and flight altitude H=18 km. It also includes present four design concepts to reduce supersonic airframe drag. The design process and principal results are described in Ref. 4 in detail.

[1] Let's recall that in flight, measured Cp distribution was slightly different from the target pressure distribution computed by JAXA

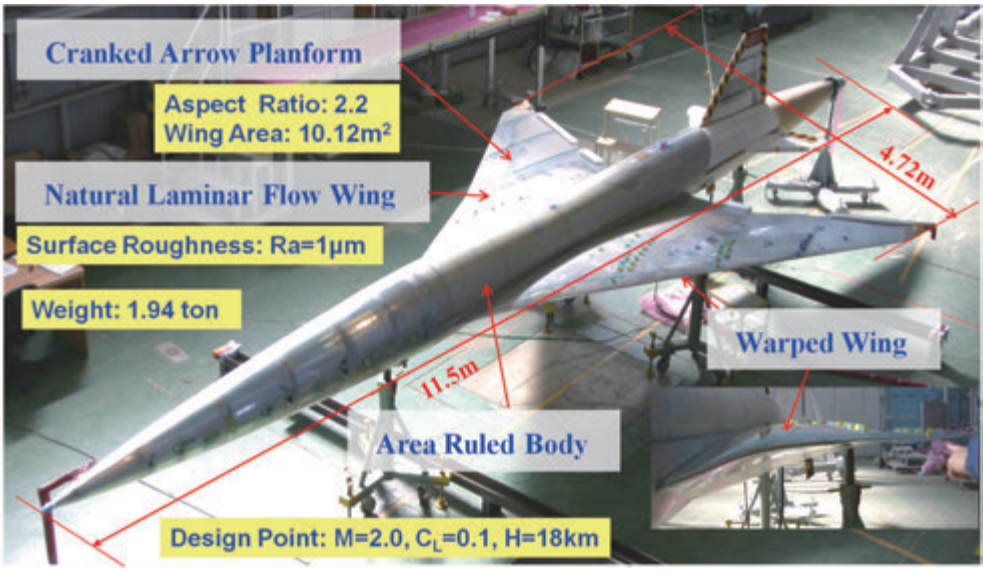

Figure 1. NEXST-1 airplane with aerodynamic design concepts

(2) Flight test and wind tunnel test validations

Before the flight test of the NEXST-1, JAXA experimentally confirmed the NLF wing design concept using a special wing-body model which consisted of adiabatic material skin (about 5 mm thickness on metal body) and multi-element type hot-films. The continuous supersonic wind tunnel of ONERA (S2MA) was chosen to investigate transition characteristics since its turbulence level "Tu" was firstly considered as rather low: 0.15%<Tu<0.20%. Nonetheless, these values remain high compared to very weak turbulence level in free flight condition: Tu<0.05%. Therefore, the NLF wing design was qualitatively confirmed but not quantitatively in terms of transition location as shown in Fig.2[6]. Furthermore, stability analysis on S2MA test conditions was also conducted, and its results were summarized in next Chapter and Ref. 7.

Then, the flight test of the NEXST-1 was conducted at Woomera test field in Australia, 2005. The test consisted of two aerodynamic measurement phases. One was "angle of attack sweep test" phase around 18 km altitude to confirm the drag characteristics of the NEXST-1. Another was

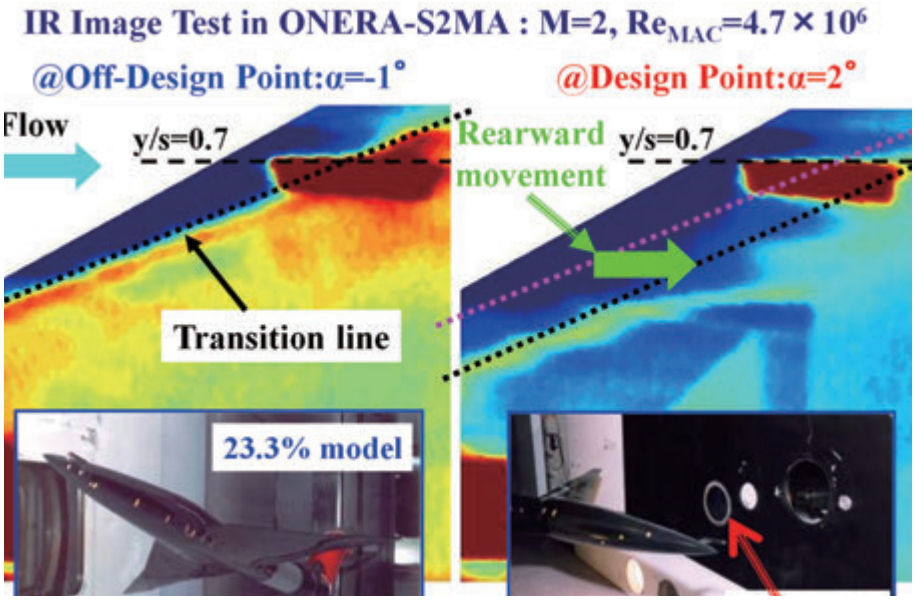

Figure 2. Experimental validation test for transition characteristics

"altitude sweep test" phase while maintaining the design value of lift coefficient C_L=0.1 to investigate the effect of JAXA's NLF wing concept at higher Reynolds number than the one of the design point (about 2.4 times higher). Outline of the flight test is illustrated in Fig.3.

To realize the NLF wing concept in real flight vehicle, severe criterion for surface smoothness condition was specified, that is, averaged roughness height was reduced less than 1 μm at least as explained later. To detect its transition characteristics, hot-film sensors (indicated by "HF"), dynamic pressure transducers ("DP"), Preston tubes ("Pr") and thermocouples ("TC") were applied. They were mounted on the upper surface of the wing and the side surface of the forebody as illustrated in Fig. 4(c) and Fig. B-5 of Appendix B.

Principal results of the flight test are summarized in Figs. 4. Fig. 4(a) shows a comparison between measured and CFD-based Cp distributions on the wing at the design condition ("α_No.4") of the NEXST-1. These computations were performed on the elastic deformed configuration designed by JAXA[8]. Especially, high correlation between them on upper surface was confirmed within measurement error bar of ΔCp=$\pm$0.0115 illustrated as symbol of "I" in Fig. 4(a). It indicates that necessary conditions to obtain extended laminar regions on the wing were satisfied during the flight test. Fig. 4(b) shows one of measured data with hot-film sensors at a typical measurement position. After analyzing whole data on the upper surface, transition line was estimated as indicated in Fig. 4(c) by the green line. At the design point, the boundary layer remains laminar in the first 40% of chord. The evolution of transition line as a function

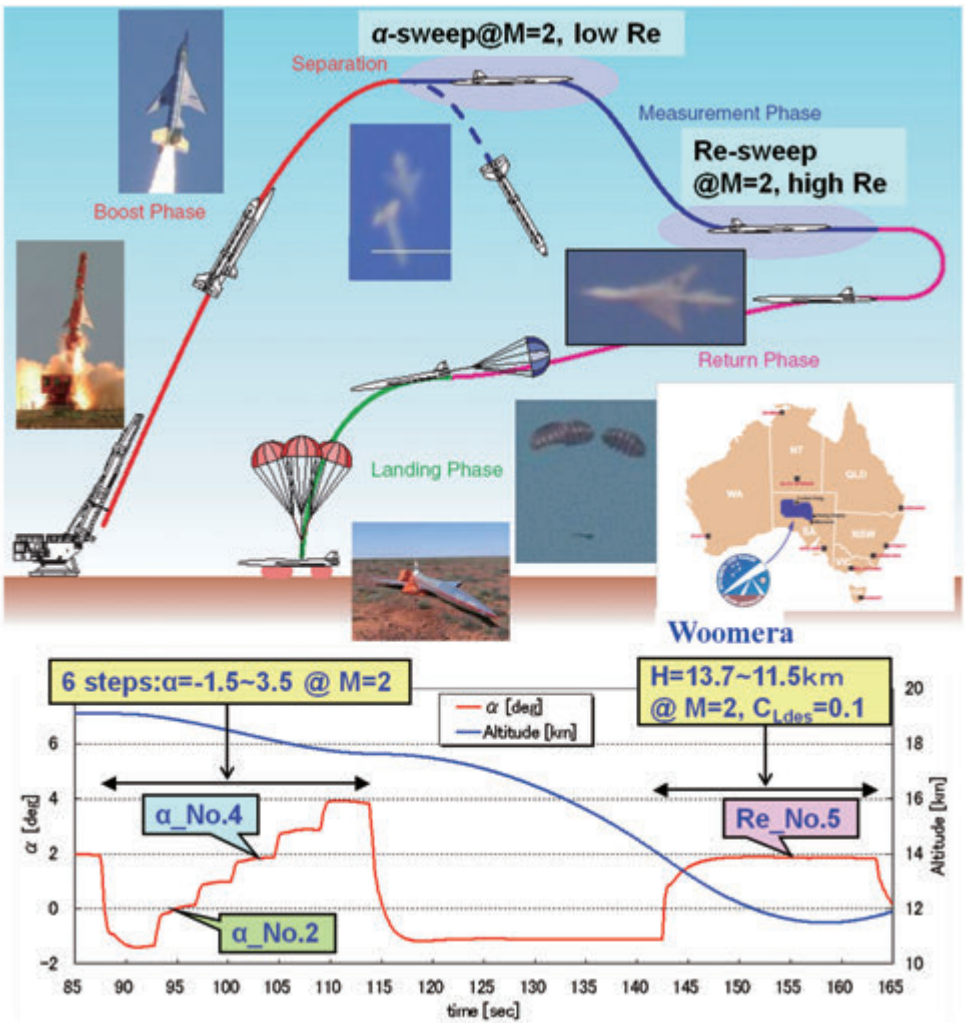

Figure 3. Overview of NEXST-1 flight test

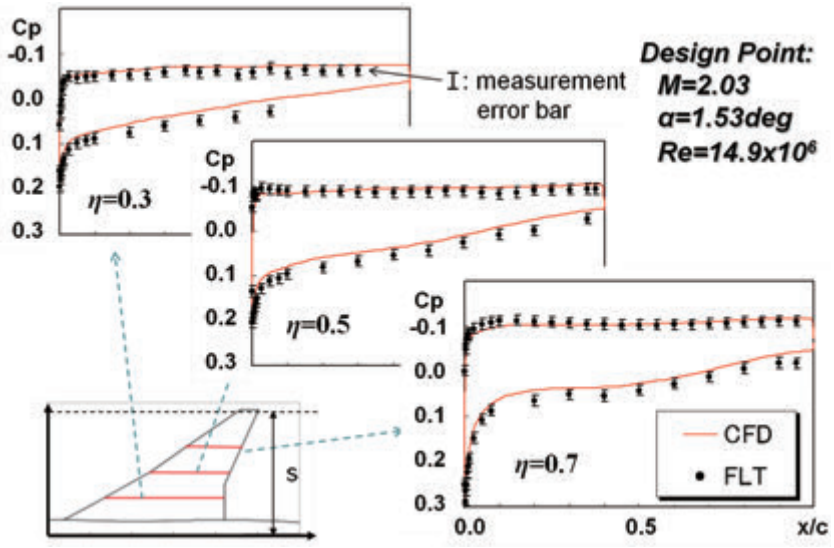

(a) Comparison of measured and CFD-based pressure distributions at design point

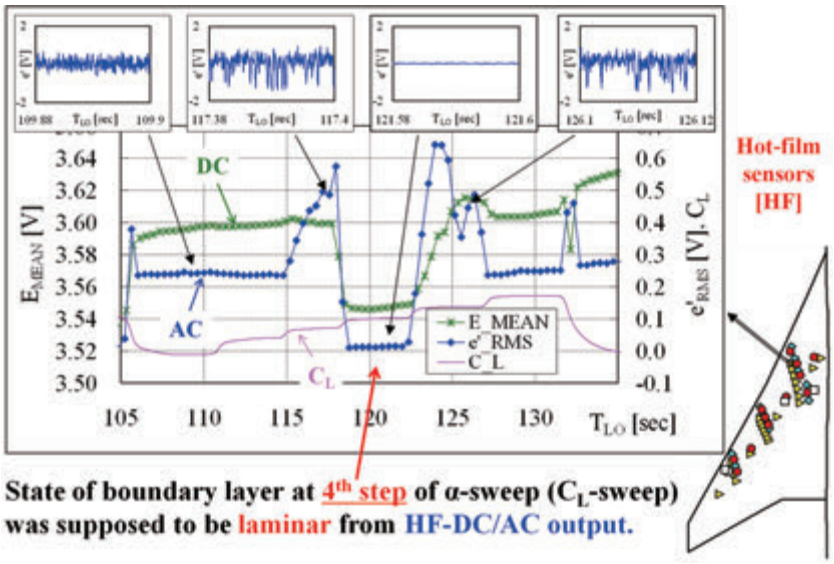

(b) Hot-film measurement data

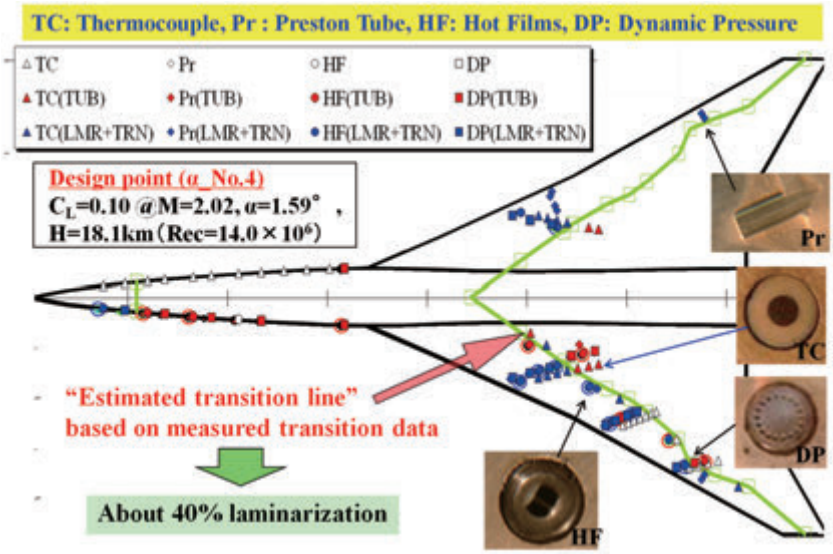

(c) Summary of transition measurement results

Figure 4. Principal flight test results

of the angle of attack is illustrated in Figs. B-8 of Appendix B.

Furthermore, Fig. 4(d) shows a comparison of measured transition data and JAXA's transition analysis results, that is N contours[5, 8]. Solid-red and open-blue symbols correspond to turbulent and non-turbulent state in boundary layer at the design point, respectively. Here non-turbulent means laminar and transitional states. Measured transition data indicate approximately 40% of laminarity on the upper surface as clearly shown in Fig. 4(c). Three solid-lines correspond to transition lines predicted with assumed transition criteria for N contours based on a current e^N method. JAXA improved an in-house e^N code under the framework of ONERA-JAXA cooperative research program[5] and used so-called envelope strategy[1] to compute amplification rates of disturbances in stability analysis. In this comparison, transition location at inner wing region predicted with N=11 seems to be in good agreement with measured data, whereas a lower value N=9 matches with measured transition pattern at outer wing region[5]. This non-unique N value corresponding to measured transition, contrary to what was expected, highlights the fact that distinct transition mechanisms may exist in inner and outer part of the wing. This is strong motivation to advance present ONERA-JAXA cooperative research activity.

2.2. Analysis approach

To reduce the discrepancy between measured and predicted transition pattern at the design condition shown in Fig. 4(d), the following subjects were investigated; (i) to check the Cp distribution to be used for computing laminar boundary layer, (ii) to understand physical mechanism, identifying the most dominant mode (Tollmien-Schlichting or crossflow instabilities), (iii) to consider the influence of surface roughness, and (iv) to quantify Reynolds number effect on transition characteristics.

Outline of our approach to the subject (i)-(iv) is summarized in the following paragraphs.

(1) Improving Cp distributions [Subject (i)]

Although CFD-based Cp distributions are definitely located within measurement error bar of measured pressure coefficients as shown in Fig. 4(a), there is slight difference between them. It may affect the properties of the LBL. Therefore, JAXA improved the Cp distributions used to compute 3D-LBL by applying a surface-interpolation technique based on the difference between measured and computed pressure coefficients. It consists of a combination of least square approximation technique for chordwise direction and constrained spline function fitting technique for spanwise direction.

The procedure of this interpolation technique is described as follows:

(i) First of all, it is assumed that the interpolated Cp distribution consists of a base part and a per-

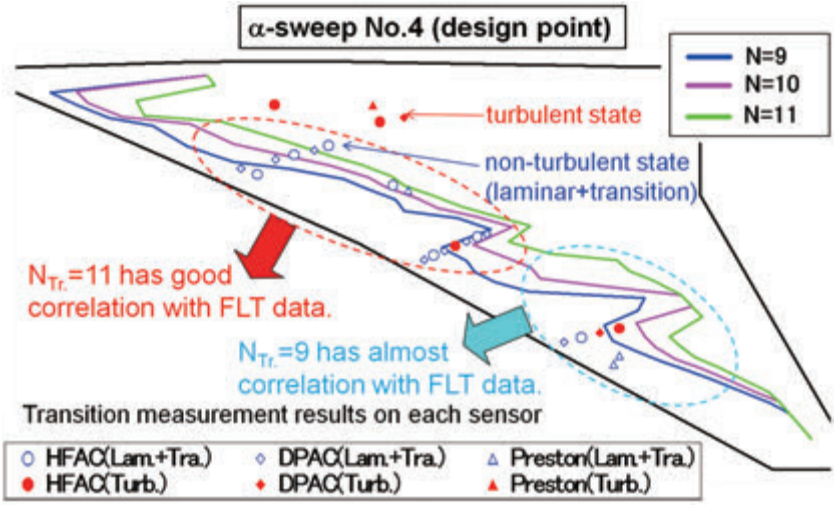

(d) Comparison of measured and analyzed transition data in previous ONERA-JAXA joint research

Figure 4. Principal flight test results

turbed part as defined by the following relation.

$$Cp_{FLT,interpolated}(\xi,\eta) = Cp_{base}(\xi,\eta) + \delta Cp(\xi,\eta)$$

Here, as the base part, JAXA used the Cp distributions on the elastic deformed configuration computed using JAXA's NS code with full turbulent boundary layer (TBL) condition.

$$Cp_{base}(\xi,\eta) = Cp_{NS(TBL)}(\xi,\eta)$$

(ii) Then, the perturbed part is estimated as follows:

a) Chordwise δCp distributions at five spanwise stations for pressure measurement are interpolated by using a least square technique.

$$\delta Cp(\xi,\eta_M) = Least\ Square\ Approximation\ with\ n-th\ polynomial\ of\ \xi$$
$$for\ two\ \xi\ regions\ on\ \delta Cp(\xi_M,\eta_M)\ at\ each\ \eta_M$$
$$where\ \delta Cp(\xi_M,\eta_M) \equiv Cp_{FLT}(\xi_M,\eta_M) - Cp_{base}(\xi_M,\eta_M)$$
$$\begin{cases} \xi_M \equiv \left(\frac{x}{c}\right) at\ measured\ chordwise\ position \\ \eta_M \equiv \left(\frac{y}{s}\right) at\ measured\ spanwise\ station \end{cases}$$

Here two ξ regions are defined as follows:

$$\begin{cases} region\ I : 0 \le \xi \le \xi_1 \\ region\ II : \xi_1 \le \xi \le \xi_{end} \end{cases}$$

To realize effective interpolation, ξ_1 and n (order of the polynomial) must be carefully selected at each pressure measurement station. Fig. 5(a) shows typical results in this process: n=4 and 3 were chosen in the region I and II respectively. As clearly seen in the figure, present interpolated Cp distributions were in close agreement with measured pressure distributions with consideration of measurement error bar.

b) Spanwise δCp distributions at each chordwise position (x/c) with finer spacing were interpolated by using a constrained spline technique.

$$\delta Cp(\xi,\eta) = Constrained\ Spline\ \ of\ \eta\ for\ \delta Cp(\xi,\eta_M)\ at\ each\ \xi$$

Figure 5(b) shows a result of present spanwise interpolation. To avoid any unexpected waviness due to application of spline approximation, it was clearly found that present constrained spline technique was very effective.

Figure 5(c) shows a comparison of present surface-interpolated and previous Cp contours. Previous one was the Cp contour computed with CFD and it was used for previous stability analysis. Present one was used to conduct present stability analysis.

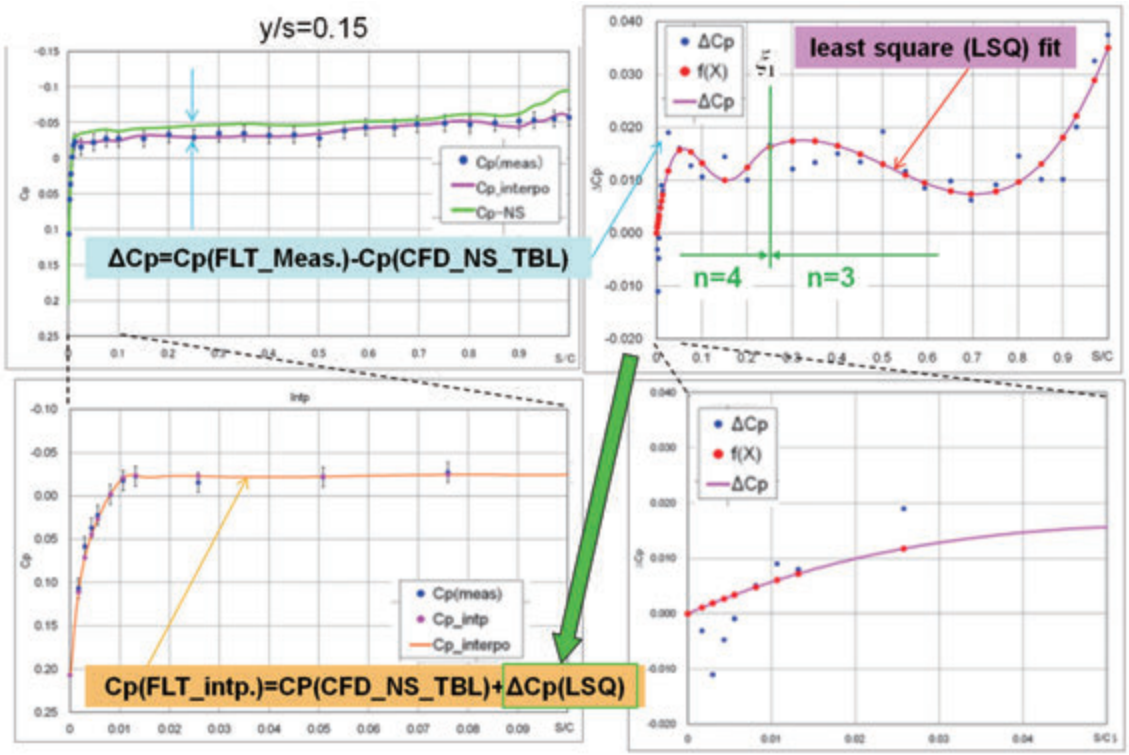

(a) Chordwise interpolation (1/3)

Figure 5. Results of Cp interpolation technique

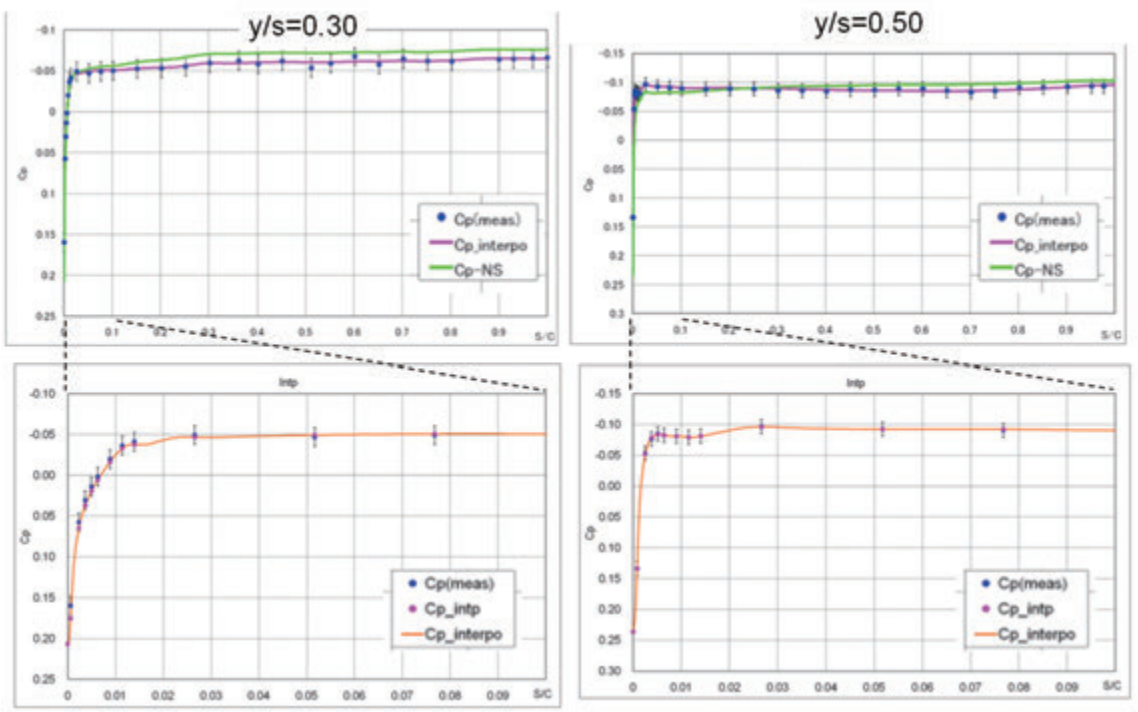

(a) Chordwise interpolation (2/3)

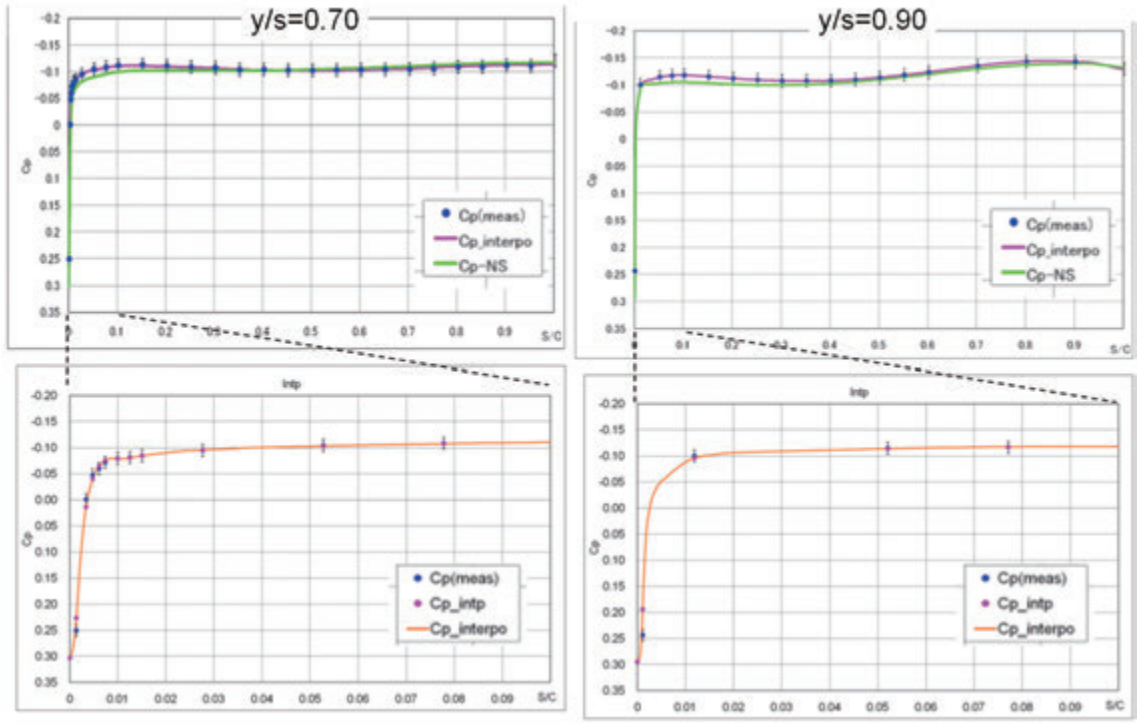

(a) Chordwise interpolation (3/3)

Figure 5. Results of Cp interpolation technique

In present stability analysis, the following four cases are mainly focused on; (A) at design point case called "α_No.4", (B) at typical two off-design point cases called "α_No.2", "α_No.3" and (C) at a higher Reynolds number case called "Re_No.5". Their detailed conditions are described in Table B-1 of Appendix B. Concerning the case Re_No.5, similar surface-interpolated Cp distribution was also applied and good interpolation result, especially near the leading edge region were obtained as shown in Fig. 5(d). However, for two off-design point cases, CFD-based pressure

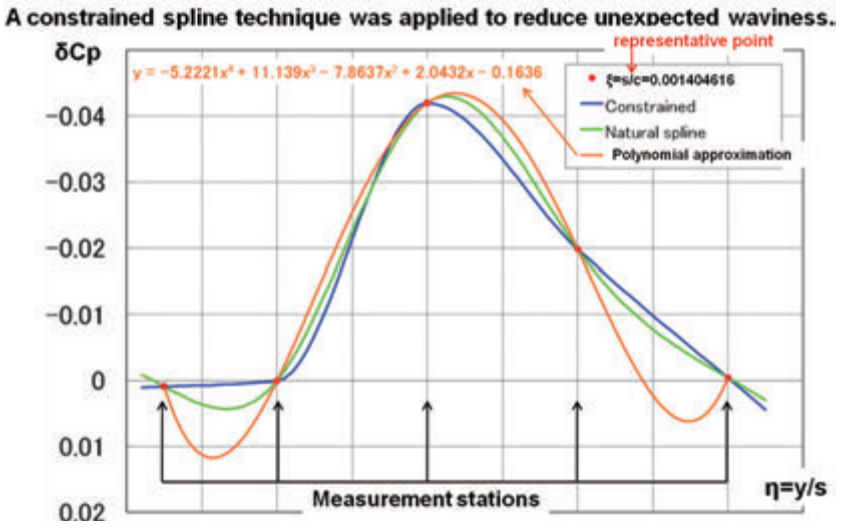

(b) Spanwise interpolation

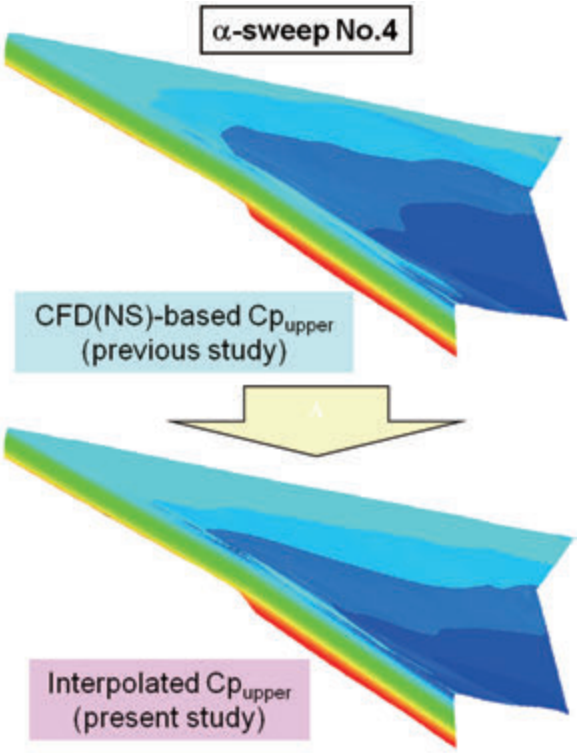

(c) Surface-interpolated Cp contour at α_No.4 case

Figure 5. Results of Cp interpolation technique

distributions were applied because they were very little different from measured ones. Fig. 6 shows a comparison of several Cp distributions along chordwise location at inner and outer wing regions (y/s=0.3 and 0.7) where s stands for the semi-span of the NEXST-1: s=2.36 m. (Furthermore, Mach number contour and external streamline at α_No.4 case were illustrated in Fig. 7 as a reference.)

Finally, to be convenient for computing 3D-LBL and stability characteristics, detailed numerical tables of present surface-interpolated pressure and velocity distributions at boundary layer edge are summarized in Appendix D.

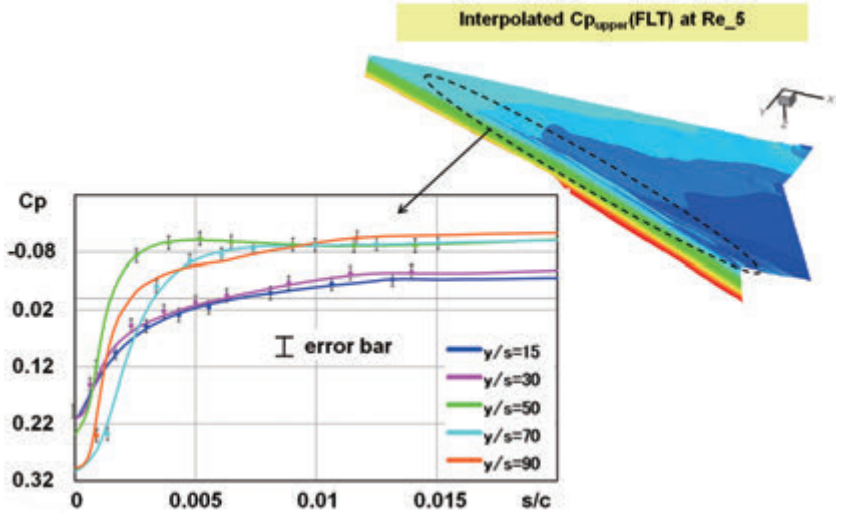

(d) Surface-interpolated Cp contour at Re_No.5 case

Figure 5. Results of Cp interpolation technique

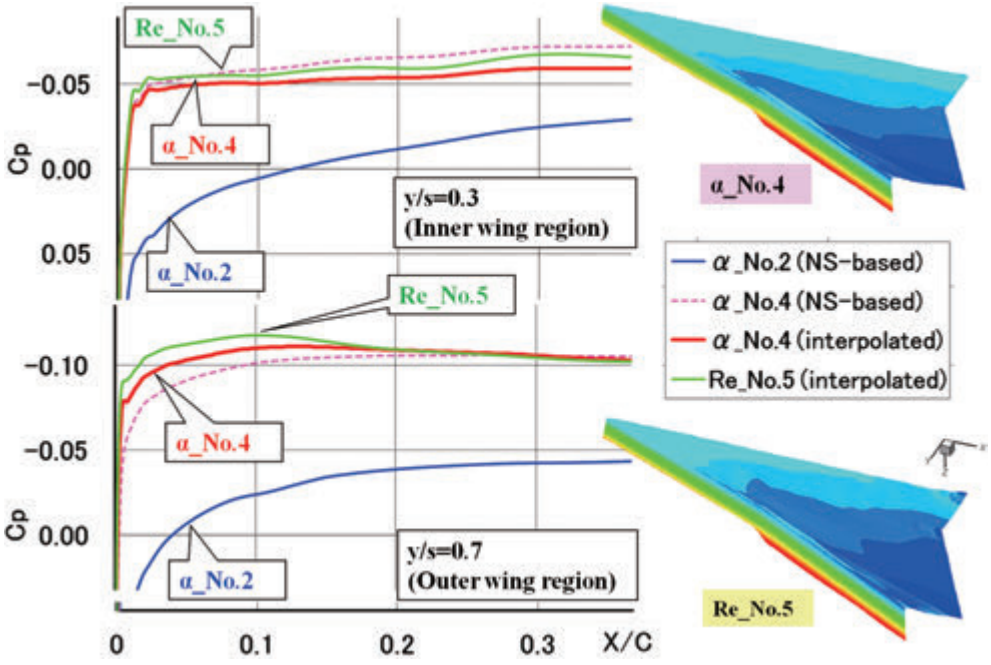

Figure 6. Pressure distributions for computing laminar boundary layer

(2) Fixed β strategy [Subject (ii)]

As mentioned before, comparison between experiments and stability computations using envelope strategy provide different values of transition N factor for the inner and the outer regions of the wing. This may indicate that distinct transition process exists in these regions: one driven by Tollmien-Schlichting instability and the other by crossflow instability. Therefore, it is important to split crossflow instability from Tollmien-Schlichting wave to understand physical nature of transition in three-dimensional boundary layer. In our previous analysis[5], both parties used envelope strategy which reduces computational cost by neglecting freedom of physical variables in three dimensional disturbances.

In the framework of classical linear stability theory, disturbances are introduced as:

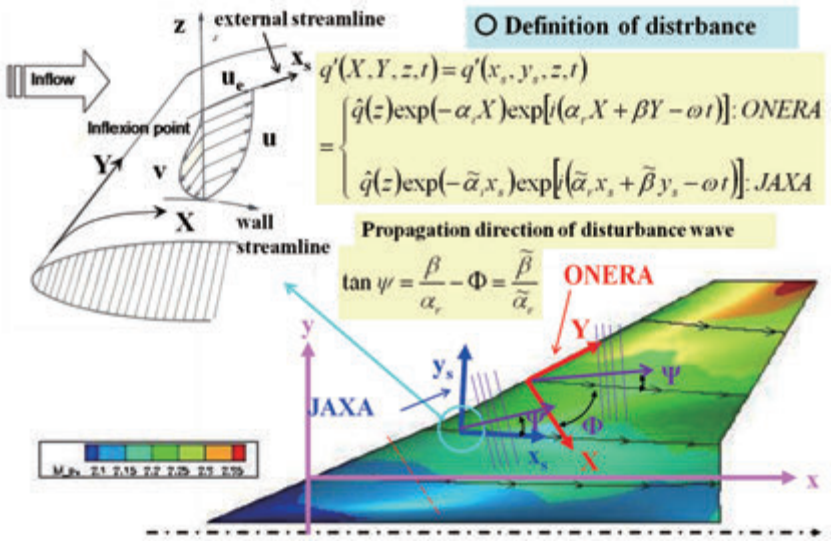

Figure7. Definition of disturbance on the wing coordinate system (X, Y, z) and external streamline coordinate system (xs, ys, z), including Mach number color map and freestream lines at α_No.4

$$
\begin{aligned}
&q'(X,Y,z,t)\\
&=q'(x_s,y_s,z,t)\\
&=\begin{cases}\hat{q}(z)\exp(-\alpha_i X)\exp[i(\alpha_r X+\beta Y-\omega t)] & : \quad ONERA\\ \hat{q}(z)\exp(-\tilde{\alpha}_i x_s)\exp[i(\tilde{\alpha}_r x_s+\tilde{\beta} y_s-\omega t)] & : \quad JAXA\end{cases}
\end{aligned}
\tag{1}
$$

where q' is a fluctuation (velocity, pressure or temperature) and $\hat{q}$ its amplitude function. ONERA and JAXA used different coordinate systems to define the disturbances. In the formulation by ONERA, X is perpendicular to the leading edge (along Y axis) and z normal to the wall. In the formulation by JAXA, x_s corresponds to the external streamline direction and y_s is perpendicular to x_s as represented in Fig. 7.

Considering the spatial approach in stability theory, $\alpha=\alpha_r+i\alpha_i$ or $\tilde{\alpha}=\tilde{\alpha}_r+i\tilde{\alpha}_i$ is complex wave-number in the X or x_s direction. The spanwise wave-numbers β (along Y direction parallel to the leading edge) and $\tilde{\beta}$ (along y_s direction parallel to crossflow direction) respectively as well as the frequency ω are real. Assuming that the spanwise wave-number is real means that there is no amplification of the disturbance in spanwise direction. This implies that formulation by ONERA or JAXA is based on different assumptions for the spanwise wave-number: this problem is discussed in Appendix C. Fortunately both parties confirmed that the assumption made little difference in computing stability characteristics.

It is common to introduce the angle between the external streamline and the wave-number vector as defined by the following relation:

$$
\begin{aligned}
\psi &= \tan^{-1}(\beta/\alpha_r)-\phi\\
&= \tan^{-1}(\tilde{\beta}/\tilde{\alpha}_r)
\end{aligned}
\tag{2}
$$

where ϕ represents the angle between the external streamline and the X direction (see Fig. 7). The angle ψ corresponds to the propagation direction of instability wave. It is an interesting parameter which allows the distinction between the two kinds of disturbances respectively TSI and CFI. As a matter of fact, for TS wave ψ remains less than $\psi<60°$, and on the contrary, dealing with CFI ψ is around $\psi\approx 89°$.

The amplification of a disturbance, i.e. the ratio between the amplitude at a given station and the initial one is given by relation (3). It is common to introduce the so-called N factor which describes the total amplification rate of the small disturbances along a path where disturbances propagate.

$$
\frac{A}{A_0}=\exp\left(-\int_{x_0}^{x}\tilde{\alpha}_i(x_s)dx_s\right)=e^N
\tag{3}
$$

To compute the N factors, generally the following two approaches can be used:

a) Envelope strategy: at a given streamwise position x_s, and for a fixed value of the frequency ω,

the value of the longitudinal wave-number $\tilde{\alpha}_i$ is calculated as a function of ψ and the N factor corresponds to the most unstable wave-number direction according to:

$$N(\omega) = -\int_{x_0}^{x} Max_{\psi}\left[\tilde{\alpha}_i(x_s;\omega,\psi)\right]dx_s$$

Envelope strategy consists of selecting a special propagation direction (ψ_m) which has maximum amplification rate ($\sigma \equiv -\alpha_i$) among whole propagation direction angles ($-90<\psi<90°$) at each frequency (f[Hz]) and streamwise Reynolds number based on chordwise location (Re_x), as illustrated in Fig. 8. This model cannot explicitly split CFI and TSI, because the selection of ψ_m always means to indicate maximum value on σ of CFI or TSI. It can be anticipated that compared to fixed β strategy the envelope strategy lacks certain physical information. Indeed, from a numerical viewpoint, it is assumed that crossflow instability can suddenly change to streamwise wave within short distance.

b) Fixed β strategy: the N factor is integrated following wave with constant frequency and constant spanwise wave-number according to:

$$N(\omega,\beta) = -\int_{x_0}^{x} \tilde{\alpha}_i(x_s;\omega,\beta)dx_s$$

Fixed β strategy represents an improvement compared to envelope strategy[1]. In this approach, several pre-set combinations of (β_r, f) are applied to compute eigenvalues (α_r, α_i) in linear stability equation in spite of selecting ψ_m, as illustrated in Fig. 8. ONERA has reported its effectiveness on several transition studies in both low and transonic speeds[9]. The application of such fixed β strategy to JAXA's NLF wing in supersonic flow is one of valuable challenges for ONERA as well as for JAXA.

(3) Rk study [Subject (iii)]

As mentioned before, surface quality and surface defaults may strongly influence the transition process. For instance, it is now established that CFI is sensitive to surface roughness and will have an initial amplitude all the more important than the surface average roughness parameter is high. In this context, the NEXST-1 airplane was carefully manufactured and polished to keep severe surface roughness condition for little influence on transition phenomenon. Before and after its flight test, surface roughness was measured with a special technique illustrated in Fig. 53(b). From the surface average roughness, JAXA computed the corresponding Reynolds number $R_k = \dfrac{U(k)\times k}{\nu(k)}$.

Using the ONERA's correlation between R_k and the transition N factor (see Fig. 55), the influence

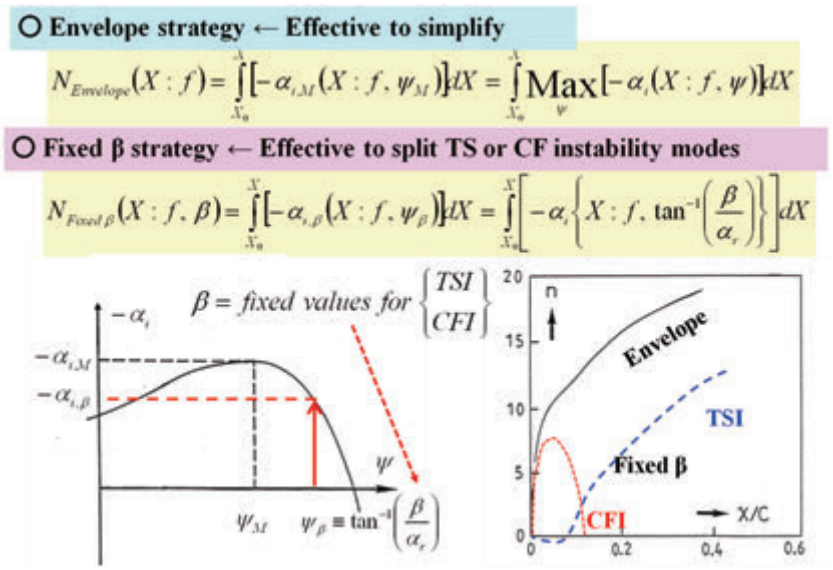

Figure 8. Comparison of envelope and fixed β strategies

of surface roughness on transition occurring on the NLF wing was investigated. The main results are described in Chapter 4.

(4) Stability analysis at higher Reynolds number conditions [Subject (iv)]

Reynolds number effect on transition phenomenon on the NLF wing is the most important subject to establish and confirm JAXA's NEXST-1 aerodynamic design technology. In the flight test, its transition characteristics at higher Reynolds number condition Re_{MAC}=35.2×10^6 (Re_No.5 case), which was about 2.4 times higher than Reynolds number at the design point Re_{MAC}=14.9×10^6 (α_No.4 case), were measured. (Here, Re_{MAC} is Reynolds number based on the mean aerodynamic chord of the NEXST-1.) Then, stability analyses were performed and compared with transition measurement data. Furthermore, transition characteristics on the target pressure distribution Cp_{Target} for the NLF wing design were carefully investigated by applying fixed β strategy. The principal results are described in Chapter 5.

2.3. Stability analysis

2.3.1. Stability analysis at design point (α_No.4)

(1) Boundary layer computations

To improve the discrepancy between measured and numerical transition locations as shown in Fig. 4(d), ONERA and JAXA directly applied present surface-interpolated Cp distribution to compute 3D-LBL characteristics, in place of using CFD(NS)-based Cp distribution as in previous study. Some comparisons of LBL results computed by ONERA and JAXA independently are summarized in Figs. 9 and 10. First of all, comparison of chordwise evolutions of Mach number (M_e), static temperature (T_e) at boundary layer edge (BLE) and wall temperature (T_w) are summarized in Fig. 9(a) at inner wing region (y/s=0.3) and Fig. 9(b) at outer wing region (y/s=0.7). Here, "NS (ES shape)" means the results computed by JAXA with a CFD code involving laminar flow condition (NS mode). "ES" indicates the configuration elastically deformed under aerodynamic load at the design point. They were used in previous stability analysis. In addition, previous results were also plotted in each figure.

In general, there is arbitrariness to define the boundary layer edge. For its computations, ONERA used two definitions: firstly, the boundary layer thickness was defined as the point where the velocity reaches 99.8% of the external velocity (U(y = δ)/U_e= 0.998) (▲); secondly, this point was little modified such as U(y= δ)/U_e=0.995 (●). JAXA used the latter definition to calculate boundary layer edge: these results correspond to the red full line (—). The evolution of the boundary layer thickness ("Delta") as well as the displacement thickness ("Delta*") are plotted in Fig. 9. The displacement thickness is defined as followed:

$$\delta^* = \int_0^{\delta} \left(1 - \frac{\rho U}{\rho_e U_e} \right) dy$$

As well as for external Mach number and static temperature, there is a remarkable correlation between ONERA and JAXA computations. The same kind of comparison, at other spanwise stations (y/s=0.5 and 0.9), are summarized in Figs. E-1 of Appendix E.

As a typical LBL result, dimensionless cross-flow velocity profiles (V/U_e) in external streamline coordinates are plotted in Figs. 10(a) for the inner wing region and Fig. 10(b) for the outer wing region. Here, "z" is the wall normal direction. As mentioned before, ONERA used two definitions of boundary layer edge: U/Ue=0.998 (open triangle symbols) and U(y = δ) / Ue = 0.995 (solid triangle symbols). On the other hand, JAXA compared previous NS-based results (coloured dashed lines) with present results computed with JAXA's 3D boundary layer code at the condition of U(y= δ)/ Ue=0.995 (coloured solid lines). As shown in each figure, ONERA's results (solid triangle symbols) are in rather good agreement with JAXA's ones (coloured solid lines). For other spanwise stations, similar comparisons are summarized in Figs. E-2 of Appendix E.

(2) Stability analysis (envelope strategy)

The laminar boundary layer mean velocity pro-

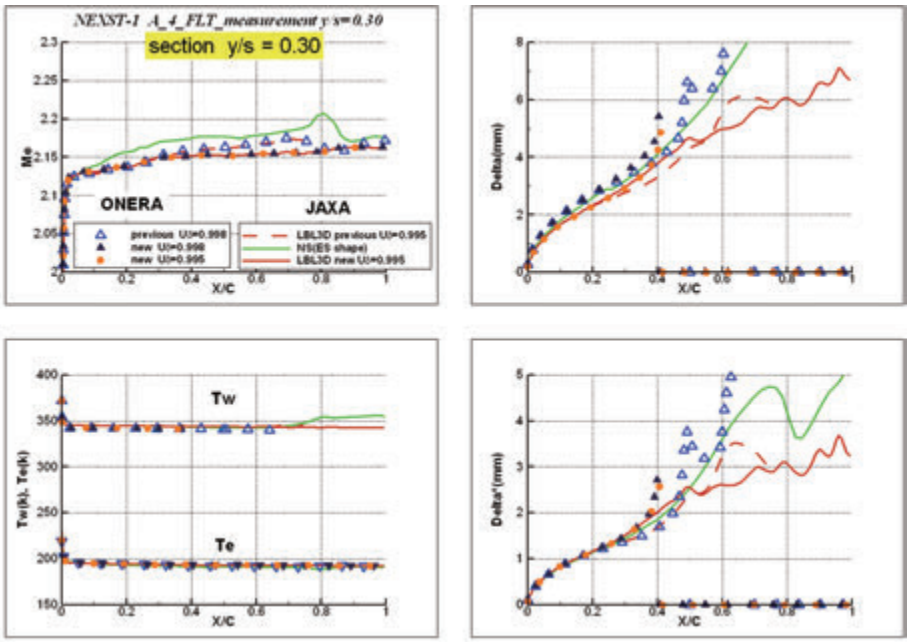

(a) Comparisons of boundary layer thickness at y/s=0.3

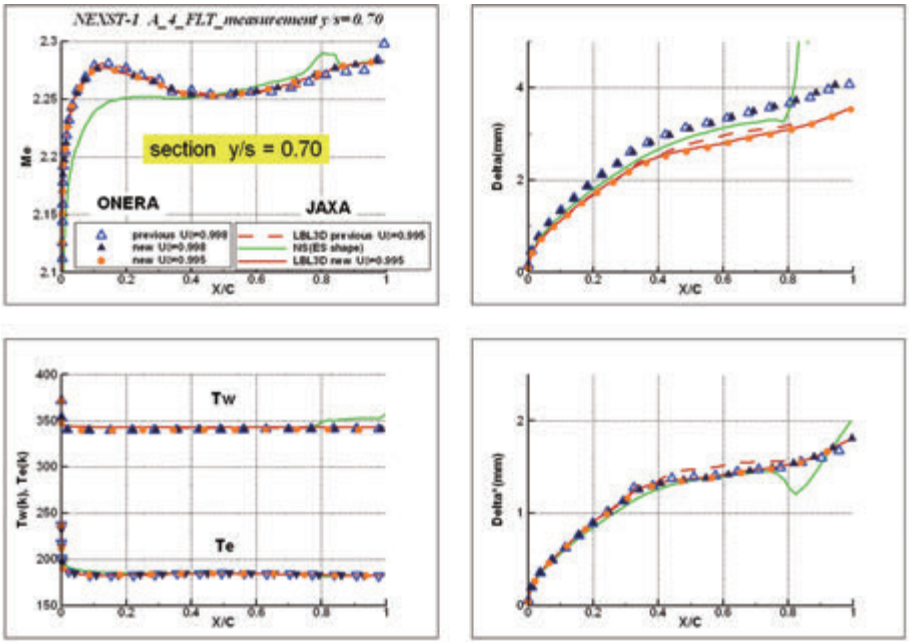

(b) Comparisons of boundary layer thickness at y/s=0.7

Figure 9. Boundary layer computations at α _No.4

files were used to conduct stability analyses. The corresponding N factors and the most amplified propagation direction angles (Ψ) using envelope strategy obtained by ONERA and JAXA are plotted in Figs. 11 and 12. These figures also include transition locations (indicated by "$X_T$exp") measured during the flight test[2] and the corresponding N factor values (called "transition N factor value: $N_{TR.}$").

As similar to previous study, JAXA's N factors are almost in good agreement with ONERA's results as shown in Figs. 11(a) and (b). At other spanwise stations (y/s=0.5 and 0.9), similar comparisons are summarized in Figs. E-3 of Appendix E. There was a slight difference between ONERA's and JAXA's results at mid-span region (y/s=0.5) as shown in Fig. E-3(a). This region corresponds to the kink of leading edge at the NEXST-1

[2] All experimental transition locations are gathered in the arrays of Figs. B-8 of Appendix B

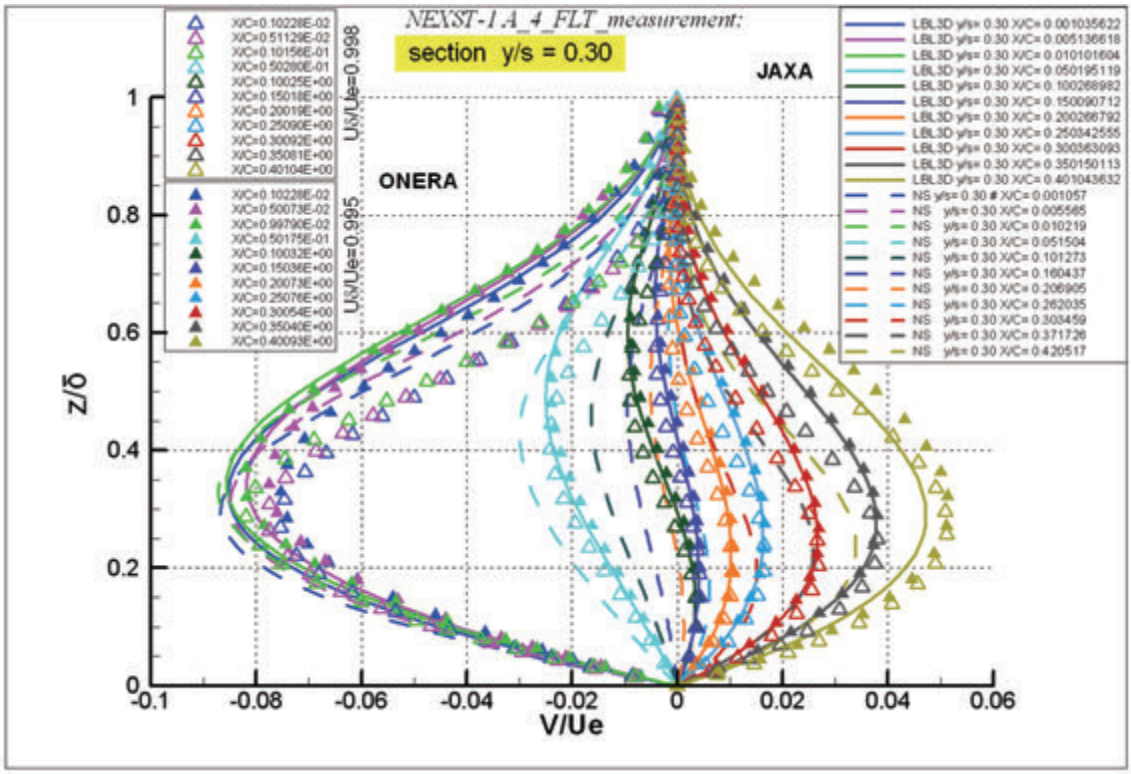

(a) Comparisons of crossflow velocity profiles at y/s=0.3

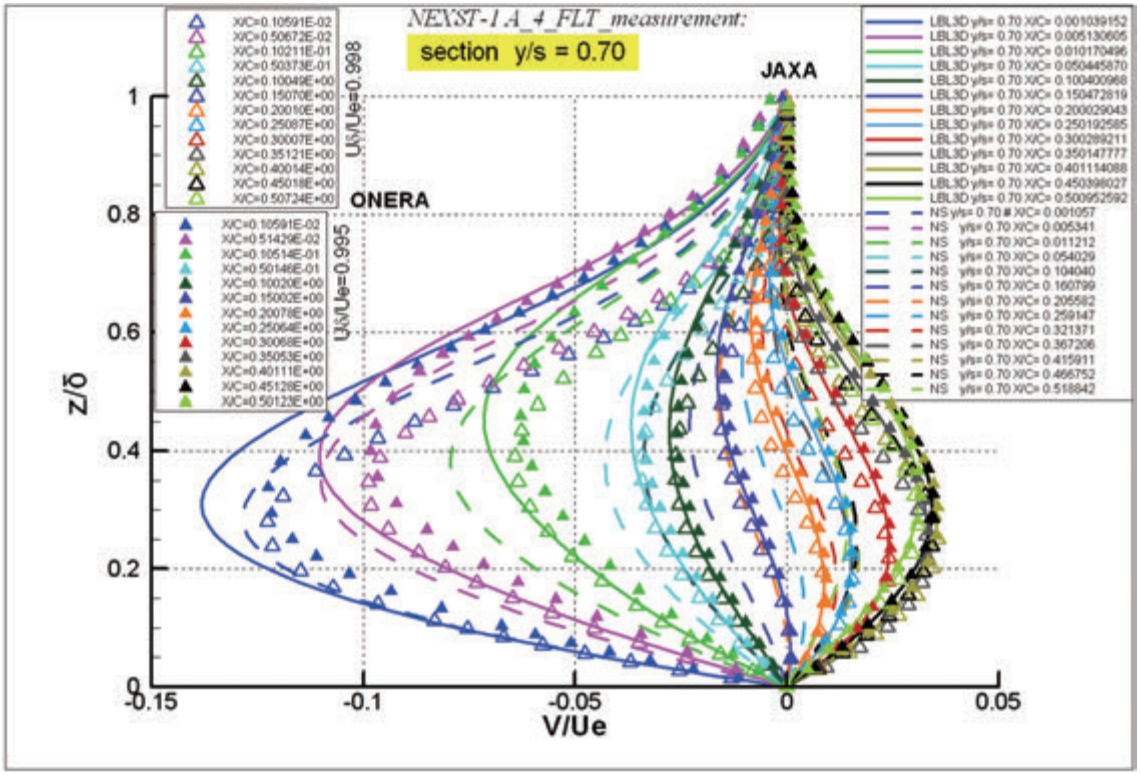

(b) Comparisons of crossflow velocity profiles at y/s=0.7

Figure 10. Boundary layer computations at α _No.4

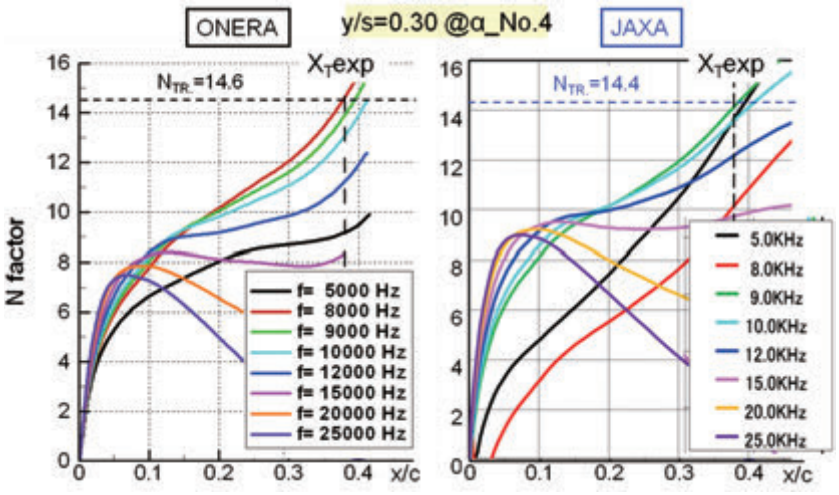

(a) y/s=0.3 (inner wing region)

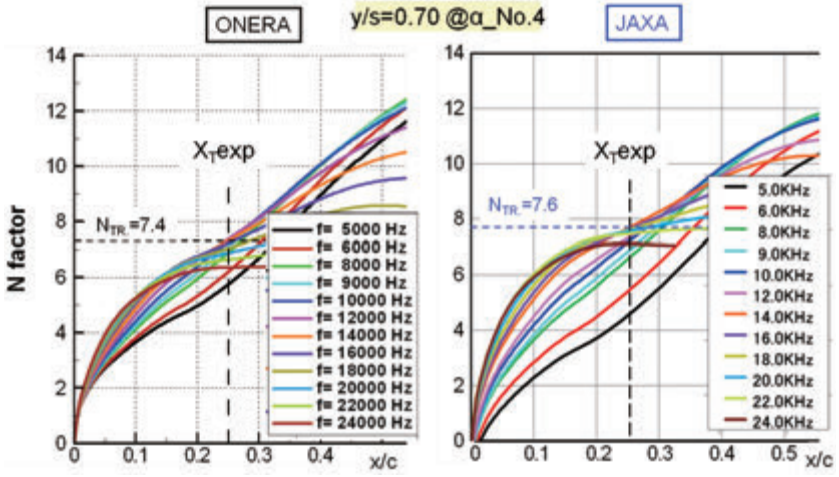

(b) y/s=0.7 (outer wing region)

Figure 11. N factors computed with envelope strategy at design point

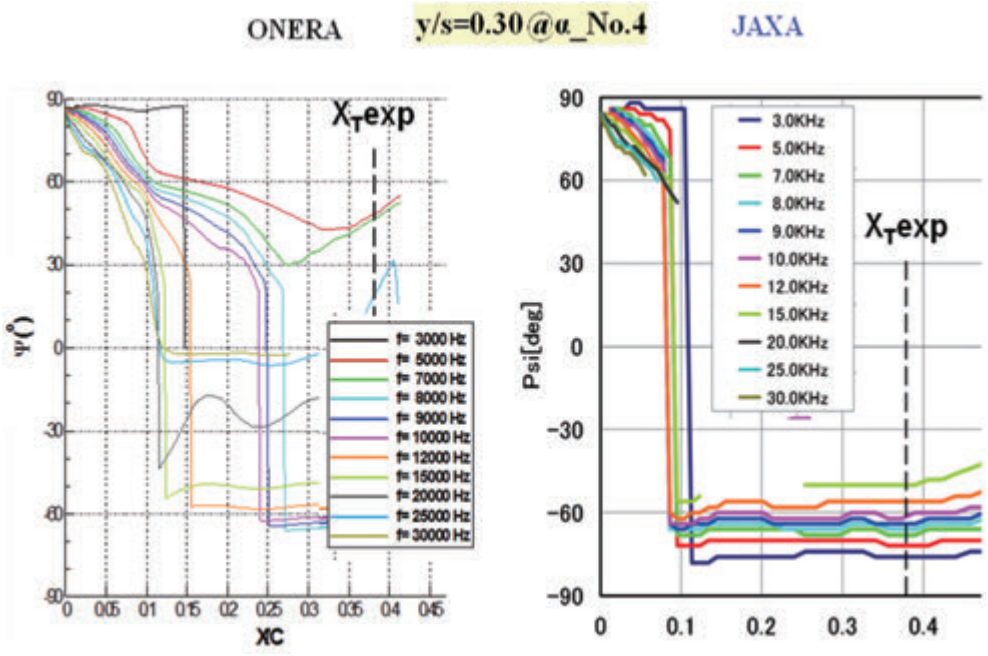

(a) y/s=0.3 (inner wing region)

Figure 12. Propagation direction computed with envelope strategy at α _No.4

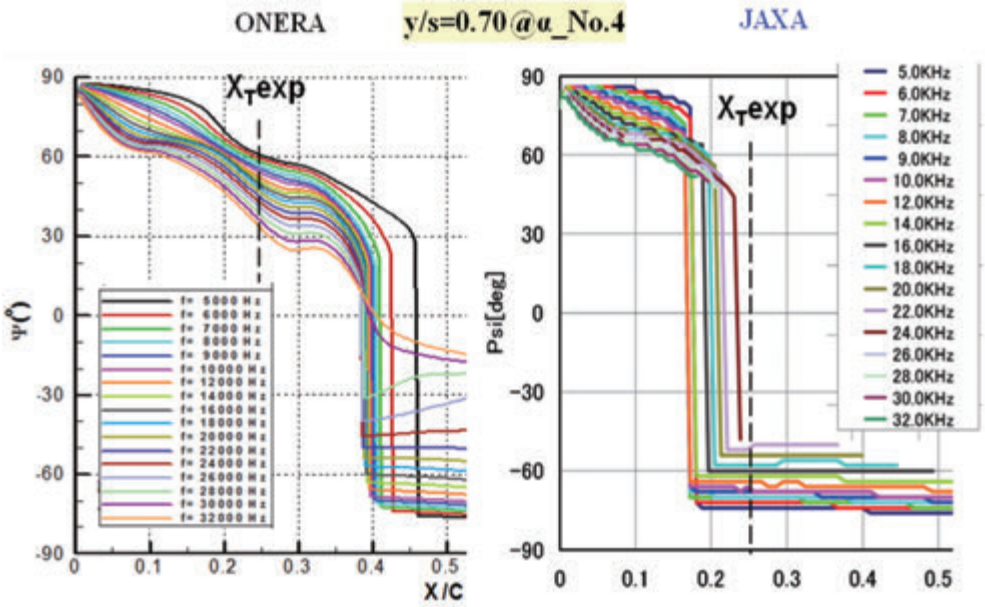

(b) y/s=0.7 (outer wing region)

Figure 12. Propagation direction computed with envelope strategy at α_No.4

wing planform. It was supposed that it generated slight distortion of both surface contour and spanwise pressure gradient. Therefore, each 3D-LBL result near this region was very sensitive to such distortion.

Against our expectation, the $N_{TR.}$ at inner wing region (y/s=0.3) is about two times higher than that at outer region (y/s=0.7) as shown in Figs. 11(a) and (b). If it is assumed that the $N_{TR.}$ should be constant in the spanwise direction, JAXA thinks that the measured transition location at outer region is forced to be located more forward than the location predicted with the constant $N_{TR.}$. This point will be discussed at Chapter 5.

The chordwise evolution of the direction of the wave vector ψ (compared to external streamline) is plotted in Figs. 12 for the inner part of the wing y/s=0.3 (a) and the outer part y/s=0.7 (b). As mentioned before, $\psi \approx 89°$ is representative of CFI whereas $\psi < 60°$ stands for TSI. There is only a qualitative agreement between ONERA and JAXA results. It is no surprising because envelope strategy is very sensitive to the selection of the direction corresponding to the locally most amplified disturbance. That is why there is some discrepancy in the evolution of ψ angle between ONERA and JAXA results. Nonetheless, the evolution of corresponding N factors which correspond to the integration of the eigenvalues α_i are in close agreement. On Figs. 12, the limitation of envelope strategy is illustrated with the suddenly change of ψ value which corresponds to a change of nature of instabilities from crossflow to Tollmien-Schlichting ones. Such a limitation can be overcome using fixed β strategy.

(3) Stability analysis (fixed β strategy)

Figs. 13 and 14 show similar comparisons of N factors and propagation direction angles (ψ) computed with fixed β strategy by both parties. The range of several combinations of (β_r, f) was specified as follows:

$$-450 \le \beta_r[m^{-1}] \le 3000,\ 3 \le f[kHz] \le 25 \quad for\ y/s = 0.3$$
$$-500 \le \beta_r[m^{-1}] \le 2000,\ 4 \le f[kHz] \le 20 \quad for\ y/s = 0.7$$

These values were defined on agreement with previous envelope strategy computations. First of all, JAXA's results of both N factors and ψ distributions are in good agreement with ONERA's ones. But there was remarkable difference between ONERA's and JAXA's results at mid-span region (y/s=0.5) as shown in Fig. E-5(a) of Appendix E: as mentioned before, this section corresponds to the kink of the leading edge.

Then, as easily seen in these figures, contrary to envelope method, fixed β strategy can clearly

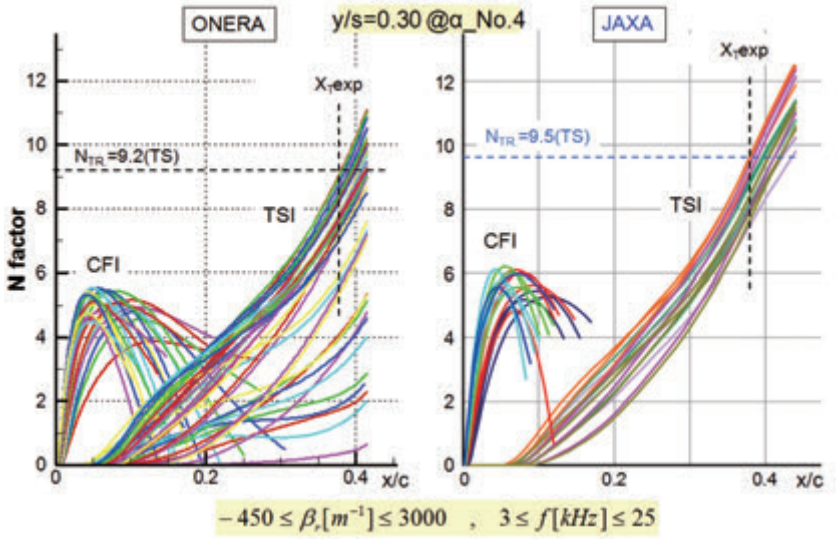

(a) y/s=0.3 (inner wing region)

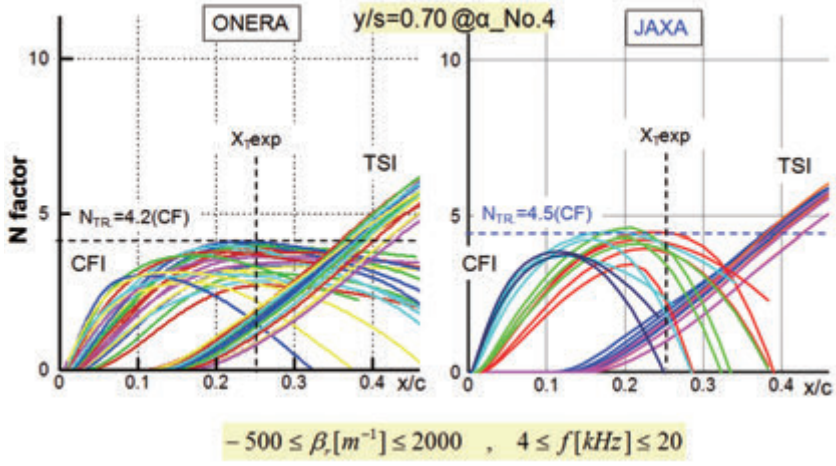

(b) y/s=0.7 (outer wing region)

Figure 13. N factors computed with fixed β strategy at design point

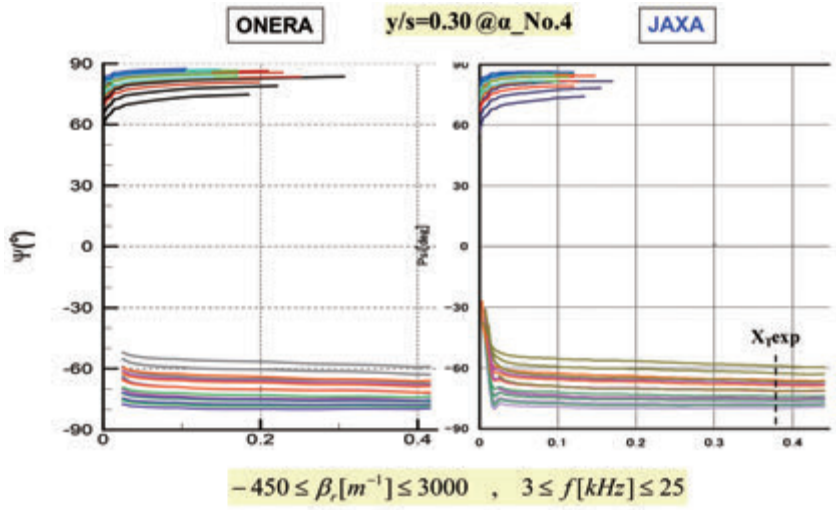

(a) y/s=0.3 (inner wing region)

Figure 14. Propagation direction computed with fixed β strategy at α_No.4

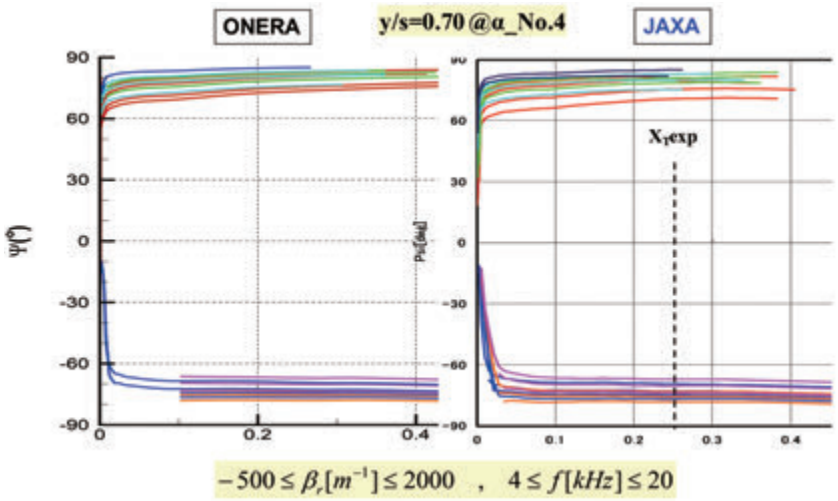

(b) y/s=0.7 (outer wing region)

Figure 14. Propagation direction computed with fixed β strategy at α_No.4

split instabilities into two modes: crossflow instabilities on one hand and Tollmien-Schlichting instabilities on the other hand. N factors due to CFI mode (N_{CFI}) rapidly increase near the leading edge where the flow is accelerated (high negative pressure gradient), then N factors due to TSI mode (N_{TSI}) gradually grows after the maximum of the N_{CFI} in region where the pressure gradient is weakly negative or positive as illustrated by the comparison between Figs 6 and 13.

According to the measured transition data, it is recognized that the most dominant instability is TSI at inner wing region (y/s=0.3) as shown in Fig. 13(a). The transition N factor obtained by fixed β strategy at the transition location is N=9.5. On the contrary for the outer part on the wing, transition process is conducted by CFI (Fig 13(b)) and occurs close to the leading edge for low value of N factor N=4.5. The evolutions of ψ angles are given in Figs. 14. Further stability results at other spanwise stations computed with fixed β strategy revealed that TSI is the most dominant instability over the whole wing region as shown in Fig. 15(b) except at y/s=0.7. This figure also includes predicted transition lines based on some typical N values provided by envelope strategy.

(4) Summary

Present comparison of N factors and ψ distributions computed by both parties for α_No.4 are summarized in Table 2. There was good correlation between ONERA's and

Table 2. Summary of stability analysis at α_No.4

a-sweep_4	Exp. (FLT)	N (envelope strategy)					
y/s	$(x/c)_{TR}$	ONERA			JAXA		
		f (Hz)	N	ψ (°)	f(Hz)	N	ψ (°)
0.30	0.38	8000	14.6	-64.6	8200	14.4	-64
0.50	0.44	6000	6.4	-71.1	7600	10	-66
0.70	0.25	12000	7.4	-65.0	18500	7.6	-56
0.90	0.50	16000	4.4	57.5	11000	5.4	66

α_4	Exp. (FLT)	N(fixed β strategy)									
y/s	$(x/c)_{TR}$	ONERA					JAXA				
			f (Hz)	β	N	ψ (°)		f (Hz)	β	N	ψ (°)
0.30	0.38	TS	5000	-300	9.2	-71.4	TS	5400	-300	9.5	-70.1
0.50	0.44	TS	6000	-300	4.1	-68.7	TS	6600	-300	7.7	-67.4
0.70	0.25	CF	15000	1000	4.2	78.9	CF	15500	850	4.5	76.1
0.90	0.50	TS	11000	-400	2.4	-64.3	TS	10000	400	2.4	63.5

JAXA's stability results as shown in this table. Comparison of previous and present stability analyses shown in Fig. 15(a), demonstrates slight improvement at inner wing region using present surface-interpolated Cp distribution. But certain discrepancy between measured and predicted transition location still exists.

From Fig. 15(b), it was confirmed that CFI was well suppressed except for a narrow zone around y/s=0.7, namely the most dominant mode responsible for transition onset was TSI. As for the transition at the narrow zone, its origin exists in the fact that the transition was measured relatively close to the leading edge as explained previously. There might be a few possibilities, for example, influence of surface roughness on transition phenomenon, small spanwise deviation between measured and target Cp contours, and so on. Before discussing them, to understand effectiveness of present Cp distribution on suppressing CFI clearly, influence of angle of attack (AOA) on transition process has been studied and summarized in the next sub-section. Finally, N=14 and 8 due to envelope strategy almost correspond to the measured transition locations based on HF/DP data at inner and outer wing regions, respectively.

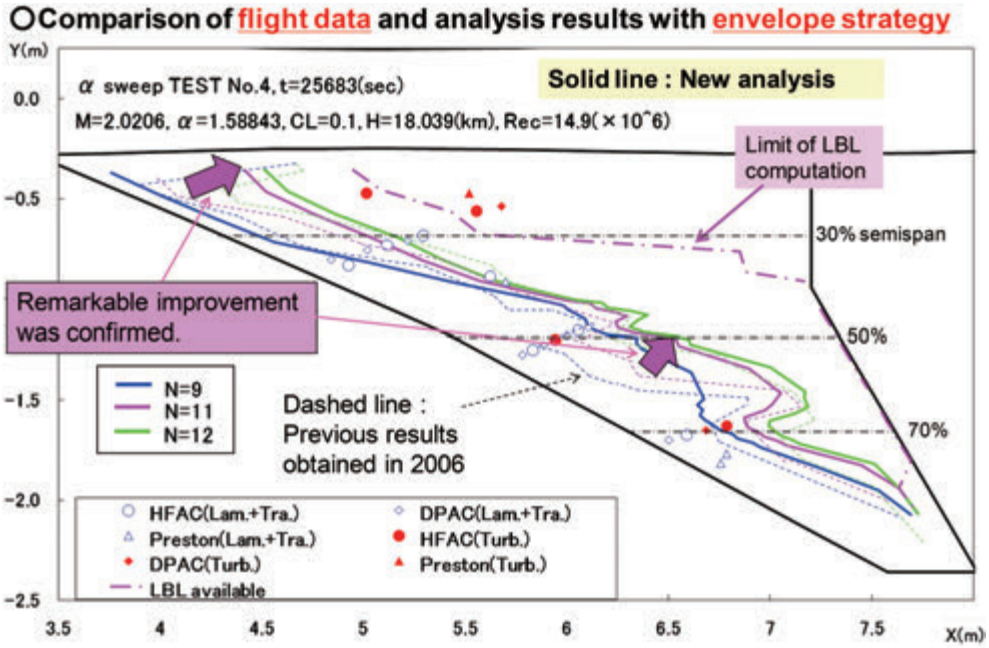

(a) Comparison of previous and present results

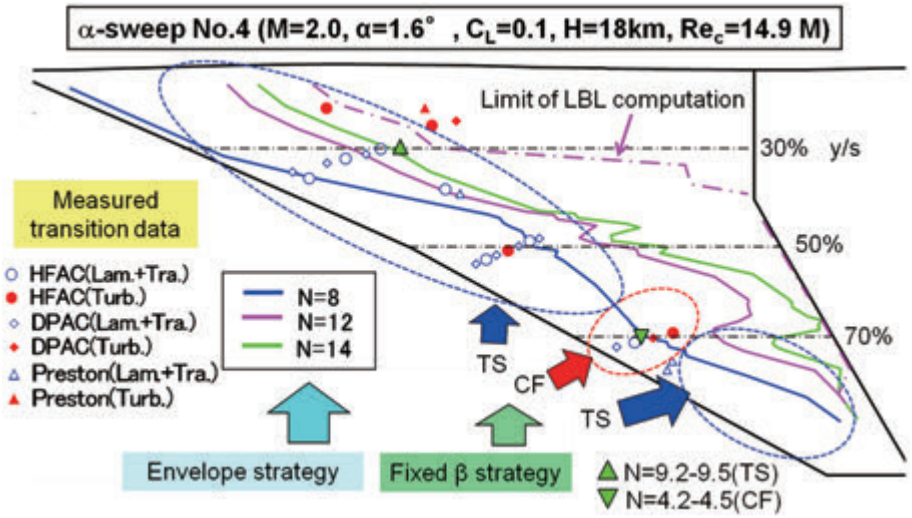

(b) Comparison of FLT data and N contours

Figure 15. Summary of stability analysis at α_No.4

2.3.2. Stability analysis at off-design points (α_No.2 and α_No.3)

(1) Boundary layer computations

In the flight test, 6 steps of angle of attack were specified and the design point was realized at the 4th step (α_No.4). As typical off-design point condition, the 2nd step (α_No.2), and the 3rd step (α_No.3) were selected in this section. The corresponding angle of attack were AOA=-0.09° and AOA=0.77° corresponding to the lift coefficients of C_L=0.04 and C_L=0.07 respectively.

As previously mentioned, JAXA did not apply the surface-interpolation technique to the Cp distributions for LBL computations at these off-design points, because the differences between measured and CFD(NS)-based Cp distributions were very small. Based on the CFD(NS)-based Cp distributions, JAXA computed 3D-LBL characteristics as shown in Figs. F-1(a) and (b) of Appendix F at each α_No.2 and α_No.3. These figures include chordwise Cp distributions, boundary layer thickness (δ) distributions, and representative crossflow velocity profiles plotted in the external streamline coordinate for two spanwise positions, y/s=0.3 and y/s=0.7, and several chorwise stations.

To help our understanding of stability characteristics, comparisons of crossflow velocity profiles at design point (α_No.4) and at α_No.2 case as one of typical off-design points are summarized in Figs. 16. As shown in these figures, the change of maximum crossflow velocity from leading edge region to front part of its chord (namely, x/c=0.3) is more remarkable at the design point than at the off-design point. It will be seen later that this generates meaningful difference in stability characteristics.

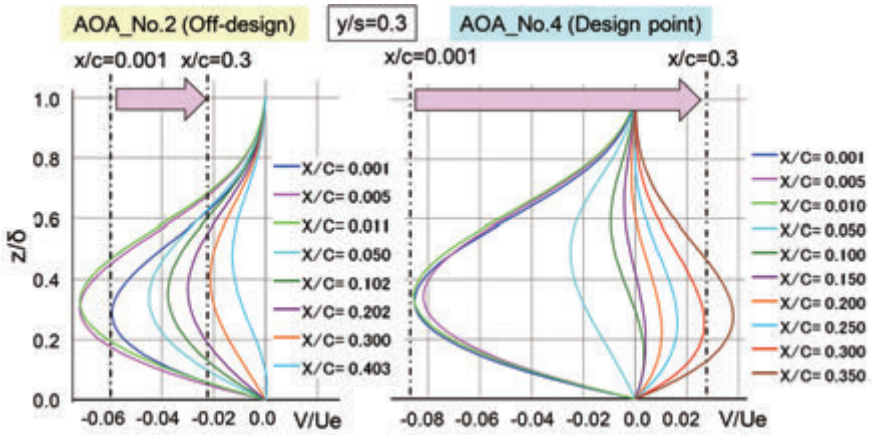

(a) y/s=0.3 (inner wing region)

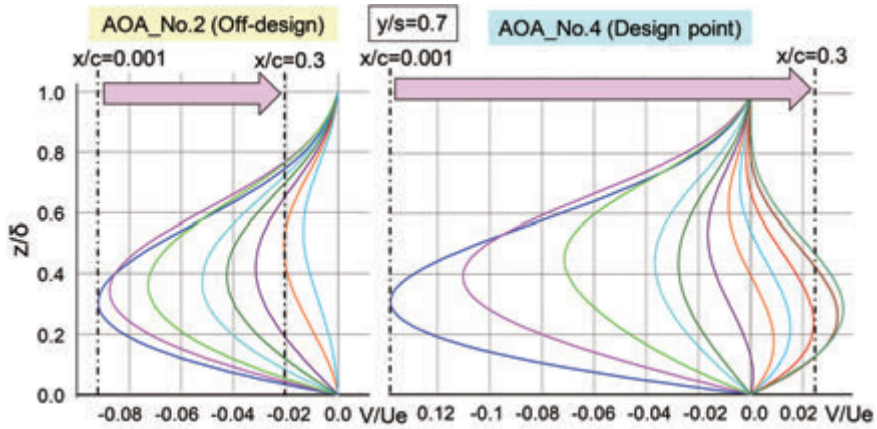

(b) y/s=0.7 (outer wing region)

Figure 16. Comparison of crossflow velocity growth at design point and typical off-design point

(2) Stability analyses (envelope strategy and fixed β strategy)

N factors computed with envelope and fixed β strategies are summarized in Figs. F-2 and F-3 of Appendix F for the off design cases α_No.2 and α_No.3. In this section, α_No.2 case is focused on. Figs. 17(a) and (b) show these N factors obtained with both envelope and fixed β strategies at α_No.2 case, respectively. The range of several combinations of (β_r, f) in fixed β strategy was specified as follows:

$-450 \le \beta_r[m^{-1}] \le 3000$, $3 \le f[kHz] \le 25$ *for* $y/s = 0.3$
$-500 \le \beta_r[m^{-1}] \le 2000$, $4 \le f[kHz] \le 30$ *for* $y/s = 0.7$

To understand the effect of JAXA's NLF wing design concept, JAXA focused on the comparison of N factors at the design point (α_No.4) and at the off-design point (α_No.2). As easily seen in Figs. 17(a) and (b), N factors at the off-design point are larger than the ones obtained at the design point (as compared with Figs. 11 and 13). By comparing N factors and measured transition location, it is clear that the CFI is dominant and responsible for an early transition. The first reason is the extension of the accelerated zone: the external flow keeps being accelerated which leads to an amplification of CFI as illustrated in Fig. 6. The second reason of non-suppression of CFI at α_No.2 lies in the evolution of crossflow velocity profiles. For the off-design point, its crossflow velocity profile (plotted in streamline coordinates) in the boundary layer thickness remains negative

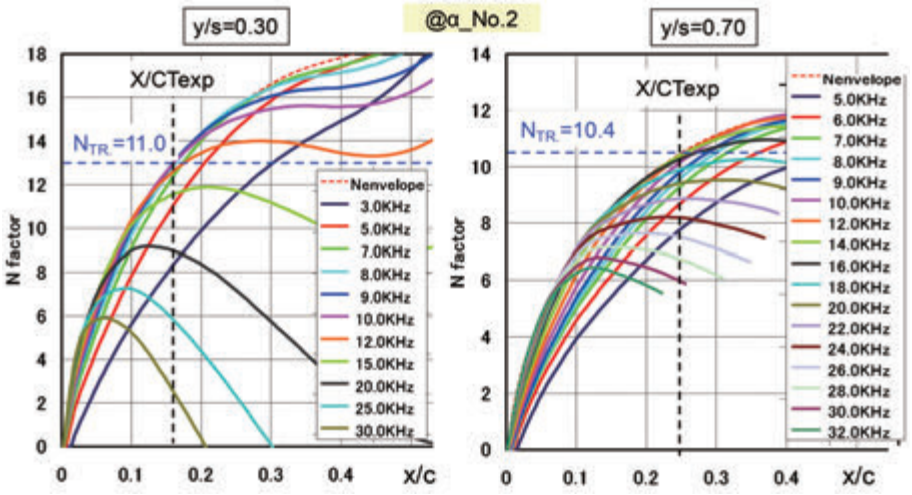

(a) Envelope strategy

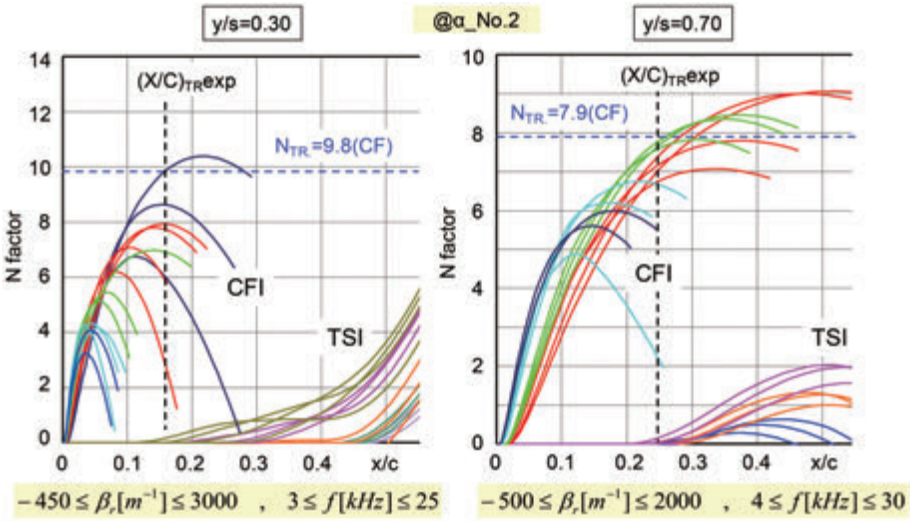

(b) Fixed β strategy

Figure 17. Stability characteristics at α_No.2 (off-design point)

moving downstream as represented in Fig. 16. This means that the crossflow velocity is orientated towards the concavity of the external streamline. On the other hand, at the design point, the crossflow velocity is still negative in the leading edge region but rapidly changes its sign and keep weak values reducing the amplification of CFI. Therefore, the NLF wing design concept is based on suppression of CFI due to existence of reverse change of crossflow velocity direction.

As illustrated in Figs. F-3(a) and (b) of Appendix F, CFI at each off-design point was also not suppressed due to large crossflow velocity and no change of the direction of crossflow velocity vector.

(3) Summary

Fig. 18 (or Fig. F-4(a)) shows a comparison of measured transition data and N factors computed with both envelope and fixed β strategies at several spanwise stations for α_No.2 case. N=10 provided by envelope strategy is in good agreement with measured transition locations. Stability analysis obtained with fixed β strategy reveals that CFI is dominant on transition phenomenon except for tip region (y/s=0.9) as shown in Fig. 18. This means that the shape of Cp distribution at the design point, which is almost the same as the Cp_{Target}, is the only effective one to suppress the CFI. On the other hand, other Cp distributions at some off-design points, especially near leading edge have no potential to suppress the CFI. It becomes one of evidences for validation of JAXA's NLF wing design concept. Another comparison at α_No.3 case, illustrated in Fig. F-4(b) of Appendix F, shows the same kind of results as the α_No.2 case.

2.3.3. Stability analysis at higher Reynolds number condition (Re_No.5)

(1) Boundary layer computations

As mentioned above, JAXA applied the surface-interpolated technique to the measured Cp distributions at Re_No.5 case as shown in Fig. 5(d) and Fig. 6. Figures 19(a) and (b) exhibit a comparison of crossflow velocity profiles computed by JAXA at the design point (α_No.4) and at Re_No.5 case as a typical higher Reynolds number condition. From the viewpoint of the aerodynamic design of the NEXST-1, Cp distributions at both α_No.4 and Re_No.5 cases should be the same. As shown in Fig. 6, both Cp distributions are comparable except in the leading edge region, which originates from elastic deformation. In general, boundary layer theory leads to no Reynolds number effect in the shape of crossflow velocity profiles normalized with boundary layer thickness and external velocity, that is z/δ vs. V/Ue. Figures 19 clearly shows such situation. Reynolds number effect only appears in the evolution of boundary layer thickness δ.

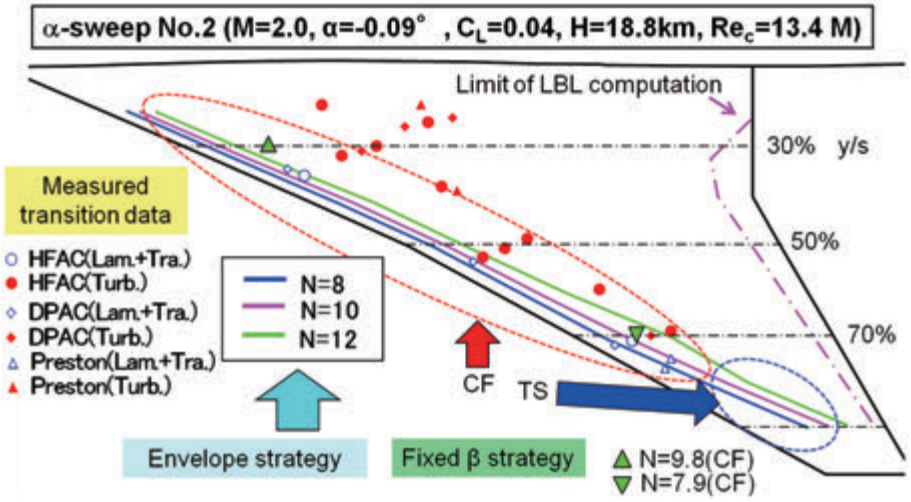

Figure 18. Comparison of transition analysis and measurement results at a typical off-design point

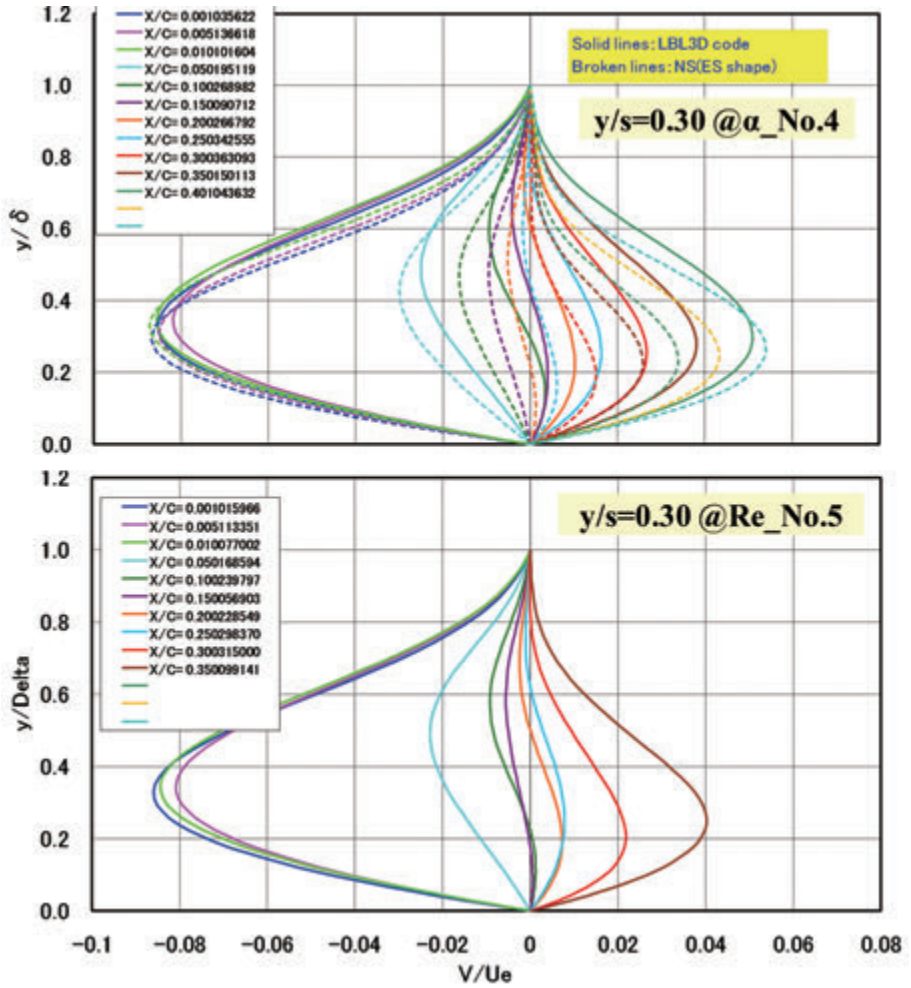

(a) Comparisons of crossflow velocity profiles at y/s=0.3

Figure 19. Boundary layer computations at Re_No.5

(2) Stability analyses (envelope strategy and fixed β strategy)

Stability analyses with both envelope and fixed β strategies were performed at Re_No.5. Figs. 20 and 21 show comparisons of N factors and propagation direction angles (ψ) by selecting the most amplified disturbance, i.e. computed with envelope strategy. There is almost good agreement between ONERA and JAXA results, but transition N value is slightly different. This is probably due to the fact that numerical error on eigenvalue computation increases with Reynolds number.

Figs. 22 and 23 show similar comparisons of N factors and propagation direction angles (ψ) computed with fixed β strategy at Re_No.5. The range of several combinations of (β_r, f) was specified as follows:

$-300 \le \beta_r[m^{-1}] \le 5000$, $6 \le f[kHz] \le 50$ *for* $y/s = 0.3$ *by ONERA*
$-450 \le \beta_r[m^{-1}] \le 3000$, $3 \le f[kHz] \le 20$ *for* $y/s = 0.3$ *by JAXA*
$-600 \le \beta_r[m^{-1}] \le 10000, 10 \le f[kHz] \le 40$ *for* $y/s = 0.7$ *by ONERA*
$-300 \le \beta_r[m^{-1}] \le 2000$, $4 \le f[kHz] \le 20$ *for* $y/s = 0.7$ *by JAXA*

There is almost good agreement between ONERA's and JAXA's results in both figures. By comparing measured transition location with N factors at y/s=0.3 and 0.7, it was cleared that the most dominant disturbances was CFI at higher Reynolds number condition as shown in Figs. 22(a) and (b).

(3) Summary

Present stability results are summarized in Tables 3(a)-(b) and Appendix G for y/s=0.5 and y/s=0.9. Consideration of whole results along several spanwise stations reveals that the CFI is nearly dominant except for tip region (y/s=0.9)

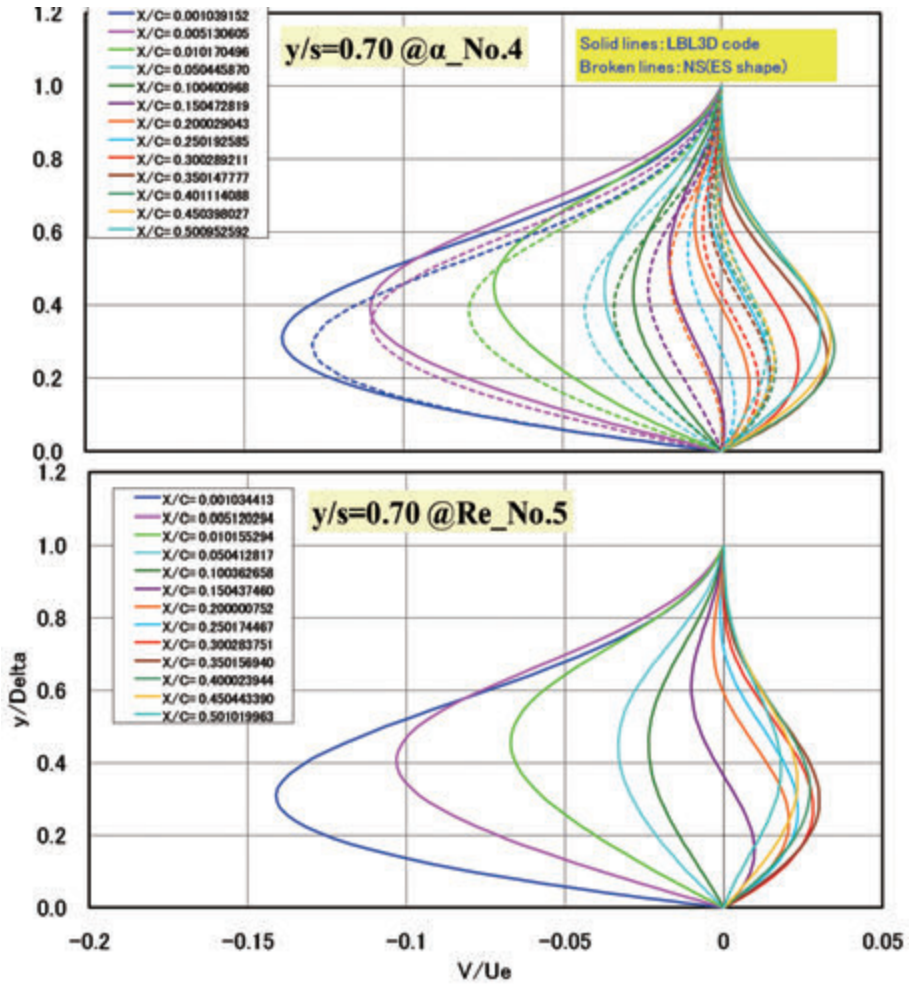

(b) Comparisons of crossflow velocity profiles at y/s=0.7

Figure 19. Boundary layer computations at Re_No.5

and kink region of leading edge (y/s=0.5) as shown in Fig. 24. From this figure, N=12 computed with envelope strategy are in good agreement with transition data measured with HF/DP at inner and outer wing regions, respectively. Against our expectation, however, CFI was not suppressed at such higher Reynolds number condition. It means present ideal pressure distribution for JAXA's NLF wing design concept is not optimum and needs to be improved. JAXA has already improved the Cp_{Target} using JAXA's transition analysis code[10]. (Recently, JAXA has tried to design a new NLF wing by using the improved Cp_{Target} and our CFD-based inverse design method.)

2.4. Summary of chapter 2

(1) Subjects

In this chapter, the following three subjects have been investigated:

a) The quantitative discrepancy between measured and predicted transition locations at outer wing region in case of the design point of the flight test. To do this, JAXA modified the Cp distributions for 3D-LBL computations to reduce the difference between CFD(NS)-based and measured Cp distributions, by using a surface interpolation technique.

b) JAXA also applied present surface-interpolation technique for improving the Cp distributions at higher Reynolds number case. However, the CFD(NS)-based Cp distributions were directly applied to compute 3D-LBL characteristics at other AOA cases, because the differences between measured and CFD(NS)-based Cp distributions were nearly negligible.

c) JAXA and ONERA computed 3D-LBL and stability characteristics with both envelope and

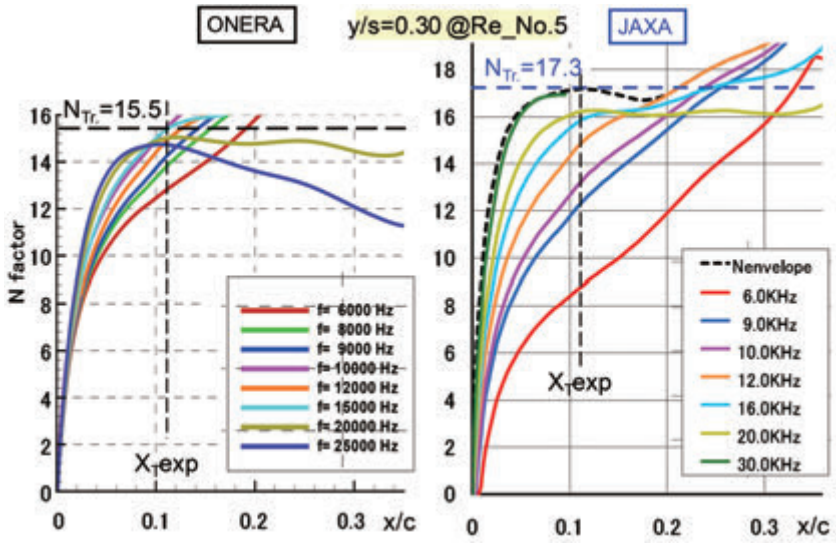

(a) y/s=0.3 (inner wing region)

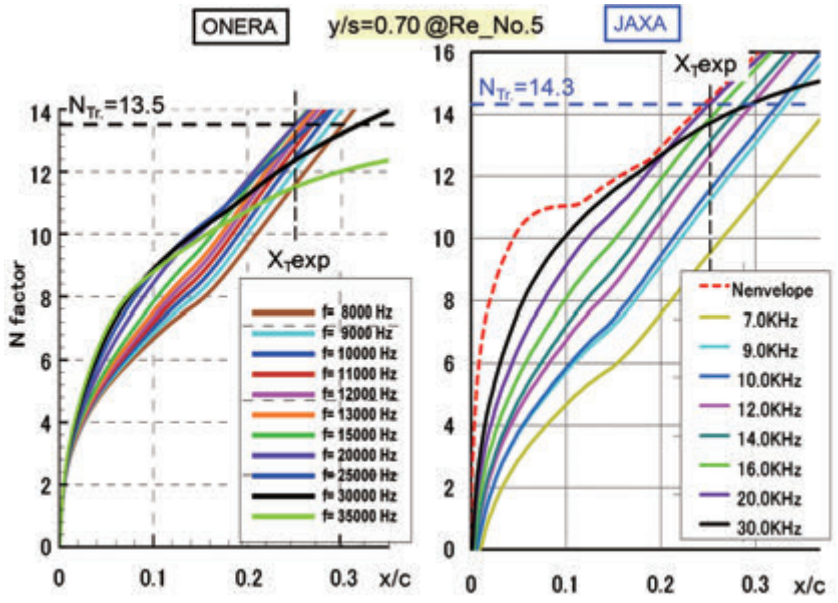

(b) y/s=0.7 (outer wing region)

Figure 20. N factors computed with envelope strategy at Re_No.5

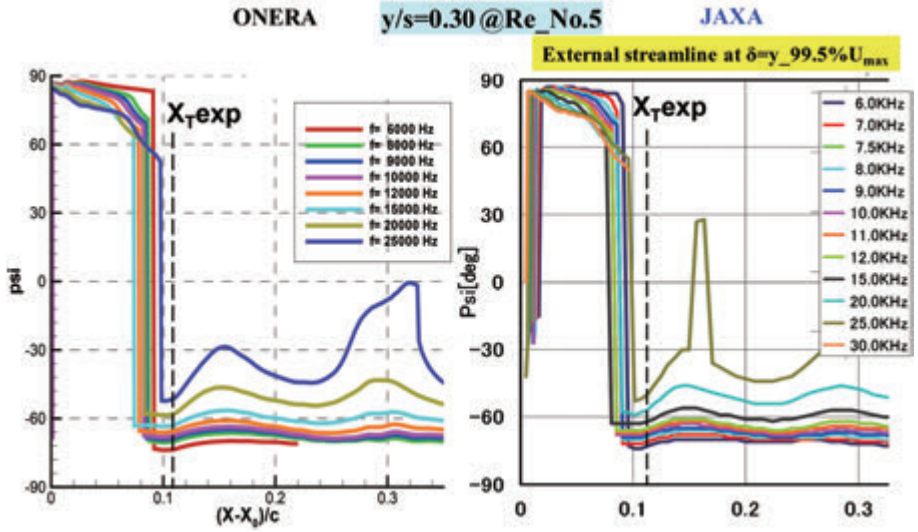

(a) y/s=0.3 (inner wing region)

Figure 21. Propagation direction computed with envelope strategy at Re_No.5

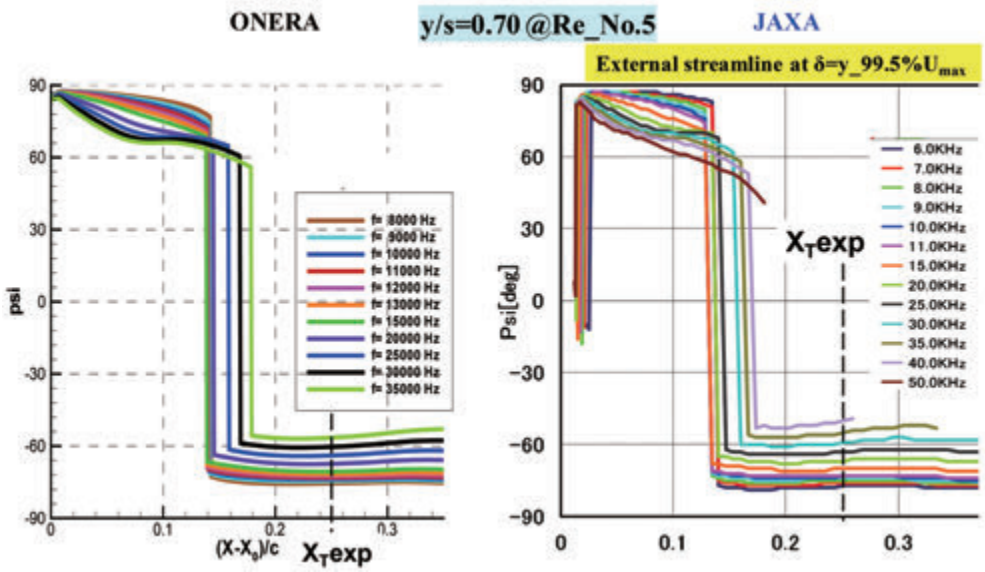

(b) y/s=0.7 (outer wing region)

Figure 21. Propagation direction computed with envelope strategy at Re_No.5

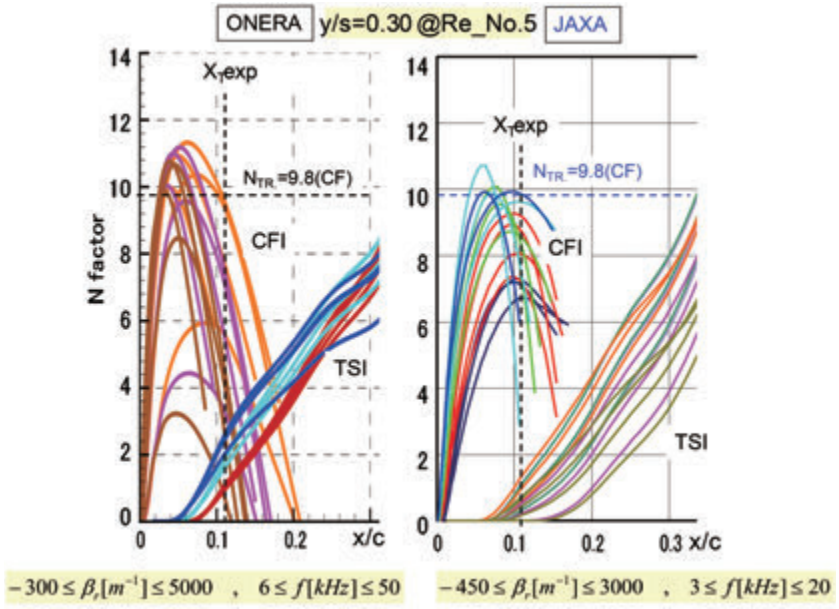

(a) y/s=0.3 (inner wing region)

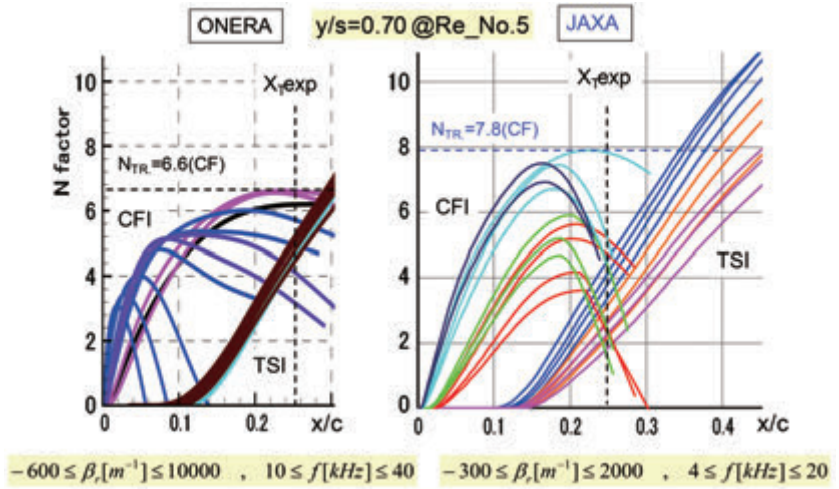

(b) y/s=0.7 (outer wing region)

Figure 22. N factors computed with fixed β strategy at Re_No.5

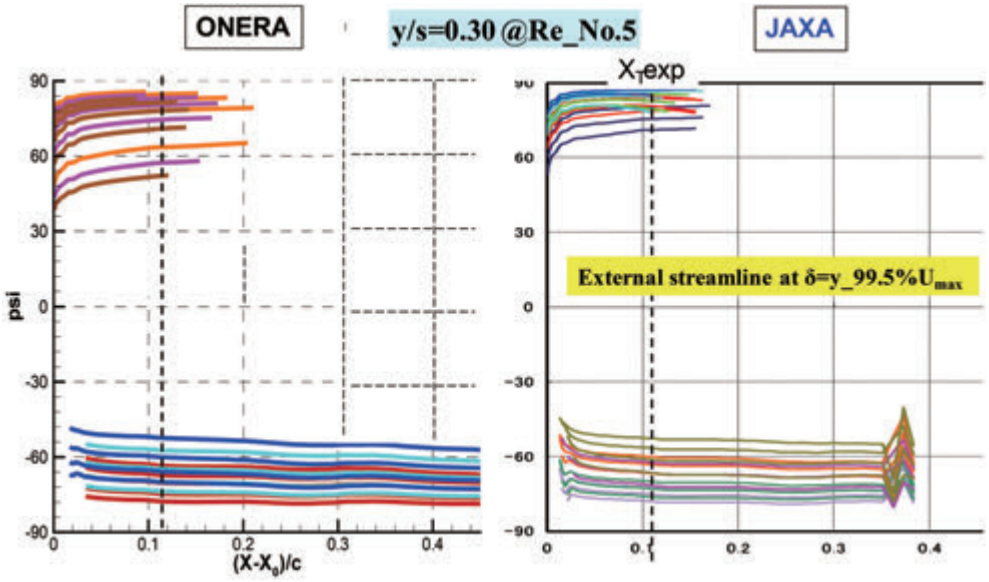

(a) y/s=0.3 (inner wing region)

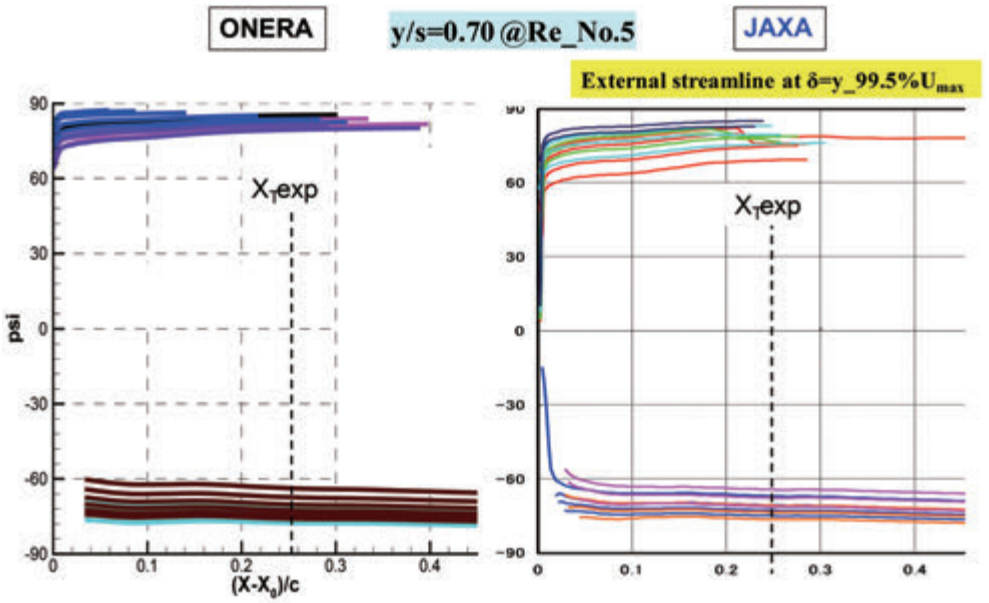

(b) y/s=0.7 (outer wing region)

Figure 23. Propagation direction computed with fixed β strategy at Re_No.5

fixed β strategies, then compared their N factors with measured transition locations. According to the fixed β strategy, both parties investigated the nature of transition by confirming the most dominant instability, namely TS or CF instabilities.

(2) Principal results

Then, the following four results were obtained:
a) For the design point, stability analysis with envelope strategy quantitatively showed good correlation between measured transition and N contours at inner wing region, namely the transition N value was nearly 12. But other N value, namely N=8 was found at outer wing region.

b) For the design point, it was confirmed that the crossflow instability was strongly suppressed in the whole part of the wing except for a narrow region near y/s=70% in spanwise direction.

c) However, the CFI was not suppressed at a higher Reynolds number condition. It means any improvement is necessary to extend JAXA's natural

Table 3. Summary of stability analysis at Re_No.5

(a) Envelope strategy

Re_5	Exp. (FLT)	N(envelope strategy)					
y/s	$(x/c)_{TR}$	ONERA			JAXA		
		f (Hz)	N	Ψ (°)	f(Hz)	N	Ψ (°)
0.15	0.11				22500	19.3	-60
0.20	0.11					20.5	
0.30	0.11	10000	15.4	-67.5	23000	17.3	-55
0.40	0.06					11.2	
0.50	0.32	10000	9.5	-60	15500	10.6	-58
0.60	0.28					10	
0.70	0.25	20000	13.5	-67.5	22500	14.3	-66
0.80	0.32					10	
0.90	0.32	21000	10	-69.6	24500	9.7	-68

(b) Fixed β strategy

Re_5	Exp. (FLT)	N(fixed β strategy)									
y/s	$(x/c)_{TR}$	ONERA					JAXA				
			f (Hz)	β	N	Ψ (°)		f (Hz)	β	N	Ψ (°)
0.15	0.11	CF	15000	2000	10.9	84.1		20000	1350	8.9	77.8
0.20	0.11						CF			13	
0.30	0.11	CF	30000	3000	9.6	82.6	CF	21000	1750	9.8	79.3
0.40	0.06						CF			5	
0.50	0.32	TS	10000	500	5.3	68.3	TS	10500	-500	6.7	-68.0
0.60	0.28						CF			4.3	
0.70	0.25	CF	20000	2000	6.6	83.5	CF	26500	1600	7.8	77.8
0.80	0.32						TS			7.6	
0.90	0.32	TS	20000	-1000	4.7	-69.9	TS	18500	-950	5.2	-70.6

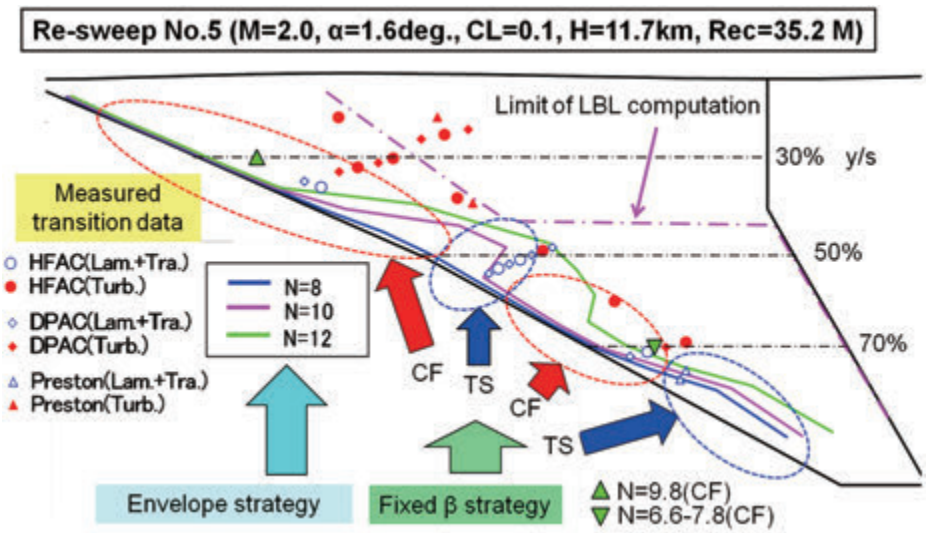

~ Comparison of FLT data and N contours ~

Figure 24. Summary of stability analysis at Re_No.5

laminar flow wing design to higher Reynolds number flows.

d) Furthermore, in the same way, the CFI was also not suppressed at off design condition corresponding to α_No.2 and α_No.3 cases.

3. Stability computations at S2MA test conditions

3.1. Outline of S2MA wind tunnel test

(1) S2MA wind tunnel

The main purpose of this wind tunnel test was to validate JAXA's NLF wing design concept experimentally. The experiment was carried out in 2000 in the continuous supersonic ONERA wind tunnel of Modane-Avrieux centre (S2MA wind tunnel)[6]. The test section, represented in Fig. 25, is 1935 mm high and 1750 mm width. Total pressure in the test section can be adjusted between 0.2 and 1.8 bar covering a wide range of Reynolds numbers. The main problem concerning laminarity studies in wind tunnel concerns the level of disturbances in the test section (pressure disturbances p_0 as well as velocity disturbances u_0).

In 1993, the quality of the flow in S2MA test section was investigated and two approaches were used. The first one consisted of a direct disturbance level measurement using an unsteady pressure sensor and a hot film probe[11]. The second way rested on combined infra-red (IR) visualizations on a 10° sharp cone coupled with stability computations. Indeed, in the 70's, adequacy of many wind tunnel facilities (in USA and Europe) to simulate flight test conditions has been tested measuring transition location on the famous AEDC cone[12].

Level of pressure and velocity fluctuations in S2MA test section are represented in Fig. 26, at Mach 2 for total pressure between $0.5 < P_0 < 1.5$ bar. (Here, in this report in agreement with NEXST-1 notation, total pressure is notified as "P_0" instead of "P_i" used by ONERA). In supersonic configurations, the wind tunnel can be considered as a quiet one since disturbances are rather low: static pressure fluctuation $Cp'_{rms} \fallingdotseq 0.2\%$ and freestream velocity fluctuation $Tu \fallingdotseq 0.15\%$. From these measurements, it is possible to compute a transitional N factor. Lying on the fact that amplitude of these disturbances depends on external disturbance level, Mack[13] used empirical correlations and proposed relation (4) which established a direct link between the N factor at transition (N_T) and the external freestream turbulence level Tu. Higher N_T value means that the flow quality is better and it corresponds to natural transition.

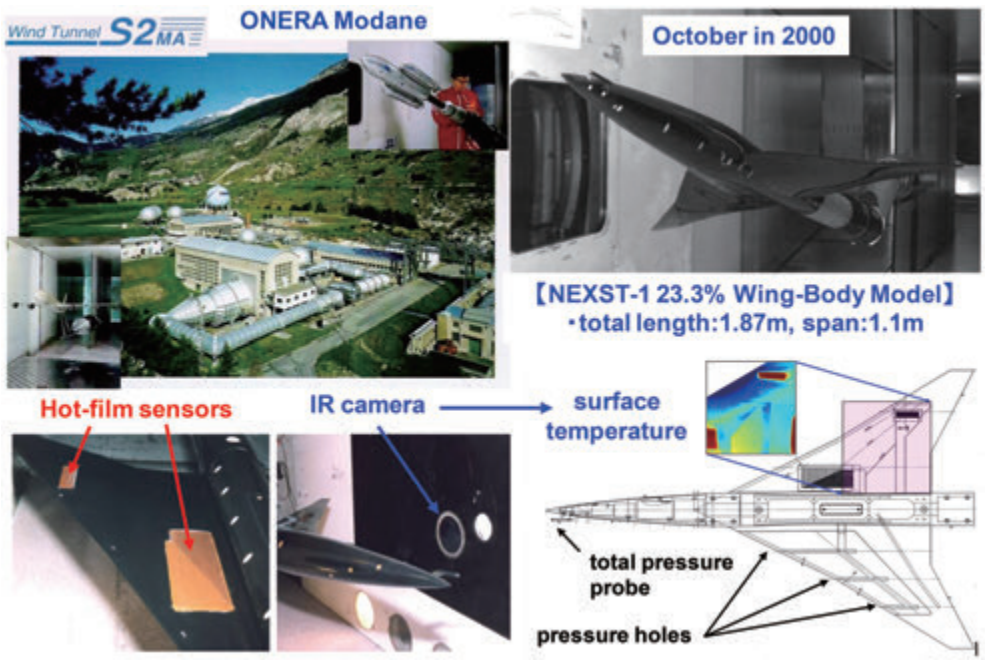

Figure 25. Transition measurement test at ONERA-S2MA

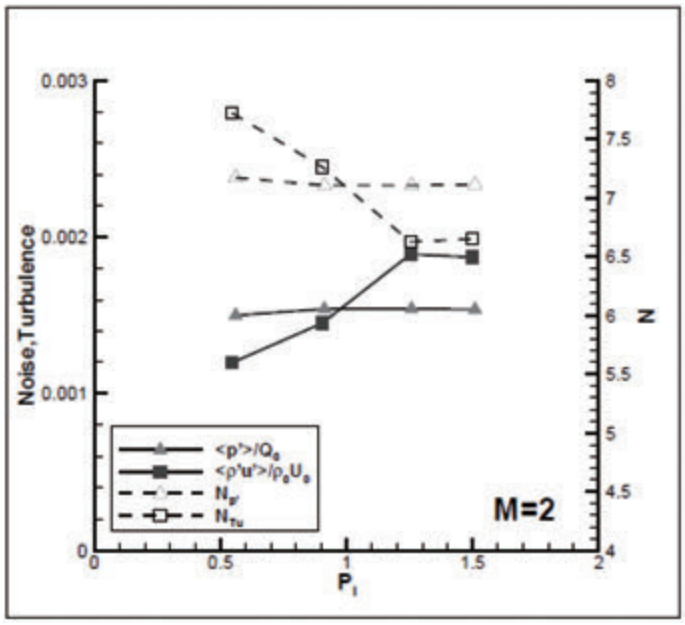

Figure 26. Freestream disturbance in S2MA test section and corresponding N factors

$$N_T = -8.42 - 2.4\ln(Tu) \tag{4}$$

For flight experiments, the transitional N factor is around N=10[21] (with fixed β strategy). A wind tunnel will so be identified as quiet for N factor close to this value. For the S2MA test section in supersonic conditions, the N factors deduced from Tu measurements according to Mack formulation decreases from $N_T \fallingdotseq 8$ at P_0=0.5 bar to $N_T \fallingdotseq 6.5$ at P_0=1.5 bar as plotted in Fig. 26.

In cases of transonic and supersonic flows, noise radiated by test section walls (in particular from suction holes) becomes prominent, and can overwhelm velocity fluctuations because of $p'_{rms} \propto M^2$. Using plane wave assumption (see equation (5)) which establishes a relation between pressure and velocity fluctuation, it is possible to define a transitional N factor involving equivalent turbulence level Tu_p (see equation (6)). N factor obtained from pressure fluctuation measurement in S2MA is plotted in Fig. 26. It does not depend on total pressure so that N_T = 7 and is in the same order of magnitude than the one provided by velocity disturbance level.

$$p' = \rho\, c\, u' \tag{5}$$

$$Tu_p = \frac{p'_{rms}}{\rho c U} = \frac{p'_{rms}}{\rho(\gamma R T)M} = \frac{1}{\gamma M}\frac{p'_{rms}}{P} \tag{6}$$

Infra-red visualizations and stability computations realized on the 10° sharp cone in 1993, are in close agreement with direct measurements. Computations give an N factor equals to 5.5 at the beginning of transition detected in IR visualizations and increases up to 7 at the end of transition region[11].

Furthermore, JAXA also independently measured freestream turbulence level during S2MA wind tunnel test. Then, according to the measured data, brief consideration on the influence of freestream turbulence was performed and summarized in Appendix H. JAXA conducted two transition measurement wind tunnel campaigns on the NEXST-1 nose cone model at S2MA and another at wind tunnel of Fuji Heavy Industry (FHI) in Japan. Comparing these transition data measured at different freestream turbulence level, an approximated relation between the N_T and Tu was roughly obtained as indicated by "curve-fitting" shown in Fig. H-5. This relation is remarkably different from Mack relation and need further investigation. Nonetheless, it might be useful as input for the database between transition N factor and Tu.

(2) Test model

The wind tunnel test model consists of a wing-body configuration which was sting mounted in

the test section (see Fig. 25). It was a 23.3% model compared to the flight demonstrator (see Ref. 14-15). The fuselage length of the model is 1870 mm and its span is 1100 mm. The geometry of the wing is depicted in Fig. 25. The leading edge is characterized by two sweep angles: $\Lambda_{LE,inner}$=66° in the inner wing part (y/s<0.5) and $\Lambda_{LE,outer}$=61.2° in the outer wing part (y/s>0.5). The trailing edge also presents two sweep angles 0° from the root to y/s=0.4 and for higher spanwise location $\Lambda_{TE,outer}$=30°. The mean aerodynamic chord (MAC) of the model is $\bar{c}$=642 mm.

In order to improve IR visualizations, the model was black painted and then polished. As a matter of fact, crossflow instabilities responsible for transition onset in the vicinity of leading edge are sensitive to surface roughness. Therefore, in order to ensure laminar flow on the wing, a great care was devoted to surface polishing. JAXA measured the average roughness height Ra by laser displacement technique on resin sample pieces. Measurements demonstrated the quality of the surface since 0.18<Ra<0.94 μm. Dealing with boundary layer stability, surface quality is often expressed as a roughness Reynolds number $R_k = k \times U(k) / \nu(k)$ based on roughness height k. Considering about 1 μm height, this Reynolds number is very low, R_k<0.1, highlighting the fact that surface roughness will have weak influence on crossflow instability initial amplitude. Principal results of those roughness measurement and R_k study are summarized in chapter 4.1.

Before explaining stability analysis, attachment-line contamination was briefly considered. In general, transition on swept wing can be triggered by attachment-line contamination. As the NEXST-1 wing is characterized by a high sweep angle (more than 60°), we have to ensure that turbulent structures propagating from the root along the attachment line are damped moving towards the tip of the wing. The radius of the leading is slowly varying in spanwise direction and remains less than r_{LE} <1 mm as plotted (dashed line) in Fig. 27.

The flow along the attachment-line can be characterized by a typical Reynolds number $\overline{R}$ defined in subsonic condition by relationship (4) where V_e and U_e are respectively the external velocities parallel (Y) and normal (X) to the leading edge. For subsonic condition, if Poll's criterion $\overline{R}$<250 is verified, turbulent spots will be damped.

$$\overline{R} = \frac{V_e \eta}{\nu_e} \quad with \quad \eta = \sqrt{\frac{\nu_e}{(dU_e / dX)_{X=0}}} \tag{4}$$

This criterion has been extended to supersonic flows by using $\overline{R^*}$ defined by the relation (5) considering the viscosity ν^* which corresponds to the reference temperature T^* obtained in a classical way. Experiments have shown that the subsonic critical value $\overline{R^*} < 250$ was still valid in supersonic condition as mentioned by Arnal[16].

$$\overline{R^*} = \frac{V_e \eta^*}{\nu^*} \quad with \quad \eta^* = \sqrt{\frac{\nu^*}{(dU_e / dX)_{X=0}}} \tag{5}$$

$$\begin{cases} T^* = T_e + 0.16 \times (T_w - T_e) + 0.54 \times (T_{ad} - T_e) \\ T_w : \text{wall temperature} \\ T_{ad} : \text{adiabatic wall temperature} \end{cases}$$

Computations concerning the NEXST-1 wing for P_0=0.6 and 1.4 bar are plotted in Fig. 27. For the higher total pressure the maximum is $\overline{R^*} = 150$, ensuring in accordance with Poll's criterion that the flow will be laminar along the whole part of the leading edge for all configurations of wind tunnel tests.

(3) Transition measurement techniques and results[6]

Two areas of hot films were flush mounted at the inner part y/s=0.3 (28 elements) and at the outer part of the wing y/s = 0.7 (40 elements) as represented in the left lower side of Fig. 25. Typical rms values deduced from hot film signals, obtained for P_0=0.6 and 1.0 bar at the two spanwise positions are shown in Fig.28. Each curve presents a well defined peak voltage corresponding to transition location. Considering the smaller total pressure P_0=0.6 bar (lines with full symbols), transition takes place at x_T/c=0.37 and 0.49 at y/s=0.3 and 0.7 respectively. When total pressure, i.e. Reynolds number, raises up to P_0=1.0 bar, transition moves towards the leading edge from x_T/c=0.37 to 0.22

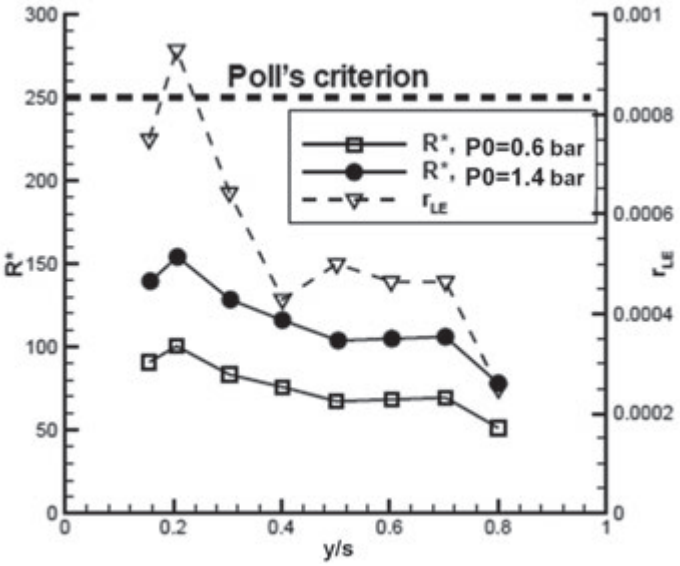

Figure 27. Leading edge contamination criterion

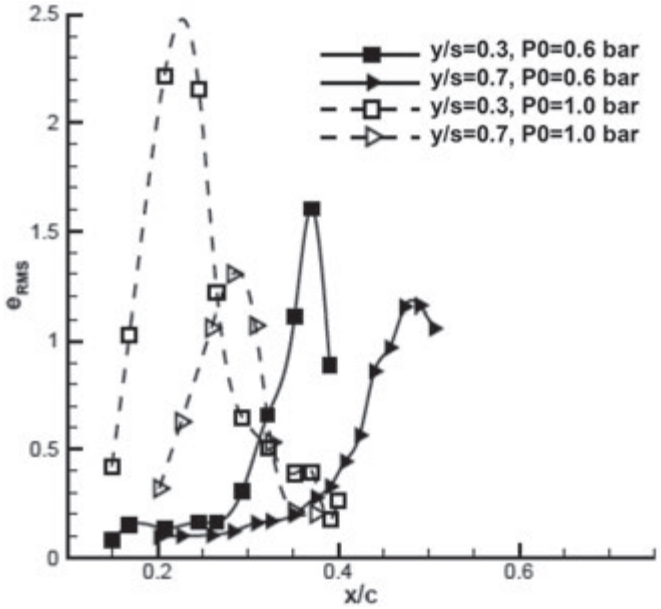

Figure 28. Hot-film measurements

at the inner wing (y/s=0.3) and from x_T/c=0.49 to 0.28 at the outer part (y/s=0.7).

Hot film measurements were completed by infra-red visualizations (see Fig. 25). In order to improve wall temperature difference between laminar and turbulent regions, the first half part of the wing was covered by an insulating material. In the same way, the whole model was black painted to increase its emissivity. These two treatments aim at improving infra-red images which are sensitive to wall temperature. As highlighted previously, transition can be detected by the fact that heat transfer increases when boundary layer becomes turbulent. Wall temperature difference between laminar and turbulent regions can be computed as a function of the Mach number as follows:

$$\frac{T_p}{T_e} = \left(1 + r\frac{\gamma - 1}{2} M_e^{\,2}\right) \quad with \quad \begin{cases} r_{lam} = 0.85 \\ r_{turb} = 0.90 \end{cases}$$
$$\Rightarrow \quad \Delta T = T_{p,turb} - T_{p,lam}$$
$$= \left(r_{turb} - r_{lam}\right)\left(\frac{\gamma - 1}{2}\right) M_e^{\,2} T_e \qquad (6)$$

This difference is linked to the increase of heat exchange coefficient (so-called recovery factor) r between laminar and turbulent states. For M = 2 and a stagnation temperature T_0=290 K, laminar to turbulent wall temperature difference is equal to

$\Delta T \sim 6$ K.

Infra-red images were corrected by a 3D affine transformation and projected on a reference mesh. Some examples of infra-red image are given in Fig. 29. It is easily judged that the remarkable change of color is corresponding to transition line. The rectangular with brown color indicates hot-film elements at the outer part (y/s=0.7). Whole transition measurements are summarized in Fig. 30, including the comparison of hot-film and IR measurements of transition location. A detailed description of this transition test and measurement results were presented in Ref. 6, and the summarized results on hot-film measurement data are described in Appendix I.

3.2. Stability analysis

3.2.1. Lower Reynolds number case (P_0=0.6 bar condition)

(1) Pressure distribution

During the S2MA wind tunnel test campaign, it was observed that an angle of attack AOA=1.5° well corresponded to the realization of the CFD-based design pressure distribution for the NLF wing design as shown in Fig.31(a), except for mid-span region (y/s=0.5). Nonetheless, as the difference between measured and CFD-based Cp distribution at y/s=0.5 near leading edge was small and not avoidable because of the kink of leading edge, JAXA finally judged that any interpolation of measured pressure distributions was not necessary. Therefore, ONERA and JAXA used present CFD-based chordwise pressure distributions at each spanwise station (shown in Fig. 31(b)) to compute boundary layer characteristics at whole Reynolds number conditions.

(2) Boundary layer computations

ONERA and JAXA computed representative boundary layer characteristics at inner and outer wing regions (y/s=0.3 and 0.7) in the case of P_0=0.6 bar condition and summarized them in Figs. 32. Plots correspond to streamwise velocity, cross-flow velocity and temperature profiles as well as chordwise thickness distributions (boundary layer thickness δ, displacement thickness δ^*). JAXA's results are in very close agreement with ONERA's ones. Similar comparison at mid-span region (y/s=0.5) is summarized in Appendix J.

(3) Stability analysis

Linear stability computations with envelope and fixed β strategies were performed by ONERA and JAXA to validate both parties' computational codes as a regard of S2MA experimental results.

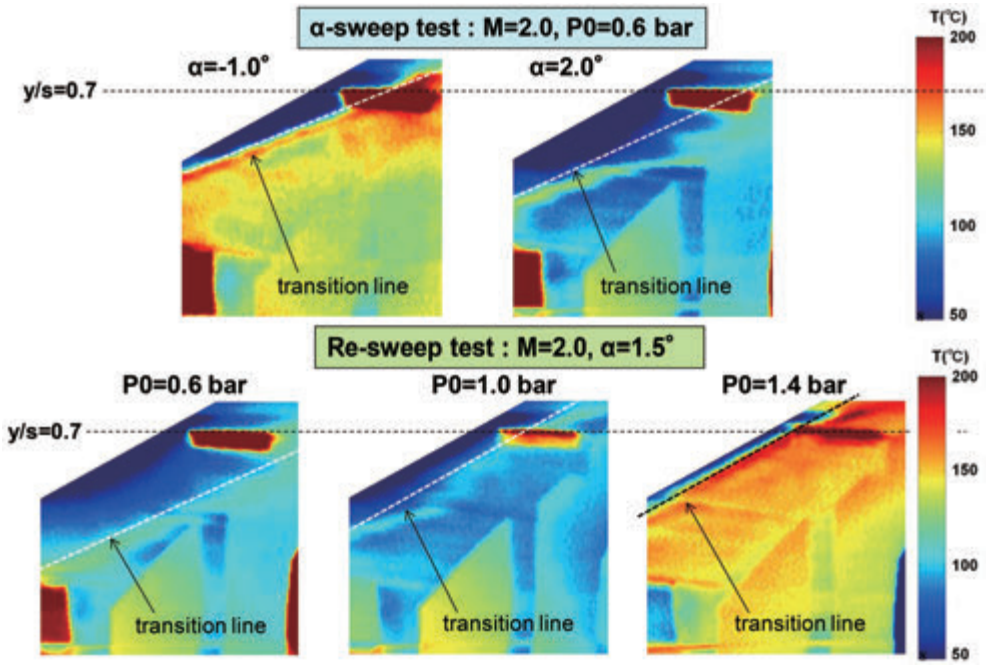

Figure 29. IR transition measurement results at S2MA test

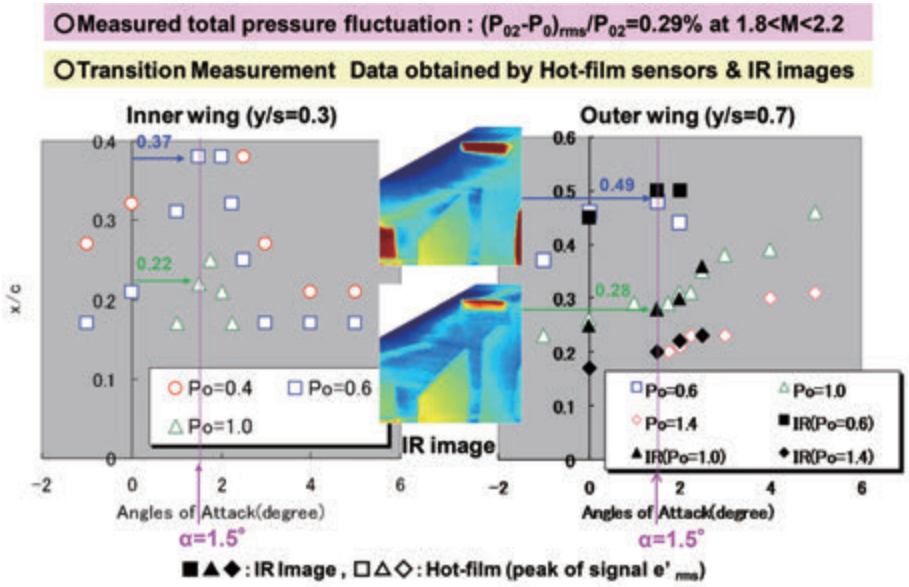

Figure 30. Summary of transition measurement results at S2MA test

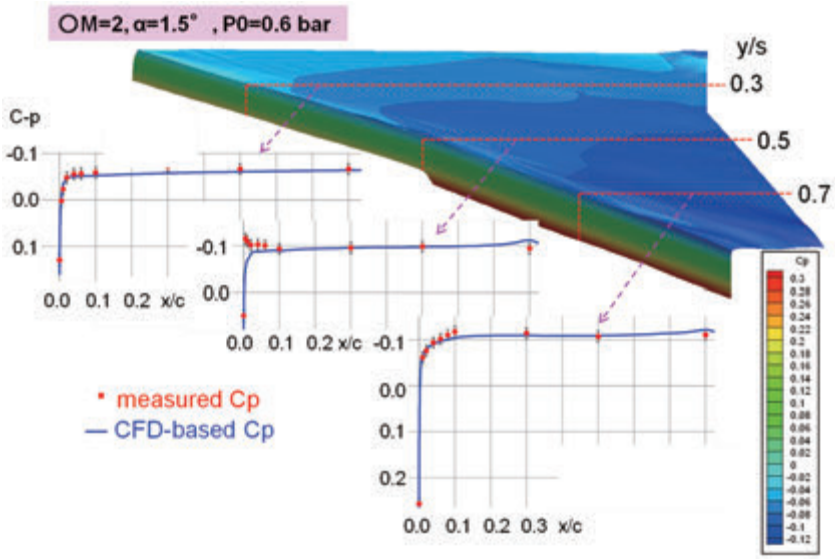

(a) Comparison of measured and NS-based pressure distributions

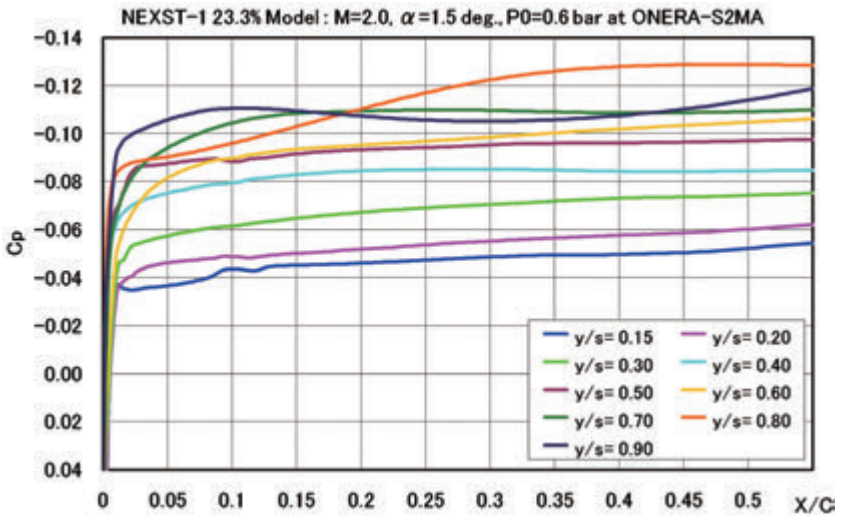

(b) CFD-based chordwise pressure distributions at each spanwise station

Figure 31. Pressure distributions at S2MA test

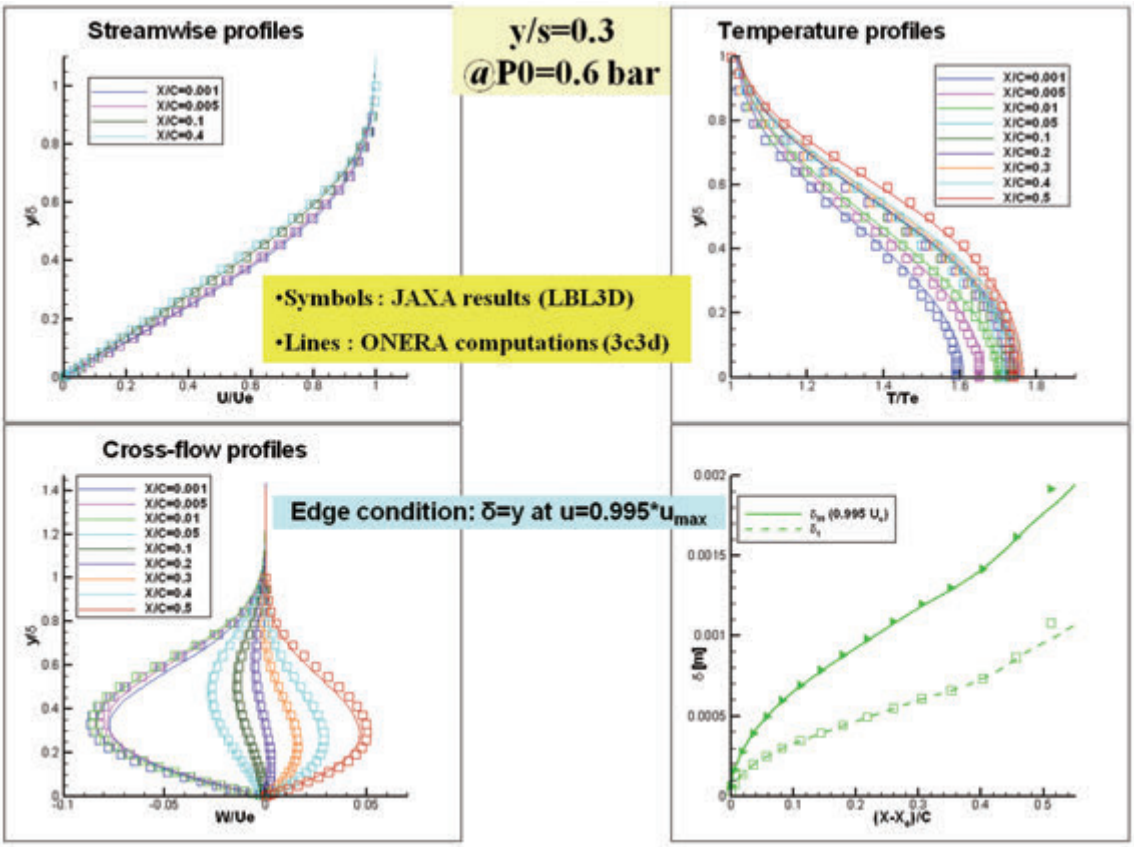

(a) Inner wing region (y/s=0.3)

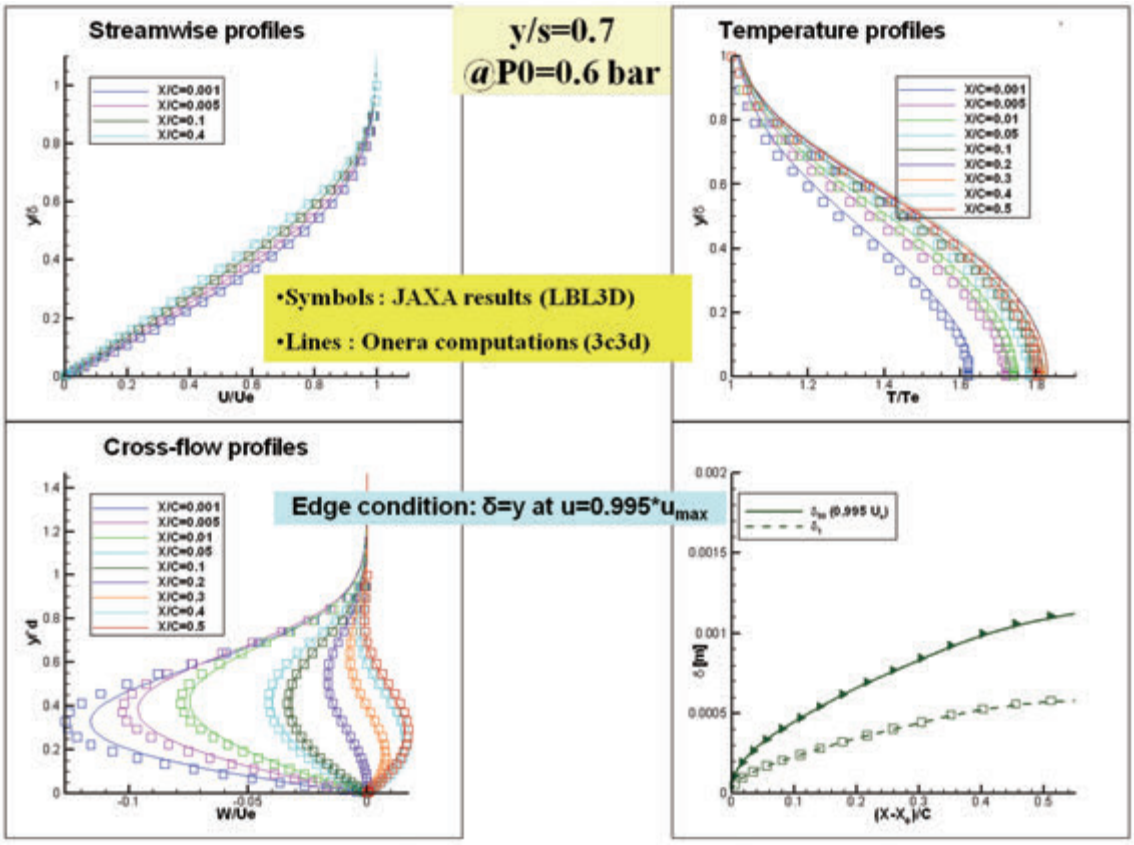

(b) Outer wing region (y/s=0.7)

Figure 32. Boundary layer computations at P0=0.6 bar condition

These computations were limited to the upper side of the reference case corresponding to an angle of attack of AOA=1.5°. Numerical results obtained by both parties were in close agreement for each spanwise station y/s=0.3 and 0.7 (see Table 4) at total pressure P_0=0.6 bar. The evolution of N factors and propagation direction angles ψ of disturbances computed with envelope strategy at y/s=0.3 and 0.7 for P_0=0.6 bar are summarized in Figs. 33 and 34 respectively. Similar results at mid-span region (y/s=0.5) are presented in Fig. J-2 and J-3 of Appendix J.

As for the inner wing region (y/s=0.3), in the first per cent of chord, i.e. in the vicinity of attachment line where the flow is strongly accelerated, N factor rise (Fig 33(a)) is due to crossflow instabilities as illustrated by the evolution of the propagation angle which starts at ψ = 89° (see Fig. 34(a)). Moving downstream, there is a change in nature of predominant disturbances: ψ rapidly decreases from 89° to 60°. In Fig. 33 (a), the vertical line stands for hot-film transition measurement at $(x_{TR.}/c)_{Exp.}$=0.37. At this position the most amplified frequency is f=15 kHz and corresponds to a numerical N factor N=5.6 in ONERA's computations, lower that the value expected in usual quiet wind tunnel tests. The corresponding wave-number vector direction is ψ =−65° as seen in Fig. 34(a) which highlights the "oblique" Tollmien-Schlichting nature of the wave responsible for transition onset.

Same computations were made for y/s=0.5 and 0.7 (see Fig. 33(b), 34(b), Fig. J-2, J-3, Table 4). The values of N factors are lower than those obtained for the inner wing indicating that amplification of TS waves is reduced. As a result, boundary layer remains laminar up to 49% of chord the outer wing region (y/s=0.7) which corresponds to an N factor equals to $N_{TR.}$=4.4~4.8 as illustrated in Fig. 33(b).

Figures 35, 36 and J-4, J-5 show the same comparisons of stability results (N factor and propagation direction) computed with fixed β strategy by ONERA and JAXA as those due to envelope strategy (shown in Fig. 33, 34 and J-2, J-3). Transition N factor values obtained by ONERA and JAXA are in close agreement for y/s=0.3, 0.5, 0.7 at P_0=0.6 bar. At the measured transition location indicated by the vertical line, it was found out that the dominant instability was TS mode as shown in Fig. 35. But, the corresponding N value is much smaller than that estimated in the process of natural transition at normal wind tunnel tests. Although it relies on higher freestream turbulence at the test condition, we have no information about it as explained in Chapter 3.1(1). This correlation between N factor obtained with fixed β strategy and measured transition data might be not enough reliable. As both parties have no way to advance results, however, present analysis is considered to be qualitatively reasonable at least.

Based on the stability results with both envelope and fixed β strategies for the complete set of spanwise stations, the comparison of measured transition location and N contours is summarized in Fig. 37. N_{env}=4.5, provided by envelope strategy, is almost in close agreement with IR test results between inner and outer wing regions. N_{env}=5.5 and 4.5 are corresponding to HF test results at inner and outer wing regions. Stability results computed with fixed β strategy reveal that measured transition is dominated by TS instability eventhough the corresponding N value is small.

(4) Parabolas method

Linear stability theory is very effective to identify properties of disturbances involved in transition process. Nonetheless, this method needs lots of computation time since it requires to solve an eigenvalue problem at each station of disturbance path. As one of ideas to improve such situation, a simplified stability method called Database method[17, 18] developed by ONERA is introduced in this section. The principle of such a method is to compute an analytical growth rate as a function of local parameters and mean flow properties. In case of 2D flows, for a given mean velocity profile and a dimensionless frequency $F = 2\pi\nu f / U_e^2$, the curve of the local growth rate $-\alpha_i$ is given as a function of Re_{δ^*} (Reynolds number based on displacement thickness δ^*) by two half parabolas[19].

This model was extended to 3D mean flow[20]: for a propagation direction angle $\psi \approx 90°$, growth

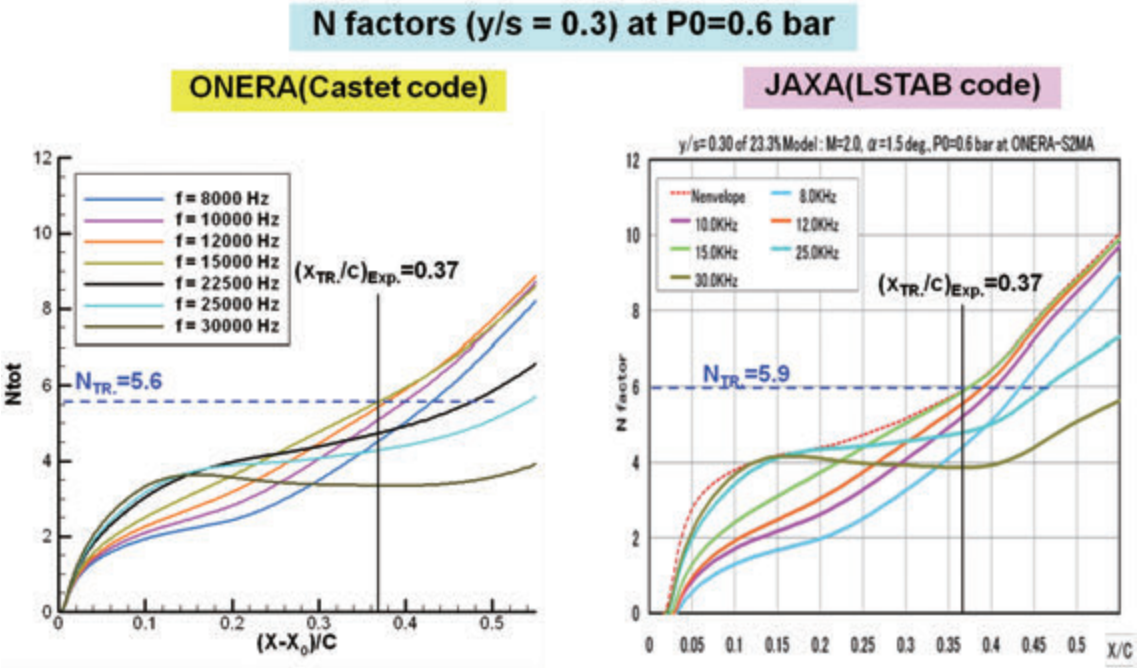

(a) Inner wing region (y/s=0.3)

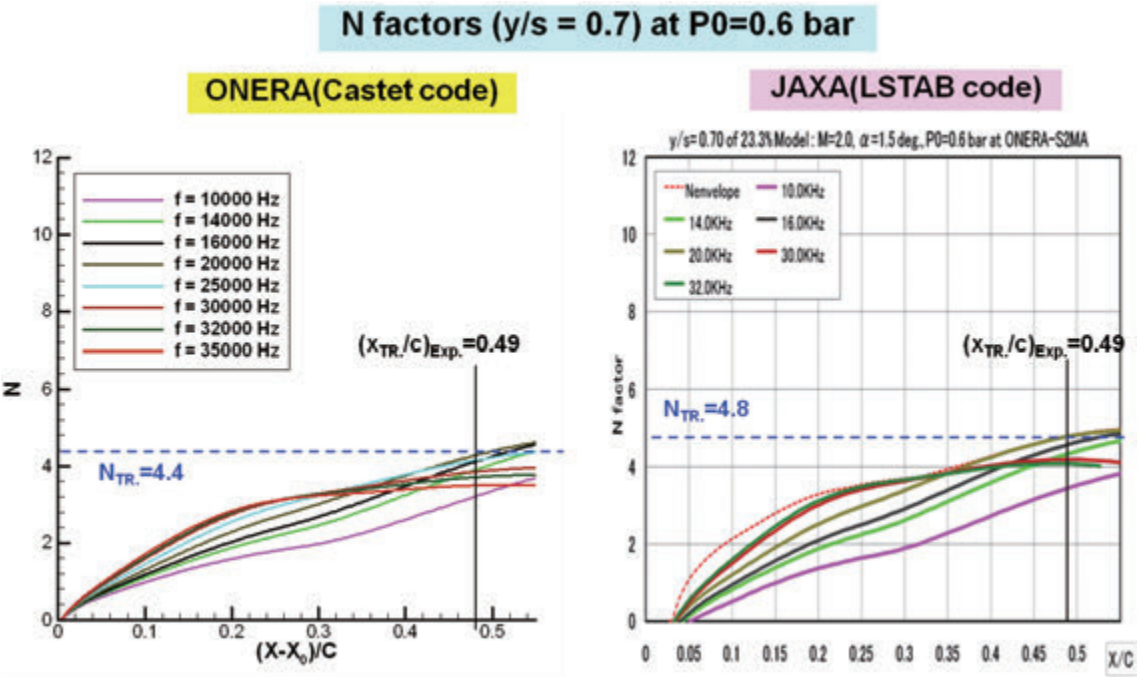

(b) Outer wing region (y/s=0.7)

Figure 33. Comparison of N factor (envelope strategy) at P0=0.6 bar

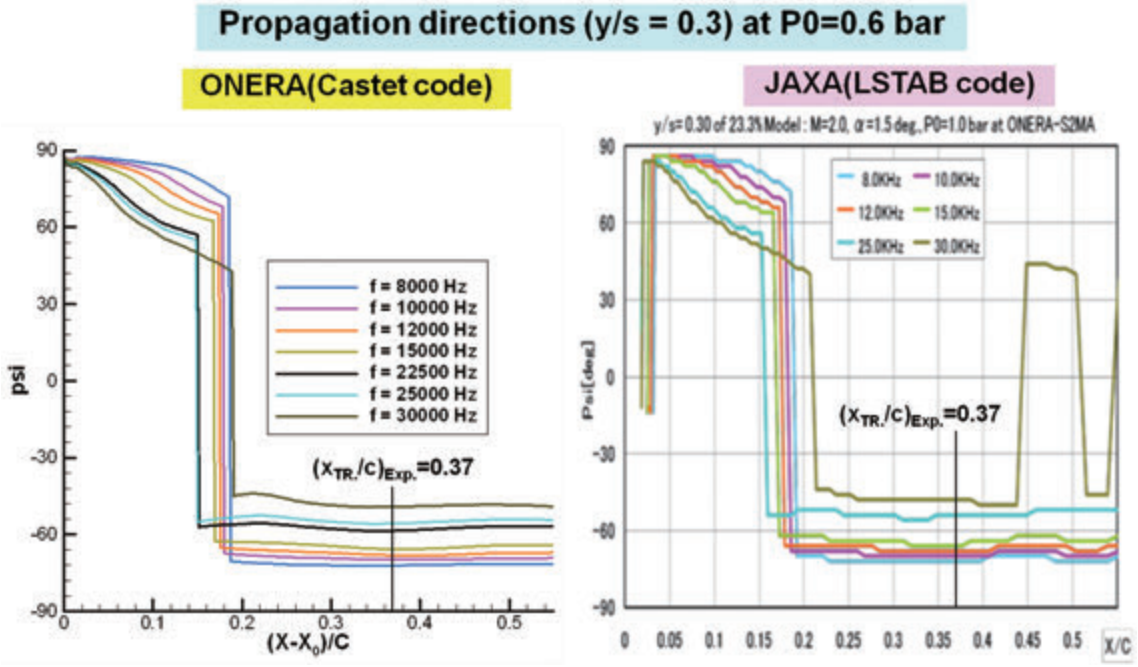

(a) Inner wing region (y/s=0.3)

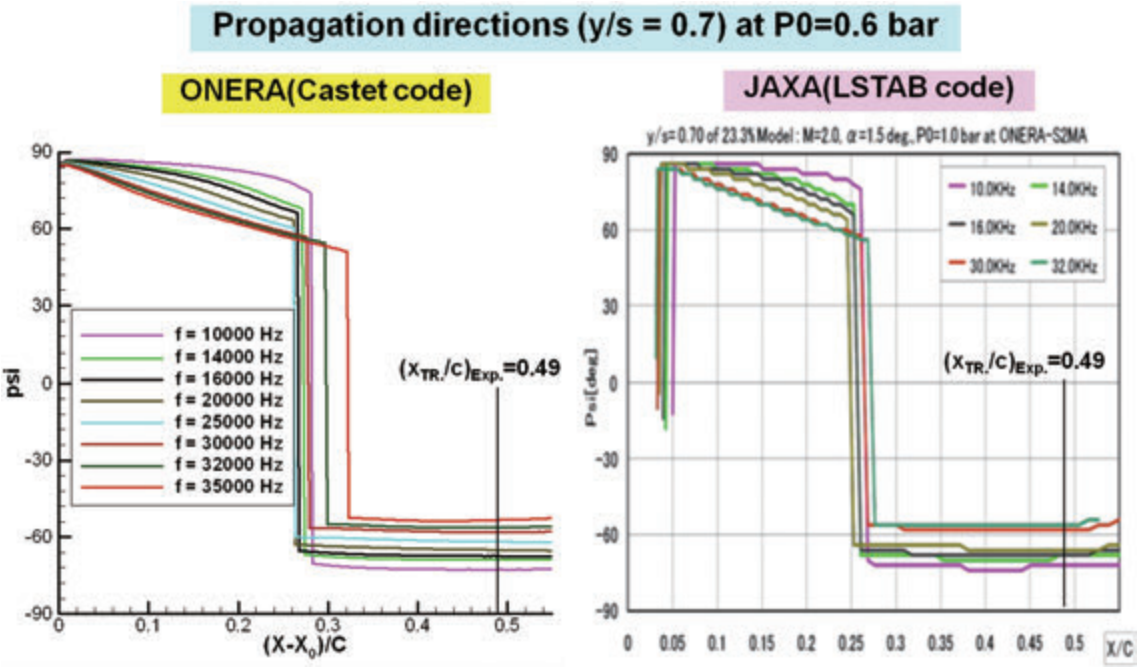

(b) Outer wing region (y/s=0.7)

Figure 34. Comparison of propagation direction (envelope strategy) at P0=0.6 bar

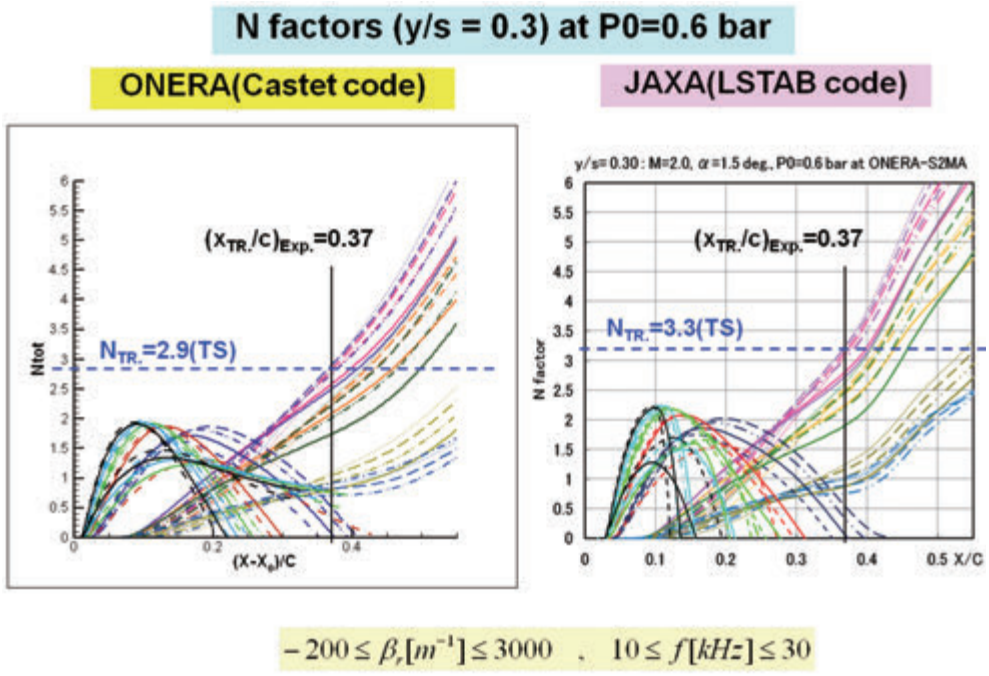

(a) Inner wing region (y/s=0.3)

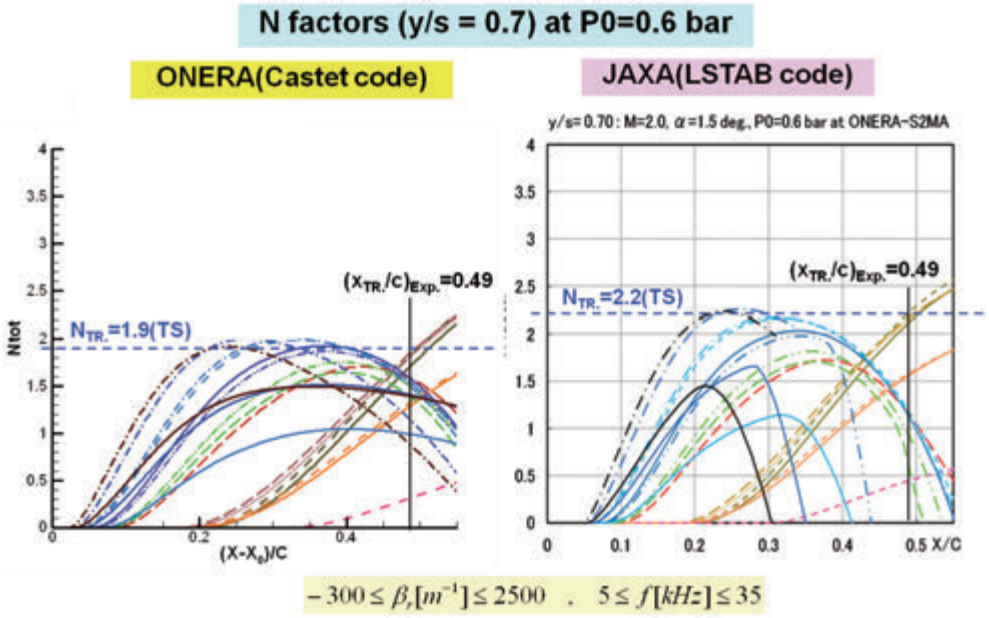

(b) Outer wing region (y/s=0.7)

Figure 35. Comparison of N factor (fixed β strategy) at P0=0.6 bar

rate depends on the mean velocity and the shear stress at the generalized inflection point. Database N factor values obtained for P_0=0.6 bar and an angle of attack of AOA=1.5° are represented by full lines in the right part of Fig. 38 and compared to exact stability computations (dashed lines). Database provides N factors higher than exact stability computations, nonetheless, the agreement is rather good between the two numerical approaches. Database can therefore be considered as a powerful tool for stability studies: since approximation of growth rate only depends on global parameters it can easily be implemented in a boundary layer code.

In the left part of Fig. 38, IR visualization and hot-film measurements were reported as well as

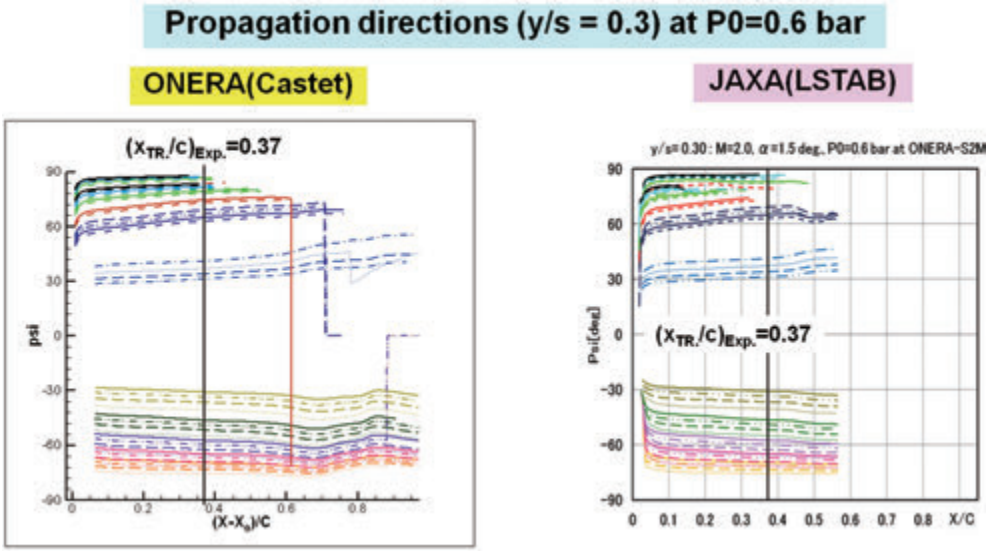

(a) Inner wing region (y/s=0.3)

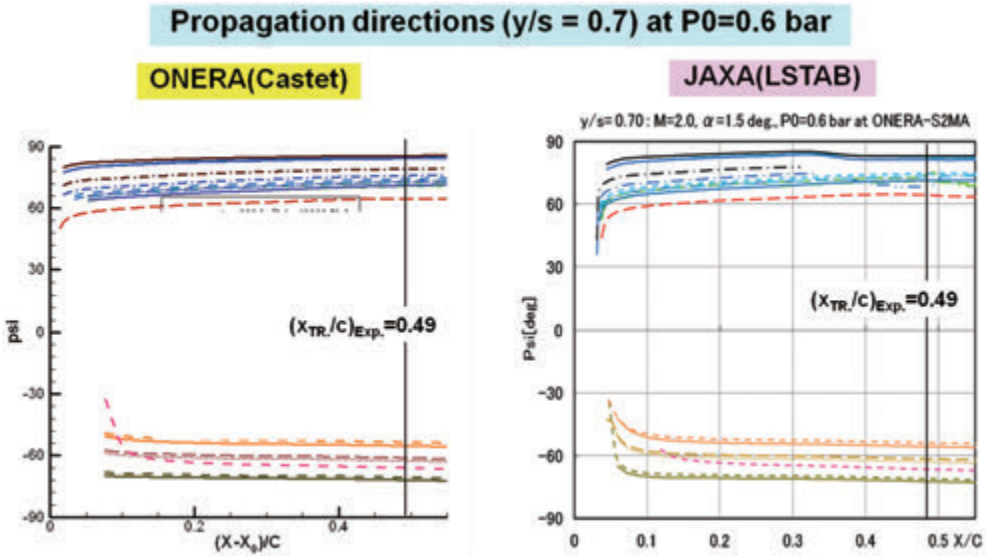

(b) Outer wing region (y/s=0.7)

Figure 36. Comparison of propagation direction (fixed β strategy) at P0=0.6 bar

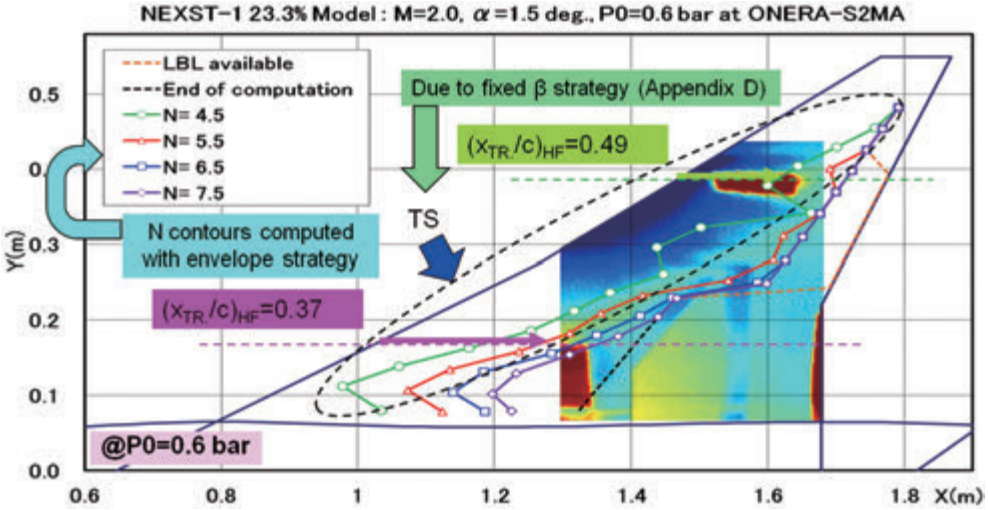

Figure 37. Comparison of measured transition location and N contours at P0=0.6 bar condition

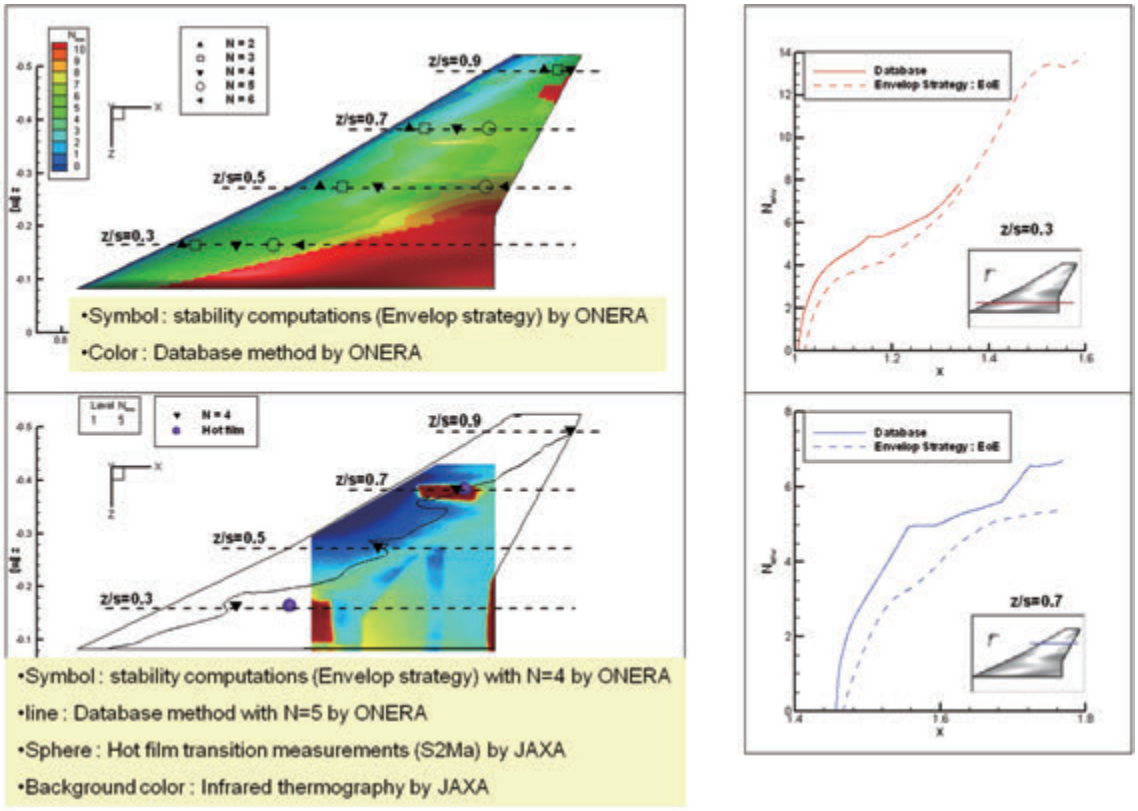

Figure 38. Comparison of measured transition location and ONERA's database method at P0=0.6 bar condition

numerical stability results. In the outer part of the wing, from y/s=0.5 to y/s=0.7, measurements are well correlated by a Database N factor around 5 (N=4.4 for linear stability computation as specified in Table 4). Concerning the inner part (y/s=0.3), hot-film transition location at x/c=0.37 is correlated by a Database N factor of 6 (N_T=5.6 for linear stability theory, see ONERA's result shown in Fig. 33(a)).

3.2.2. Middle Reynolds number case (P_0=1.0 bar condition)

(1) Pressure distribution

As mentioned above, the pressure distribution measured at AOA=1.5° and P_0=0.6 bar condition was in almost good agreement with CFD-based numerical design pressure distribution. Therefore, both parties also used the CFD-based pressure distribution for boundary layer computations corresponding to the other values of total pressure.

(2) Boundary layer computations

Two comparisons of boundary layer characteristics at y/s=0.3 and 0.7 computed by both parties at P_0=1.0 bar condition are summarized in Figs. 39(a) and (b). Plots correspond to streamwise and crossflow velocity profiles, temperature profiles and chordwise thickness distributions (boundary layer thickness δ, displacement thickness δ^*). JAXA's results are in very close agreement with ONERA's results as same as for P_0=0.6 bar.

(3) Stability analysis

As mentioned before, for an angle of attack of AOA=1.5° and a total pressure P_0=0.6 bar, corresponding to a MAC-based Reynolds number Rec=5×10^6, even though N factors are lower than those expected, the high swept wing designed by JAXA remains laminar up to about 40% of chord. The optimized pressure distribution manages to damp initial crossflow disturbance and so transition is triggered by TS waves. The influence

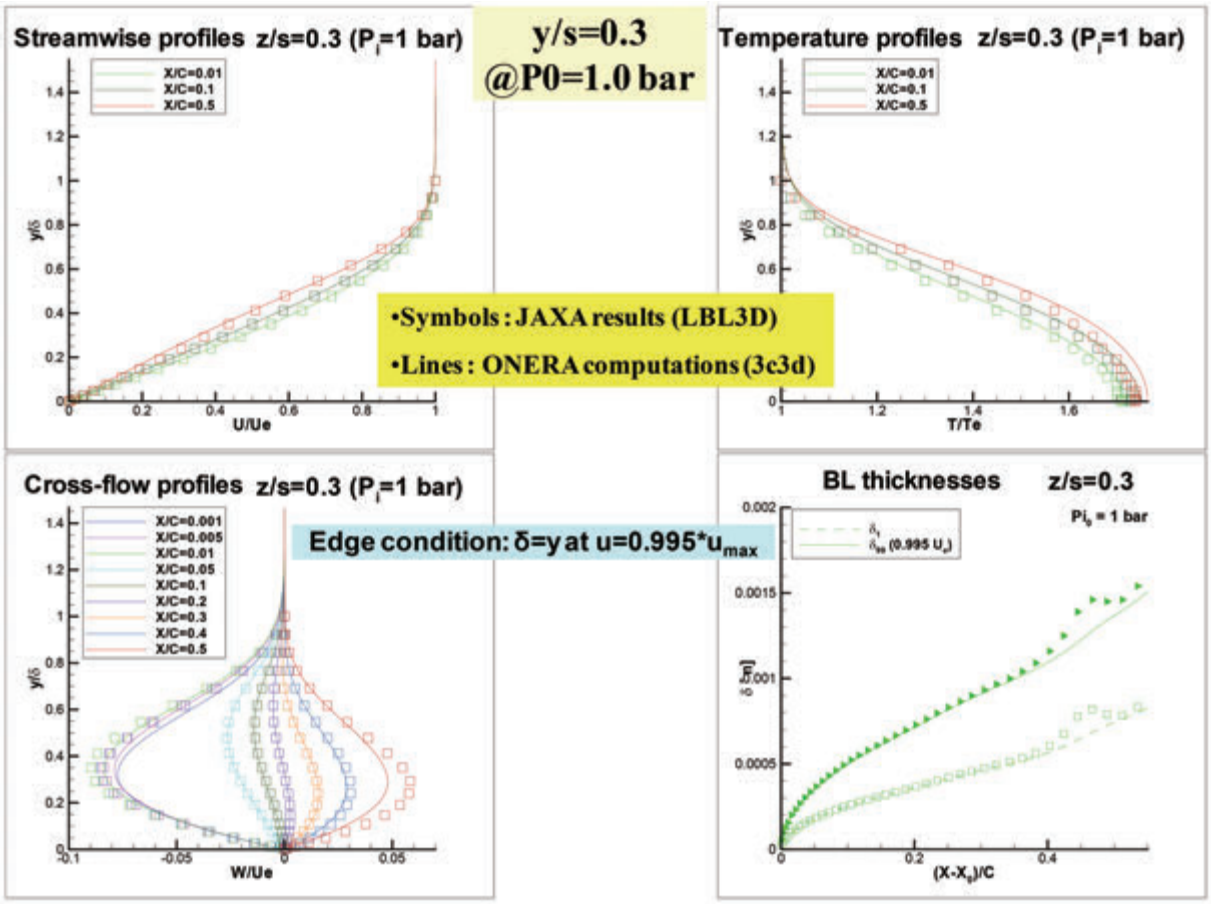

(a) Inner wing region (y/s=0.3)

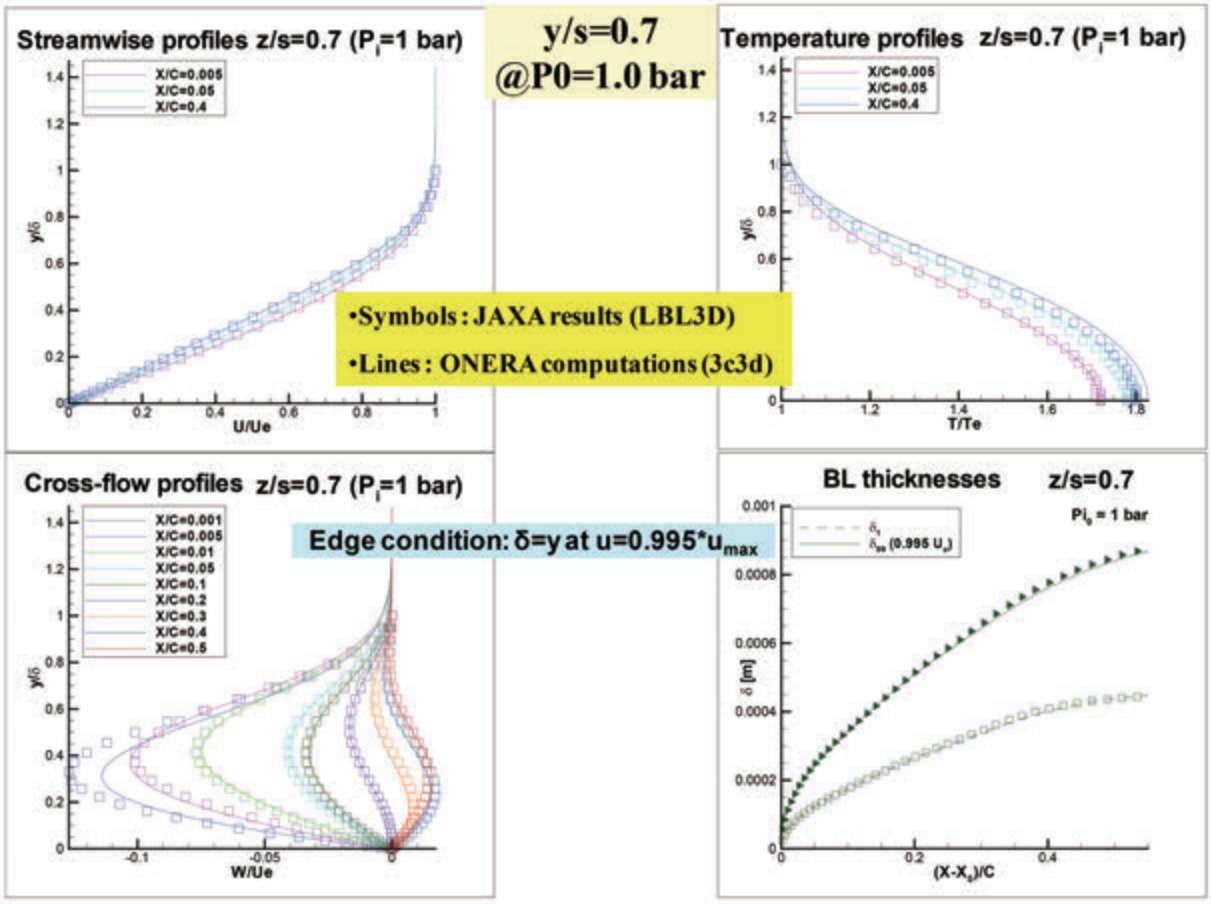

(b) Outer wing region (y/s=0.7)

Figure 39. Boundary layer computations at P0=1.0 bar condition

of Reynolds number on transition process was then analyzed. Hot-film measurements have shown that when total pressure increased at P_0=1.0 and 1.4 bar, i.e. when Reynolds number increased respectively at 8 and 11×10^6, the transition moved towards the leading edge.

Exact stability computations (N factor and propagation direction angle ψ) computed with envelope strategy at y/s=0.3 and 0.7 for P_0=1.0 bar are summarized in Figs. 40 and 41. When the Reynolds number increases, transition at inner wing region (y/s=0.3) moves towards the leading edge and in the same time, the transitional N factor as well as frequency of the most unstable disturbance are increased, as shown in Fig. 40(a) compared with Fig. 33(a). The same trend is observed for the outer part of the wing (y/s=0.7). As mentioned previously, in envelope strategy framework, growth rate corresponds to the most unstable wave-number direction. This means that there is a cumulative effect of firstly CFI and then TSI complicating results interpretation.

Therefore to complete stability analyses, in particular to settle on the nature of disturbance, additional fixed β strategy computations were conducted. The results of N factors and propagation direction angles at higher total pressure P_0 = 1.0 bar are shown in Figs. 42 and 43. The path to transition is fully dominated by crossflow disturbance as easily seen by the evolution of N factor in Figs. 42(a) and (b). Figs. 43 show the corresponding propagation direction corresponding to the same spanwise wave-number β values as same as Fig. 36. Corresponding infra-red visualizations are presented in Fig. 44: laminar zone is drastically reduced up to a maximum of 28% of chord. N=5.5 is almost in good agreement with IR test results between inner and outer wing regions. N=6.5 and 5.5 match with HF transition positions at inner and outer wing regions, respectively.

Transition location corresponding to N=5 both for Database method and linear stability computation are summarized in Fig. 45 and superimposed to IR visualizations. At the inner part (y/s=0.3), considering a numerical N factor N=5 underestimates the position of transition compared to hot-film data. For the outer region (y/s=0.5 to 0.7), numerical studies give transition locations in remarkable agreement with infra-red visualizations and hot-film data.

3.2.3. Higher Reynolds number case (P_0=1.4 bar condition)

(1) Boundary layer computations

Some comparisons of boundary layer characteristics computed by both parties at P_0=1.4 bar condition are summarized in Figs. 46. JAXA and ONERA results are in very close agreement as for the results obtained at P_0=0.6 and 1.0 bar.

(2) Stability analysis

Stability results of N factors and propagation direction angles computed with envelope strategy at y/s = 0.3 and 0.7 for P_0=1.4 bar are summarized in Figs. 47 and 48. When the Reynolds number increases, transition at inner wing region moves further towards the leading edge than at P_0=1.0 bar and the transitional N factors of the most unstable disturbance are increased, as shown in Fig. 47(a) compared with Fig. 40(a). The same trend as the inner part is observed for the outer part of the wing.

Stability results computed with fixed β strategy are summarized in Figs. 49 and 50. At this higher total pressure condition of P_0=1.4 bar, the path to transition is also fully dominated by crossflow disturbance as easily seen in Figs. 49(a) and (b). Propagation directions are exhibited in Figs 50. Corresponding infra-red visualization is presented in Fig. 51: laminar zone is drastically reduced less than 20% of chord. N=4.5 is almost in good agreement with IR test results between inner and outer wing regions. N=7.5 and 6.5 correspond to HF measurements at inner and outer wing regions, respectively.

On these infra-red visualizations, the transition location corresponding to N=5 both for Database method and linear stability computation are summarized in Fig. 52. At the inner part (y/s=0.3), considering a numerical N factor N=5 underestimates the position of transition compared to hot-film data. For the outer region (y/s=0.5 to 0.7), numerical studies give transition locations in remarkable

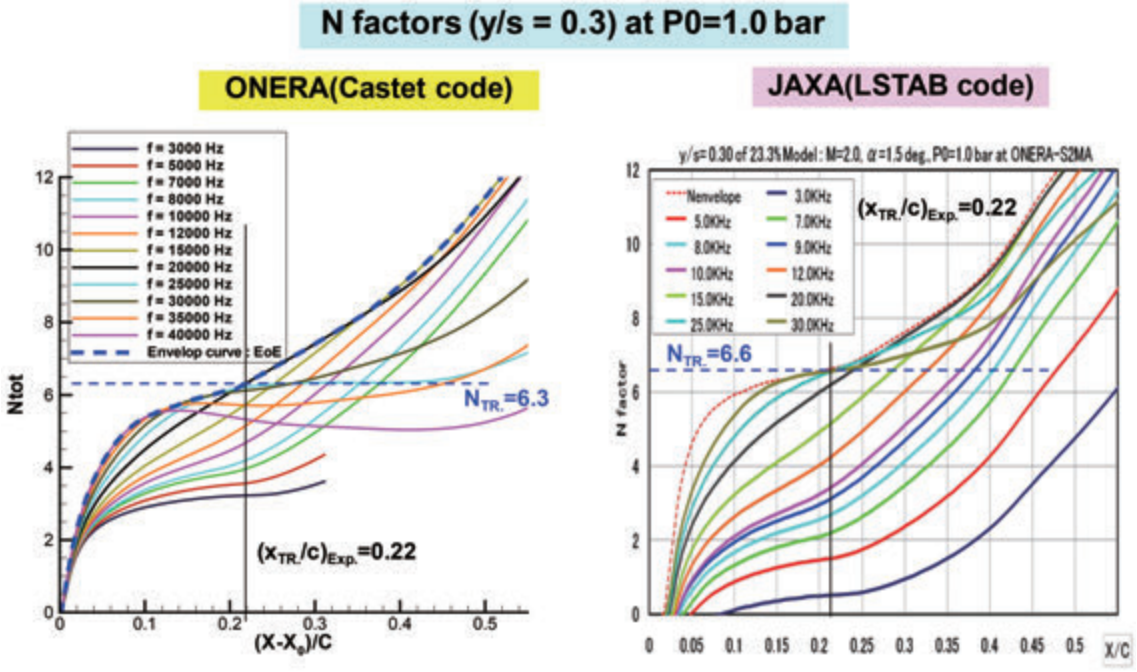

(a) Inner wing region (y/s=0.3)

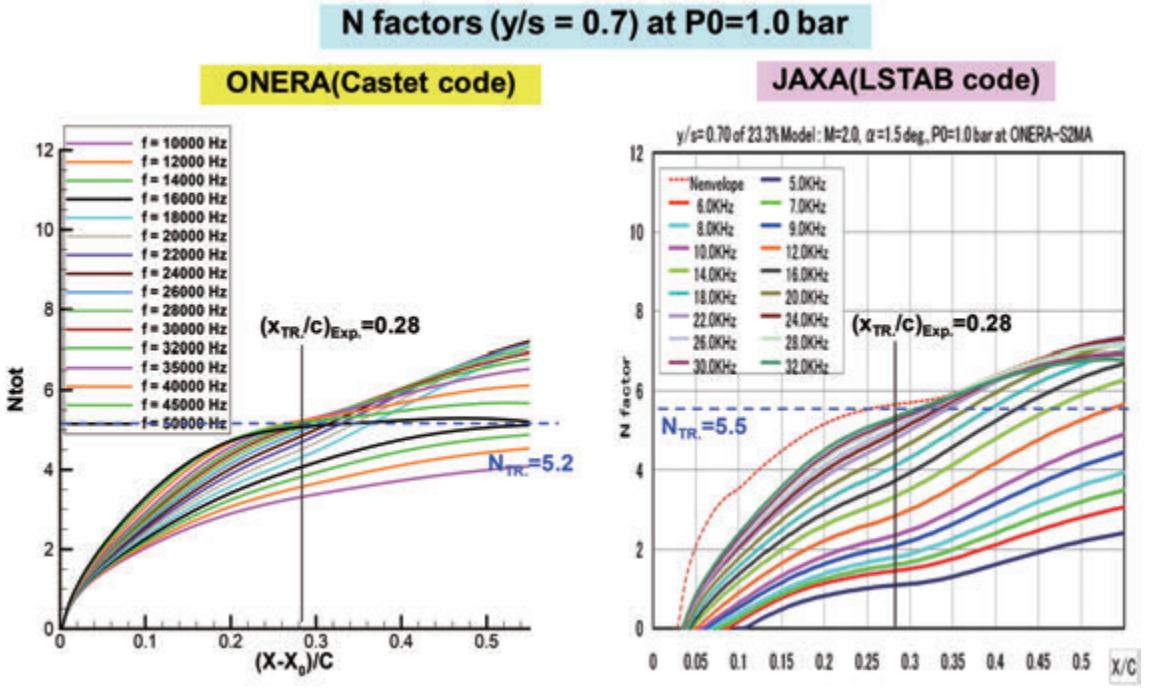

(b) Outer wing region (y/s=0.7)

Figure 40. Comparison of N factor (envelope strategy) at P0=1.0 bar

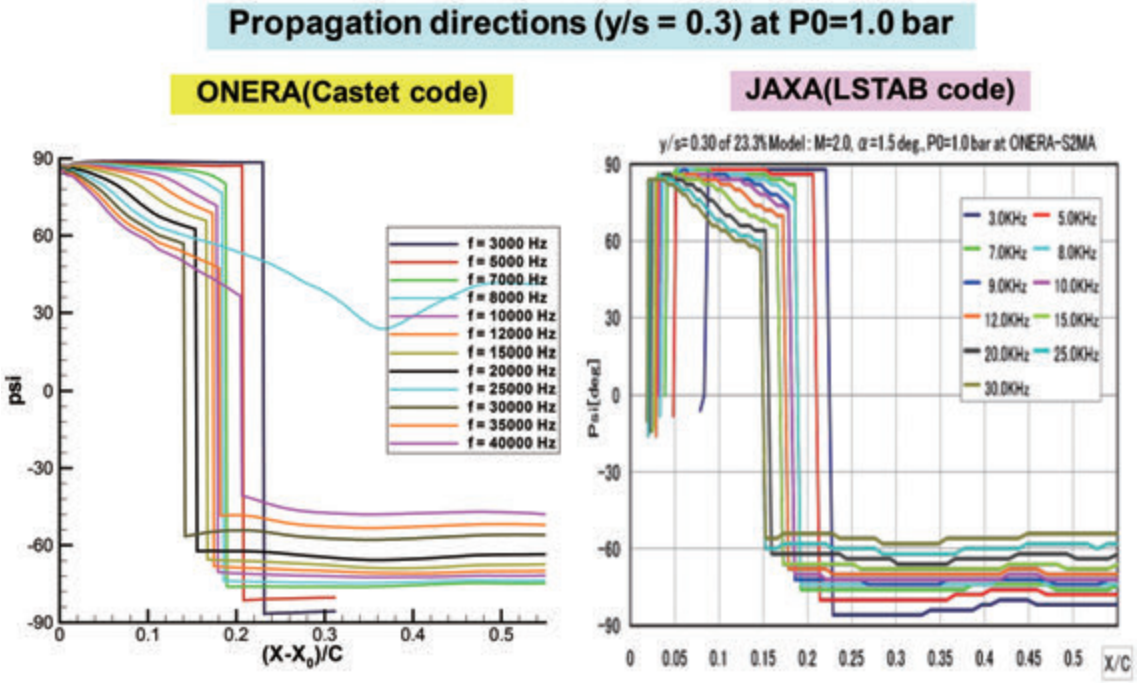

(a) Inner wing region (y/s=0.3)

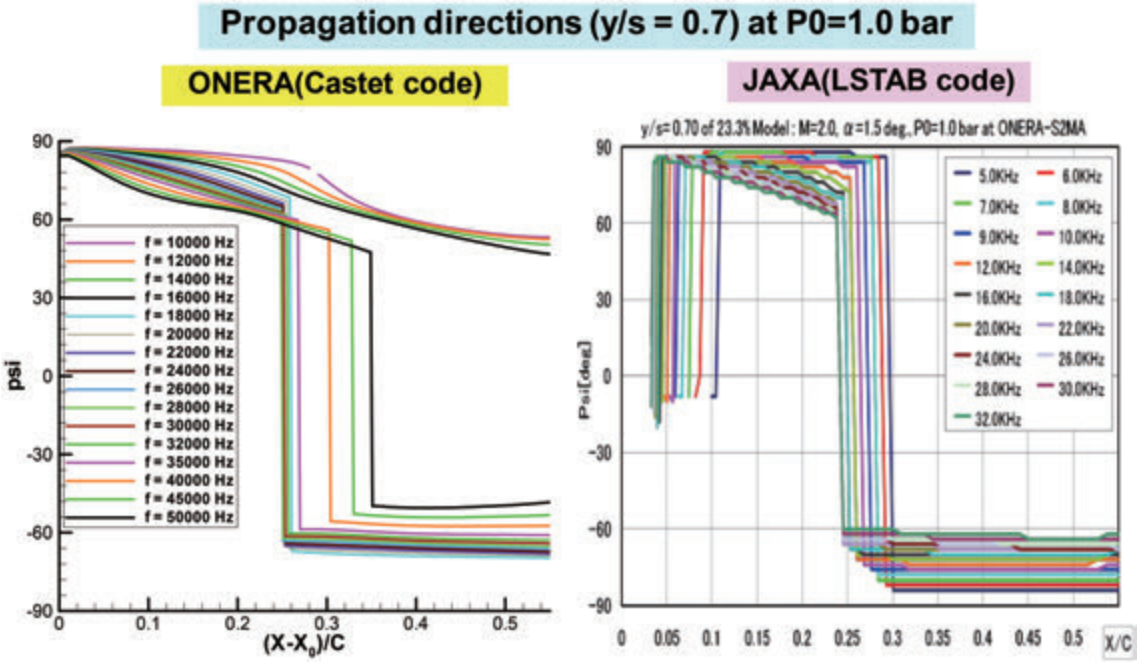

(b) Outer wing region (y/s=0.7)

Figure 41. Comparison of propagation direction (envelope strategy) at P0=1.0 bar

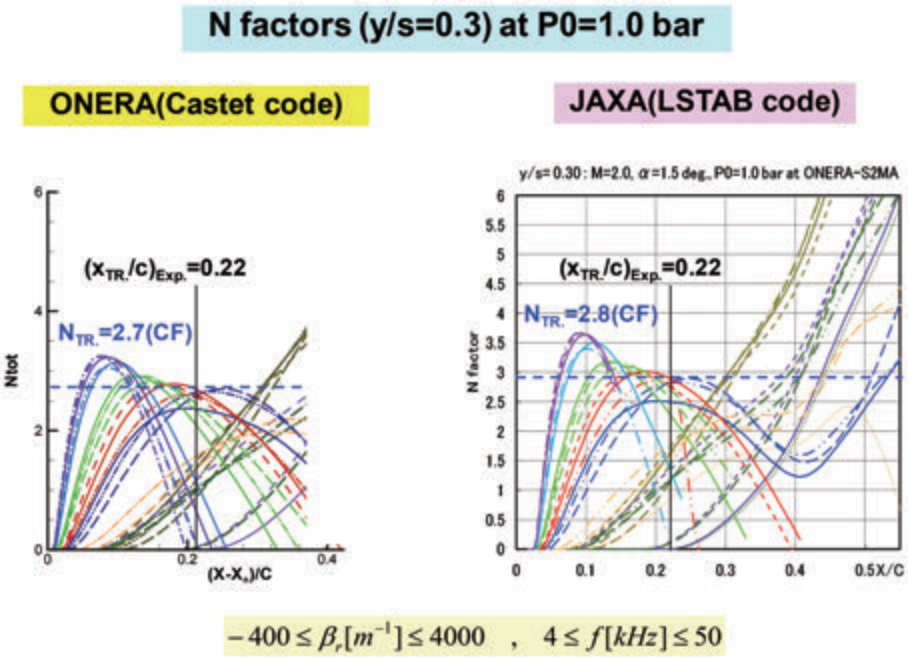

$-400 \le \beta_r[m^{-1}] \le 4000 \quad , \quad 4 \le f[kHz] \le 50$

(a) Inner wing region (y/s=0.3)

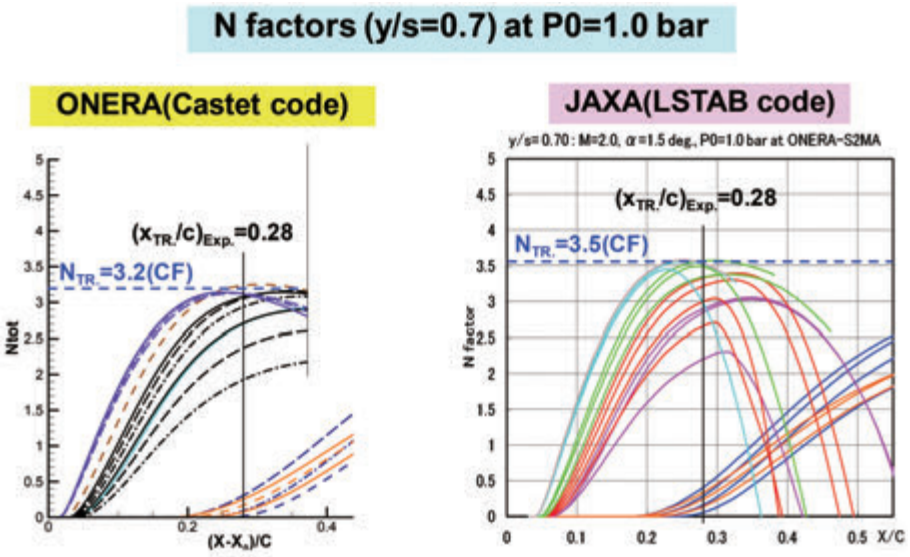

$-400 \le \beta_r[m^{-1}] \le 3500 \quad , \quad 8 \le f[kHz] \le 42.5$

(b) Outer wing region (y/s=0.7)

Figure 42. Comparison of N factor (fixed β strategy) at P0=1.0 bar

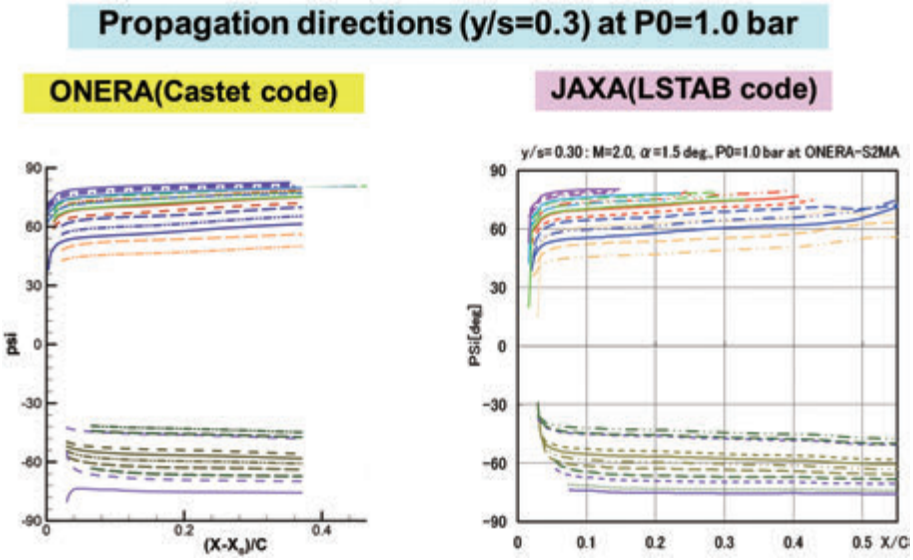

(a) Inner wing region (y/s=0.3)

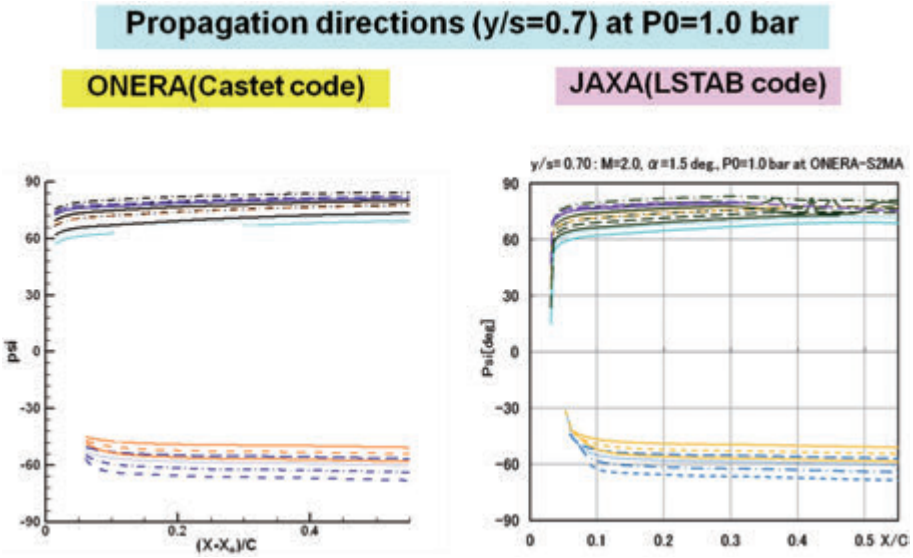

(b) Inner wing region (y/s=0.7)

Figure 43. Comparison of propagation direction (fixed β strategy) at P0=1.0 bar

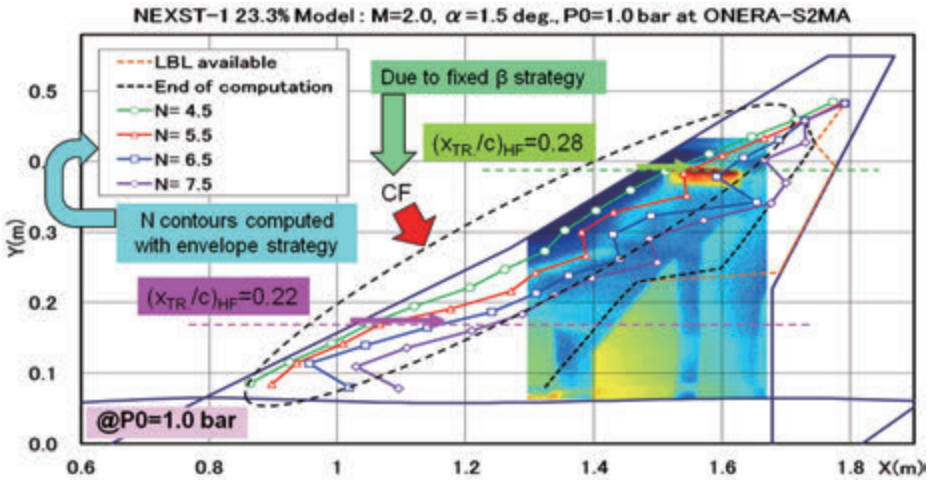

Figure 44. Comparison of measured transition location and N contours at P0=1.0 bar condition

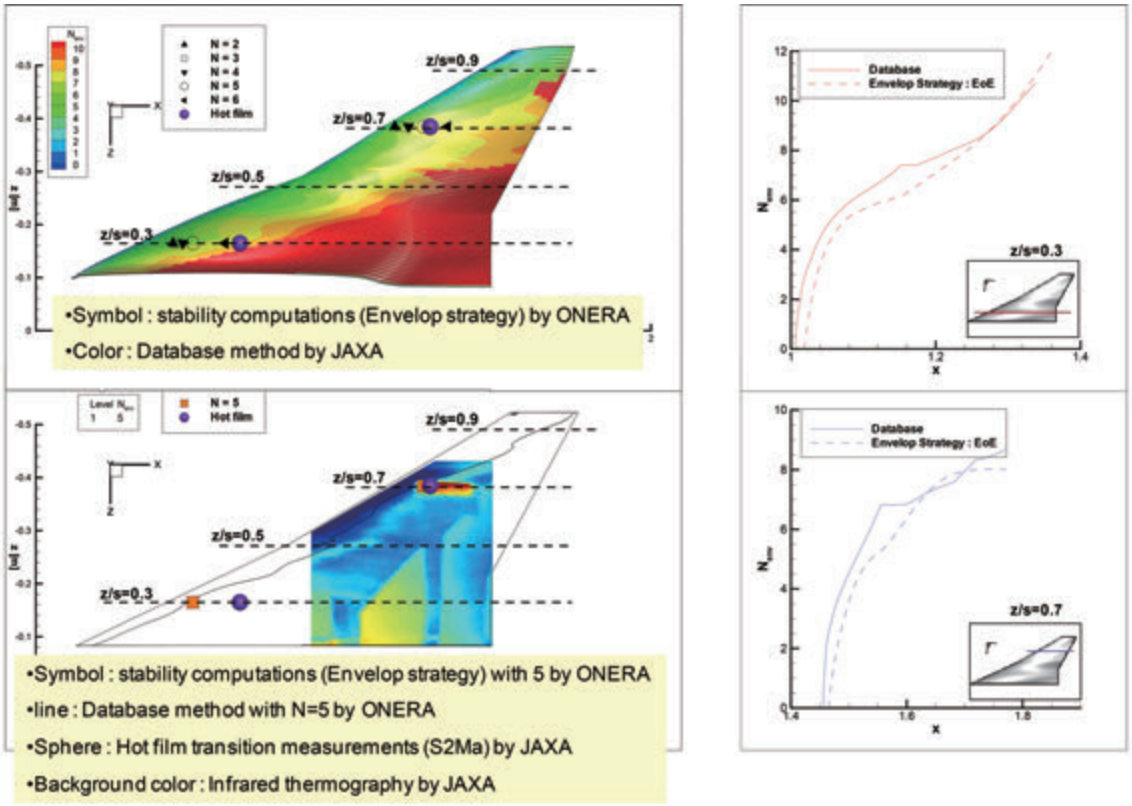

Figure 45. Comparison of measured transition location and ONERA's database method at P0=1.0 bar condition

agreement with infra-red visualizations and hot-film data.

3.3. Summary of chapter 3

Stability results computed with envelope and fixed β strategies for wind tunnel test campaign are summarized in Tables 4(a) and (b) respectively and compared with experimental results. Naturally, JAXA's results are in very close agreement with ONERA's ones. As expected, fixed β strategy provides good information to understand transition mechanism occurring in the S2MA wind tunnel.

As a conclusion, transition on a supersonic NLF wing with a highly sweep angle was characterized experimentally by hot-film measurements and infra-red visualizations. Experimental results on the upper side obtained for an AOA=1.5° angle of attack and several total pressures P_0=0.6, 1.0 and 1.4 bar were presented. These experiments provide accurate transition location, nonetheless, there is a lack in the understanding of this process, in particular the nature of instability triggering the transition. Stability studies, involving linear stability and Database computations were therefore carried out. They showed that for a MAC-based Reynolds number Rec = 5×10^6, present pressure distribution for the NEXST-1 NLF wing manages to damp crossflow instability and so a significant part of the wing remains laminar before transition onset due to Tollmien-Schlichting waves. In this wind tunnel campaign, when Reynolds number increased beyond Rec>8×10^6, crossflow amplification was sufficient to trigger the transition. This early transition is attributed to the not-so-low external distance level in the test section compared to flight condition. Indeed, as mentioned in previous chapter, the flight test data (at Rec=15×10^6) has demonstrated the ability of the NEXST-1 wing to remain laminar on an extended region validating its natural laminar flow design.

Finally, present subjects and principal results of this chapter are summarized again as follows:

(1) Subjects

a) To investigate the effect on the natural laminar flow wing design concept created by JAXA in detail, both parties analyzed the stability

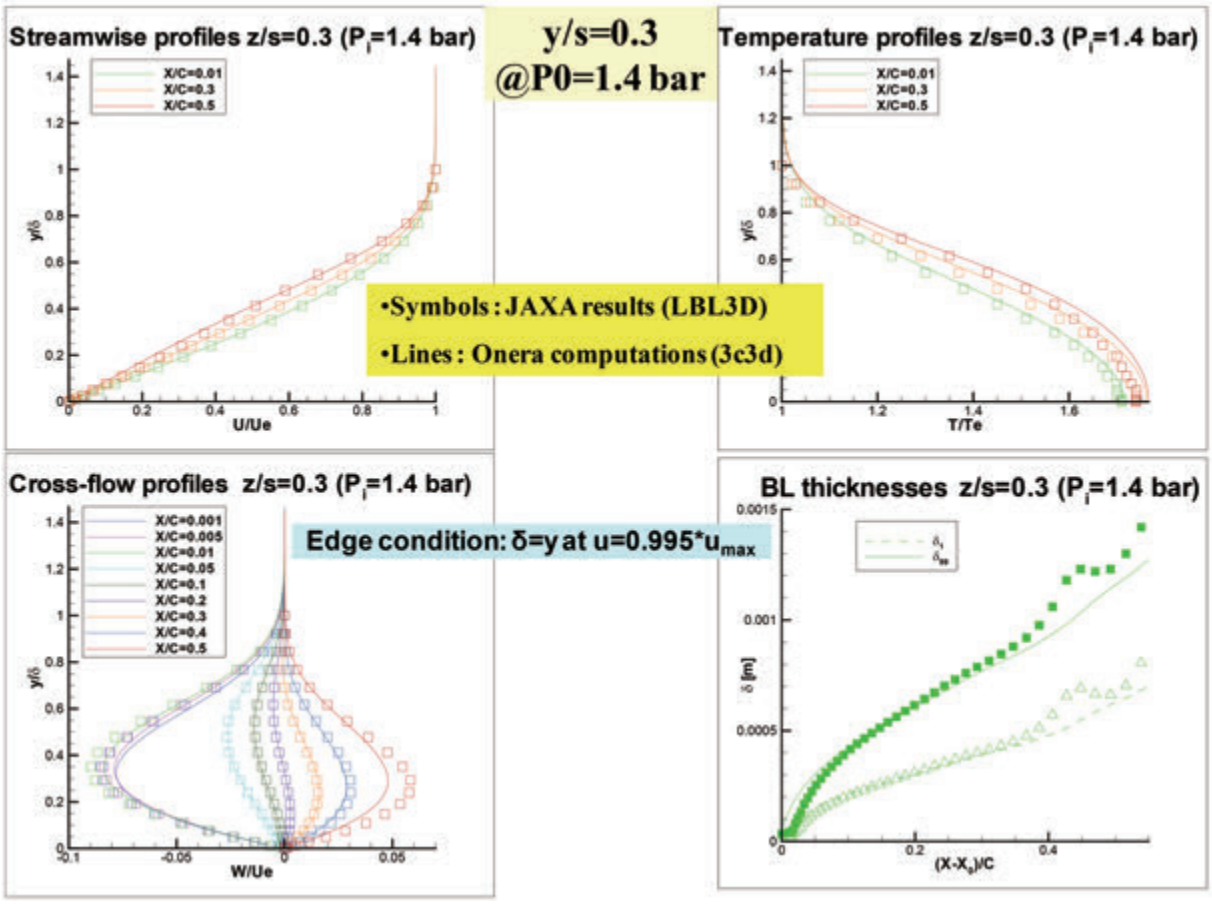

(a) Inner wing region (y/s=0.3)

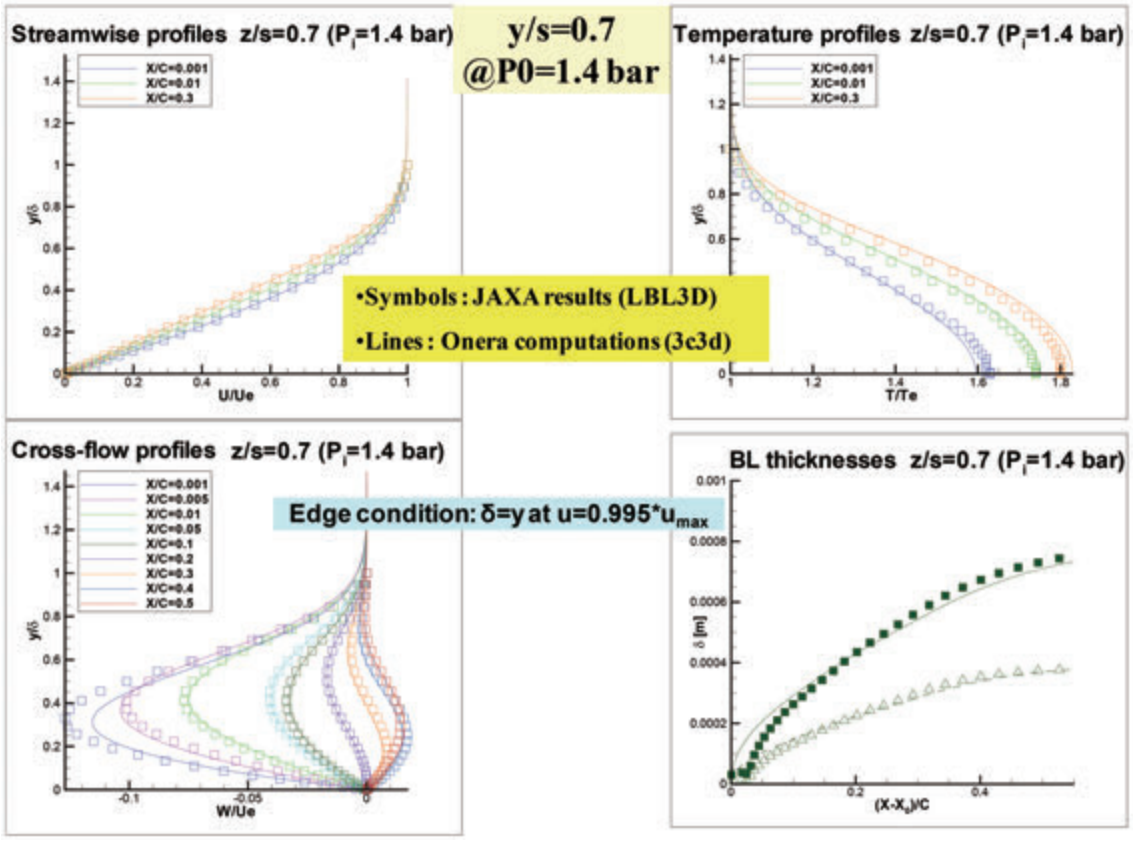

(b) Outer wing region (y/s=0.7)

Figure 46. Boundary layer computations at P0=1.4 bar condition

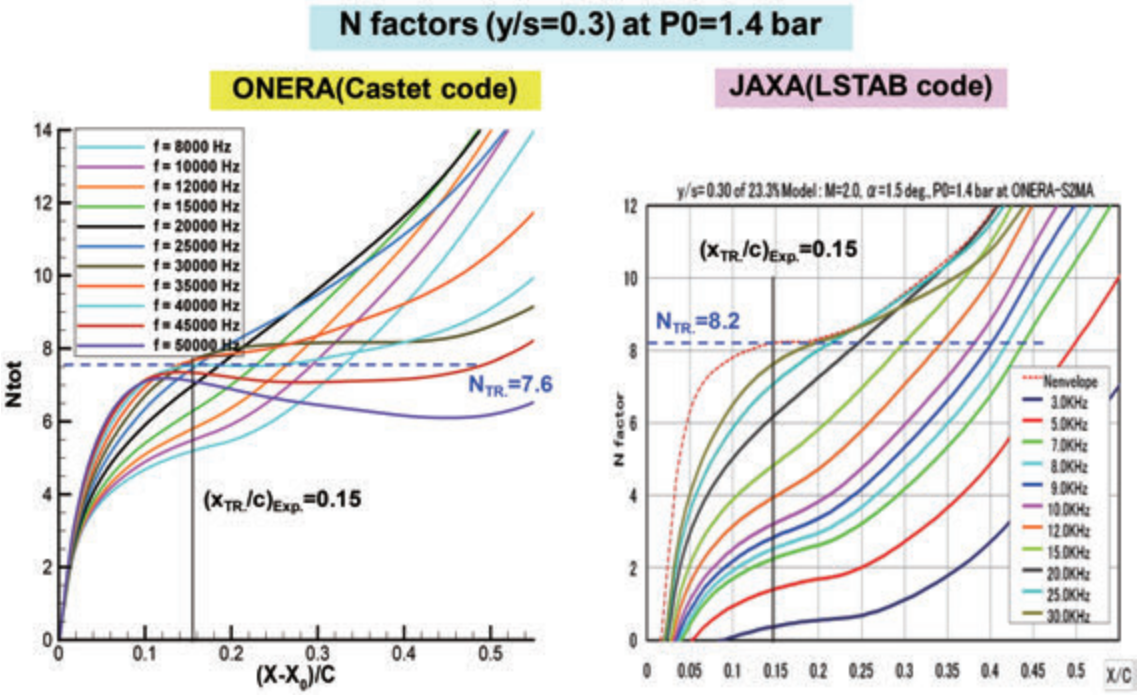

(a) Inner wing region (y/s=0.3)

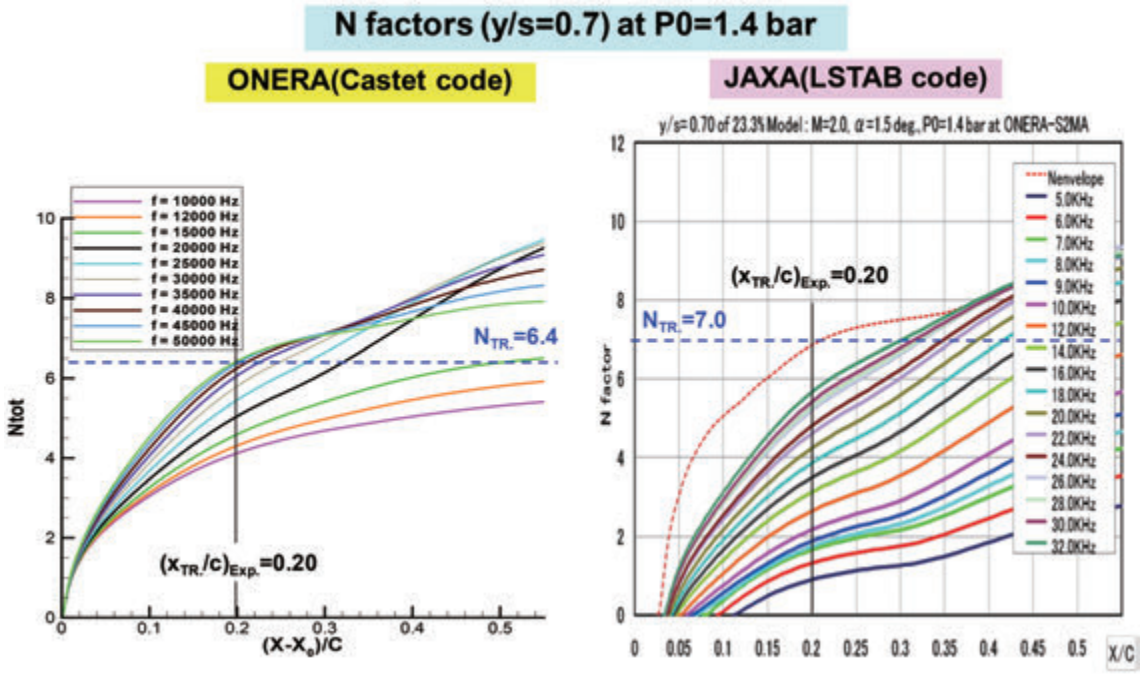

(b) Outer wing region (y/s=0.7)

Figure 47. Comparison of N factor (envelope strategy) at P0=1.4 bar

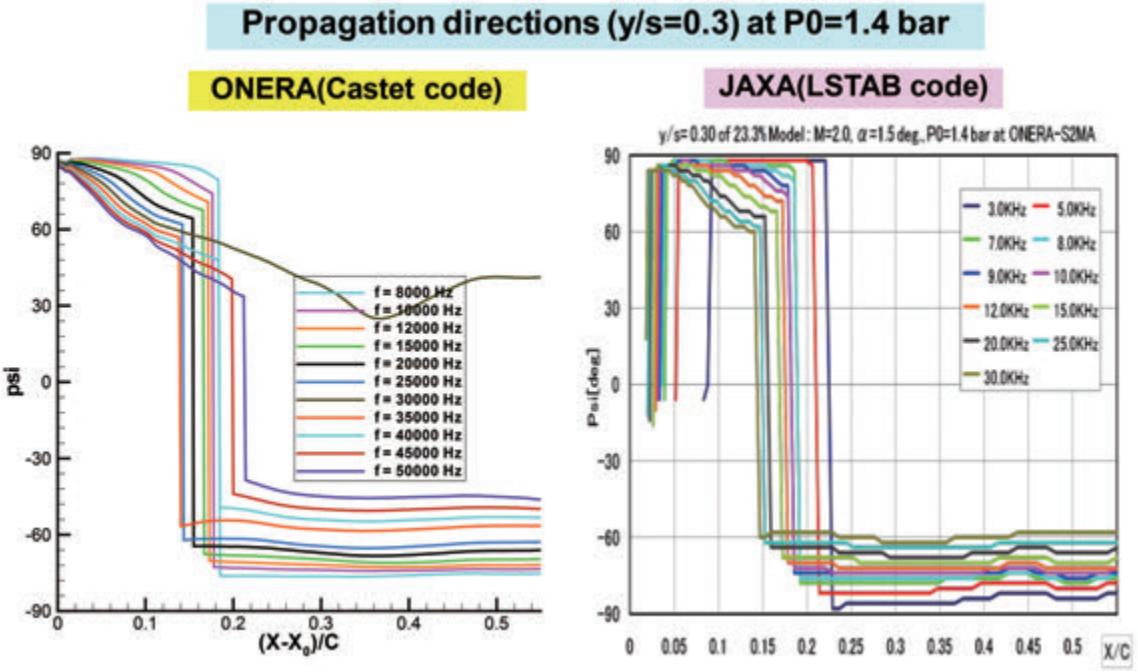

(a) Inner wing region (y/s=0.3)

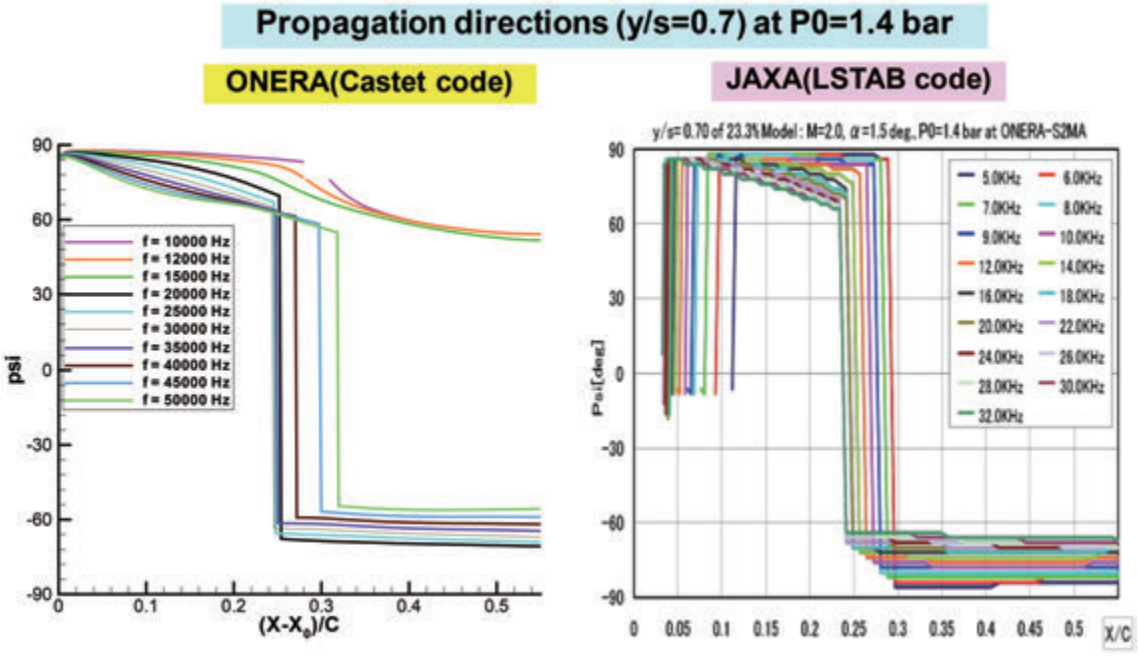

(b) Outer wing region (y/s=0.7)

Figure 48. Comparison of propagation direction (envelope strategy) at P0=1.4 bar

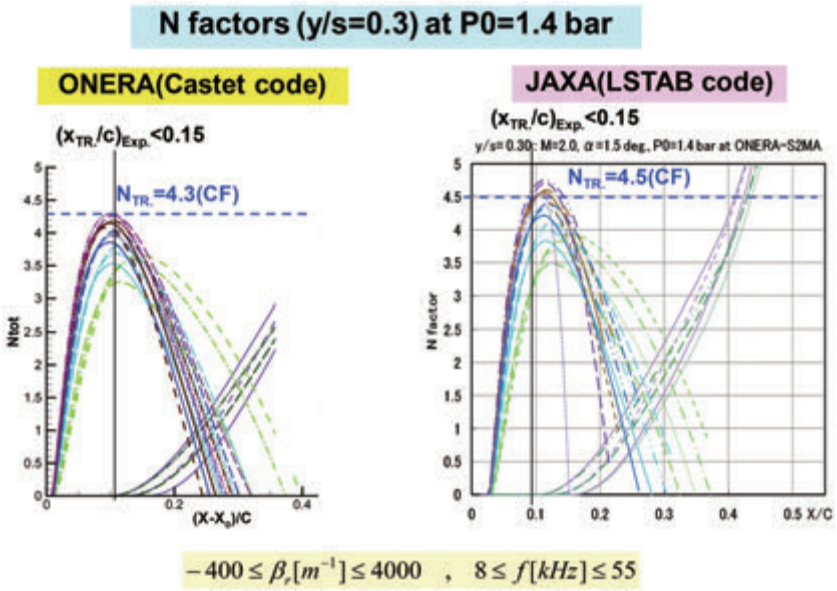

(a) Inner wing region (y/s=0.3)

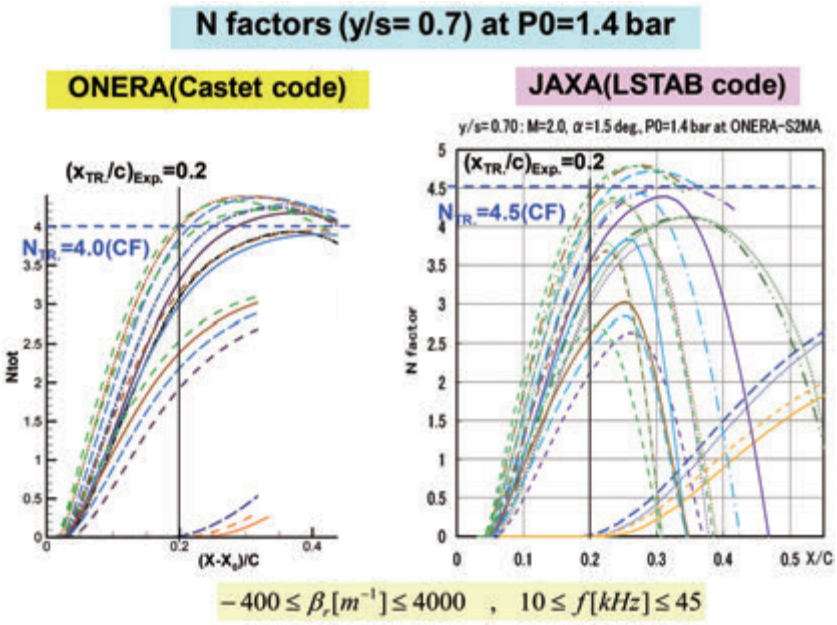

(b) Outer wing region (y/s=0.3)

Figure 49. Comparison of N factor (fixed β strategy) at P0=1.4 bar

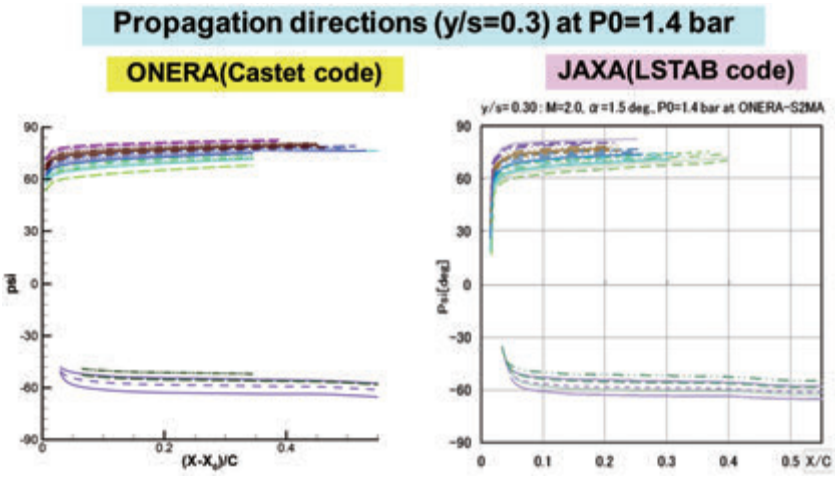

(a) Inner wing region (y/s=0.3)

Figure 50. Comparison of propagation direction (fixed β strategy) at P0=1.4 bar

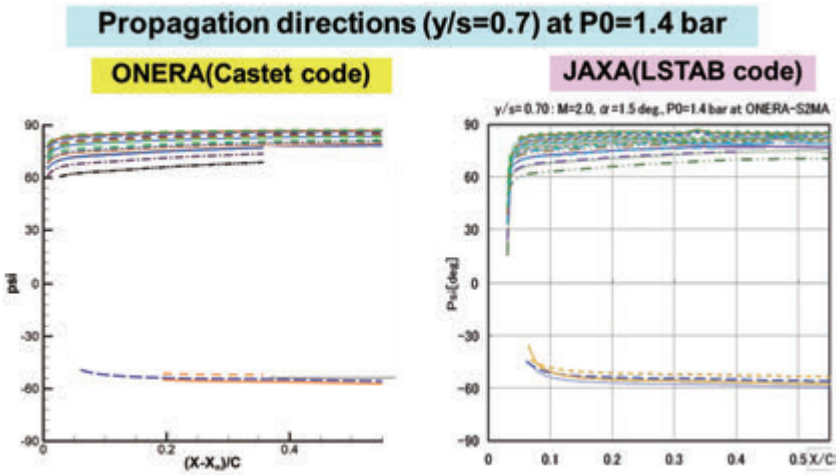

(b) Outer wing region (y/s=0.7)

Figure 50. Comparison of propagation direction (fixed β strategy) at P0=1.4 bar

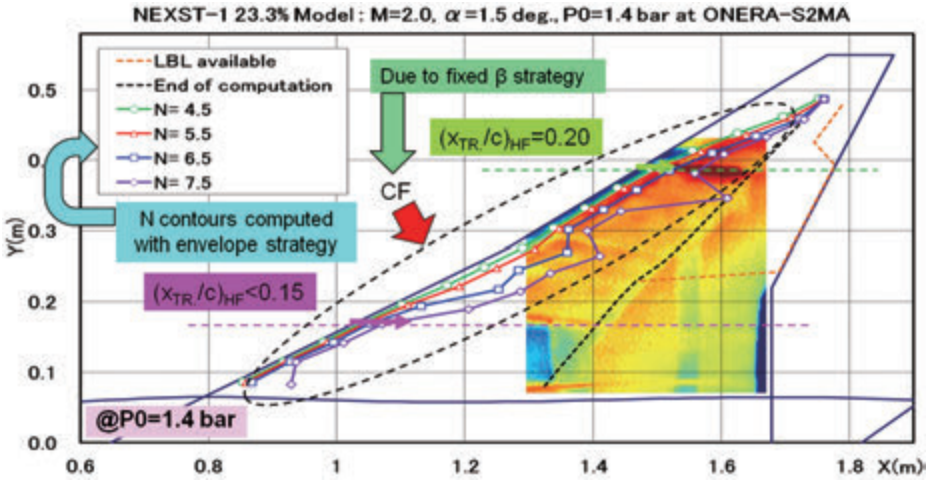

Figure 51. Comparison of measured transition location and N contours at P0=1.4 bar condition

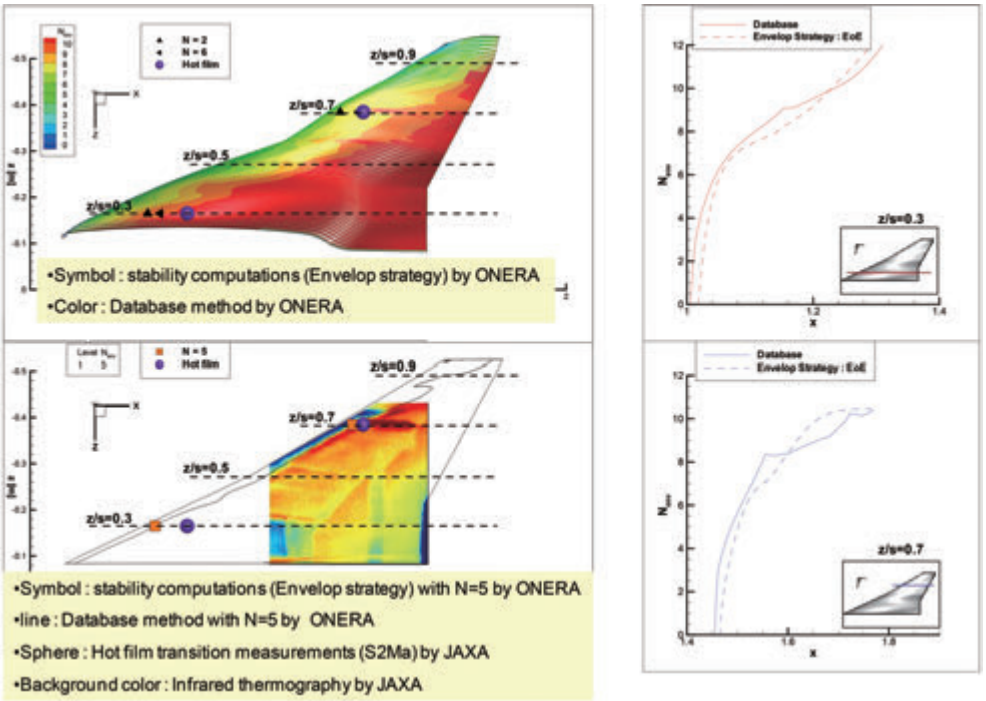

Figure 52. Comparison of measured transition location and ONERA’ s database method at P0=1.4 bar condition

Table 4. Summary of stability analysis at S2MA test

(a) Comparison of stability results due to envelope strategy

			Envelope Method					
			ONERA			JAXA		
		xt/c (Exp)	N	f(Hz)	Ψ	N	f(Hz)	Ψ
y/s=0.3 (c=0.659)	P_0=0.6	0.37	5.6	15000	-65	5.9	16500	-64
	P_0=1	0.22	6.4	20000	-62	6.6	23000	-60
	P_0=1.4	<0.15	7.6	35000	59	8.2	41500	52

			Envelope Method					
			ONERA			JAXA		
		xt/c (Exp)	N	f(Hz)	Ψ	N	f(Hz)	Ψ
y/s=0.7 (c=0.308)	P_0=0.6	0.49	4.4	20000	-65	4.8	19500	-66
	P_0=1	0.28	5.2	40000	58	5.5	44500	56
	P_0=1.4	0.2	6.4	50000	66	7	57000	66

(b) Comparison of stability results due to fixed β strategy

			Fixed Beta Strategy									
			ONERA					JAXA				
		xt/c (Exp)		N	Beta	f	Psi		N	beta	f	Psi
y/s=0.3 (c=0.659)	P_0=0.6	0.37	TS	2.9	-800	14000	-69	TS	3.3	-650	13000	-66
	P_0=1	0.22	CF	2.7	1500	25000	72	CF	2.8	1250	24000	69
	P_0=1.4	0.1-0.15	CF	4.3	4000	45000	80	CF	4.5	3250	43000	76

			Fixed Beta Strategy									
			ONERA					JAXA				
		xt/c (Exp)		N	beta	f	Psi		N	beta	f	Psi
y/s=0.7 (c=0.308)	P_0=0.6	0.49	TS	1.9	-800	13000	-70	TS	2.2	-850	16500	-68
	P_0=1	0.28	CF	3.2	3500	32500	75	CF	3.5	2700	42000	76
	P_0=1.4	0.2	CF	4	4000	45000	80	CF	4.5	4250	55000	78

characteristics on transition experiments conducted by JAXA at S2MA wind tunnel in 2000.

b) In this analysis, the CFD(NS)-based Cp distributions by JAXA were applied for the 3D-LBL computations, because they were in good agreement with the measured Cp distributions except for that at mid-spanwise station (y/s=0.5).

c) JAXA and ONERA computed the 3D-LBL and stability characteristics with both envelope and fixed β strategies, then both parties compared their N factors with measured transition locations. According to the fixed β strategy, both parties investigated the nature of transition by confirming the most dominant unstable mode, namely TS or CF instabilities.

d) Furthermore, ONERA used "Database" simplified stability method and compared it to experimental measurements and exact stability computations.

(2) Principal results

a) ONERA and JAXA confirmed good agreement in their stability results computed with both envelope and fixed β strategies.

b) Comparison of the N contour based on their stability results and experimental transition locations provides the following relations:

i) At P_0=0.6 bar condition, N=4.5 corresponds to the transition location measured with IR technique. N=5.5 and 4.5 (values obtained with envelope strategy) correspond to the transition location estimated with HF data at inner and outer wing regions

ii) At P_0=1.0 bar condition, N=5.5 corresponds to the transition location measured with IR technique. N=6.5 and 5.5 correspond to the transition location estimated with HF data at inner and outer wing regions

iii) At P_0=1.4 bar condition, N=4.5 corresponds to the transition location measured with IR technique. N=7.5 and 6.5 correspond to the transition location estimated with HF data at inner and outer wing regions

c) Furthermore, ONERA confirmed good relation among exact stability analysis with envelope strategy, ONERA's simplified method called "Database" and experimental results.

d) Finally, JAXA independently investigated the freestream turbulence level at the S2MA tunnel by using a dynamic pressure transducer to measure total pressure fluctuation. Then, JAXA compared them with ONERA's original data, and found 1.5 times higher level of Cp_{rms} as described in Appendix H.

4. Numerical study on influence of roughness

4.1. Measured roughness data

As mentioned above, surface quality has important influence on transition process. As a matter of fact, crossflow instabilities are very sensitive to surface roughness but any effective correction approaches on current e^N method have not been established yet. Before and after the flight test of the NEXST-1, JAXA measured roughness height distributions on the surface of both the S2MA test model and the NEXST-1 airplane, by using lots of sample pieces made of "resin" and laser displacement measurement system as shown in Figs. 53-54. Fig. 53(a) exhibits measurement points for those sample pieces on the wing and forebody surfaces of the S2MA wind tunnel test model. Fig. 53(b) indicates outline of present measurement technique and a summary of measured results on the S2MA model. From these data, we found that the averaged roughness height was less than about 1 μm as a metric of "Ra". Fig. 54(a) shows measurement points on the wing and body surfaces of the NEXST-1 airplane before the flight test. Fig. 54(b) indicates a summary of measured roughness data including the data measured after the flight test. It was obtained that the NEXST-1 had a similar averaged roughness height of about 1 μm to the one of the S2MA test model.

4.2. Influence of roughness condition on transition process

A couple of years ago, ONERA has proposed a useful relation between Reynolds number based on roughness height R_k, which is defined by the following equation and transition N value in supersonic flow condition[9] as summarized in Fig. 55. ONERA approximately found out linear relation between R_k and the N value as illustrated in the figure.

Then, both parties computed R_k value on the S2MA test model at each test condition, using 3D laminar boundary layer characteristics. ONERA's and JAXA's results were compared as shown in Figs. 56 and 57 and demonstrated a good agreement. The maximum R_k value was less than 0.1 even at the most highest test Reynolds number, P_0=1.4 bar condition.

Then, JAXA independently computed R_k contours on the NEXST-1 airplane over the same spanwise stations as the S2MA test model at two flight test conditions (namely α_No.4 and Re_No.5) and summarized them in Figs. 58. Based on these data, it was finally found that the maximum R_k value was less than 0.05 even at the higher Reynolds number condition (Re_No.5).

These R_k values were so small that they are not located within the database shown in Fig. 55.

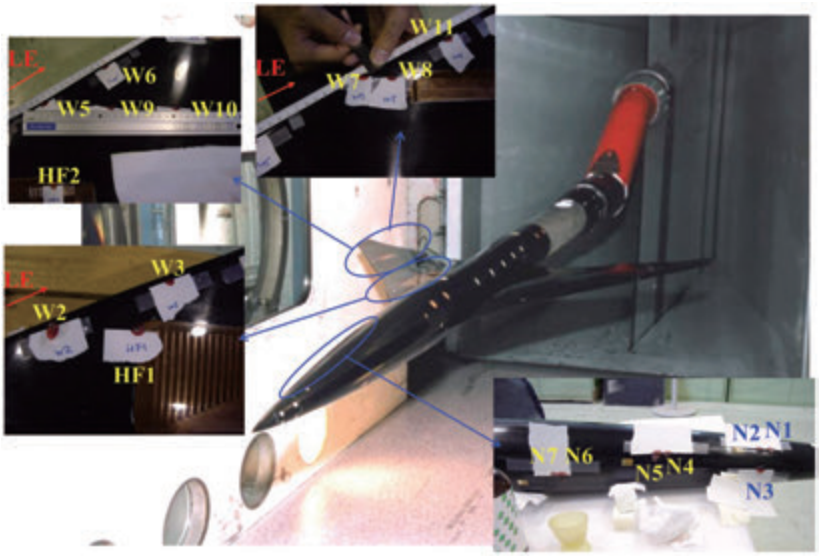

(a) Measurement points

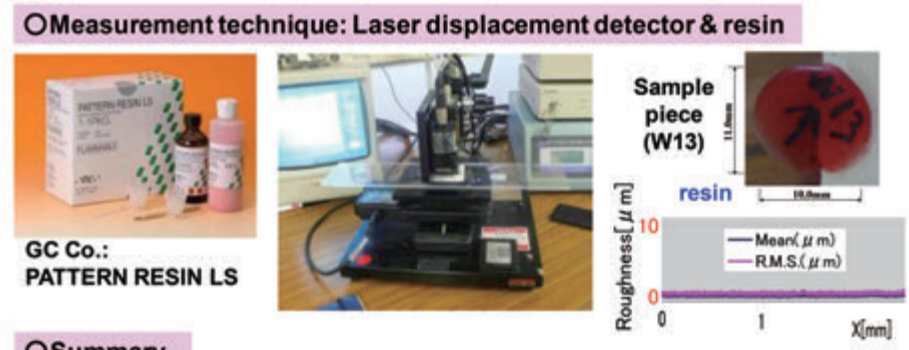

○Summary

	Ra,avg.		Ra,max		Ra,min	
	X[μm]	Y[μm]	X[μm]	Y[μm]	X[μm]	Y[μm]
N1	0.641	0.641	0.796	0.749	0.501	0.579
N3	0.617	0.617	0.938	0.684	0.421	0.543
W2	0.583	0.583	0.879	0.632	0.418	0.543
W6	0.303	0.605	0.616	0.671	0.181	0.559
W8	0.590	0.590	0.777	0.717	0.471	0.520
W14	0.566	0.566	0.728	0.669	0.426	0.475

Measured roughness
0.18μm< Ra < 0.94μm

$k_{averaged} \fallingdotseq 1$ μm

(b) Summary of measurement technique and results

Figure 53. Measured roughness data on S2MA test model

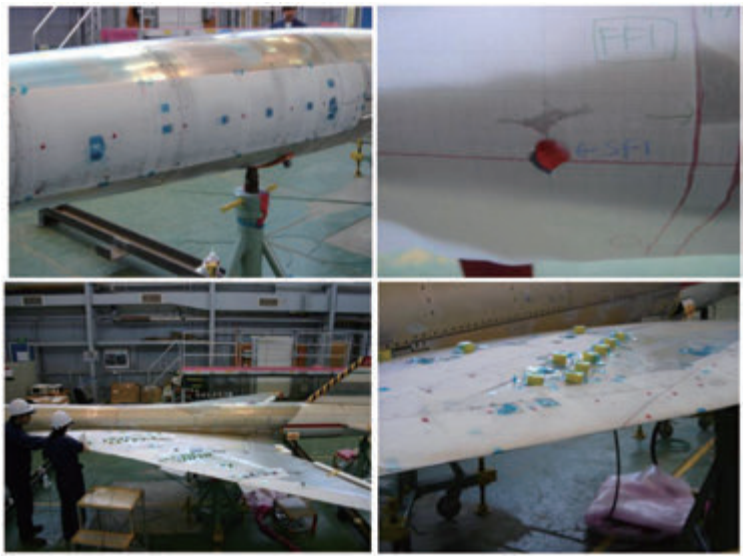

(a) Measurement points

Figure 54. Measured roughness data on NEXST-1 airplane

Therefore, JAXA approximated ONERA's database by using the following relation:

$$N = 16.25 - 6.61 \log_{10} R_k \quad where \quad R_k \equiv \frac{u_k k}{\nu_k}$$

According to this approximation, it is supposed that for such low value of R_k<0.1, the corresponding critical N value is very high N>22. Thus, present N value is too high to predict transition location due to influence of roughness. Based on present ONERA's database, it means that these R_k values have little influence on transition phenomenon. Naturally this consideration is also valid for transition phenomenon at α_No.4, because boundary layer thickness at this angle of attack is larger than at Re_No.5 case. Therefore, both parties finally judged that those measured roughness data on both the S2MA test model and the NEXST-1 airplane had no influence on transition process at test conditions.

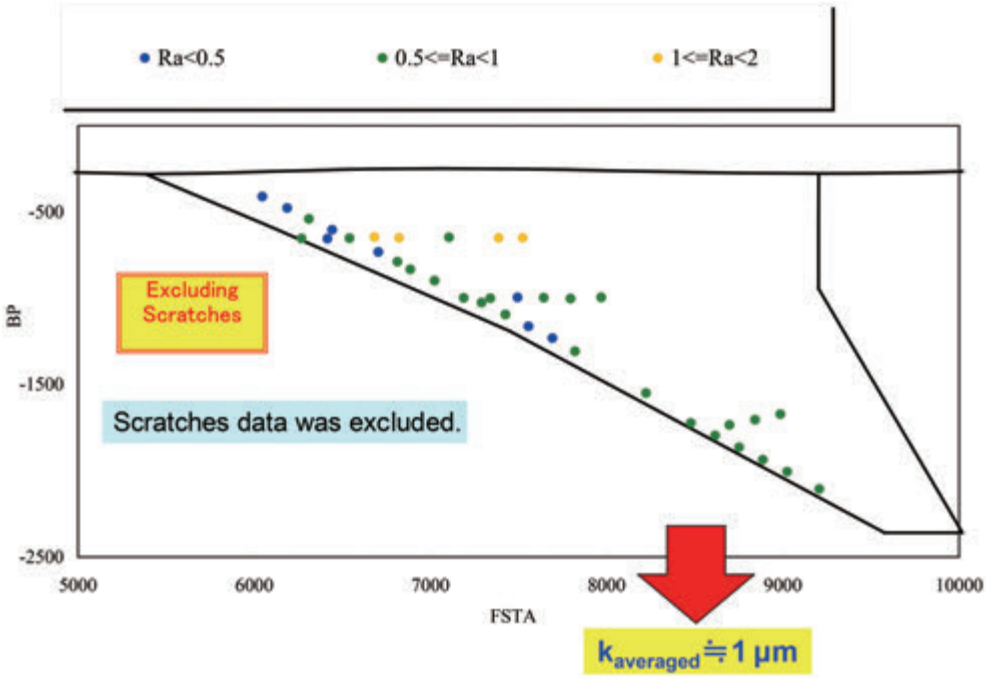

(b) Summary of measured results

Figure 54. Measured roughness data on NEXST-1 airplane

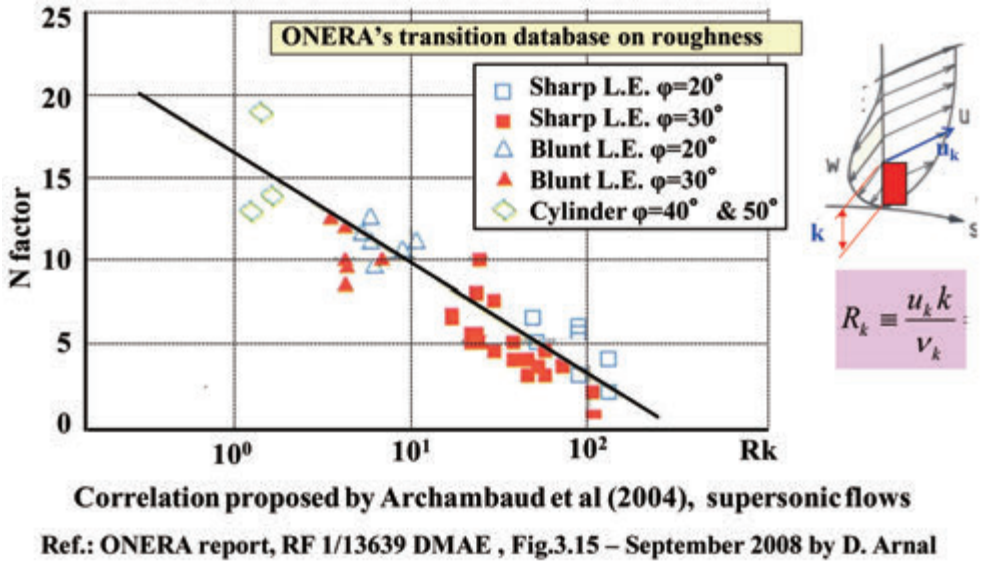

Figure 55. ONERA's transition database on roughness condition

4.3. Summary of chapter 4

(1) Subjects

To investigate the roughness effect on transition characteristics, both parties analyzed the Reynolds number based on measured roughness height R_k along the chordwise location of both the NEXST-1 airplane and the S2MA test model. Then, both parties compared them with ONERA's roughness database, which was approximately summarized in the linear relation between R_k and transition N values.

(2) Principal results

a) Measured roughness height was about 1 μm, using a laser displacement detector and several sample pieces made of resin.

b) Computed R_k values were less than about 0.1

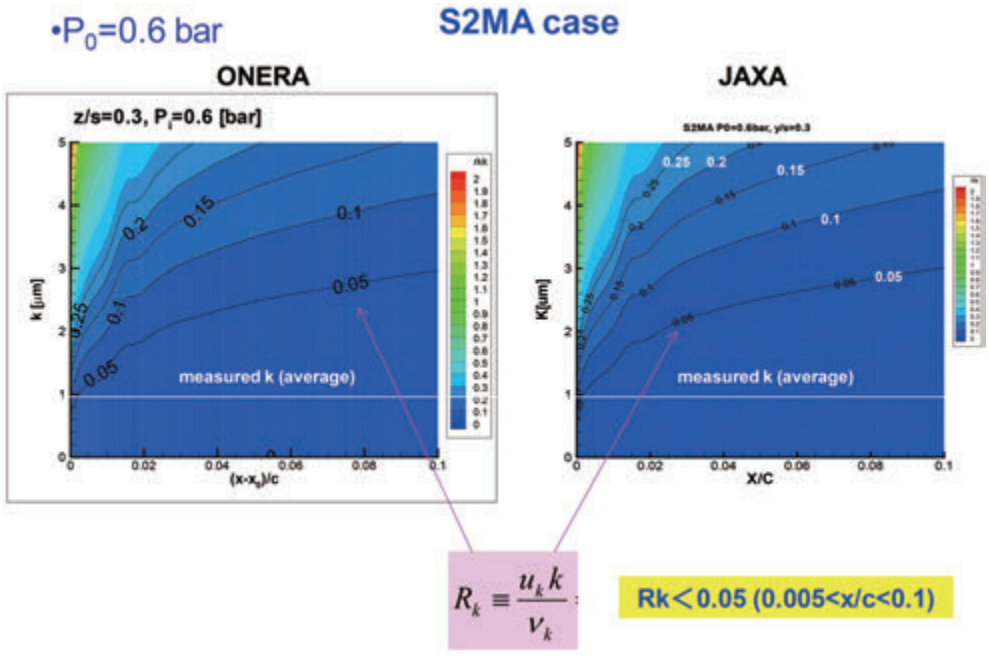

(a) y/s=0.3

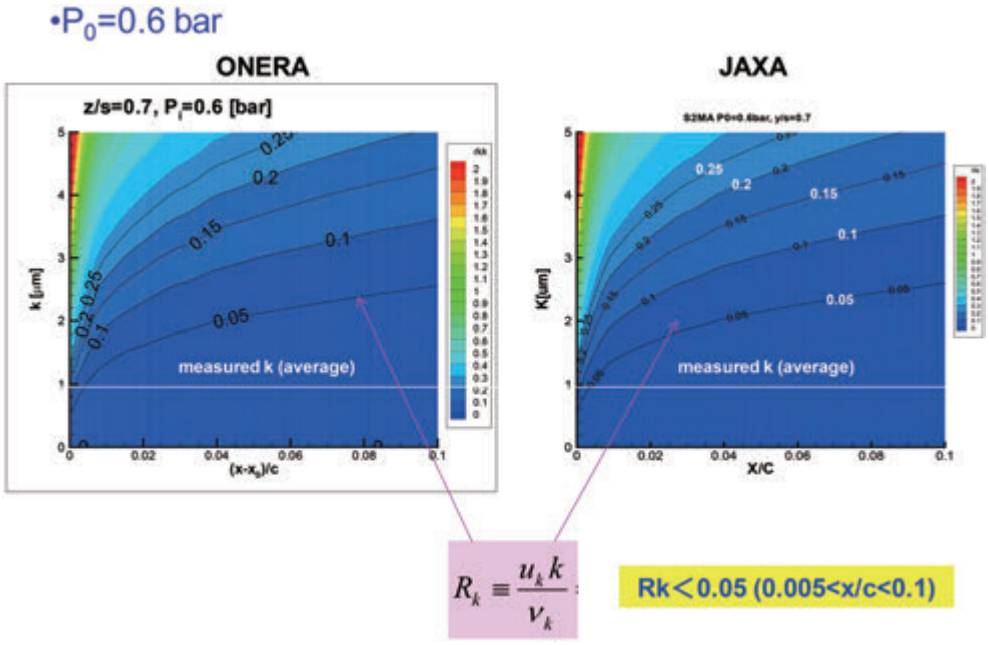

(b) y/s=0.7

Figure 56. R_k contours computed at P0=0.6 bar of S2MA test model

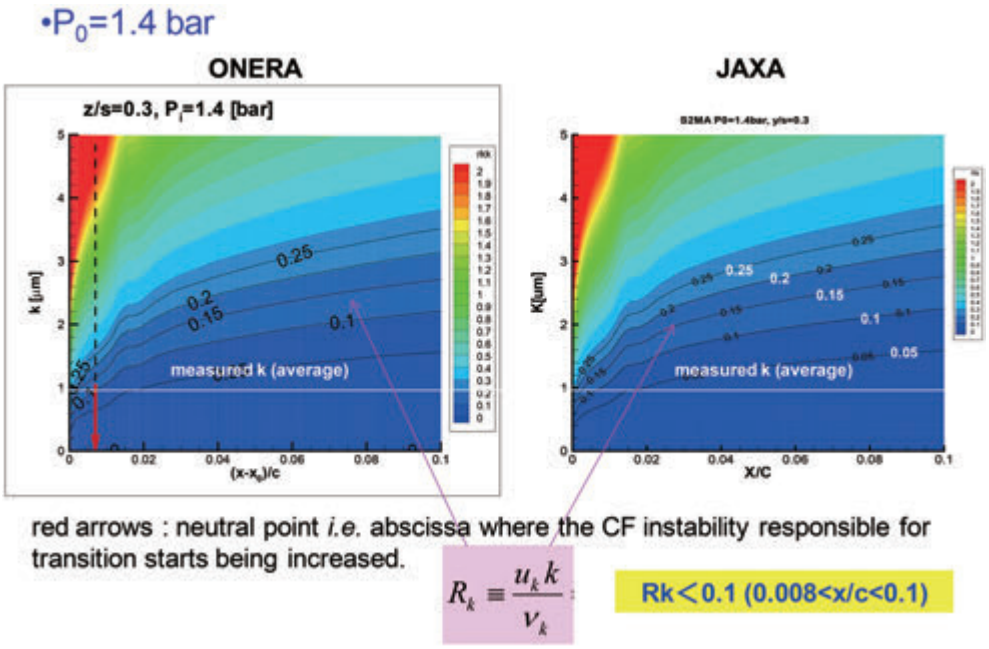

(a) y/s=0.3

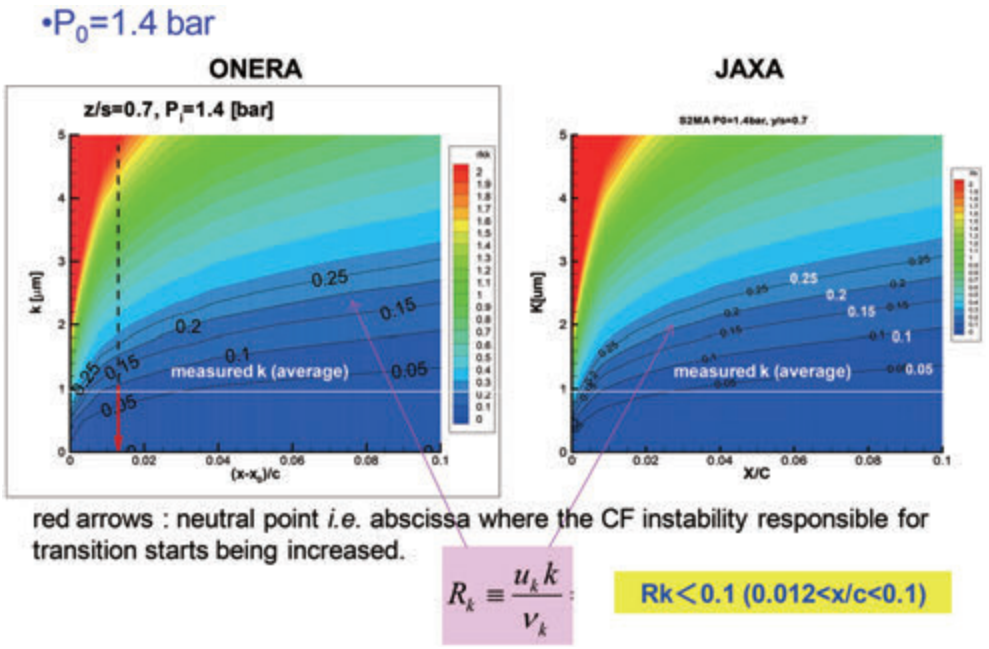

(b) y/s=0.7

Figure 57. R_k contours computed at P0=1.4 bar of S2MA test model

after the neutral point in chordwise location. Therefore, according to the comparison of the R_k values and ONERA's original experimental roughness database, both parties found the special N value due to natural transition was above 22. It means that such roughness condition makes no influence on transition process.

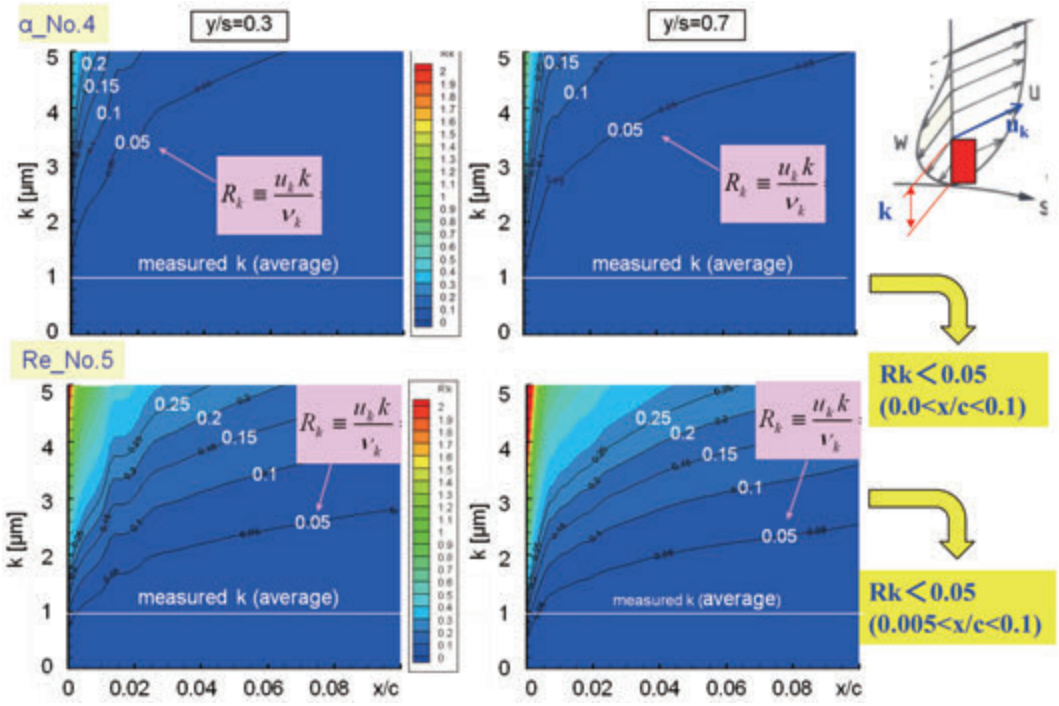

Figure 58. R_k contours on NEXST-1 airplane

5. Consideration of Reynolds number effect

As mentioned above, JAXA's NLF wing design concept of the NEXST-1 was not effective at higher Reynolds number condition (Re_No.5). To understand this situation, the influence of Reynolds number on transition process in fully 3D laminar boundary layer is considered in this section. First of all, the complete set of experimental transition data is summarized. In a second time, experimental transition locations are compared to the predicted numerical ones obtained with an assumed critical value of N factor. Finally, the influence of Reynolds number on the nature of instability and transition process using theoretical target external pressure distribution is investigated.

5.1. Summary of experimental transition data

Figures 59 and Table 5 summarize transition measurement results of S2MA wind tunnel and NEXST-1 flight tests mentioned above. As seen in Fig.59(a), behavior of transition location at outer wing region in the S2MA test case is different from that in the NEXST-1 flight test case when the MAC-based Reynolds number Re_{MAC} increases. Fig. 59(b) shows such behavior more clearly in the spanwise variation of measured transition location. The left part of Fig. 59(b) shows the spanwise trend of measured transition position normalized with each local chord $(x/c)_{TR}$ for the case α_No.4, and the right part of the figure indicates transition Reynolds number based on streamwise distance from the leading edge of the models. In this figure, the measured transition location at y/s=0.7 for α_No.4 case has relatively a strange feature compared with other transition locations. Both parties turned their attention to the fact that the transition measured at y/s=0.7 was too close to the leading edge at α_No.4.

According to the R_k study for the S2MA test model and the NEXST-1 airplane, the influence of roughness on transition process was estimated to be weak. As mentioned before, freestream turbulence level is supposed to be very low for flight test condition, Tu≈0.05% and increases for wind tunnel tests (Tu=0.15% at S2MA). Therefore, the evolution of transition location along the spanwise direction is only influence by freestream turbulence and external pressure distribution.

In addition, if it is assumed that transition is predicted with a constant N factor value over the whole part of the wing, the transition lines obtained imposing N=4.5 for the S2MA test cases and N=12 for the NEXST-1 flight test cases are plotted in Fig. 60 (corresponding values appear in Table 6). Experimental results are in almost close agreement with these predicted ones as seen in Fig. 60. Therefore, the Reynolds number trend on measured and predicted transition locations can be summarized in Figs. 61. Fig. 61(a) shows unit Reynolds number effect on transition location (both transition Reynolds number $\mathrm{Re}_{x_T} = U_\infty \times x_T / \nu_\infty$ and dimensionless transition location x_T/c). Fig. 61(b) indicates MAC-based Reynolds number effect. As seen in both

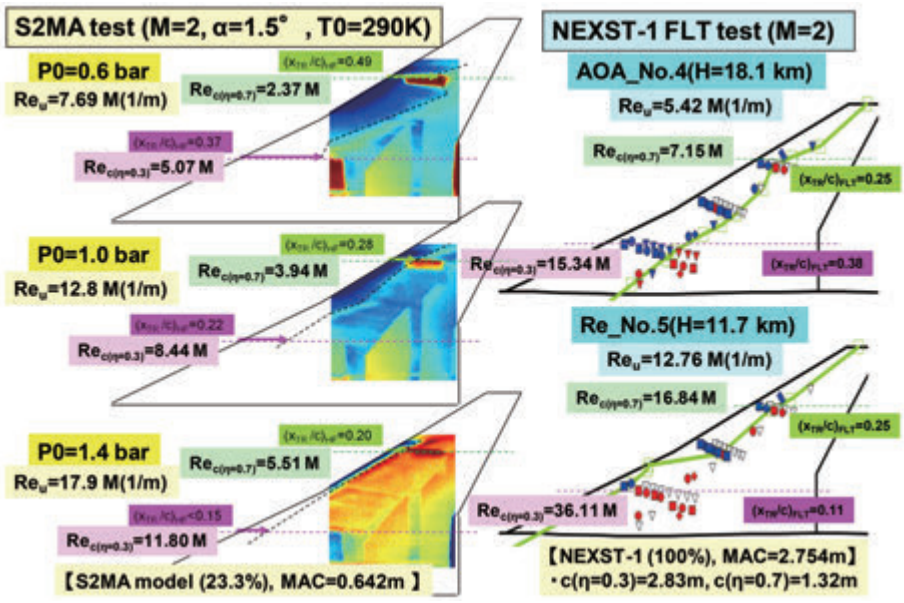

(a) Surface pattern

Test	Case	Re_u[Million] (1/m)	MAC (m)	Re_{MAC}[M]
NEXST-1 (100%)	AOA_No.4	5.42	2.754	14.93
	Re_No.5	12.76	2.754	35.14
S2MA (23.3%)	P0=0.6bar	7.69	0.642	4.93
	P0=1.0bar	12.80	0.642	8.21
	P0=1.4bar	17.90	0.642	11.49

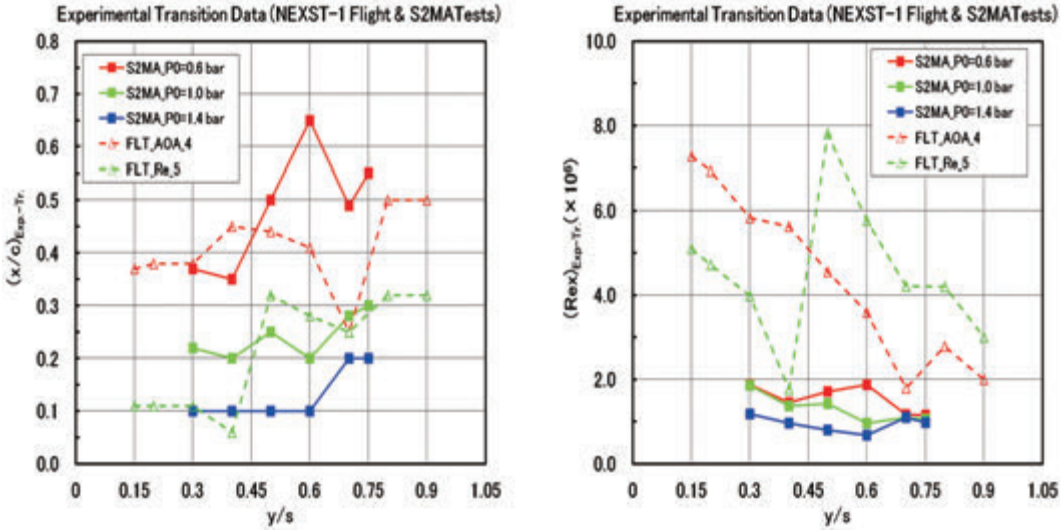

(b) Spanwise pattern

Figure 59. Summary of experimental transition data

Table 5. Summary of experimental transition data

FLIGHT TEST		α_No.4			Re_No.5		
Scale=	100%	Reu(1/m)=		5.42	Reu(1/m)=		12.76
MAC(m)=	2.754	Re_{MAC}[M]=		14.93	Re_{MAC}[M]=		35.14
y/s	c(m)	$(X/C)_{TR}$	X_{TR}(m)	ReX_{TR}[M]	(x/c)TR.	X_{TR}(m)	ReX_{TR}[M]
0.15	3.630	0.37	1.343	7.28	0.11	0.399	5.09
0.2	3.365	0.38	1.279	6.93	0.11	0.370	4.72
0.3	2.835	0.38	1.077	5.84	0.11	0.312	3.98
0.4	2.305	0.45	1.037	5.62	0.06	0.138	1.77
0.5	1.912	0.44	0.841	4.56	0.32	0.612	7.81
0.6	1.614	0.41	0.662	3.59	0.28	0.452	5.77
0.7	1.321	0.25	0.330	1.79	0.25	0.330	4.22
0.8	1.028	0.5	0.514	2.79	0.32	0.329	4.20
0.9	0.735	0.5	0.368	1.99	0.32	0.235	3.00

S2MA TEST		P0=0.6 bar			P0=1.0 bar			P0=1.4 bar		
Scale=	23/3%	Reu(1/m)=		7.69	Reu(1/m)=		12.8	Reu(1/m)=		17.9
MAC(m)=	0.642	Re_{MAC}[M]=		4.94	Re_{MAC}[M]=		8.22	Re_{MAC}[M]=		11.49
y/s	c(m)	$(X/C)_{TR}$	X_{TR}(m)	ReX_{TR}[M]	$(X/C)_{TR}$	X_{TR}(m)	ReX_{TR}[M]	$(X/C)_{TR}$	X_{TR}(m)	ReX_{TR}[M]
0.3	0.661	0.37	0.244	1.88	0.22	0.145	1.86	0.1	0.066	1.18
0.4	0.537	0.35	0.188	1.45	0.2	0.107	1.38	0.1	0.054	0.96
0.5	0.445	0.5	0.223	1.71	0.25	0.111	1.43	0.1	0.045	0.80
0.6	0.376	0.65	0.245	1.88	0.2	0.075	0.96	0.1	0.038	0.67
0.7	0.308	0.49	0.151	1.16	0.28	0.086	1.10	0.2	0.062	1.10
0.75	0.274	0.55	0.151	1.16	0.3	0.082	1.05	0.2	0.055	0.98

figures, Reynolds number has opposite influence on measured transition location at y/s=0.7 in the NEXST-1 flight test case, compared to the other curves.

From the Fig. 61(b), if the outer part of the wing, namely y/s=0.7, is considered, the evolution of transition Reynolds number in the flight test condition (indicated as "FLT") is different from that in the wind tunnel test condition. It also implies that the measured transition location at y/s=0.7 at α_No.4 case was too close to the leading edge compared with the transition location predicted with the constant N value.

This upstream movement of measured transition location at y/s=0.7 may originate in the following subjects:

(a) Interpolated Cp contour did not completely coincide with measured Cp contour, especially spanwise variation of Cp distributions near y/s=0.7 was not well-interpolated.

(b) Measured Cp contour did not reflect the target Cp contour, especially near the outer wing region.

As for the subject (a), additional stability analysis on the Cp distributions based on our surface-interpolation technique with carefully tunned parameters near the region at y/s=0.7 indicates that correlation between measured and predicted transition locations was slightly improved, but not fully. JAXA has not cleared this point yet. As for the subject (b), further stability analysis on the Cp_{Target} contour was performed as described in next section.

Therefore, JAXA reconsidered the stability characteristics at outer wing region for the α_No.4 case and discussed them, compared with stability results on the JAXA's target pressure distribution for the NEXST-1 NLF wing design. These results are described in section 3. But, in next section, both parties show important results on investigation of the nature of measured transition under the help of fixed β strategy.

5.2. Consideration on nature of transition and Reynolds number effect

Figs. 62 show two comparisons of spanwise variation of N factors corresponding to measured transition location computed by ONERA and JAXA. The nature of instability responsible for transition onset is specified on the graphs in agreement with fixed β strategy computations. The N factor computed with envelope strategy in Fig. 62(a) is larger than that with fixed β strategy in Fig. 62(b). However, of course, spanwise trend of transition movement in Fig. 62(a) is qualitatively

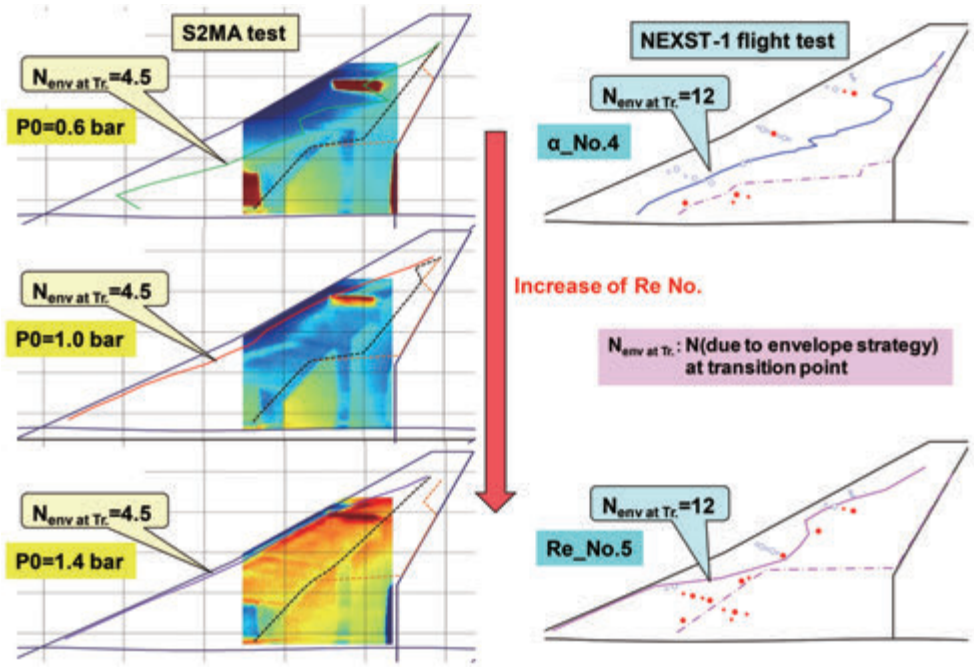

Figure 60. Comparison of measured and predicted transition locations

Table 6. Summary of transition analysis data

Test	Case	Re_∞[Million] (1/m)	MAC (m)	Re_{MAC}[M]	N_{TR}	z/c=0.3				
						$(x_{TR}/c)_N$	c(m)	Rec	x_{TR}(m)	Rex_{TR}[M]
NEXST-1 (100%)	AOA_No.4	5.42	2.754	14.93	12	0.28	2.830	15.34	0.80	4.32
	Re_No.5	12.76	2.754	35.14	12	0.03	2.830	36.11	0.07	0.92
S2MA (23.3%)	P0=0.6bar	7.69	0.642	4.93	4.5	0.22	0.659	5.07	0.15	1.12
	P0=1.0bar	12.80	0.642	8.21	4.5	0.05	0.659	8.44	0.03	0.41
	P0=1.4bar	17.90	0.642	11.49	4.5	0.03	0.659	11.80	0.02	0.40

Test	Case	Re_∞[Million] (1/m)	MAC (m)	Re_{MAC}[M]	N_{TR}	z/c=0.7				
						$(x_{TR}/c)_N$	c(m)	Rec	x_{TR}(m)	Rex_{TR}[M]
NEXST-1 (100%)	AOA_No.4	5.42	2.754	14.93	12	0.54	1.320	7.15	0.71	3.85
	Re_No.5	12.76	2.754	35.14	12	0.15	1.320	16.84	0.19	2.47
S2MA (23.3%)	P0=0.6bar	7.69	0.642	4.93	4.5	0.43	0.308	2.37	0.13	1.03
	P0=1.0bar	12.80	0.642	8.21	4.5	0.15	0.308	3.94	0.05	0.59
	P0=1.4bar	17.90	0.642	11.49	4.5	0.08	0.308	5.51	0.02	0.43

the same as that in Fig. 62(b) because it depends on measured transition location. The trend of transition N factors computed with both envelope strategy (N_{env}) and with fixed β strategy (N_{beta}) corresponding to measured transition location show that they qualitatively decrease as spanwise station (y/s) increases. It means that disturbances are weakly amplified in the outer region than in inner wing region. Furthermore, at a given spanwise station, the N_{env} and N_{beta} generally increase as the Reynolds number increases. This is due to the enhancement of CFI growth in the vicinity of the leading edge.

As seen in these figures, at low Reynolds number conditions, TS instability is dominant except for y/s=0.7 at α_No.4. As Reynolds number increases, instability changes from TS to CF. These results mean that JAXA's target pressure distribution well suppresses CF instability at the design point, but is not adapted to high Reynolds number conditions.

Finally, N factor on the S2MA test case indicates relatively lower value than that at the NEXST-1 flight test condition. In the same way, the decrease of N factor, obtained with envelope method, from inner to outer wing region at

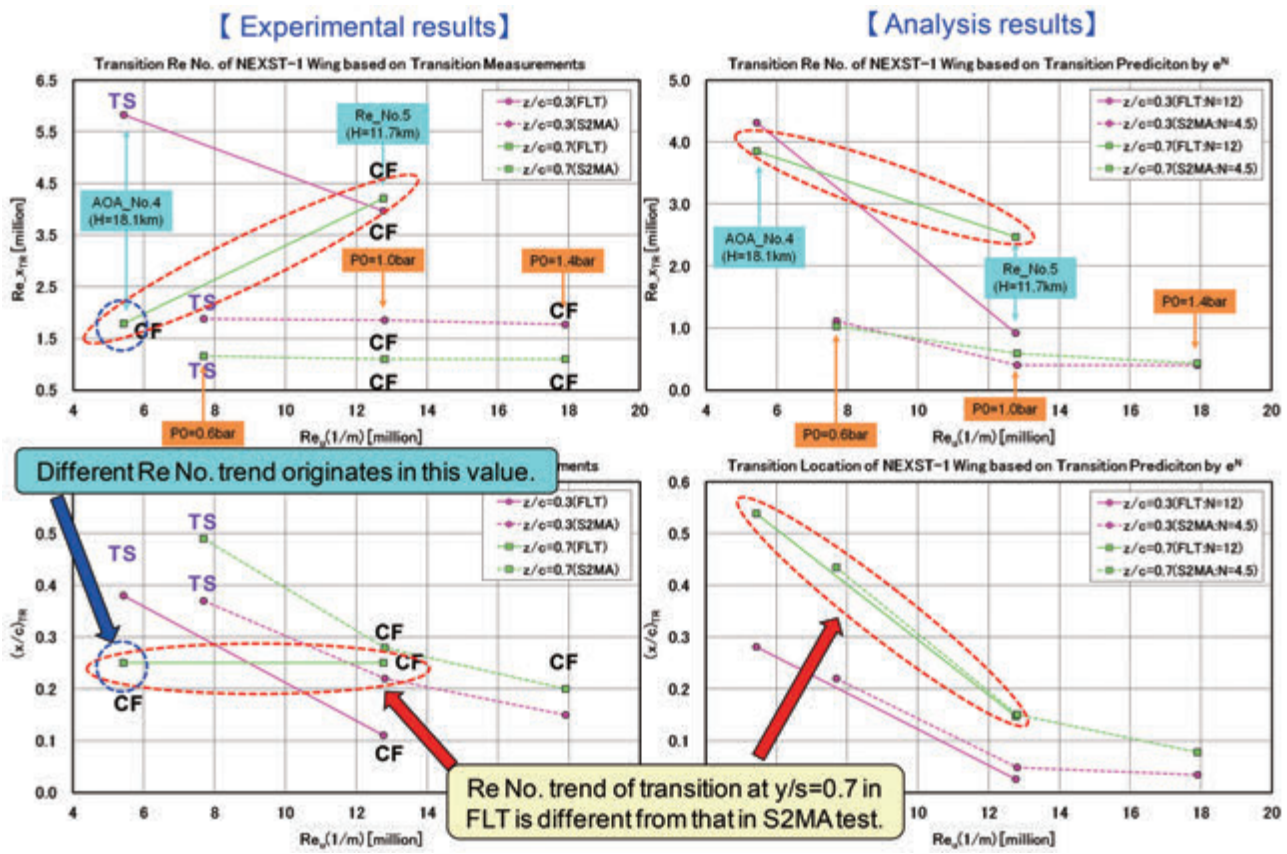

(a) Unit Re No. effect

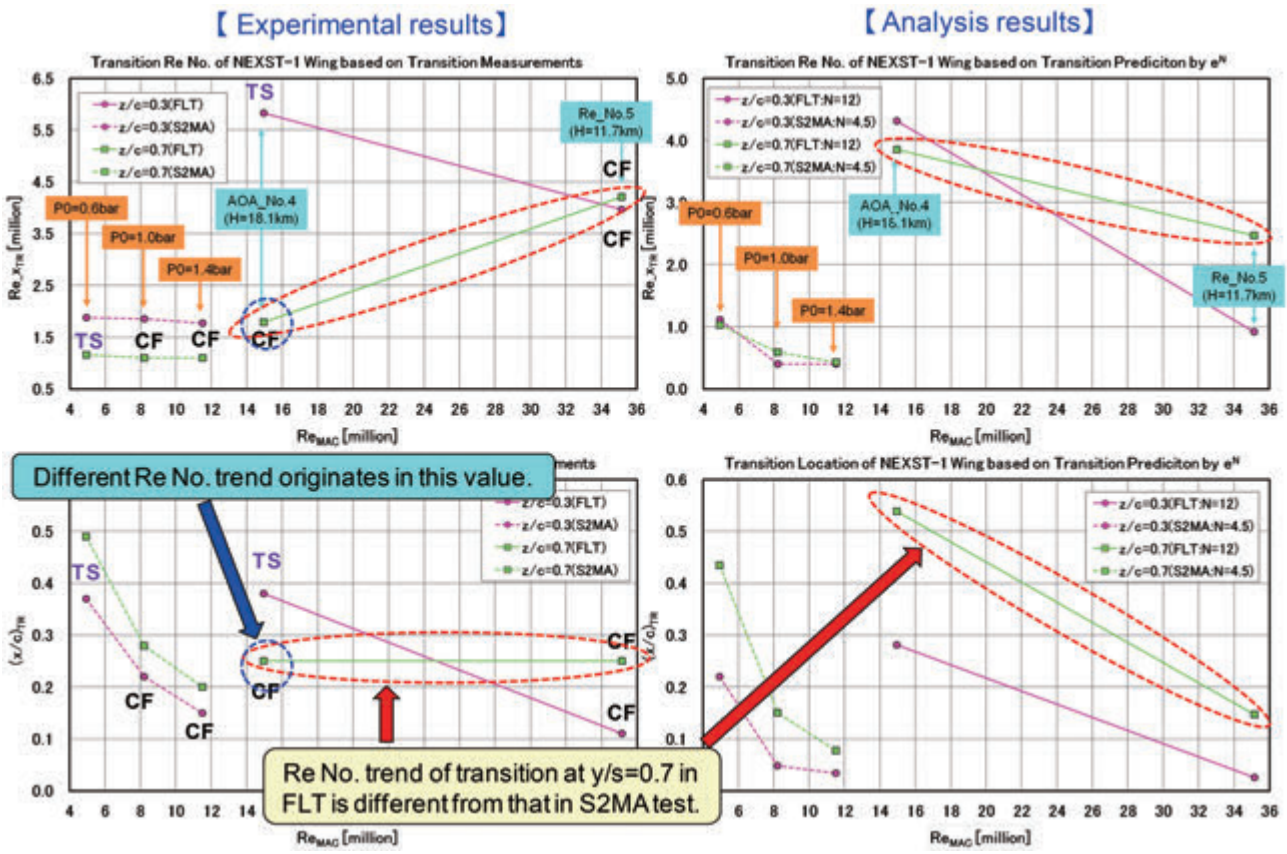

(b) MAC-based Re No. effect

Figure 61. Comparison of Re No. effect

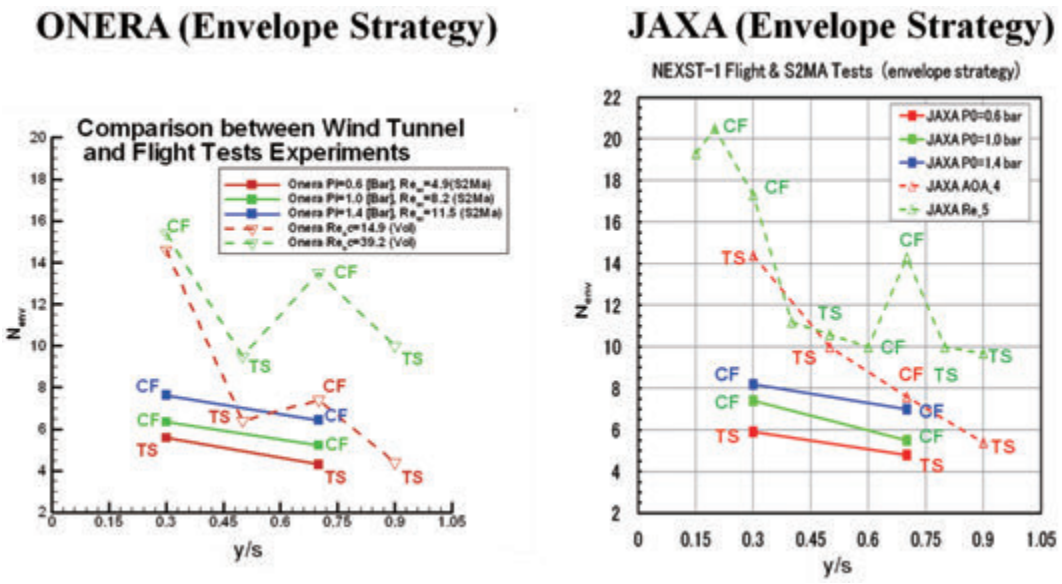

(a) Envelope strategy

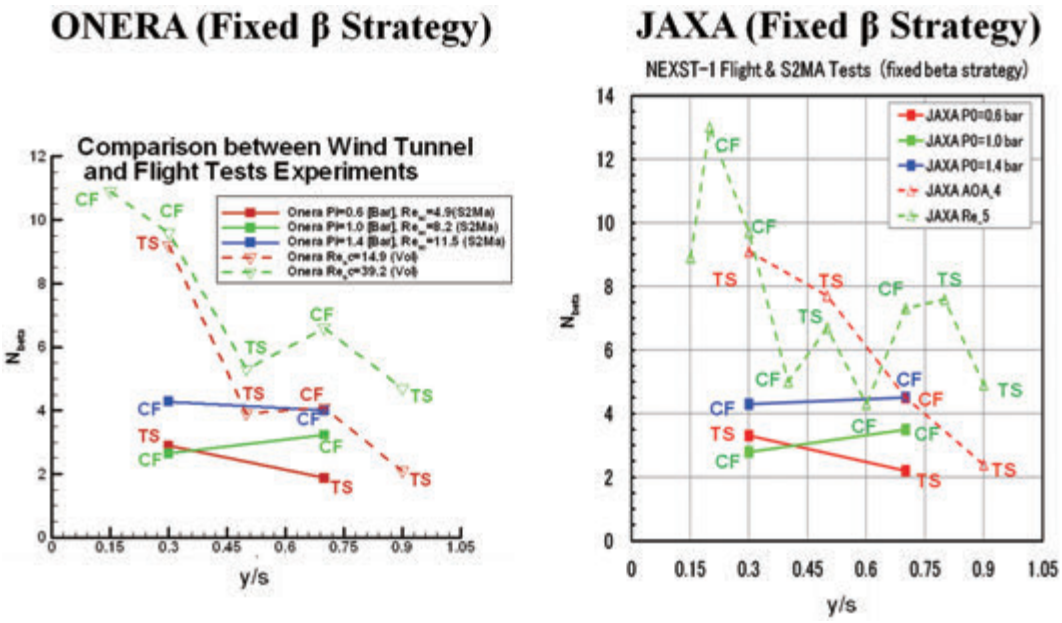

(b) Fixed β strategy

Figure 62. Spanwise variation of transition N values

the NEXST-1 case is much larger than that at the S2MA case: this implies that earlier transition at outer wing region for the α_No.4 case was measured against JAXA's prediction.

5.3. Reynolds number effect on the NEXST-1 target Cp distributions

At first, comparison of the target pressure (Cp_{Target}) and present surface-interpolated Cp contours is shown in Fig. 63. As easily seen, there is remarkable difference at outer wing region, including slight difference near leading edge region. These difference originated in non-completion of convergence in the inverse design process of the NEXST-1 NLF wing. As shown in Fig. B-2 of Appendix B, the final CFD-based design Cp distributions had already slight difference at outer wing region[4]. Therefore, JAXA computed 3D boundary layer flow using this target pressure distribution. A comparison of new boundary layer characteristics and previous results computed with surface-interpolated pressure distribution is shown in Fig. 64.

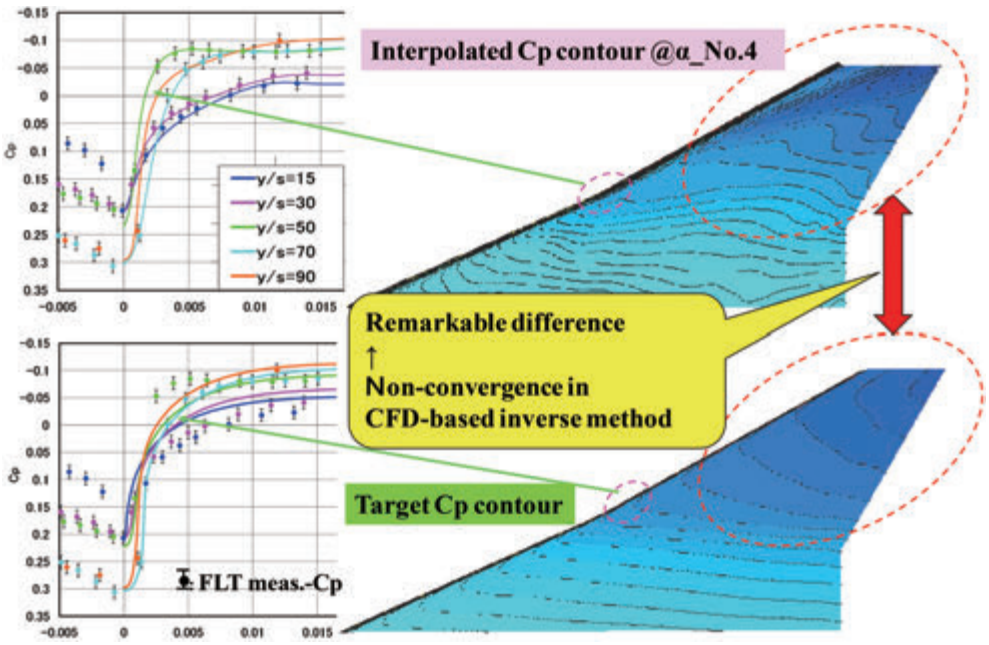

Figure 63. Comparison of target and surface-interpolated measured pressure distributions at α_No.4

It was clearly found remarkable difference in both maximum values of CF velocity profile.

A comparison of stability results on target and surface-interpolated Cp contours computed with envelope strategy are summarized in Fig. 65. This figure indicates that the Cp_{Target} contour has possibility to delay the transition at outer wing region more strongly than at the surface-interpolated one.

Then, Reynolds number influence on transition process (nature of instability and transition location), was numerically investigated using the theoretical target pressure distribution. N factors provided by envelope strategy over full spanwise wing region and by fixed β strategy at the mid-span region (y/s=0.5) are plotted in Fig. 66 and Fig. 67 at representative Reynolds number conditions. It was naturally confirmed that the predicted transition location corresponding to a certain N value moved towards the leading edge when Reynolds number increased.

To understand physical nature of transition, namely to identify the most dominant instability, fixed β strategy computations were also performed. Here, to study Reynolds number effect on transition movement, a critical value of N factor corresponding to transition onset must be set. Based on previous results shown in Fig. 65, since N=6 for fixed β strategy had good correlation with measured transition location, it was selected in present study as the transitional N factor value.

According to this criterion, the dominant mode is Tollmien-Schlichting instability for the lower Reynolds number case as shown in Fig. 67. When Reynolds number increases above $Re_{MAC}>22.4\times10^6$, transition is triggered by cross-flow instability. As a matter of fact, as chord Reynolds number Re_{MAC} increases, amplification of CFI near the leading edge region is enhanced. The evolution of dimensionless transition location $(x/c)_{TR}$ corresponding to $N_{TR.}=6$ is plotted in Fig. 68 (green line for y/s=0.5) as a function of chord Reynolds number, and summarized in Table 7. Open symbols stand for TSI driven transition whereas full symbols represent CFI induced transition. Up to $Re_{MAC} < 22.4\times10^6$, transition is triggered by TSI and its position slightly moves upstream when Re_{MAC} increases. At $Re_{MAC}=22.4\times10^6$, as represented in Fig. 67, CFI are sufficiently amplified to reach the critical transition N value: therefore, the transition dramatically moves towards the leading edge and will take place all the more close to the leading edge than the Reynolds number increases.

This physical change of transition phenomenon is illustrated by the drop of the green line represented $(x/c)_{TR}$ as a function of chord Reynolds number at $Re_{MAC}\approx22.4\times10^6$ in Fig. 68. Same

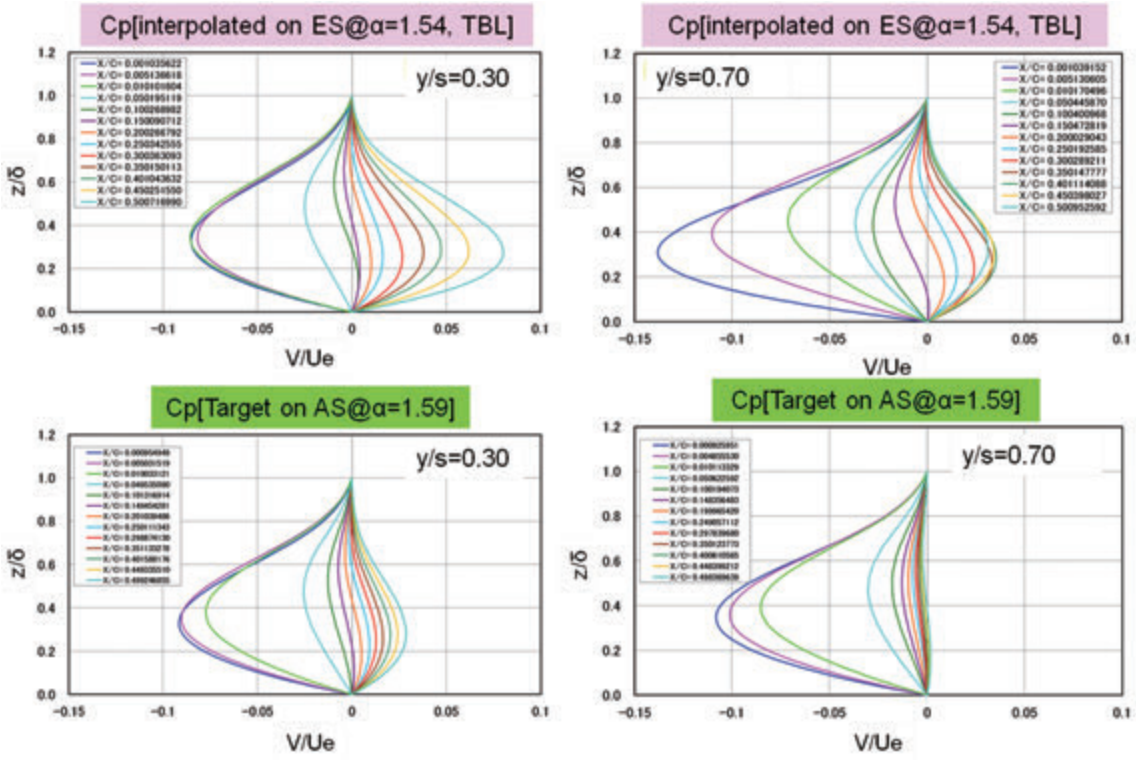

Figure 64. Comparison of CF velocity profiles at inner and outer wing regions

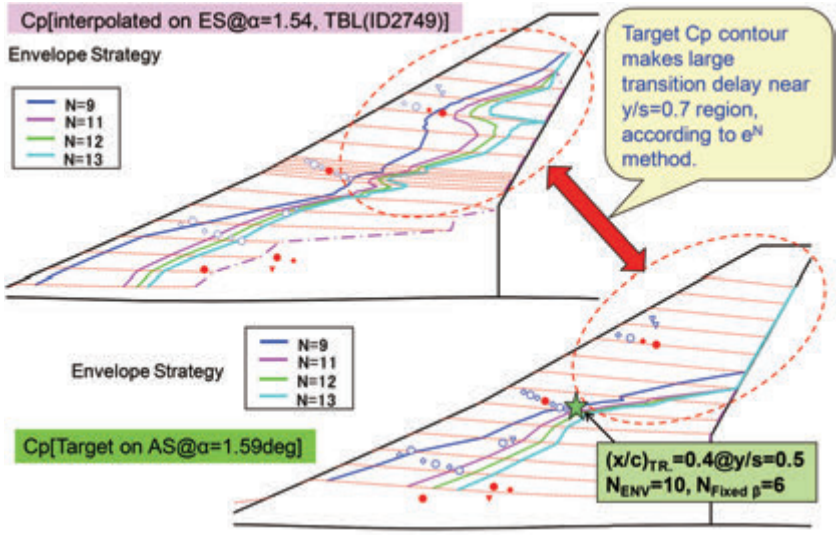

Figure 65. Comparison of N factors (envelope strategy) on target and surface-interpolated Cp contours

kind of analysis has been carried out for y/s=0.3 and 0.7. All the results are also gathered in Fig. 68. For the inner part of the wing, namely y/s=0.3, transition is induced by CFI even for low Reynolds number. For the outer part of the wing, y/s=0.7, the evolution is very similar to the one obtained at y/s=0.5. N factors on present target Cp contour computed with envelope and fixed β strategies at y/s=0.3, 0.5 and 0.7 for whole Reynolds number conditions are summarized in Appendix K.

As mentioned before, the predicted transition near mid-span region rapidly moves near the leading edge region, around $Re_{MAC} \approx 22.4 \times 10^6$, because of the change of instability nature from TSI to CFI. Therefore, JAXA's NLF wing design concept completely based on the Cp_{Target} contour has possibility of large laminarity at outer wing region for a Reynolds number range such that Re_{MAC}

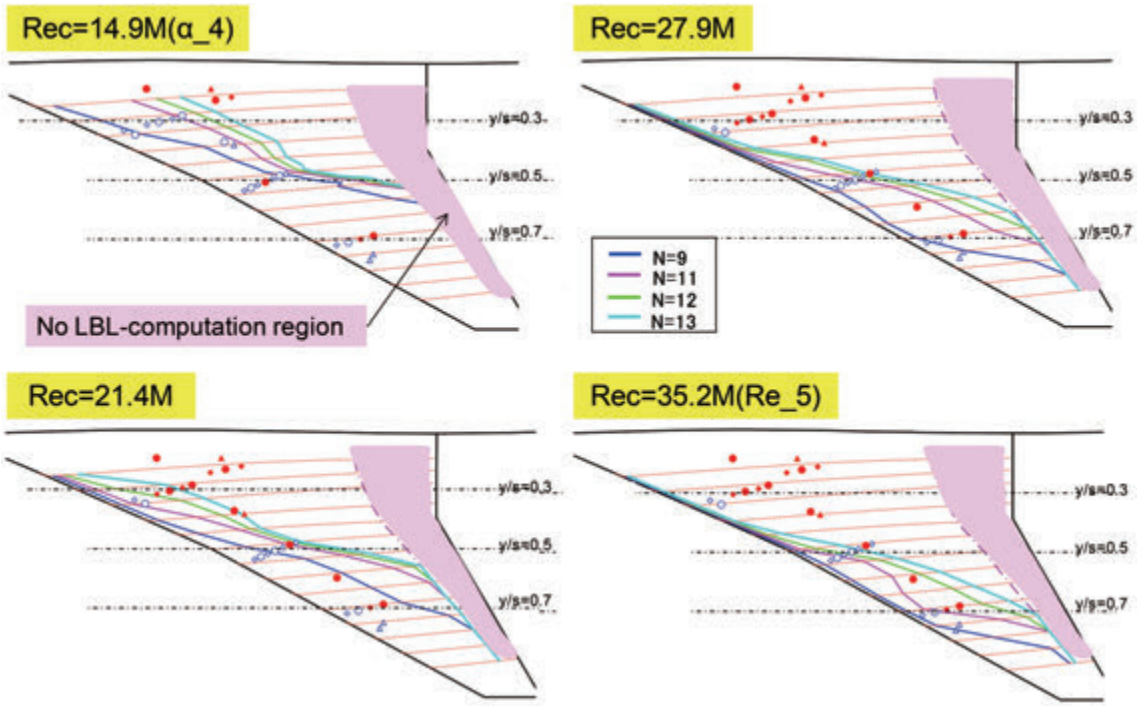

Figure 66. N contours (envelope strategy) on target pressure distribution

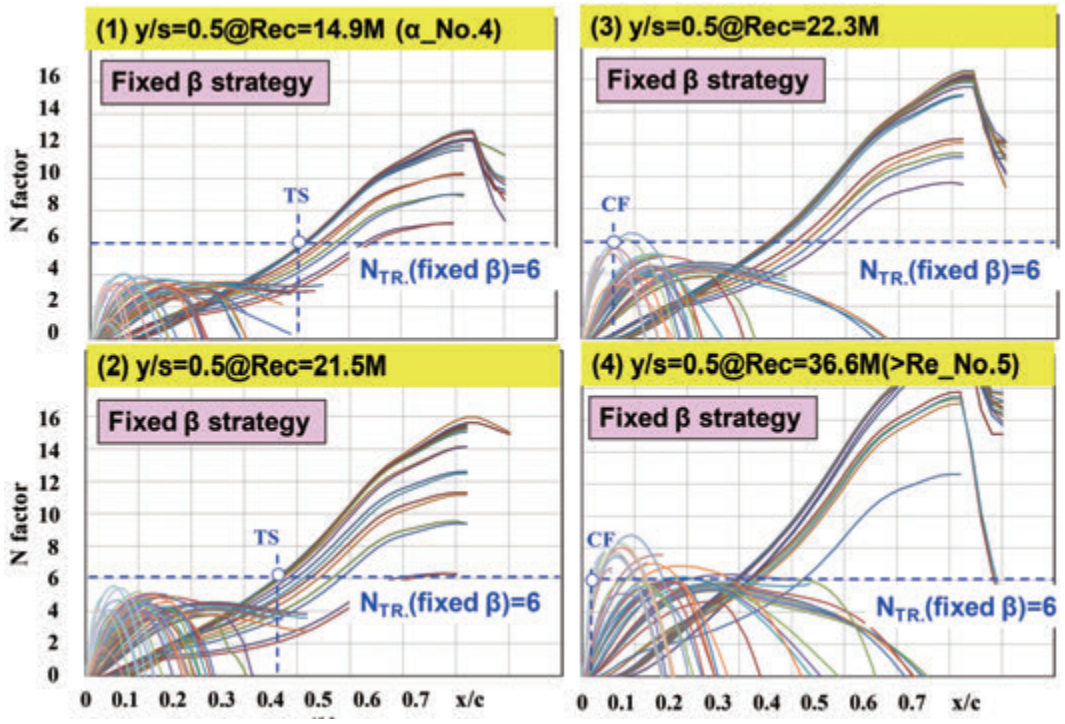

Figure 67. Predicted transition location on target Cp distribution based on N factors computed with fixed β strategy

$< 22.4\times10^6$ under the approximation of selecting N=6 as a transition criterion.

Finally, according to present investigation, Reynolds number effect on transition movement and nature of instability are schematically summarized in Fig. 69. As Reynolds number increases, transition location firstly gradually moves forward, and beyond a certain Reynolds number, it suddenly jumps up to the region near the leading edge. Approximately, three patterns for transition movement are found as illustrated in Fig. 69. In the NEXST-1 NLF wing case, the design point at higher Reyn-

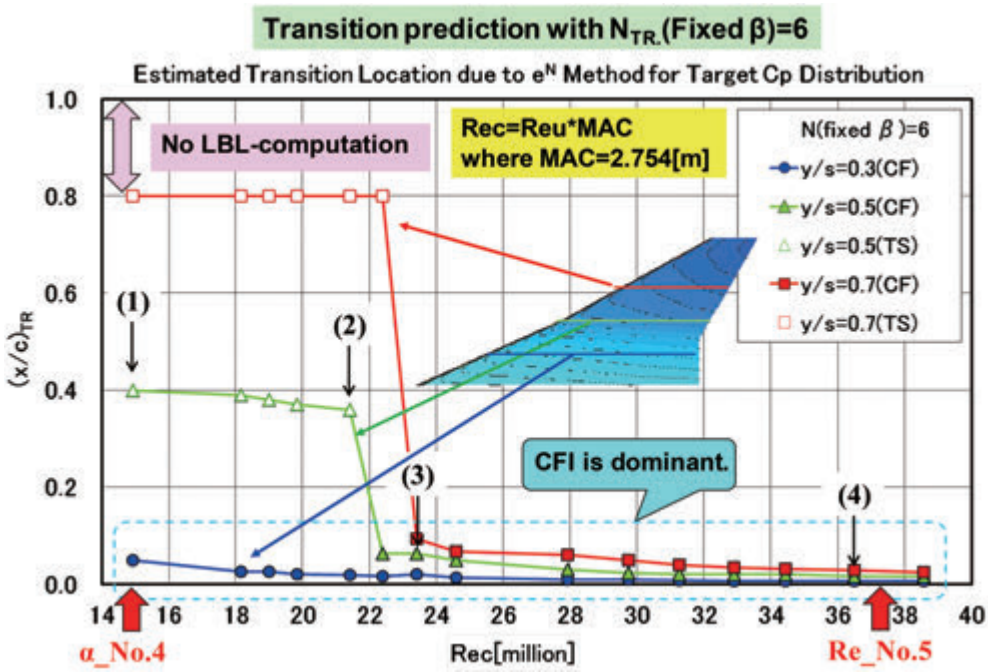

Figure 68. Reynolds number effect on target Cp distribution

Table 7. Summarized results of Reynolds number effect on target Cp distribution
- Transition location and nature due to fixed β strategy -

NEXST-1 FLT Test		MAC[m]=	2.754	$N_{fixed\beta,TR}$=		6			
Case No.	Condition	Re_{∞}[M] (1/m)	Re_{MAC}[M]	y/s=0.3		y/s=0.5		y/s=0.7	
				$(x/c)_{TR}$	Nature	$(x/c)_{TR}$	Nature	$(x/c)_{TR}$	Nature
1	AOA_No.4	5.4	14.9	0.050	CF	0.400	TS	0.800	TS
2	Ps=9KPa	6.6	18.2	0.026	CF	0.390	TS	0.800	TS
3	Ps=9.4KPa	6.9	19.0	0.026	CF	0.380	TS	0.800	TS
4	Ps=9.8KPa	7.2	19.8	0.020	CF	0.370	TS	0.800	TS
5	Ps=10.6KPa	7.8	21.4	0.019	CF	0.360	TS	0.800	TS
6	Ps=11.1KPa	8.1	22.4	0.016	CF	0.064	CF	0.800	TS
7	Ps=11.6KPa	8.5	23.4	0.020	CF	0.063	CF	0.094	CF
8	Ps=12.2KPa	8.9	24.6	0.014	CF	0.050	CF	0.068	CF
9	Ps=13.8KPa	10.1	27.9	0.010	CF	0.030	CF	0.060	CF
10	Ps=14.7KPa	10.8	29.7	0.009	CF	0.024	CF	0.050	CF
11	Ps=15.5KPa	11.4	31.3	0.008	CF	0.020	CF	0.040	CF
12	Ps=16.3KPa	11.9	32.9	0.007	CF	0.020	CF	0.035	CF
13	Ps=17.1KPa	12.5	34.4	0.007	CF	0.020	CF	0.032	CF
14	Ps=18.1KPa	13.3	36.5	0.007	CF	0.017	CF	0.029	CF
15	Ps=19.1KPa	14.0	38.6	0.007	CF	0.016	CF	0.025	CF

olds number condition (Re_No.5) is supposed to be located beyond the line of rapid change where transition suddenly moves up to the region near the leading edge. Therefore, JAXA's target pressure distribution should be improved. The main point of the improvement is that the rapid change line must be increased up to the region beyond the design point at high Reynolds number condition as illustrated in Fig. 69.

5.4. Summary of chapter 5

(1) Subjects

a) According to several comparisons of experimental transition data and stability analysis results (computed with both envelope and fixed β strategies), transition N values were summarized at each spanwise station.

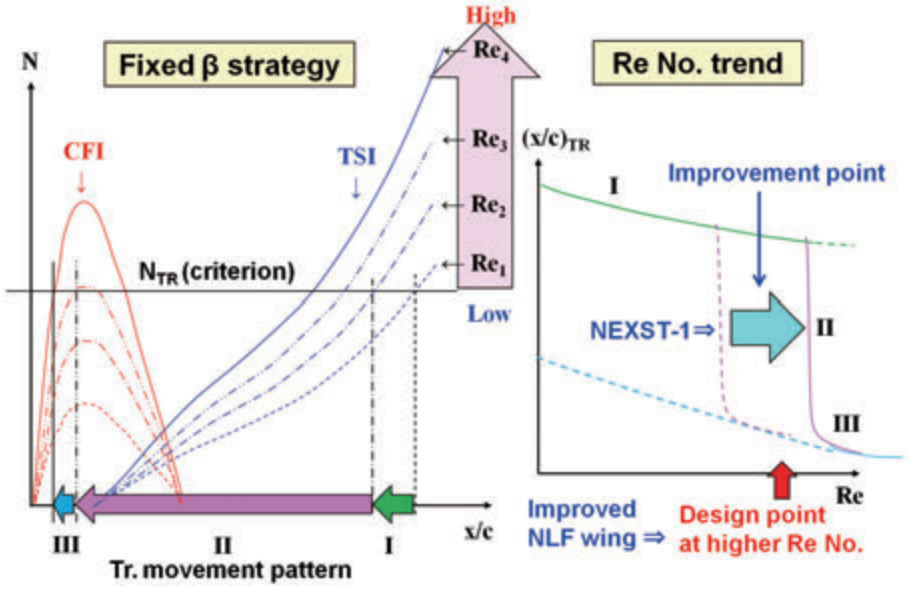

Figure 69. General feature of Reynolds number effect on transition movement on an ideal pressure distribution improved to suppress CFI of a highly swept wing

b) JAXA estimated transition locations based on the assumed transition N value due to envelope strategy and compared them with experimental results. More specifically, JAXA focused on the Reynolds number effect on transition location at outer wing region near y/s=0.7.

c) As for the detailed analysis of the transition characteristics on the NEXST-1 target Cp distributions at several Reynolds number conditions, JAXA investigated the Reynolds number effect of the transition characteristics that the target Cp distributions inherently have.

(2) Principal results

a) The trend of transition N values corresponding to experimental transition location, namely N_{env} due to envelope strategy and N_{beta} due to fixed β strategy show that they qualitatively decrease as spanwise station (y/s) increases. Furthermore, they generally increase as Reynolds number increases.

b) By comparing experiments with N contours due to envelope strategy, JAXA estimated N=12 and 4.5 in the flight test and S2MA wind tunnel test respectively, as approximated transition criteria.

c) According to the comparison of experimental transition data and transition locations predicted with these criteria, it was found that transition location at outer wing region near y/s=0.7 at the design point condition (α _No.4) was detected close to the leading edge than the JAXA numerical prediction. As the main reason, JAXA supposes that the NEXST-1 airplane was not able to realize the complete target Cp distributions at outer wing region in the flight test condition.

d) According to JAXA's new investigation on transition characteristics on the target Cp distribution, the following Reynolds number trend was revealed: at lower Reynolds number condition, the target Cp distributions well suppressed CF instability and transition location due to TS instability was delayed. As Reynolds number increases, the suppression of CFI is lost, then the change of instability from TSI to CFI makes transition location moves forward rapidly. This change spreads from the inner to outer wing region as the Reynolds number increases.

6. Concluding Remarks

Principal results in present research are as follows;

a) Stability analysis with envelope strategy shows good correlation between measured transition location and N contour, for example N_{TR}=12 for the NEXST-1 flight test and 4.5 for the S2MA wind tunnel test conditions.

b) Stability analysis with fixed β strategy makes clear dominant instability at measured transition location. Both parties confirmed well-suppression of CFI on the NEXST-1 at the design point in flight test and at lower Reynolds number case in S2MA wind tunnel test.

c) Investigation of chord Reynolds number (Re_{MAC}) effect on transition characteristics on experimental results shows similar feature on predicted transition results for variation of Re_{MAC}, except for the outer wing region (y/s=0.7) in flight test. This exception is thought to be induced by non-completeness of realizing the Cp_{Target} at the design point in flight test.

d) According to roughness study with measured roughness height of about 1 μm on the NEXST-1 and the S2MA test model, there is no influence of surface roughness on transition location based on ONERA's experimental database.

e) It was obtained that the Cp_{Target} distribution for the NEXST-1 NLF wing design has great potential to delay transition onset at the design point. Nonetheless, transition moves rapidly from mid-chord position (TSI-dominant) to forward position (CFI-dominant) as Re_{MAC} increases above 22.4 millions. Therefore, further improvement of present Cp_{Target} distribution is necessary, because of no suppression of CFI at higher Reynolds number case (Re_No.5) in flight test.

Finally, as conclusion of present and previous joint research activities, ONERA and JAXA obtained valuable knowledge of transition in supersonic flow, for example, cross-validated e^N methods, NLF wing effect (well-suppressed CFI), useful relations (as database) on roughness, freestream turbulence and Reynolds number effects.

Acknowledgements

The authors would like to express special thanks to Dr. Jean-Pierre Archambaud of ONERA for stability analysis of the NEXST-1 flight test conditions. It was very regrettable for him to have to reach the time for retiring from ONERA in the middle of present cooperative research. Furthermore, the authors also would like to thank Mr. Hiroaki Ishikawa of JAXA for CFD computations of several flow conditions, and Mr. Hiroki Sugiura and Dr. Naoko Tokugawa of JAXA for the transition measurement test of the NEXST-1 wing-body model at ONERA-S2MA wind tunnel.
Finally, JAXA and ONERA members greatly thank each other for keeping good relationship during about 10 years when present and previous joint research activities were conducted.

References

1. Arnal D - *Boundary layer transition: prediction based on linear theory*, AGARD FDP/ VKI Special Course on Progress in Transition Modeling, AGARD Report 793, 3, 1993

2. Yoshida K, Ueda Y, Sugiura H, Tokugawa N, Atobe T, Arnal D. Archambaud J.P, Seraudie A - *Boundary layer transition analysis on NEXST-1 airplane: NAL-ONERA cooperative research project*. 3rd SST-CFD Workshop, JAXA-SP-06-029E, pp.508-519, 2001

3. Yoshida K, Makino Y - *Aerodynamic Design of Unmanned and Scaled Supersonic Experimental Airplane in Japan*. ECCOMAS 2004, Jyväskylä, July 2004.

4. Yoshida K - *Supersonic drag reduction technology in the scaled supersonic experimental airplane project by JAXA*. Progress in Aerospace Sciences, vol.45, pp.124-146, 2009

5. Yoshida K, Sugiura H, Ueda Y, Ishikawa H, Tokugawa N, Atobe T, Takagi S, Arnal D, Archambaud J.P, Seraudie A - *Experimental and Numerical Research on Boundary Layer Transition Analysis at Supersonic Speed: JAXA-ONERA cooperative research project*. JAXA-RR-08-007E, March, 2009

6. Sugiura H, Yoshida K, Tokugawa N, Takagi S, Nishizawa A - *Transition measurements on the natural laminar flow wing at Mach 2*. Journal of Aircraft, vol.39, No.6, pp.996-1002, 2002.

7. Vermeersch O, Yoshida K, Ueda Y, Arnal D - *Transition Prediction on A Supersonic Natural Laminar Flow Wing: Experiments and Computations*. 47th International Symposium of Applied Aerodynamics, Paris, 26-28 March 2012.

8. Yoshida K, Kwak D.Y, Tokugawa N, Ishikawa H - *Concluding Report of Flight Test Data Analysis On The Supersonic Experimental Airplane Of NEXST Program By JAXA*. ICAS2010-2.8.2, 2010

9. Arnal D, Casalis G, Houdeville R - *Practical Transition Prediction Methods: Subsonic and Transonic Flows*. ONERA Report, RF 1/13639 DMAE – September 2008.

10. Ueda Y, Yoshida K, Matsushima K, Ishikawa H - *Method of Designing Natural Laminar Flow Wing for Reynolds Number Equivalent to Actual Supersonic Aircraft*. European Patent, Application No. EP11192278.7, 7 December 2011 (Japanese Patent Application No. 2010-278021 of 14 December 2010)

11. Fontaine J, Arnal D, Juillen J.C - *Qualification de la veine supersonique de S2MA avec le cône pression 10° en Uréol du CEAT*. Technical Report RSF 75/5018.62, ONERA, April 1993.

12. Fisher D.L, Dougherty N.S Jr - *Flight and wind-tunnel correlation of boundary-layer transition on the AEDC transition cone*. Technical Report STI/Recon Technical Report No. 14433, NASA, 1982.

13. Mack L.M - *Transition prediction and linear stability theory*. In AGARD Conf. Proc. No. 224, Paris, 1977.

14. Archambaud J.P - *Etude de la laminarité naturelle sur l'avion supersonique NEXST-1 du JAXA ; phases de vol de croisière (H=18 Km) et à fort nombre de Reynolds (H= 12 Km)*. Technical Report RF 1/17010 DMAE, ONERA, February 2011.

15. Yoshida K, Makino Y - *An experimental study on unmanned scaled supersonic experimental airplane*. In 32nd AIAA Fluid Dynamics Conference and Exhibit, Saint Louis (Missouri), AIAA-2002-2842, 24-26 June 2002.

16. Arnal D - *Laminar-turbulent transition prediction in supersonic flow: state-of-the-art at ONERA*. In SST Workshop, 3-5 December 2001.

17. Arnal D - *Practical transition prediction methods: subsonic and transonic flows*. In VKI Lectures Series Advances in Laminar-Turbulent Transition Modelling, Rhode-St-Genèse. Belgium, 2008.

18. Perraud J, Arnal D, Casalis G, Archambaud J.P, Donelli R - *Automatic transition predictions using simplified methods*. AIAA Journal, vol.47, No.11, November 2009.

19. Arnal D - *Transition prediction in transonic flow*. In Zierep and Oertel, Springer Verlag, editor, IUTAM Symposium Transsonicum III, Göttingen, 1989.

20. Casalis G, Arnal D - ELFIN II Subtask 2.3 : *Database method. Development and validation of the simplified method for pure cross-flow instability at low speed*. Technical Report No.145, ELFIN II, December 1996.

21. Fisher D.F, Dougherty N.S Jr - *In-flight transition measurement on a 10° cone at Mach numbers from 0.5 to 2.0*. Technical Report TP-1971, NASA, 1982.

Appendixes

A. Background of cooperative research

In previous cooperative work, both parties conducted three research tasks as summarized in Fig. A-1. This research work continued during about 8 years, because JAXA mainly spent three years to recover the second flight test of the NEXST-1 airplane after the failure of the first flight test in 2002. Time history of previous cooperative work is illustrated in Fig. A-2, including the main events of JAXA's NEXST-1 project.

Figure A-3 shows principal results of previous cooperative work[5]. First of all, both parties obtained useful and meaningful results as follows: (i) Both e^N codes were well cross-validated. (ii) Both e^N codes had good correlation with measured transition data from inner to mid-span region. However, both parties also found the following points: (a) There was little correlation between measured

	Task	JAXA	ONERA
1	10° Sharp cone 	[W/T test] ①$x_{onset, end, Tr.}$, Transition map ②Condition: M=2.0, α=0, ≠0 [Analysis] ①Cp: Analytic, Euler, NS ②LBL: BL(α=0), NS(α≠0) ③e^N: Linear (α=0, α≠0) ④Condition: W/T, Flight	[Analysis] ①e^N: Linear(α=0, ≠0) ②PSE (α=0) ③Condition: W/T, Flight
2	Nose cone of NEXST-1 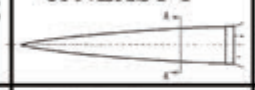		
3	NLF wing of NEXST-1 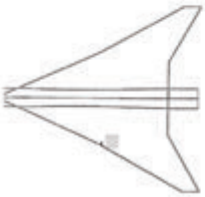	[W/T test] ①$(x/c)_{Tr.}$@y/s, Transition map ②Condition: M=2.0, α-sweep [Analysis] ①Cp: NS(TBL, LBL, Exp.) ②LBL: BL, NS(α-sweep) ③e^N: Linear (α-sweep) ④Condition: W/T, Flight ⑤ALC: Poll method	[Analysis] ①LBL: 3-D BL code ②e^N: Linear (α_{Design}) ③Condition: W/T, Flight ④ALC: Poll method

Figure A-1 Previous research tasks

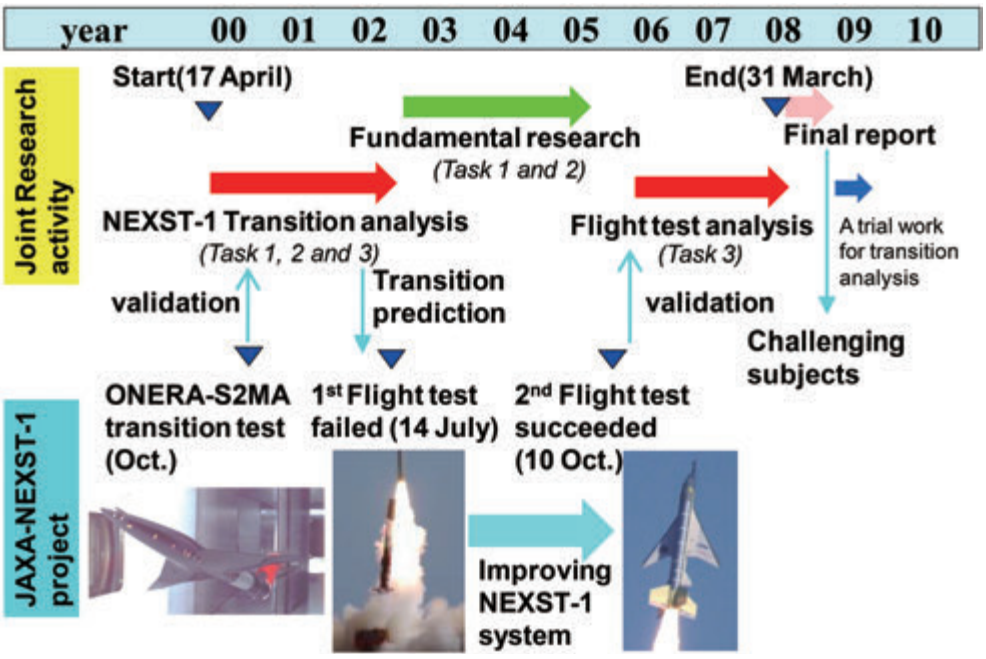

Figure A-2 History of cooperative research and JAXA's NEXST-1 project

and predicted transition location at outer wing region, that is, lower N value than that at inner wing region was required in order to predict transition at measured position. (b) There was different N behavior along the spanwise direction. As a result, both parties recognized that more research subjects were still remained, for example to advance previous transition analysis for understanding transition nature, that is, to quantify the most dominant instability of boundary layer, Reynolds number effect and influence of roughness condition on transition process, etc.

In preliminary investigation and discussion from May to June in 2009, both parties found out some possibilities to solve present subjects by applying the fixed β strategy proposed by ONERA into the stability analysis at the NEXST-1 flight test condition. Figure A-4 shows the main result of this investigation. By comparing measured transition data with stability results computed with fixed β strategy, the following results were obtained: (i) At the region from inner wing to mid-span, cross-flow instability (CFI) was fully suppressed up to the measured transition location. (ii) On the other

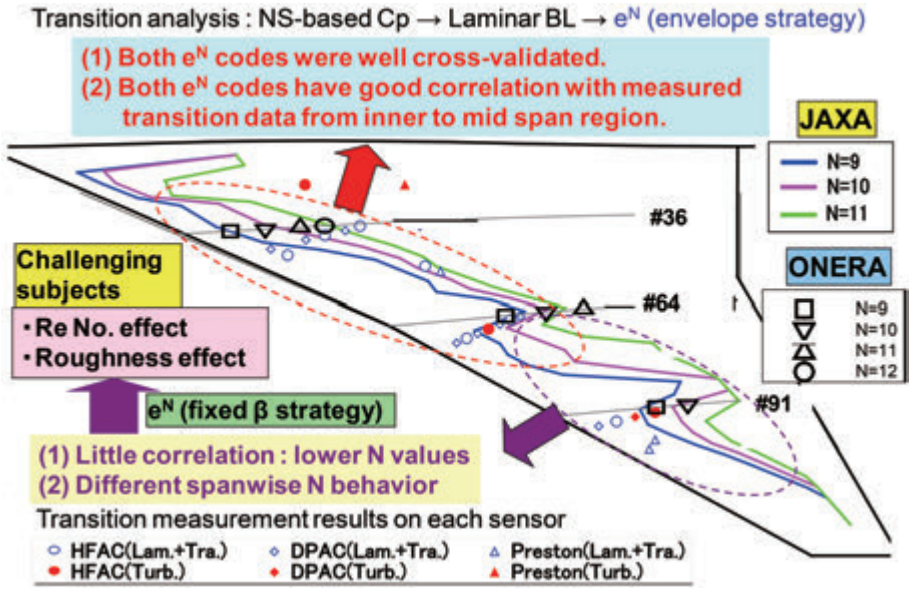

Figure A-3 Principal results of previous cooperative research

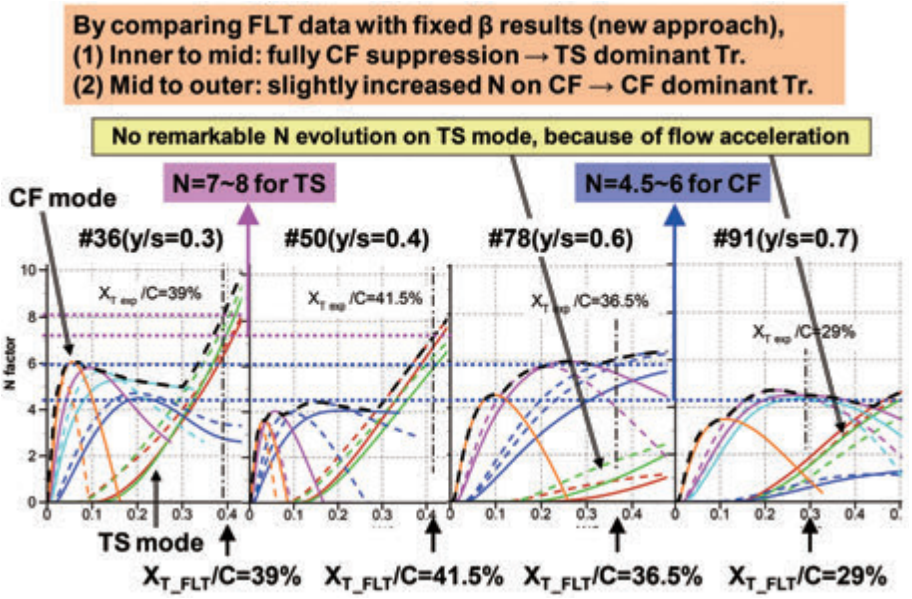

Figure A-4 Main results of a trial work in May, 2009

hand, at the region from mid-span to outer wing, CFI was dominant at measured transition location. Therefore, such fixed β strategy is a very powerful approach to understand physical nature in transition process. According to this investigation and discussion, both parties made new tasks as described in section (2) of Chapter 1.

B. Aerodynamic design and measured transition data on the NEXST-1 airplane

JAXA promoted the National EXperimental Supersonic Transport program called "NEXST" program from 1997 to 2006, in order to develop new drag reduction technologies for next generation of SSTs. In this program, four design concepts to reduce supersonic drag were applied to the development of an unmanned and scaled supersonic experimental vehicle called "NEXTS-1" airplane. Although three design concepts of an arrow planform, a warped wing and an area-ruled body were based on conventional supersonic linear theory, a supersonic natural laminar flow wing design concept was originally created in this program.

The key technology for the NLF wing design was to develop a CFD-based inverse design method, and to derive an optimum and ideal pressure distribution for the NLF wing design. Figure B-1 shows the procedure of present inverse design method for the NLF wing concept. According to this procedure, JAXA firstly prepared an initial configuration designed with three pressure drag reduction concepts mentioned above. Then, the difference between the Cp_{Target} and CFD-computed Cp

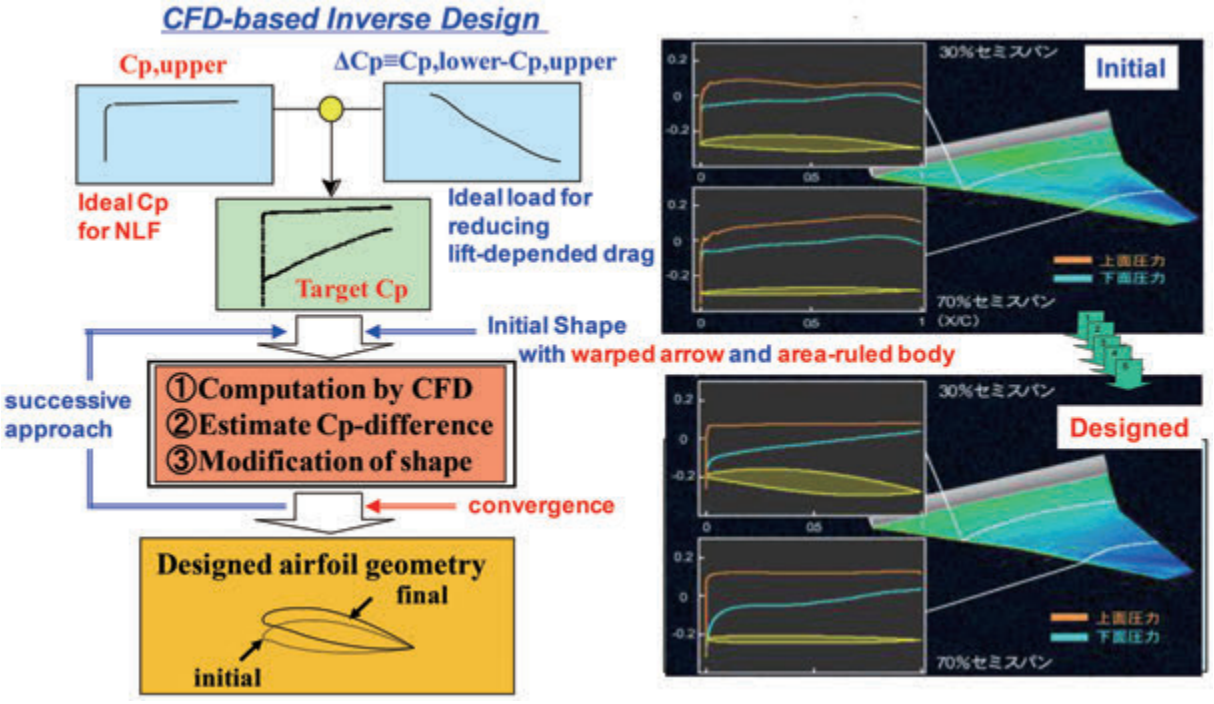

Figure B-1 CFD-based inverse method for NLF wing design

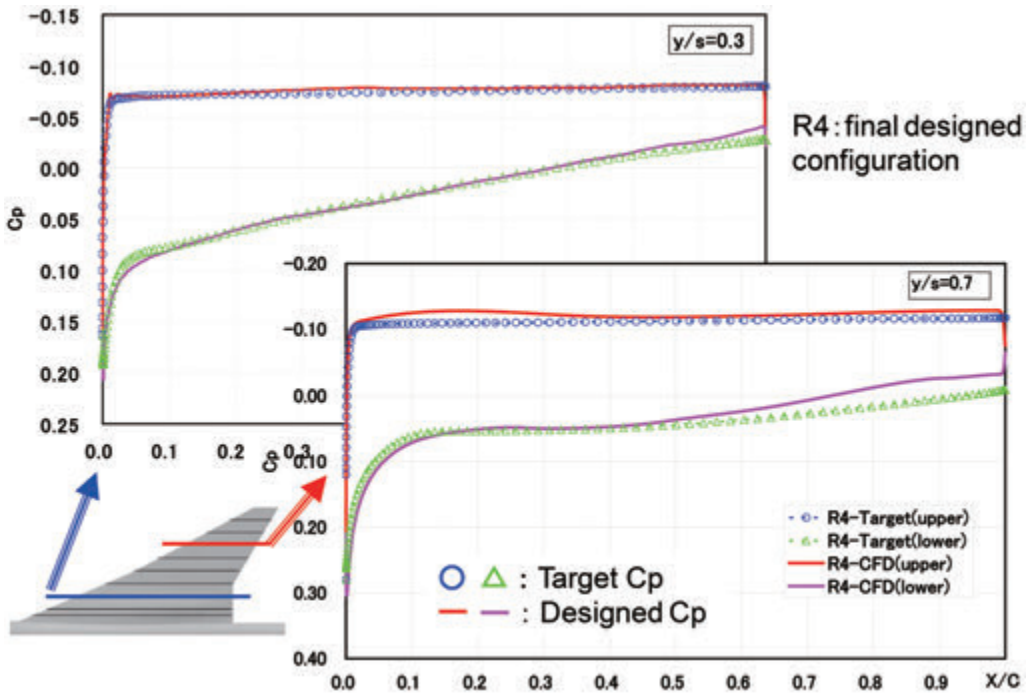

Figure B-2 Comparison of inverse-designed and target pressure distributions at final step

distributions on the initial configuration was estimated. After that, the configuration was modified to reduce the difference of Cp distributions by using supersonic lifting surface theory. Finally, such a step was continued to reduce the difference.

To demonstrate the NLF wing design concept in flight test, JAXA designed and developed an 11%-scaled experimental vehicle (NEXST-1) shown in Fig. 1. Its design point was Mach number M=2.0, lift coefficient C_L=0.1 and flight altitude H=18 km. The CFD-based inverse design method was applied to design the NEXST-1. Almost good convergence between the Cp_{Target} and CFD-based design pressure distributions was obtained as shown in Fig. B-2 for two spanwise stations y/s=0.3 and y/s=0.7. The NEXST-1

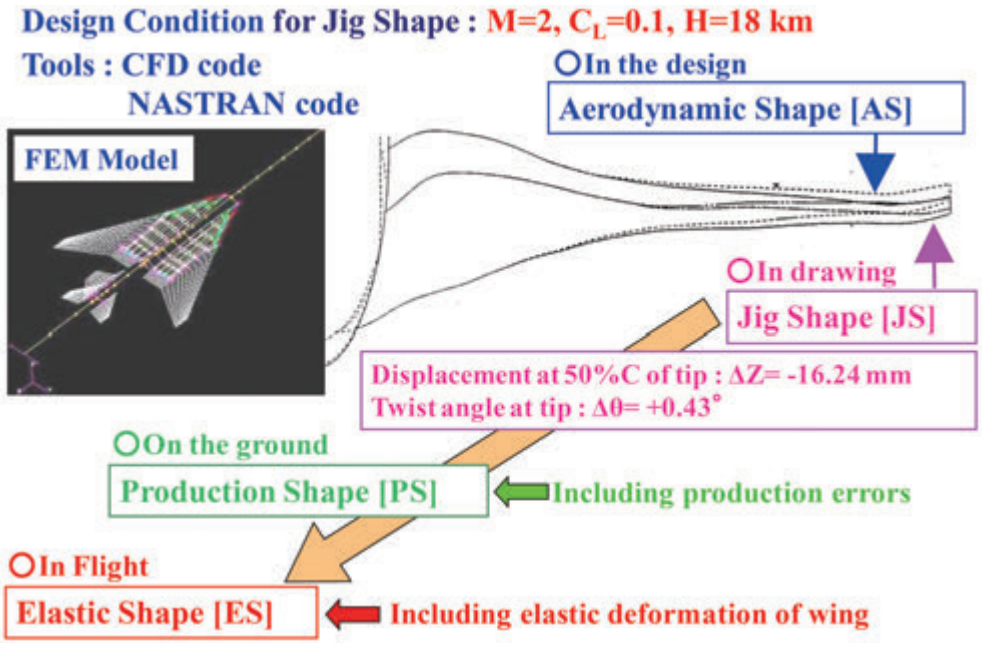

Figure B-3 Consideration of elastic deformation of NEXST-1 airplane

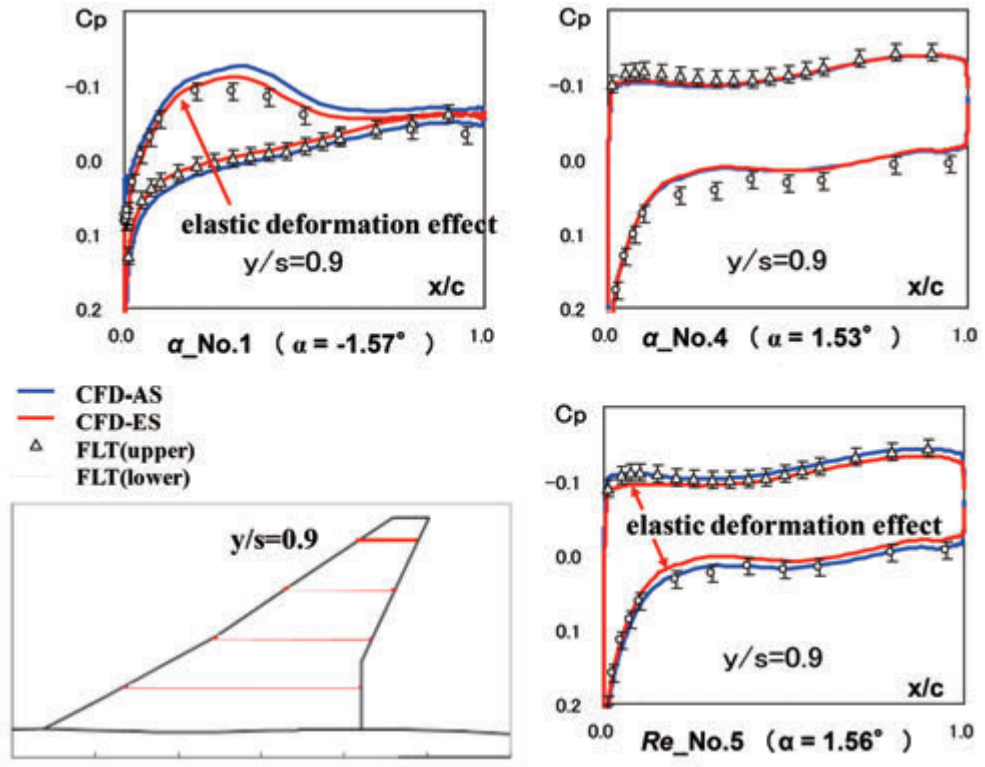

Figure B-4 Effect of elastic deformation on pressure distributions

was manufactured taking account of elastic deformation at the design point, according to the design procedure as illustrated in Fig. B-3. Such an elastic deformed configuration was called "ES". On the other hand, the original aerodynamic configuration without any elastic deformation was called "AS". Fig. B-4 shows the effect of elastic deformation on the pressure distributions at flight test conditions, α_No.1, α_No.4 and Re_No.5 cases.

Before the flight test of the NEXST-1, JAXA investigated the NLF wing effect experimentally. Fig. 2 shows the principal result of experimental validation[6] at the design angle of attack. JAXA qualitatively confirmed remarkable rearward movement of transition by detecting surface temperature using IR camera technique.

During the flight test, JAXA measured pressure distributions and transition locations using several aerodynamic sensors as illustrated in Fig. B-5. Transition location was estimated from steady and unsteady measured quantities indicating laminar or turbulent boundary layer states. JAXA used four kinds of transition detection sensors, namely hot-films (HF), dynamic pressure transducers (DP), Preston tubes (Pr) and thermocouples (TC). Correlations of these sensors in detecting transition were already investigated in preliminary wind tunnel test on the nose cone of the NEXST-1 and the main result of the test was summarized in Fig. B-6: in this figure, sensors are located at x=250 mm from the apex of the cone and transition occurs at this location for an angle of attack of AOA=2°.

Figure B-7 illustrates outline of the flight test of the NEXST-1 and Table B-1 gathers flight measurement conditions. Figure 4(a) shows a comparison of measured and CFD-computed Cp distributions at the design point. It was confirmed that there was good correlation between them. Figure 4(b) shows one of typical time histories of measured HF signals: laminar state indicated by little fluctuation on measured HF signal was clearly observed at the design point (4^{th} step of α-sweep test). Figure 4(c) gathers all the detection sensor measurements for several spanwise locations, blue color stands for non-turbulent boundary layer

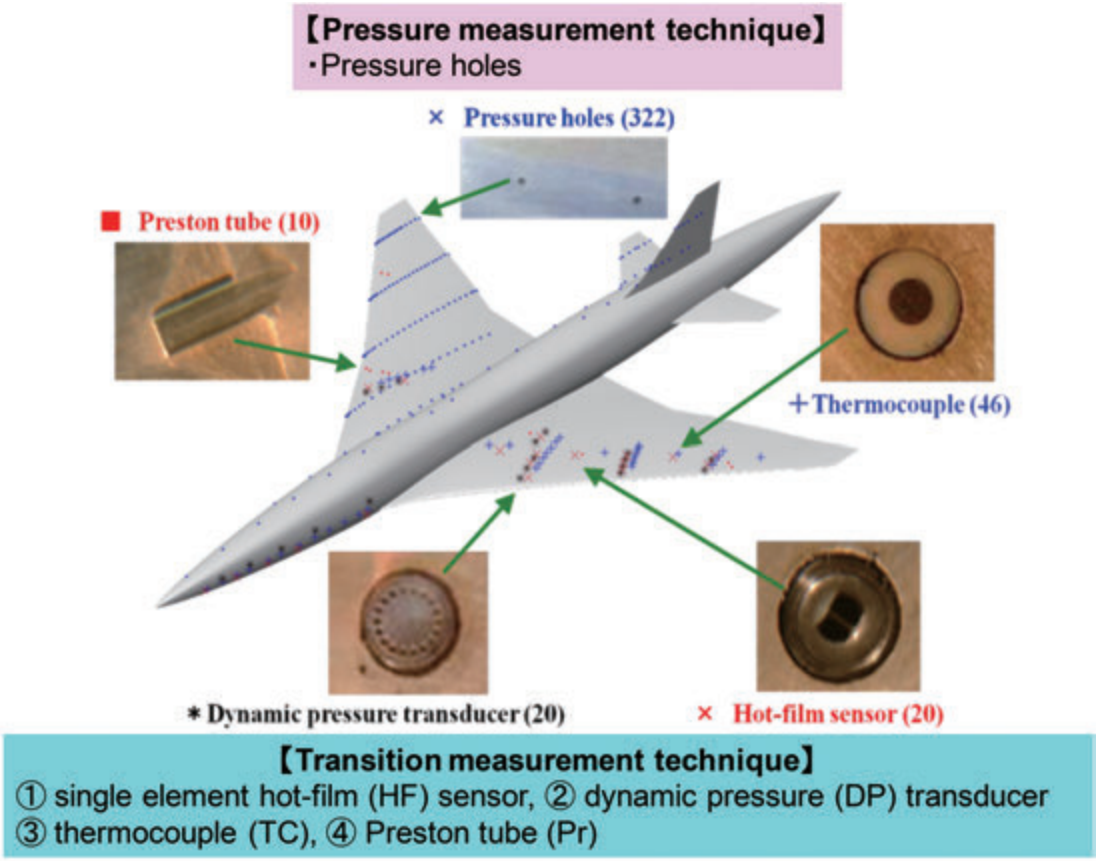

Figure B-5. Aerodynamic measurement technique

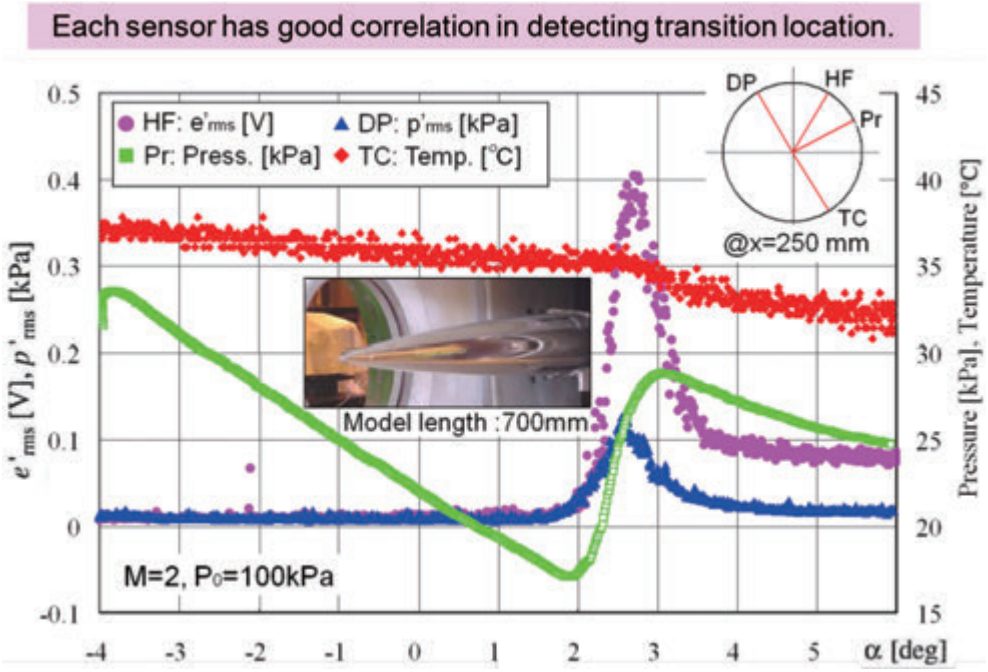

Figure B-6. Correlation of transition measurement sensors

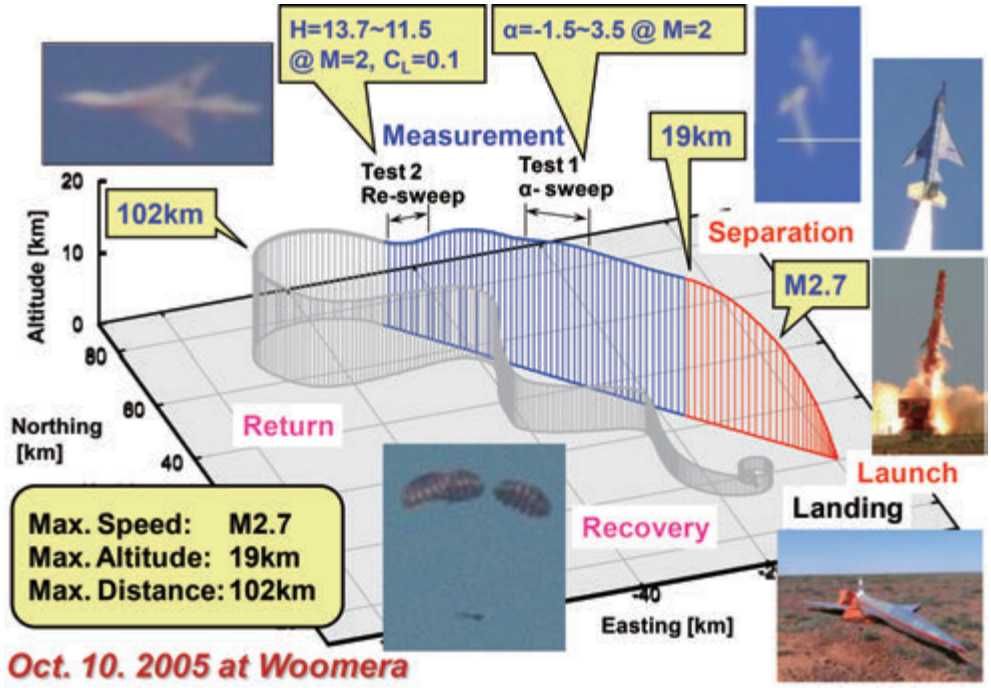

Figure B-7. Flight test trajectory

Table B-1. Flight test conditions

Phase		TLO[sec]	M	α [deg]	β [deg]	H [km]	Re[million] based on MAC
α-sweep phase	α1	110.22	2.00	-1.57	-0.08	18.94	12.72
	α2	114.22	2.04	-0.14	-0.14	18.91	13.37
	α3	117.72	2.04	0.71	-0.01	18.51	14.25
	α4	121.92	2.03	1.53	-0.08	18.10	14.93
	α5	126.43	2.00	2.51	-0.08	17.68	15.54
	α6	131.25	1.97	3.44	0.00	17.47	15.84
Re-sweep phase	Re1	167.35	2.01	1.56	-0.08	12.24	34.25
	Re5	171.35	1.96	1.58	-0.15	11.69	35.15
	Re9	175.33	1.90	1.56	-0.18	11.45	34.70

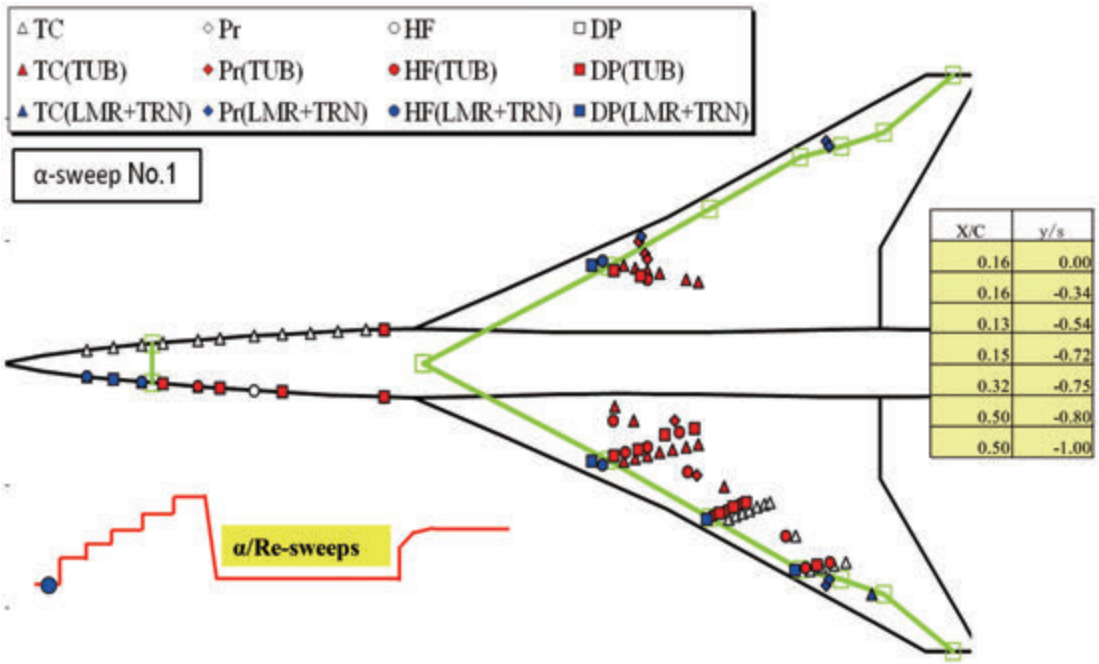

(a) α_No.1 case

Figure B-8. Measured transition data on NEXST-1 flight test

whereas red one corresponds to turbulent region: the deduced transition location is plotted by the green line. As a result, JAXA roughly estimated about 40% of chord the extension of laminar and transitional boundary layer region over the upper surface of the wing. This validation leads to estimation of quantitative effect of the NEXST-1 aerodynamic design technology when it is applied to the design of a real size SST. Figures B-8(a) to B-8(g) exhibit measured transition data at whole flight test conditions.

Detailed design process and results, including the flight test results can be found in Ref. 4.

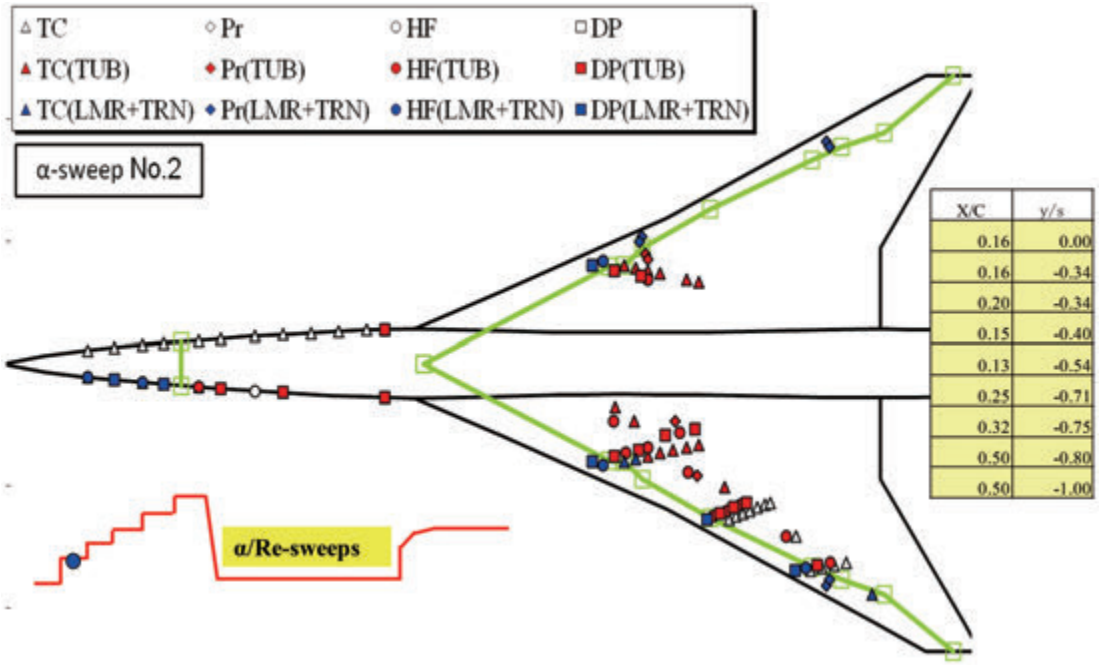

(b) α_No.2 case

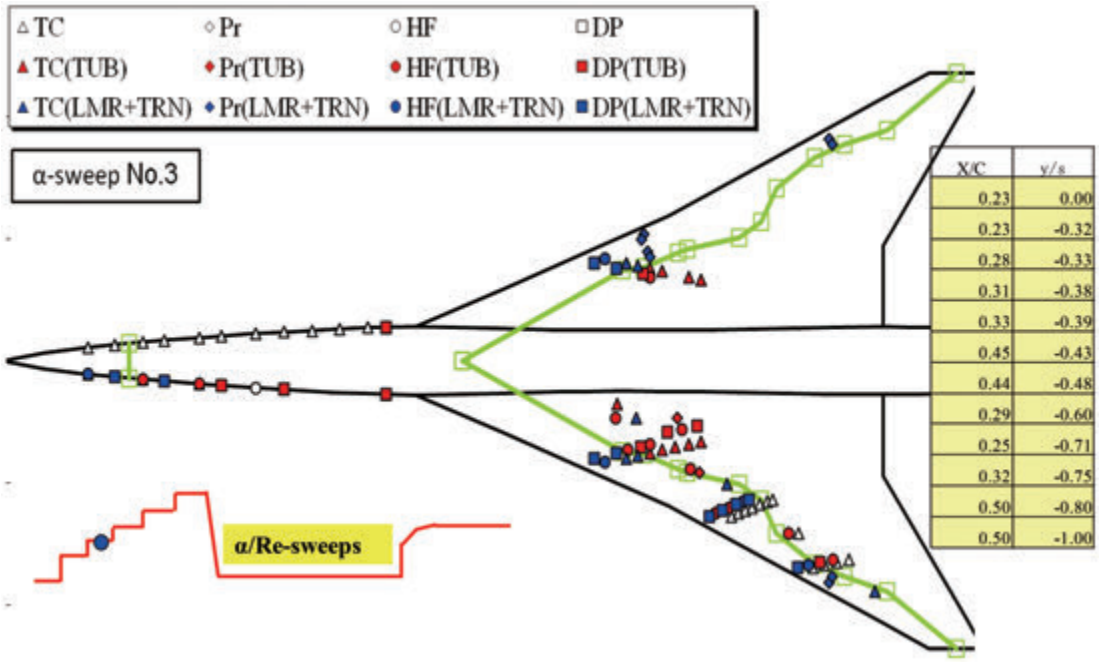

(c) α_No.3 case

Figure B-8. Measured transition data on NEXST-1 flight test

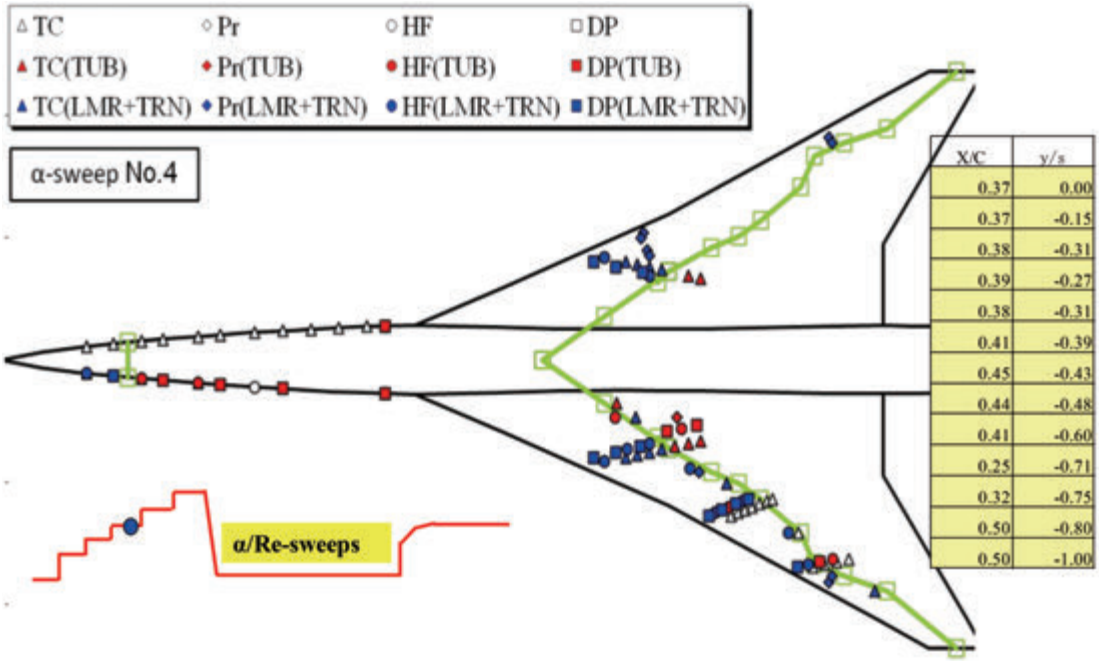

(d) α_No.4 case (design point)

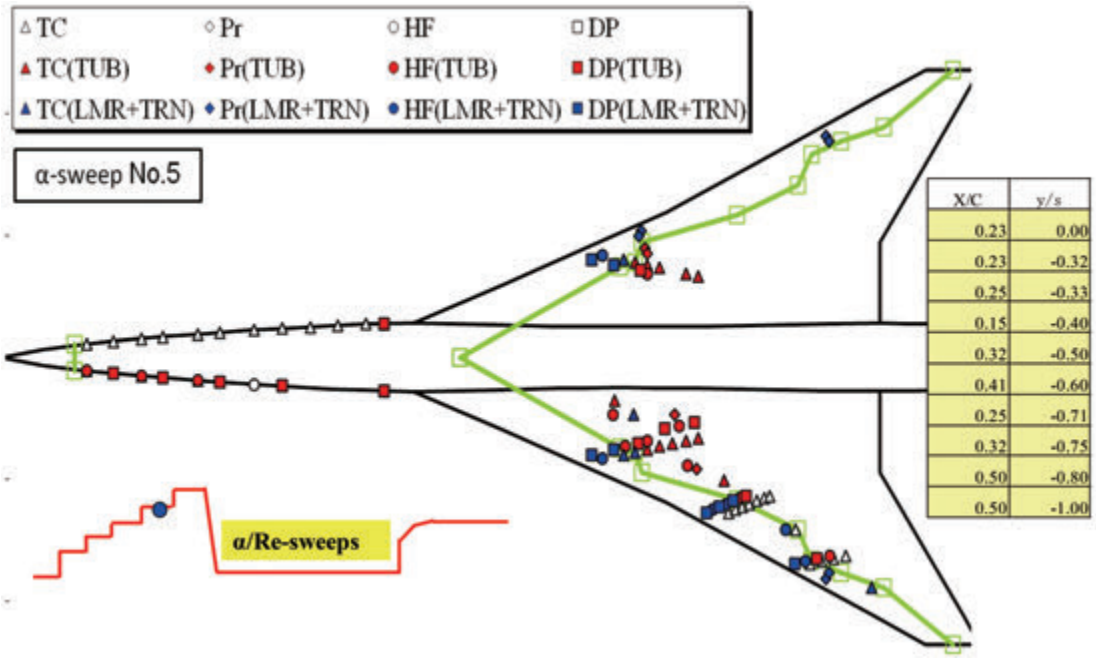

(e) α_No.5 case

Figure B-8. Measured transition data on NEXST-1 flight test

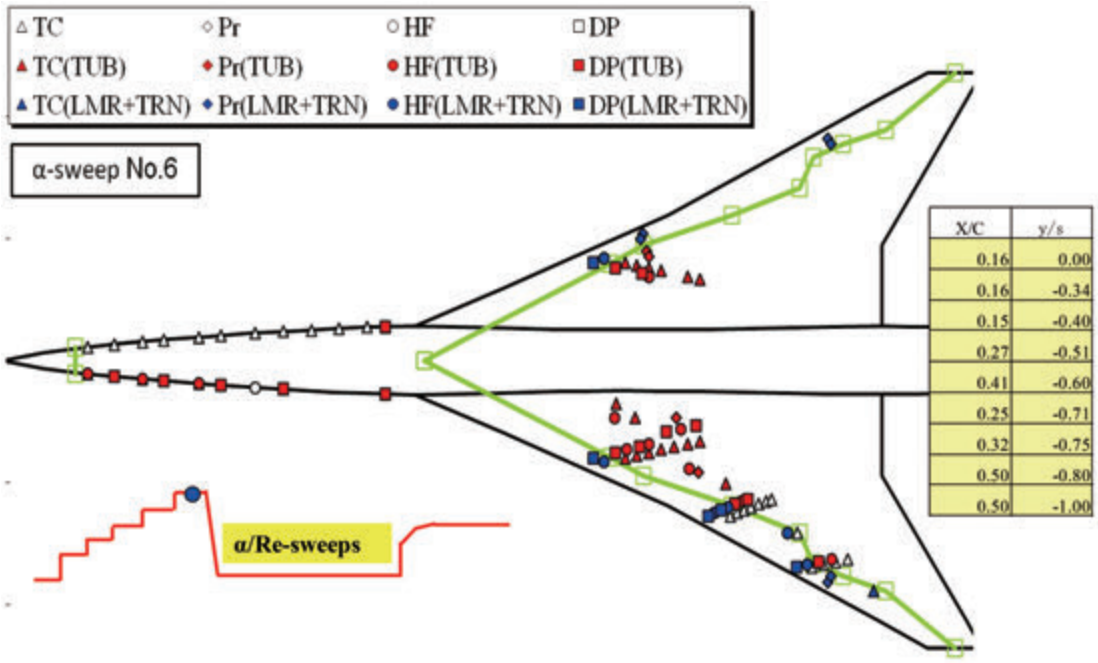

(f) α_No.6 case

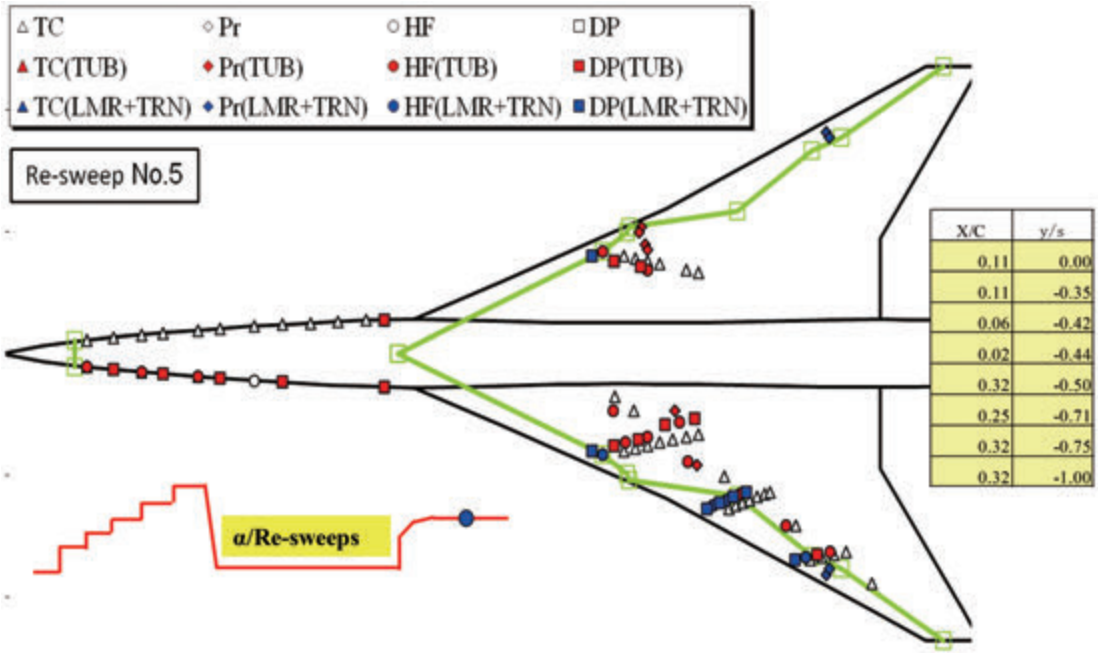

(g) Re_No.5 case

Figure B-8. Measured transition data on NEXST-1 flight test

C. Comparison of formulation of stability codes

ONERA and JAXA used distinct formulation of disturbance based on each different coordinate system. A comparison of these formulations is illustrated in Fig. C-1. ONERA used wing-based coordinate system: leading edge is placed along Y direction and X direction is perpendicular to the leading edge. In this coordinate system, ONERA applied so-called infinite swept-wing approximation for spanwise wave-number β. Since this approximation means two dimensional flow exists along the X direction, the growth of disturbance might have two-dimensionality, that is, $\beta_i = 0$. This implies that amplification of disturbances in the spanwise direction is neglected. But it is general that three-dimensionality exists on its propagation direction, that is, $\beta_r \neq 0$. It is supposed to

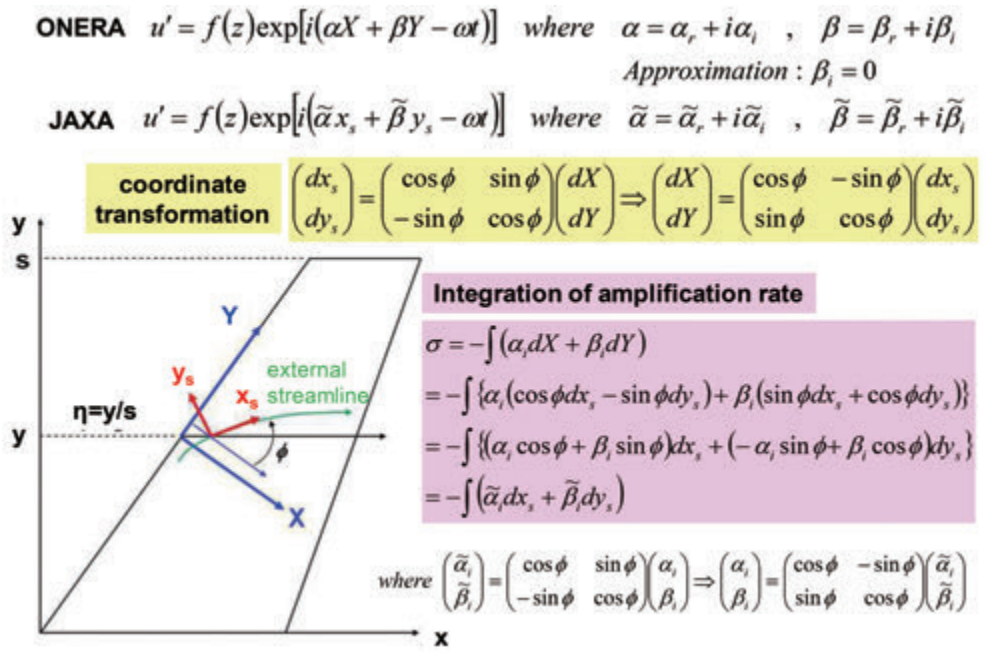

(a) Definition of disturbance

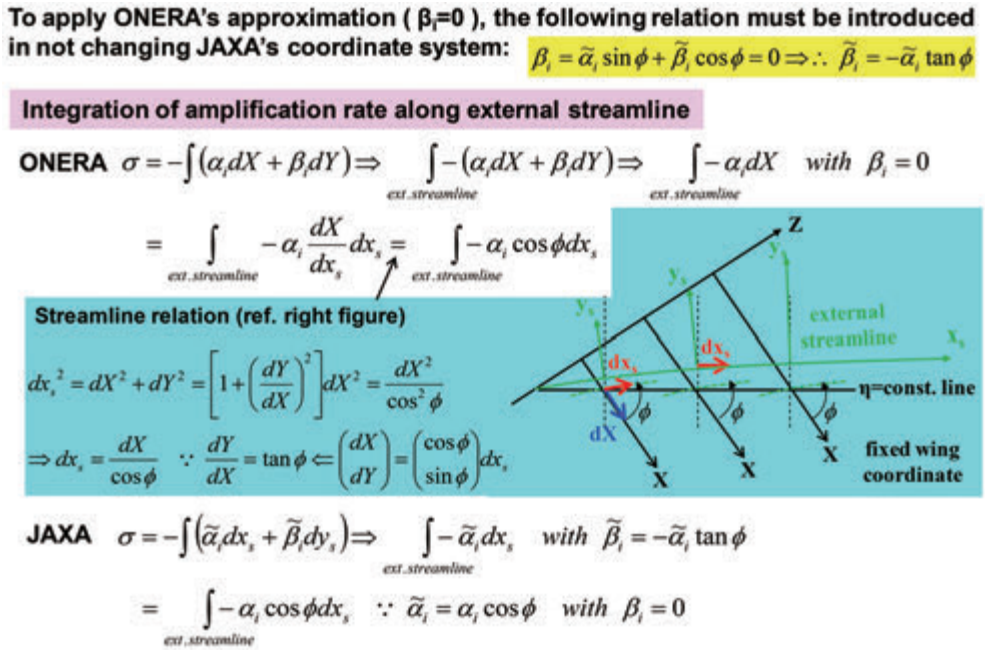

(b) Consideration of infinite swept wing approximation

Figure C-1. Consideration of stability formulation

be reasonable as one of the simplest assumptions among several proposed models.

On the other hand, JAXA used so-called external streamline coordinate system, because it is physically approximated that any disturbance mainly propagates along external streamline (x_s direction). In practice, in the stability computations, $\tilde{\beta}_i$ is set equal to zero. This assumption originates in the same consideration on the disturbance along the x_s direction, which has three-dimensionality in its propagation direction, that is, $\tilde{\beta}_r \neq 0$. Difference between these two approaches is illustrated in Figure C-1 (a-b).

To realize the same approximation as ONERA's one, $\tilde{\beta}_i$ in the formulation by JAXA should be satisfied with the following relation:

$$\beta_i = \tilde{\alpha}_i \sin\phi + \tilde{\beta}_i \cos\phi = 0 \quad \Rightarrow \quad \therefore \tilde{\beta}_i = -\tilde{\alpha}_i \tan\phi$$

In addition, similar transformation on the propagation direction ψ is also derived as follows:

$$\psi = \tan^{-1}(\beta_r / \alpha_r) - \phi = \tan^{-1}(\tilde{\beta}_r / \tilde{\alpha}_r)$$

where ϕ represents the angle between the external streamline direction (x_s direction) and the X direction (see Fig. 7 and C-1).

JAXA checked N factors computed without and with such a relation at the design point. Figure C-2(a) shows the N factors and ψ distributions computed without that relation, namely with a usual assumption of $\tilde{\beta}_i = 0$, and Fig. C-2(b) indicates the N factors and ψ distributions computed with present relation. By comparing Fig. C-2(a) with (b), the application of present relation leads to a slight improvement in agreement between both N factors. JAXA also found little improvement in the N factors at other spanwise stations and Reynolds number cases.

Although this subject based on different formulation of each stability code should be further investigated, fortunately the difference of stability

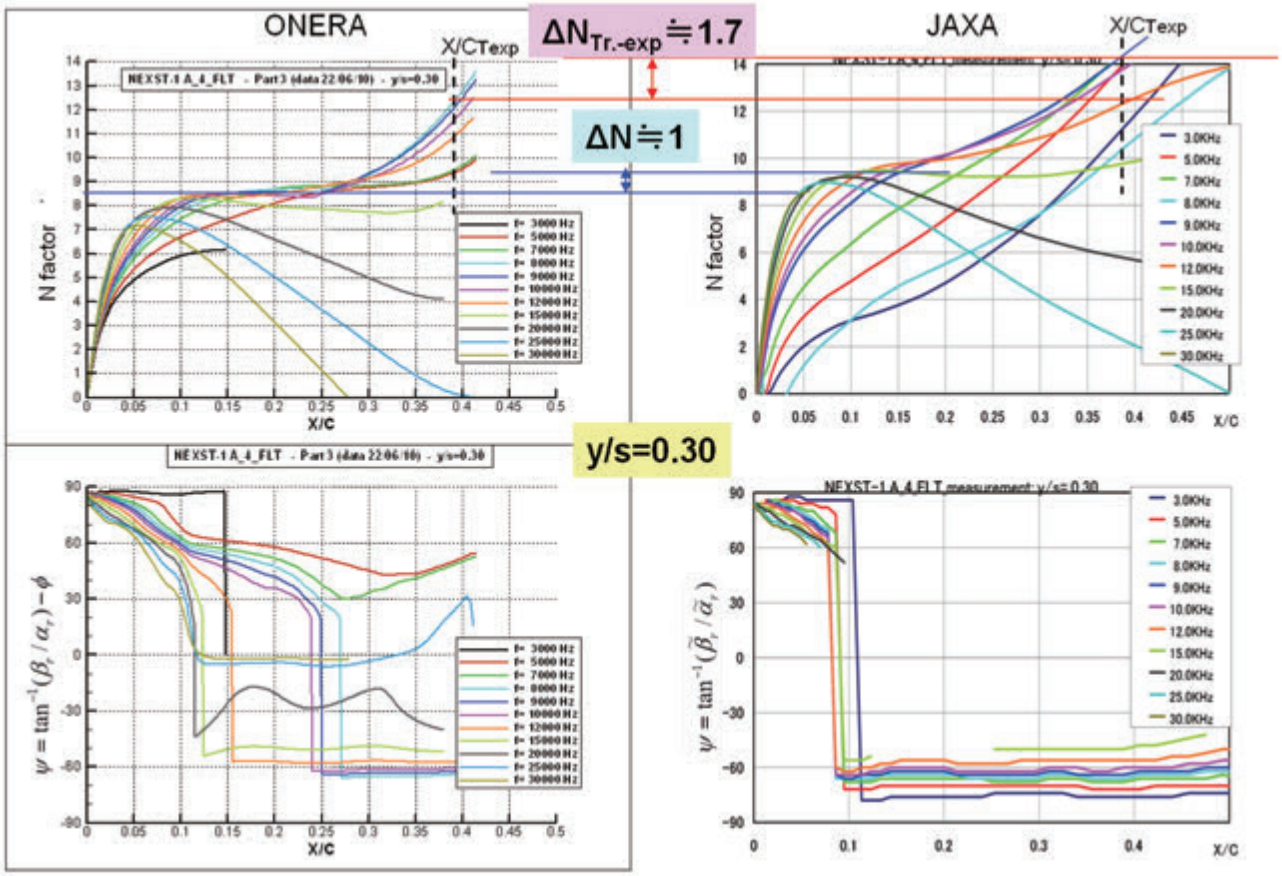

(a) Previous JAXA results computed with

Figure C-2. Check of N factors at α_No.4

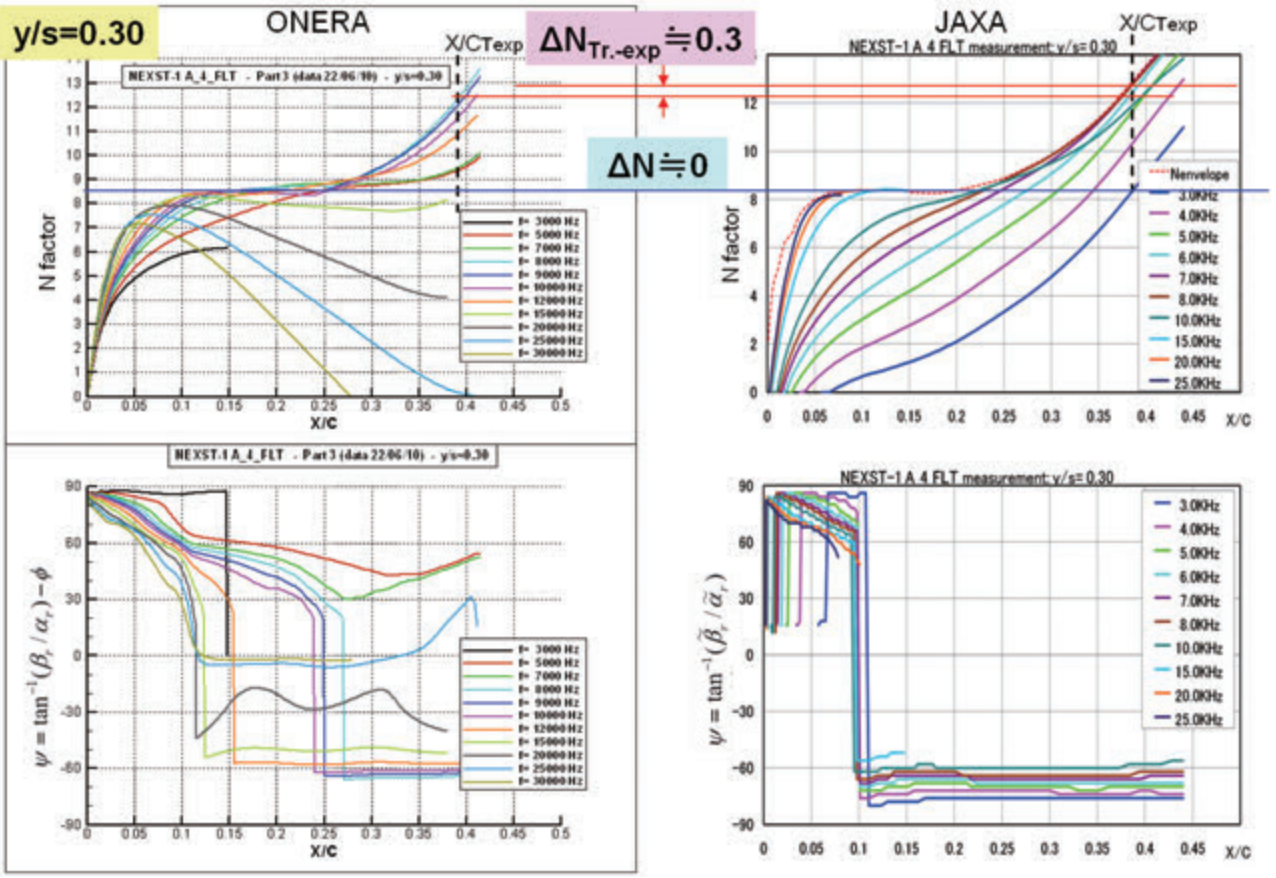

(b) Improvement of JAXA computation with

Figure C-2. Check of N factors at α_No.4

results between $\beta_i = 0$ and $\tilde{\beta}_i = 0$ is relatively small, as seen in the comparison of Fig. C-2(a) and (b). Therefore, for sake of simplicity, JAXA basically decided to apply the condition of $\beta_i = 0$ to present stability analysis, and compared JAXA's results with ONERA's ones.

D. Surface-interpolated pressure and edge velocity distribution data

Present surface-interpolated pressure coefficient (Cp) distributions and external streamwise velocity (U_e) distributions at boundary layer edge of the NLF wing at representative spanwise stations (near y/s=0.3 and 0.7) are summarized in tables D-1 ～D-3 and Figs. D-2～D-4. These data respectively correspond to the design point (α_No.4), higher Reynolds number point (Re_No.5), and P_0=0.6 bar point of S2MA test. Here X, Y, Z, U_e, V_e, W_e are defined in Fig. D-1. These data are used to perform boundary layer computations.

Table D-1. Pressure coefficient and edge velocity distributions at α _No.4 of NEXST-1 flight test

(a) y/s=0.3 (1/2)

	y/s=0.30		Y[m]=	0.707400		
S/C	X[m]	Z[m]	Ue[m/s]	Ve[m/s]	We[m/s]	Cp
0.000000	4.366800	−0.049663	482.809253	214.937723	−9.303147	0.206682
0.000010	4.366777	−0.049647	482.292063	216.211443	−6.884606	0.206654
0.000020	4.366754	−0.049630	482.083061	216.722079	−5.886401	0.206626
0.000030	4.366731	−0.049613	481.923786	217.112265	−5.080615	0.206596
0.000072	4.366637	−0.049538	481.458636	218.308582	−1.893641	0.206421
0.000177	4.366423	−0.049333	480.149996	221.664537	9.359063	0.205055
0.000212	4.366357	−0.049259	479.878754	222.521318	13.632440	0.204281
0.000382	4.366091	−0.048857	479.283722	224.000830	39.155873	0.196639
0.000542	4.365973	−0.048422	483.153373	217.652967	69.596843	0.181258
0.000728	4.366044	−0.047903	491.733853	201.823731	96.188994	0.160833
0.001257	4.366959	−0.046735	512.300067	154.848082	132.259576	0.111754
0.001914	4.368513	−0.045709	529.010103	117.674552	140.598365	0.078181
0.002575	4.370197	−0.044885	539.507114	94.227403	140.157050	0.057686
0.004011	4.374000	−0.043437	552.643114	64.561599	134.627297	0.031521
0.005070	4.376864	−0.042532	559.160892	49.819708	130.325050	0.017785
0.006065	4.379579	−0.041766	563.864116	39.163804	126.492337	0.007622
0.007139	4.382527	−0.041005	568.147739	29.495871	122.798163	−0.002088
0.008093	4.385158	−0.040376	571.571262	21.784636	119.878300	−0.010260
0.009099	4.387945	−0.039754	574.981187	14.116285	116.507961	−0.018406
0.010159	4.390886	−0.039142	578.220557	6.826166	112.515563	−0.025940
0.012670	4.397890	−0.037850	583.927218	−6.108630	101.090473	−0.037525
0.017580	4.411654	−0.035750	586.616743	−12.171377	87.273042	−0.039266
0.020153	4.418883	−0.034768	588.479645	−16.225866	82.637916	−0.043361
0.022569	4.425683	−0.033914	590.007888	−19.591103	77.485020	−0.046295
0.025107	4.432832	−0.033083	590.747285	−21.193683	72.873314	−0.046946
0.030187	4.447157	−0.031554	591.355880	−22.361682	66.474851	−0.046621
0.035300	4.461589	−0.030148	592.085709	−23.738988	61.480618	−0.047389
0.040364	4.475892	−0.028865	592.680286	−24.793017	57.437396	−0.048119
0.045305	4.489854	−0.027699	593.165266	−25.601891	54.014938	−0.048742
0.050055	4.503284	−0.026647	593.545562	−26.183702	51.126509	−0.049213
0.055015	4.517311	−0.025611	593.874502	−26.634862	48.487057	−0.049614
0.060182	4.531929	−0.024592	594.175421	−27.011983	45.997386	−0.049991
0.065057	4.545725	−0.023681	594.409787	−27.258854	43.874660	−0.050258
0.070101	4.560000	−0.022786	594.615844	−27.434620	41.880874	−0.050479
0.075311	4.574749	−0.021906	594.802965	−27.563345	39.937463	−0.050665
0.080142	4.588427	−0.021130	594.953503	−27.637035	38.218633	−0.050794
0.085106	4.602483	−0.020368	595.070672	−27.629860	36.658227	−0.050852
0.090202	4.616915	−0.019620	595.141207	−27.527263	35.116244	−0.050766
0.095429	4.631721	−0.018885	595.169826	−27.324252	33.851797	−0.050595
0.100185	4.645193	−0.018238	595.206129	−27.155032	32.923181	−0.050521
0.110004	4.673010	−0.016971	595.388838	−27.065558	30.748657	−0.050717
0.120229	4.701982	−0.015751	595.672729	−27.158017	28.532681	−0.051275
0.130181	4.730182	−0.014660	595.941056	−27.226634	26.452407	−0.051826
0.140482	4.759378	−0.013627	596.200889	−27.271649	24.369904	−0.052368
0.150411	4.787519	−0.012721	596.428630	−27.297353	22.332881	−0.052836
0.160639	4.816513	−0.011876	596.625340	−27.268553	20.398931	−0.053230

Table D-1. Pressure coefficient and edge velocity distributions at α _No.4 of NEXST-1 flight test
(a) y/s=0.3 (2/2)

	y/s=0.30		Y[m]=	0.707400		
S/C	X[m]	Z[m]	Ue[m/s]	Ve[m/s]	We[m/s]	Cp
0.170404	4.844195	−0.011151	596.769321	−27.178196	18.697749	−0.053493
0.180424	4.872603	−0.010487	596.881919	−27.050350	16.936708	−0.053662
0.190698	4.901732	−0.009878	596.966884	−26.848860	15.351416	−0.053765
0.200405	4.929256	−0.009362	597.027251	−26.572826	14.129316	−0.053821
0.210326	4.957386	−0.008881	597.105355	−26.229832	13.287329	−0.053957
0.220459	4.986120	−0.008434	597.240602	−25.976112	11.686838	−0.054241
0.230804	5.015454	−0.008048	597.438464	−25.689077	10.492748	−0.054751
0.240472	5.042868	−0.007758	597.687391	−25.545973	8.410552	−0.055407
0.250315	5.070782	−0.007530	597.962295	−25.263462	7.321197	−0.056182
0.260334	5.099193	−0.007394	598.259456	−25.168216	4.212188	−0.057003
0.270527	5.128099	−0.007338	598.543063	−24.748266	3.596544	−0.057818
0.280893	5.157498	−0.007322	598.783692	−24.334648	2.203258	−0.058491
0.291433	5.187386	−0.007419	598.971908	−23.983163	−0.319335	−0.059019
0.300184	5.212204	−0.007547	599.077355	−23.486091	−0.863639	−0.059286
0.325095	5.282846	−0.008166	599.171119	−22.295384	−4.346699	−0.059481
0.339430	5.323494	−0.008671	599.163755	−21.602622	−5.806370	−0.059417
0.366778	5.401041	−0.009818	599.211324	−20.421792	−8.245245	−0.059524
0.400610	5.496964	−0.011787	599.421185	−19.255093	−12.689812	−0.060295
0.420861	5.554375	−0.013271	599.480153	−18.426854	−15.032964	−0.060564
0.450893	5.639503	−0.015882	599.470903	−17.111188	−18.890145	−0.060751
0.475820	5.710145	−0.018453	599.387674	−16.011459	−22.416584	−0.060775
0.500112	5.778977	−0.021271	599.252184	−14.793284	−24.281043	−0.060483
0.522433	5.842215	−0.024070	599.101165	−13.845473	−27.119888	−0.060322
0.550302	5.921150	−0.027980	599.066780	−12.935653	−30.539467	−0.060661
0.570973	5.979685	−0.031151	599.047327	−12.370372	−32.850674	−0.060941
0.590659	6.035420	−0.034367	599.022949	−11.907317	−35.081183	−0.061227
0.601280	6.065484	−0.036186	598.988804	−11.669177	−36.395046	−0.061348
0.620068	6.118658	−0.039551	598.939242	−11.232110	−38.140124	−0.061504
0.640482	6.176427	−0.043339	598.818922	−10.669510	−39.702444	−0.061414
0.661190	6.235017	−0.047330	598.769370	−10.109739	−41.365245	−0.061578
0.680782	6.290433	−0.051299	598.729632	−9.604033	−44.079815	−0.062026
0.700627	6.346552	−0.055537	598.687027	−8.985661	−45.932587	−0.062293
0.741075	6.460903	−0.064576	598.299285	−7.310898	−48.542219	−0.061662
0.781032	6.573812	−0.074125	598.172834	−5.519364	−52.629162	−0.062277
0.820388	6.684964	−0.084197	598.220985	−3.615859	−55.969328	−0.063310
0.860601	6.798480	−0.095117	598.368034	−1.755199	−59.129001	−0.064665
0.900072	6.909851	−0.106333	598.289697	0.391949	−61.283115	−0.065080
0.950105	7.050971	−0.121093	598.005766	3.703463	−63.604518	−0.064988
1.001338	7.195409	−0.136809	597.740570	7.397897	−65.757834	−0.064995

Table D-1. Pressure coefficient and edge velocity distributions at α _No.4 of NEXST-1 flight test
(b) y/s=0.7 (1/2)

	y/s=0.70		Y[m]=	1.650600		
S/C	X[m]	Z[m]	Ue[m/s]	Ve[m/s]	We[m/s]	Cp
0.000000	6.289516	-0.078219	444.764000	244.087926	3.657500	0.302955
0.000010	6.289506	-0.078211	443.262737	246.737392	9.364565	0.302758
0.000020	6.289496	-0.078202	442.597878	247.910207	11.899487	0.302561
0.000030	6.289486	-0.078193	442.110075	248.770282	13.771190	0.302364
0.000072	6.289445	-0.078155	440.710400	251.232262	19.310050	0.301534
0.000177	6.289344	-0.078060	438.777711	254.646690	28.753791	0.299408
0.000212	6.289312	-0.078028	438.280333	255.507912	31.436594	0.298646
0.000382	6.289158	-0.077863	436.402341	258.695286	44.061909	0.294191
0.000542	6.289025	-0.077698	435.367978	260.453369	56.006734	0.288815
0.000728	6.288888	-0.077495	434.914055	260.878281	70.967516	0.280596
0.001257	6.288655	-0.076842	442.933350	248.033418	124.457308	0.238028
0.001914	6.288852	-0.076009	469.111488	197.771539	186.283161	0.150300
0.002575	6.289428	-0.075356	500.582884	139.314565	211.466360	0.073893
0.004011	6.291048	-0.074377	545.594482	57.556531	206.831082	-0.016679
0.005070	6.292343	-0.073844	563.965640	24.419147	191.380727	-0.048386
0.006065	6.293589	-0.073422	574.483259	5.479223	177.406549	-0.064668
0.007139	6.294951	-0.073023	582.047777	-8.043993	163.154327	-0.074571
0.008093	6.296172	-0.072706	586.283153	-15.586688	152.111233	-0.078635
0.009099	6.297467	-0.072399	589.027639	-20.426683	141.763442	-0.079510
0.010159	6.298836	-0.072099	590.631643	-23.237993	133.421976	-0.078804
0.012670	6.302094	-0.071460	594.161777	-29.462926	118.737550	-0.080797
0.017580	6.308500	-0.070407	599.556816	-38.958830	98.773656	-0.087449
0.020153	6.311868	-0.069930	601.443378	-42.260904	91.426793	-0.090168
0.022569	6.315037	-0.069518	603.115366	-45.177909	84.943575	-0.092843
0.025107	6.318368	-0.069117	604.223209	-47.075804	80.004078	-0.094491
0.030187	6.325045	-0.068382	605.814508	-49.758119	71.737745	-0.096676
0.035300	6.331773	-0.067720	607.165563	-52.031907	64.926114	-0.098870
0.040364	6.338442	-0.067127	608.184506	-53.726897	59.308711	-0.100541
0.045305	6.344953	-0.066597	608.904615	-54.902863	54.756656	-0.101662
0.050055	6.351217	-0.066126	609.485759	-55.844550	50.970947	-0.102613
0.055015	6.357759	-0.065669	610.022591	-56.712603	47.463245	-0.103549
0.060182	6.364576	-0.065226	610.517043	-57.512502	44.317687	-0.104481
0.065057	6.371011	-0.064835	610.954233	-58.222404	41.622634	-0.105361
0.070101	6.377669	-0.064455	611.376732	-58.910733	39.076379	-0.106255
0.075311	6.384548	-0.064087	611.777693	-59.561465	36.671352	-0.107132
0.080142	6.390927	-0.063766	612.118723	-60.111486	34.648567	-0.107902
0.085106	6.397483	-0.063455	612.435087	-60.616857	32.764586	-0.108630
0.090202	6.404215	-0.063153	612.725651	-61.069939	30.862262	-0.109286
0.095429	6.411120	-0.062861	612.979276	-61.438357	29.085710	-0.109850
0.100185	6.417404	-0.062610	613.169088	-61.677241	27.535256	-0.110244
0.110004	6.430378	-0.062134	613.469367	-61.930130	24.627080	-0.110803
0.120229	6.443891	-0.061690	613.688929	-61.969942	21.996673	-0.111145
0.130181	6.457044	-0.061304	613.829908	-61.856524	19.623889	-0.111282
0.140482	6.470660	-0.060947	613.905001	-61.591864	17.396100	-0.111232
0.150411	6.483784	-0.060641	613.925582	-61.231994	15.435717	-0.111047
0.160639	6.497306	-0.060360	613.904321	-60.783463	13.683847	-0.110752

Table D-1. Pressure coefficient and edge velocity distributions at α _No.4 of NEXST-1 flight test
(b) y/s=0.7 (2/2)

	y/s=0.70		Y[m]=	1.650600		
S/C	X[m]	Z[m]	Ue[m/s]	Ve[m/s]	We[m/s]	Cp
0.170404	6.510215	−0.060124	613.859917	−60.315954	12.149117	−0.110414
0.180424	6.523462	−0.059910	613.806368	−59.829655	10.572687	−0.110056
0.190698	6.537045	−0.059717	613.745738	−59.334974	9.130452	−0.109692
0.200405	6.549879	−0.059561	613.689307	−58.883403	7.966497	−0.109372
0.210326	6.562996	−0.059424	613.636225	−58.444557	6.629356	−0.109066
0.220459	6.576395	−0.059305	613.579930	−58.007320	5.615308	−0.108768
0.230804	6.590073	−0.059208	613.522966	−57.573830	4.549663	−0.108474
0.240472	6.602855	−0.059133	613.469886	−57.177351	3.475432	−0.108205
0.250315	6.615870	−0.059077	613.414454	−56.777948	2.820704	−0.107940
0.260334	6.629117	−0.059035	613.357088	−56.376905	1.604738	−0.107667
0.270527	6.642595	−0.059015	613.278673	−55.939623	0.868191	−0.107334
0.280893	6.656302	−0.059005	613.198390	−55.492577	0.161578	−0.106997
0.291433	6.670238	−0.059013	613.096481	−55.006429	−0.876904	−0.106594
0.300184	6.681809	−0.059034	612.984077	−54.555874	−1.200309	−0.106171
0.325095	6.714747	−0.059139	612.653925	−53.255114	−2.612342	−0.104943
0.339430	6.733700	−0.059231	612.487875	−52.562925	−3.484812	−0.104324
0.366778	6.769860	−0.059467	612.252770	−51.425591	−4.803884	−0.103421
0.400610	6.814592	−0.059862	612.070133	−50.296868	−6.355129	−0.102687
0.420861	6.841368	−0.060151	612.010416	−49.751437	−7.203148	−0.102422
0.450893	6.881074	−0.060646	611.972845	−49.092477	−8.436280	−0.102215
0.475820	6.914030	−0.061115	611.989799	−48.687662	−9.392019	−0.102214
0.500112	6.946146	−0.061621	612.045471	−48.428729	−10.283403	−0.102357
0.522433	6.975655	−0.062125	612.115779	−48.292832	−11.085301	−0.102567
0.550302	7.012498	−0.062806	612.218048	−48.213504	−12.057839	−0.102893
0.570973	7.039824	−0.063348	612.303602	−48.184999	−12.828947	−0.103175
0.590659	7.065849	−0.063894	612.391058	−48.159420	−13.575691	−0.103463
0.601280	7.079888	−0.064201	612.441421	−48.143689	−13.967076	−0.103628
0.620068	7.104724	−0.064767	612.536277	−48.113009	−14.708457	−0.103939
0.640482	7.131709	−0.065413	612.653892	−48.083370	−15.511173	−0.104321
0.661190	7.159081	−0.066102	612.794381	−48.072399	−16.332568	−0.104775
0.680782	7.184977	−0.066787	612.953071	−48.099544	−17.135464	−0.105289
0.700627	7.211206	−0.067513	613.144474	−48.183694	−17.995885	−0.105915
0.741075	7.264665	−0.069097	613.592593	−48.502335	−19.831346	−0.107398
0.781032	7.317470	−0.070804	614.043891	−48.843561	−21.729418	−0.108911
0.820388	7.369476	−0.072625	614.462331	−49.062449	−23.642198	−0.110319
0.860601	7.422609	−0.074632	614.829466	−49.084106	−25.590571	−0.111557
0.900072	7.474757	−0.076737	615.077456	−48.840829	−27.327980	−0.112396
0.950105	7.540852	−0.079577	615.251297	−48.066592	−29.362878	−0.112968
1.001338	7.608522	−0.082698	615.466559	−47.172937	−31.464669	−0.113657

Table D-2. Pressure coefficient and edge velocity distributions at Re_No.5 of NEXST-1 flight test

(a) y/s=0.3 (1/2)

	y/s=0.30		Y[m]=	0.707400		
S/C	X[m]	Z[m]	Ue[m/s]	Ve[m/s]	We[m/s]	Cp
0.000000	4.36695823	-0.0502437	486.136303	216.367984	-8.2912546	0.209193
0.000010	4.36693534	-0.0502269	485.527117	217.8592152	-5.4521207	0.209156
0.000020	4.36691248	-0.0502101	485.281713	218.4533145	-4.2974534	0.209119
0.000030	4.36688969	-0.0501933	485.095386	218.9050025	-3.3852469	0.209079
0.000072	4.36679489	-0.0501201	484.528925	220.2854503	-4.94E-02	0.208872
0.000177	4.36657668	-0.0499185	483.198827	223.6557802	11.1725522	0.207465
0.000212	4.36650943	-0.0498465	482.870654	224.6341971	15.7379616	0.206607
0.000382	4.36623193	-0.0494513	482.17563	226.4668499	41.9634603	0.198693
0.000542	4.36609702	-0.0490218	487.588771	219.7908811	74.1686613	0.182406
0.000728	4.36614885	-0.0485009	494.337265	204.1977881	102.196149	0.160864
0.001257	4.36704248	-0.0473174	516.432767	154.0621611	140.758265	0.108112
0.001914	4.36859013	-0.0462825	534.146237	114.65329	149.083083	0.072747
0.002575	4.37027078	-0.0454531	545.083412	90.18560584	148.356484	0.051469
0.004011	4.37407136	-0.0439969	558.695338	59.45916366	141.927484	0.024818
0.005070	4.37693311	-0.0430873	565.412967	44.28075997	137.205261	0.010820
0.006065	4.37964719	-0.0423166	570.24584	33.34619747	132.953782	0.000570
0.007139	4.38259442	-0.0415514	574.63667	23.4481286	128.979954	-0.009294
0.008093	4.38522462	-0.0409182	578.149072	15.54798575	125.80626	-0.017594
0.009099	4.38801077	-0.0402920	581.630629	7.734688415	122.249323	-0.025872
0.010159	4.39095101	-0.0396760	584.945445	0.30095861	118.003472	-0.033508
0.012670	4.39795326	-0.0383743	590.63495	-12.544279	105.802216	-0.044581
0.017580	4.41171514	-0.0362557	593.236833	-18.4028426	91.2374427	-0.045580
0.020153	4.41894256	-0.0352653	595.115616	-22.5044494	86.3864597	-0.049631
0.022569	4.42574201	-0.0344023	596.57442	-25.7362347	80.9896201	-0.052218
0.025107	4.43289006	-0.0335616	597.238694	-27.2018196	76.133169	-0.052498
0.030187	4.44721318	-0.0320154	597.782986	-28.2962712	69.4971904	-0.051831
0.035300	4.46164383	-0.0305915	598.480391	-29.6803253	64.3447768	-0.052418
0.040364	4.47594588	-0.0292906	599.033451	-30.7301697	60.1625137	-0.052951
0.045305	4.4899067	-0.0281069	599.47757	-31.5379574	56.6501956	-0.053400
0.050055	4.50333572	-0.0270377	599.823611	-32.132149	53.67857	-0.053725
0.055015	4.5173617	-0.0259836	600.12096	-32.60511	50.9617676	-0.053992
0.060182	4.53197825	-0.0249459	600.393841	-33.0087383	48.3925493	-0.054249
0.060662	4.5333361	-0.0248525	600.417387	-33.0421148	48.1603182	-0.054270
0.065057	4.54577345	-0.0240180	600.608962	-33.2871411	46.189508	-0.054427
0.070101	4.56004751	-0.0231055	600.801455	-33.5010354	44.1197564	-0.054579
0.075311	4.57479635	-0.0222090	600.979825	-33.6714832	42.126742	-0.054719
0.080142	4.58847303	-0.0214160	601.127513	-33.787136	40.3814025	-0.054826
0.085106	4.6025285	-0.0206374	601.247688	-33.8285477	38.7920769	-0.054882
0.090202	4.61696007	-0.0198717	601.332448	-33.7850855	37.2985908	-0.054843
0.095429	4.63176515	-0.0191170	601.388342	-33.6609406	36.0769871	-0.054764
0.100185	4.64523661	-0.0184503	601.459467	-33.5761668	35.2026365	-0.054809
0.110004	4.67305267	-0.0171400	601.777388	-33.7598039	33.0591518	-0.055453
0.120229	4.70202342	-0.0158753	602.218517	-34.1185722	30.8370641	-0.056523
0.130181	4.73022228	-0.0147424	602.640014	-34.4117342	28.6712038	-0.057552
0.140482	4.75941745	-0.0136708	603.051899	-34.6663611	26.4151294	-0.058556
0.150411	4.78755776	-0.0127347	603.400605	-34.8581309	24.1890078	-0.059381

Table D-2. Pressure coefficient and edge velocity distributions at Re_No.5 of NEXST-1 flight test
(a) y/s=0.3 (2/2)

	y/s=0.30		Y[m]=	0.707400		
S/C	X[m]	Z[m]	Ue[m/s]	Ve[m/s]	We[m/s]	Cp
0.160639	4.81655205	-0.0118654	603.6769	-34.9510954	22.0861204	-0.060003
0.170404	4.84423443	-0.0111241	603.836389	-34.935713	20.2277014	-0.060292
0.180424	4.87264264	-0.0104452	603.891275	-34.8234842	18.2881257	-0.060250
0.190698	4.90177164	-0.0098176	603.893702	-34.5979927	17.0826538	-0.060108
0.200405	4.92929544	-0.0092680	603.860582	-34.2962769	16.1346788	-0.059872
0.210326	4.9574252	-0.0087161	603.851129	-33.8326022	16.4106244	-0.059785
0.220459	4.98615759	-0.0081575	604.013519	-33.6637082	15.0500537	-0.060150
0.230804	5.0154906	-0.0076541	604.332815	-33.5218046	13.9156081	-0.061029
0.240472	5.04290436	-0.0072614	604.829358	-33.6687614	11.282568	-0.062419
0.250315	5.07081811	-0.0069496	605.401244	-33.6327102	9.87713865	-0.064097
0.260334	5.09922957	-0.0067531	606.042654	-33.8045303	5.93051406	-0.065938
0.270527	5.12813613	-0.0066574	606.673408	-33.563821	5.05272097	-0.067802
0.280893	5.15753524	-0.0066283	607.199911	-33.2627785	2.91944998	-0.069313
0.300184	5.21224244	-0.0068931	607.790861	-32.3810901	-0.8101437	-0.070944
0.325095	5.28288465	-0.0076518	607.712689	-30.7594968	-4.9514965	-0.070509
0.350885	5.35601606	-0.0086726	607.132395	-28.789421	-5.1169966	-0.068450
0.400610	5.49701114	-0.0111089	607.043695	-27.0953065	-11.32018	-0.068196
0.425421	5.56735381	-0.0128510	607.112491	-26.3079841	-14.18516	-0.068484
0.450893	5.63955936	-0.0149911	607.136485	-25.4500571	-17.737293	-0.068730
0.475820	5.71020383	-0.0175245	607.025306	-24.6460456	-22.58309	-0.068779
0.500112	5.77903869	-0.0203066	606.79121	-23.3519747	-22.436607	-0.067891
0.526196	5.8529451	-0.0234131	606.516857	-22.4110336	-26.258593	-0.067411
0.550302	5.92122942	-0.0266987	606.684274	-21.9526602	-29.511353	-0.068328
0.576193	5.99455375	-0.0305990	606.818301	-21.5286204	-32.510106	-0.069157
0.601280	6.06557749	-0.0347159	606.833436	-21.2241332	-36.280888	-0.069820
0.625483	6.13407912	-0.0390539	606.797814	-20.8175217	-38.061366	-0.070002
0.650110	6.20377341	-0.0435652	606.495821	-20.0734424	-39.18066	-0.069221
0.675158	6.27464948	-0.0483324	606.565441	-19.5920225	-42.549853	-0.070075
0.700627	6.3466796	-0.0536667	606.68514	-19.0373945	-46.253733	-0.071207
0.741075	6.46104448	-0.0625561	606.048807	-17.2554744	-47.683191	-0.069449
0.781032	6.57397471	-0.0718812	606.12486	-15.6340246	-52.665667	-0.070800
0.820388	6.68514393	-0.0817951	606.33941	-13.7745709	-56.234383	-0.072283
0.860601	6.79867558	-0.0925763	606.621937	-11.9754528	-59.633687	-0.073999
0.900072	6.9100638	-0.1036538	606.551093	-9.90873652	-61.943836	-0.074371
0.950105	7.05120414	-0.1182417	606.104773	-6.79123736	-64.449217	-0.073687
1.001338	7.19566379	-0.1337864	605.498322	-3.77938925	-66.936818	-0.072594

Table D-2. Pressure coefficient and edge velocity distributions at Re_No.5 of NEXST-1 flight test
(b) y/s=0.7 (1/2)

	y/s=0.70		Y[m]=	1.650600		
S/C	X[m]	Z[m]	Ue[m/s]	Ve[m/s]	We[m/s]	Cp
0.000000	6.29059515	-0.0686034	447.80401	245.4942118	8.36944818	0.3035228
0.000010	6.29058528	-0.0685946	446.004467	248.5485081	15.0469093	0.3032578
0.000020	6.29057541	-0.0685858	445.193578	249.9240617	18.0642576	0.3029934
0.000030	6.29056555	-0.0685770	444.599834	250.9305411	20.2871313	0.3027297
0.000072	6.29052404	-0.0685396	442.902205	253.7977988	26.8353807	0.3016187
0.000177	6.29042315	-0.0684446	440.555738	257.7404804	37.871835	0.2988093
0.000212	6.29039061	-0.0684122	439.952258	258.731529	40.9556983	0.2978176
0.000382	6.2902363	-0.0682478	437.77814	262.1681374	55.0805614	0.2922645
0.000542	6.29010312	-0.0680840	436.704673	263.7583086	67.8711469	0.2859965
0.000728	6.28996541	-0.0678809	436.334427	263.7340721	83.501822	0.2768282
0.001257	6.28973449	-0.0672265	445.085934	248.7611084	139.388384	0.2303859
0.001914	6.28993614	-0.0663953	472.60098	194.4266042	203.713418	0.1363097
0.002575	6.29051364	-0.0657430	505.901666	132.0364067	229.647594	0.0549615
0.004011	6.29213182	-0.0647601	553.250603	46.09382272	222.518993	-0.0379805
0.005070	6.29342442	-0.0642229	572.084468	12.44821727	204.43832	-0.0678991
0.006065	6.29466875	-0.0637963	582.248221	-5.55625146	188.375093	-0.0810063
0.007139	6.29602973	-0.0633922	589.418967	-18.0736567	172.46921	-0.0881547
0.008093	6.29724913	-0.0630696	593.418819	-24.9605056	160.29238	-0.0904746
0.009099	6.29854349	-0.0627574	596.068948	-29.4336232	149.389945	-0.0905111
0.010159	6.29991042	-0.0624519	598.085406	-32.841516	140.932268	-0.0908938
0.012670	6.30316625	-0.0617982	601.793852	-39.1279706	125.636712	-0.0928507
0.017580	6.30956745	-0.0607162	607.06138	-48.0482781	104.642074	-0.0982787
0.020153	6.31293295	-0.0602238	608.953221	-51.2343788	96.9238215	-0.1007442
0.022569	6.31609991	-0.0597961	610.697599	-54.1717276	90.2399531	-0.1034855
0.025107	6.31942973	-0.0593794	611.829121	-56.0246125	85.0658622	-0.1050478
0.030187	6.3261029	-0.0586131	613.4038	-58.532291	76.4602157	-0.1069365
0.035300	6.33282816	-0.0579184	614.756622	-60.6948623	69.4118057	-0.1089639
0.040364	6.33949484	-0.0572931	615.747829	-62.2447953	63.5672109	-0.1103970
0.045305	6.34600334	-0.0567317	616.418175	-63.2550169	58.8504897	-0.1112441
0.050055	6.35226443	-0.0562298	616.952499	-64.0485567	54.9204319	-0.1119494
0.055015	6.35880428	-0.0557404	617.440924	-64.7716164	51.3057185	-0.1126513
0.060182	6.36561979	-0.0552629	617.893123	-65.4443625	48.064106	-0.1133789
0.060662	6.36625294	-0.0552201	617.935197	-65.5069824	47.7548866	-0.1134475
0.065057	6.3720525	-0.0548395	618.296898	-66.0500511	45.2700404	-0.1140915
0.070101	6.37870863	-0.0544263	618.685947	-66.637081	42.6465367	-0.1148261
0.075311	6.38558627	-0.0540234	619.052992	-67.1892574	40.1576675	-0.1155450
0.080142	6.39196402	-0.0536698	619.360995	-67.6512553	38.0814414	-0.1161717
0.085106	6.39851845	-0.0533249	619.642247	-68.068141	36.1247112	-0.1167498
0.090202	6.40524833	-0.0529887	619.893525	-68.426601	34.1697779	-0.1172452
0.095429	6.41215248	-0.0526611	620.104399	-68.6944557	32.3510645	-0.1176390
0.100185	6.41843494	-0.0523780	620.247489	-68.8269544	30.7386371	-0.1178478
0.110004	6.43140733	-0.0518342	620.430999	-68.8176557	27.7394575	-0.1179625
0.120229	6.44491821	-0.0513202	620.490706	-68.5079031	25.035864	-0.1177183
0.130181	6.45806884	-0.0508652	620.468659	-68.027579	22.6029181	-0.1172575
0.140482	6.47168369	-0.0504369	620.327245	-67.2942936	20.3237398	-0.1164319
0.150411	6.48480617	-0.0500612	620.126139	-66.4507373	18.3439183	-0.1154567

Table D-2. Pressure coefficient and edge velocity distributions at Re_No.5 of NEXST-1 flight test
(b) y/s=0.7 (2/2)

	y/s=0.70		Y[m]=	1.650600		
S/C	X[m]	Z[m]	Ue[m/s]	Ve[m/s]	We[m/s]	Cp
0.160639	6.49832642	-0.0497090	619.881625	-65.5165305	16.5493374	-0.1143663
0.170404	6.51123451	-0.0494033	619.64765	-64.6352722	14.9763531	-0.1133507
0.180424	6.52448072	-0.0491178	619.429489	-63.7903509	13.3968791	-0.1124010
0.190698	6.53806285	-0.0488523	619.237324	-63.0127544	11.972778	-0.1115634
0.200405	6.55089654	-0.0486259	619.092386	-62.3732073	10.7636724	-0.1109171
0.210326	6.56401307	-0.0484169	618.971043	-61.7926955	9.4763136	-0.1103574
0.220459	6.57741088	-0.0482250	618.863883	-61.2575809	8.42592538	-0.1098672
0.230804	6.59108848	-0.0480513	618.765848	-60.7490134	7.33705527	-0.1094143
0.240472	6.60387081	-0.0479063	618.680699	-60.2973735	6.36363528	-0.1090225
0.250315	6.61688594	-0.0477770	618.596852	-59.8545686	5.51930814	-0.1086449
0.260334	6.63013279	-0.0476613	618.515368	-59.4174709	4.58038107	-0.1082772
0.270527	6.64361035	-0.0475615	618.426629	-58.9744031	3.80786403	-0.1078950
0.280893	6.65731761	-0.0474752	618.331514	-58.5169351	2.85933911	-0.1074918
0.300184	6.68282522	-0.0473577	618.100681	-57.594267	1.53848669	-0.1065859
0.325095	6.71576441	-0.0472729	617.776625	-56.3769665	-8.72E-02	-0.1053504
0.350885	6.74986569	-0.0472541	617.536926	-55.338102	-0.9711593	-0.1044104
0.400610	6.81561539	-0.0474021	617.3381	-53.9445014	-3.3053615	-0.1035246
0.425421	6.84842277	-0.0475606	617.325013	-53.4596915	-4.3327788	-0.1033887
0.450893	6.88210318	-0.0477772	617.35055	-53.0672863	-5.3168968	-0.1033899
0.475820	6.91506179	-0.0480394	617.417622	-52.7990046	-6.2355502	-0.1035425
0.500112	6.94718125	-0.0483405	617.528035	-52.6742031	-7.0911497	-0.1038548
0.526196	6.98166907	-0.0487104	617.683546	-52.6831836	-7.9716492	-0.1043318
0.550302	7.01354161	-0.0490930	617.85549	-52.7873093	-8.7939589	-0.1048789
0.576193	7.04777483	-0.0495493	618.070495	-52.9505188	-9.7089168	-0.1055690
0.601280	7.08094212	-0.0500373	618.300251	-53.1122156	-10.637377	-0.1063039
0.625483	7.11294127	-0.0505518	618.540025	-53.2526569	-11.5428	-0.1070633
0.650110	7.1454997	-0.0511202	618.802665	-53.3783429	-12.495741	-0.1078886
0.675158	7.1786149	-0.0517455	619.092915	-53.5047263	-13.488073	-0.1087966
0.700627	7.2122844	-0.0524310	619.41804	-53.662484	-14.532617	-0.1098159
0.741075	7.26575519	-0.0536261	619.957258	-53.9601314	-16.312538	-0.1115242
0.781032	7.31857261	-0.0549389	620.454331	-54.16906	-18.156357	-0.1131065
0.820388	7.37059217	-0.0563639	620.910356	-54.2252988	-20.012192	-0.1145481
0.860601	7.42374135	-0.0579557	621.355327	-54.0985316	-21.900545	-0.1159285
0.900072	7.47590564	-0.0596451	621.748684	-53.7053385	-23.571661	-0.1170915
0.950105	7.54202384	-0.0619436	622.204745	-52.6359234	-25.497768	-0.1183066
1.001338	7.60972	-0.0644904	622.864804	-51.2366	-27.519457	-0.1200356

Table D-3. Pressure coefficient and edge velocity distributions at P0=0.6 bar of S2MA test

(a) y/s=0.3 (1/2)

	y/s=0.30		Y[m]=	0.707400		
S/C	X[m]	Z[m]	Ue[m/s]	Ve[m/s]	We[m/s]	Cp
0.000000	1.01745511	-0.0117066	422.632221	187.9519587	-8.1354311	0.2059736
0.000010	1.01744989	-0.0117031	422.968184	187.3002389	-6.8581255	0.2059648
0.000026	1.01744085	-0.0116967	423.200447	186.8127364	-5.7560419	0.2059419
0.000049	1.01742895	-0.0116875	423.592641	186.0066144	-3.7466475	0.2058544
0.000077	1.01741459	-0.0116756	424.119967	184.9327232	-0.9596276	0.2056436
0.000190	1.01735973	-0.0116247	425.874914	181.5625398	10.3422614	0.2038889
0.000237	1.01733903	-0.0116021	426.268691	180.7217676	15.732272	0.2026153
0.000342	1.01729752	-0.0115463	426.778808	179.7858598	29.6326202	0.1979854
0.000528	1.01725574	-0.0114326	424.040654	186.4184558	57.0244164	0.1836700
0.000597	1.01725249	-0.0113865	424.489831	186.0358563	68.4072337	0.1751645
0.000746	1.01726681	-0.0112895	428.99599	178.0647276	88.4032342	0.1568830
0.001271	1.01747494	-0.0110181	449.268585	133.9547288	119.44116	0.1063596
0.001905	1.01782245	-0.0107848	463.57129	101.9219277	126.682949	0.0732126
0.002511	1.0181805	-0.0106052	472.156258	82.47900291	126.653162	0.0539031
0.004078	1.01914587	-0.0102319	485.093629	52.91765278	121.352402	0.0245078
0.005060	1.01976435	-0.0100350	490.259662	41.03958307	117.814203	0.0121960
0.006128	1.02044286	-0.0098412	494.725271	30.76532986	114.319651	0.0010471
0.007082	1.02105226	-0.0096818	498.13796	22.92941272	111.403092	-0.0078095
0.008091	1.02170036	-0.0095245	501.362642	15.55108621	108.488645	-0.0164676
0.009155	1.02238621	-0.0093698	504.501148	8.397016756	105.197962	-0.0249128
0.010045	1.0229615	-0.0092484	506.894063	2.956682586	102.367277	-0.0313632
0.012169	1.0243406	-0.0089862	511.64146	-7.85573895	93.5521931	-0.0426546
0.017474	1.02780405	-0.0084472	515.166545	-15.8415976	79.1464644	-0.0472723
0.020114	1.02953196	-0.0082109	516.56947	-18.9237065	74.3577481	-0.0501213
0.022587	1.03115326	-0.0080073	517.807991	-21.6701393	69.2515826	-0.0523967
0.025177	1.03285298	-0.0078088	518.491325	-23.116656	65.6621228	-0.0533866
0.025508	1.03307086	-0.0077843	518.565447	-23.2723621	65.2124897	-0.0534730
0.030340	1.03624531	-0.0074455	519.393195	-24.9422669	59.8361258	-0.0543866
0.035131	1.0393959	-0.0071374	520.008228	-26.1250156	55.6010334	-0.0551047
0.040207	1.04273661	-0.0068362	520.553265	-27.1314193	51.9219639	-0.0558703
0.045141	1.04598502	-0.0065637	520.995404	-27.915779	48.8207854	-0.0565190
0.050307	1.04938815	-0.0062966	521.393991	-28.5902603	46.0480504	-0.0571638
0.055243	1.05264101	-0.0060565	521.727792	-29.12996	43.7066375	-0.0577353
0.060368	1.0560192	-0.0058211	522.035277	-29.6029225	41.5613981	-0.0582942
0.065189	1.05919735	-0.0056110	522.295523	-29.9843546	39.7530625	-0.0587903
0.070160	1.06247604	-0.0054049	522.54373	-30.335602	38.0444811	-0.0592862
0.075282	1.06585395	-0.0052030	522.784084	-30.6702151	36.381535	-0.0597824
0.080017	1.06897786	-0.0050249	522.991537	-30.9549969	34.9049835	-0.0602154
0.085418	1.07254091	-0.0048312	523.191464	-31.2004731	33.4330127	-0.0606288
0.090401	1.07582957	-0.0046608	523.348843	-31.3782349	32.1247858	-0.0609283
0.095501	1.07919501	-0.0044936	523.480173	-31.4947764	31.0305299	-0.0611791
0.100130	1.0822503	-0.0043469	523.583675	-31.5666963	30.205674	-0.0613853
0.110265	1.08893991	-0.0040427	523.849562	-31.8382831	28.2541744	-0.0619884
0.120168	1.09547763	-0.0037682	524.129326	-32.1438689	26.3555525	-0.0626832
0.130419	1.10224603	-0.0035070	524.390187	-32.3837075	24.4940357	-0.0633276
0.140341	1.10879795	-0.0032751	524.631323	-32.5811886	22.7755603	-0.0639387

Table D-3. Pressure coefficient and edge velocity distributions at P0=0.6 bar of S2MA test

(a) y/s=0.3 (2/2)

	y/s=0.30		Y[m]=	0.707400		
S/C	X[m]	Z[m]	Ue[m/s]	Ve[m/s]	We[m/s]	Cp
0.150560	1.1155471	-0.0030567	524.872306	-32.7664108	21.0342553	-0.0645631
0.160364	1.12202208	-0.0028656	525.087686	-32.9016281	19.4714212	-0.0651303
0.170421	1.12866482	-0.0026880	525.283531	-32.9711015	18.0130369	-0.0656432
0.180728	1.13547352	-0.0025248	525.474964	-33.0137561	16.4866084	-0.0661414
0.190521	1.14194294	-0.0023861	525.653048	-33.0425641	14.9593554	-0.0666057
0.200526	1.14855261	-0.0022608	525.826962	-33.0169218	13.6942672	-0.0670827
0.201305	1.14906682	-0.0022517	525.840835	-33.0183661	13.5617342	-0.0671191
0.210741	1.15530125	-0.0021501	525.995529	-32.9762906	12.2735302	-0.0675356
0.220355	1.16165302	-0.0020598	526.141891	-32.9094905	10.9128589	-0.0679234
0.230145	1.1681212	-0.0019837	526.275469	-32.782313	9.77286825	-0.0682801
0.240109	1.17470486	-0.0019204	526.405995	-32.6878724	8.15338621	-0.0686155
0.250247	1.18140313	-0.0018715	526.527783	-32.4898194	7.28155905	-0.0689501
0.260556	1.18821514	-0.0018387	526.652122	-32.4316077	5.07898184	-0.0692788
0.270157	1.19455868	-0.0018236	526.757233	-32.1894327	4.6527788	-0.0695777
0.280792	1.20158635	-0.0018169	526.867095	-31.9970469	3.42216484	-0.0698853
0.290690	1.20812622	-0.0018275	526.955222	-31.8409508	1.91596007	-0.0701320
0.300728	1.21475906	-0.0018495	527.042558	-31.5641999	1.49E+00	-0.0703728
0.325010	1.23080292	-0.0019552	527.247675	-31.1194502	-1.4718599	-0.0709955
0.350063	1.24735551	-0.0021454	527.473933	-30.6721556	-4.4145855	-0.0717518
0.375876	1.26440967	-0.0024287	527.676057	-30.1440587	-7.4065719	-0.0724711
0.400371	1.28059124	-0.0027784	527.813167	-29.5478636	-10.144174	-0.0729966
0.425500	1.2971892	-0.0032171	527.88816	-28.854955	-12.899344	-0.0733437
0.450169	1.31348171	-0.0037245	527.913757	-28.1368029	-15.470617	-0.0735507
0.475408	1.33014789	-0.0043199	527.927355	-27.468135	-18.089236	-0.0737791
0.500078	1.34643515	-0.0049797	527.95632	-27.0071948	-20.998343	-0.0741853
0.525259	1.36305646	-0.0057391	527.983976	-26.7072732	-23.691328	-0.0746389
0.550947	1.38000877	-0.0065928	527.992546	-26.5928112	-26.262176	-0.0750866
0.575937	1.39649632	-0.0074963	528.020252	-26.6497095	-28.674713	-0.0756432
0.600160	1.41247389	-0.0084387	528.044348	-26.7416861	-30.951755	-0.0762034
0.641021	1.4394175	-0.0101719	528.062341	-26.6972449	-34.752223	-0.0771021
0.680410	1.46537923	-0.0120040	528.127003	-26.1289491	-37.476788	-0.0778961
0.720761	1.49195677	-0.0141221	527.681854	-24.9797831	-44.247796	-0.0780065
0.760717	1.51825985	-0.0163960	527.158794	-23.5756163	-46.471943	-0.0766773
0.800181	1.54423109	-0.0187320	526.469946	-22.3532706	-48.271061	-0.0747089
0.840463	1.57073396	-0.0211912	525.772278	-21.3874398	-49.729746	-0.0726546
0.880126	1.59682409	-0.0236689	525.271543	-20.6902814	-50.825732	-0.0712047
0.920539	1.62339843	-0.0262867	524.814039	-20.0212973	-55.35638	-0.0711290
0.960213	1.64946987	-0.0290274	524.827072	-19.4347389	-56.873567	-0.0716673
0.999067	1.6749951	-0.0317791	524.439739	-18.5139815	-58.454109	-0.0708201

Table D-3. Pressure coefficient and edge velocity distributions at P0=0.6 bar of S2MA test
(b) y/s=0.7 (1/2)

	y/s=0.70		Y[m]=	1.650600		
S/C	X[m]	Z[m]	Ue[m/s]	Ve[m/s]	We[m/s]	Cp
0.000000	1.46526681	-0.0190501	388.805483	213.7275866	0.3914707	0.3031640
0.000010	1.46526463	-0.0190481	389.215624	212.9710658	2.01041582	0.3031420
0.000026	1.46526081	-0.0190446	389.534701	212.3854725	3.27158377	0.3031026
0.000049	1.46525562	-0.0190399	389.814863	211.8742552	4.37438799	0.3030479
0.000077	1.46524922	-0.0190340	390.076278	211.3905565	5.46456663	0.3029764
0.000190	1.46522387	-0.0190101	390.897539	209.891265	9.21506856	0.3025994
0.000237	1.4652137	-0.0190000	391.22531	209.2791269	10.9400249	0.3023661
0.000342	1.46519124	-0.0189767	392.218369	207.4621388	16.3887324	0.3013436
0.000528	1.46515405	-0.0189331	393.652852	204.8612093	27.0157019	0.2983378
0.000597	1.46514115	-0.0189161	394.067929	204.1042338	31.4847463	0.2966885
0.000746	1.46511546	-0.0188781	394.812165	202.8291579	41.9153863	0.2919704
0.001271	1.46506	-0.0187280	390.145139	210.3473992	89.3938753	0.2568348
0.001905	1.4650965	-0.0185390	406.742404	181.4521878	143.9162	0.1802310
0.002511	1.46521309	-0.0183940	430.936762	137.0980241	167.859375	0.1124424
0.004078	1.46562109	-0.0181392	471.767949	62.89842569	167.131079	0.0178860
0.005060	1.46590036	-0.0180228	485.994095	37.09554147	156.557517	-0.0117088
0.006128	1.46621157	-0.0179161	495.843779	19.2038283	145.471934	-0.0313347
0.007082	1.46649311	-0.0178325	502.023217	7.984774789	136.34208	-0.0430684
0.008091	1.46679369	-0.0177529	506.739906	-0.58173566	127.647103	-0.0514365
0.009155	1.46711245	-0.0176765	510.145552	-6.77632071	119.893038	-0.0568901
0.010045	1.46738006	-0.0176170	512.172546	-10.4669616	114.473584	-0.0598305
0.012169	1.46802156	-0.0174871	515.488543	-16.5117823	104.380513	-0.0644107
0.017474	1.46963301	-0.0172153	521.148309	-26.7505106	85.8352622	-0.0736175
0.020114	1.47043787	-0.0170997	522.937525	-29.9653556	79.3952522	-0.0768315
0.022587	1.47119315	-0.0169999	524.309998	-32.4218062	74.2601626	-0.0794247
0.025177	1.47198509	-0.0169028	525.480846	-34.5020686	69.7271746	-0.0817257
0.025508	1.47208661	-0.0168908	525.609337	-34.7293488	69.2069021	-0.0819772
0.030340	1.47356605	-0.0167272	527.184822	-37.5085518	62.4089128	-0.0850557
0.035131	1.47503474	-0.0165810	528.449139	-39.7302109	57.0351913	-0.0877934
0.040207	1.4765923	-0.0164403	529.46176	-41.5037754	52.3505785	-0.0900050
0.045141	1.47810699	-0.0163150	530.186285	-42.7678258	48.5057469	-0.0915279
0.050307	1.47969393	-0.0161939	530.907173	-44.0264255	44.9926815	-0.0932294
0.055243	1.48121088	-0.0160865	531.510273	-45.0779437	42.0771549	-0.0947213
0.060368	1.48278634	-0.0159827	532.062308	-46.0389524	39.4104563	-0.0961356
0.065189	1.48426855	-0.0158913	532.528011	-46.8479577	37.1574572	-0.0973632
0.070160	1.48579766	-0.0158027	532.965559	-47.6062413	35.0185074	-0.0985408
0.075282	1.48737307	-0.0157169	533.376392	-48.3155694	32.9684282	-0.0996636
0.080017	1.48883001	-0.0156421	533.716277	-48.8986463	31.2918051	-0.1006148
0.085418	1.49049176	-0.0155617	534.06616	-49.4930394	29.539987	-0.1016058
0.090401	1.49202554	-0.0154917	534.373946	-50.008611	27.9563964	-0.1024836
0.095501	1.49359512	-0.0154240	534.684617	-50.514215	26.464187	-0.1033979
0.100130	1.49502009	-0.0153660	534.924678	-50.8869476	25.1259142	-0.1040795
0.110265	1.4981401	-0.0152490	535.369658	-51.5205639	22.5461374	-0.1053400
0.120168	1.50118923	-0.0151467	535.741856	-51.987507	20.325006	-0.1063968
0.130419	1.50434587	-0.0150518	536.042789	-52.2939707	18.2223842	-0.1072162
0.140341	1.50740146	-0.0149697	536.277728	-52.4674869	16.3558045	-0.1078310

Table D-3. Pressure coefficient and edge velocity distributions at P0=0.6 bar of S2MA test
(b) y/s=0.7 (2/2)

	y/s=0.70		Y[m]=	1.650600		
S/C	X[m]	Z[m]	Ue[m/s]	Ve[m/s]	We[m/s]	Cp
0.150560	1.51054894	-0.0148942	536.468614	-52.5364816	14.5668227	-0.1082989
0.160364	1.51356847	-0.0148296	536.608539	-52.5119381	13.1021508	-0.1086182
0.170421	1.51666615	-0.0147708	536.721661	-52.424034	11.7020286	-0.1088490
0.180728	1.51984112	-0.0147178	536.818025	-52.2947891	10.3050989	-0.1090252
0.190521	1.52285781	-0.0146735	536.896851	-52.1490996	9.03233901	-0.1091585
0.200526	1.52593982	-0.0146342	536.968951	-51.9859923	7.98335111	-0.1092851
0.201305	1.52617959	-0.0146314	536.974569	-51.9736953	7.88430187	-0.1092946
0.210741	1.52908656	-0.0146000	537.039924	-51.8220257	6.8118633	-0.1094095
0.220355	1.53204819	-0.0145724	537.102772	-51.66695	5.88001724	-0.1095272
0.230145	1.53506405	-0.0145493	537.162688	-51.5104645	4.99285135	-0.1096417
0.240109	1.53813372	-0.0145300	537.219831	-51.3554556	3.97755419	-0.1097494
0.250247	1.54125678	-0.0145151	537.265804	-51.1822033	3.32866347	-0.1098291
0.260556	1.54443285	-0.0145041	537.303962	-51.0073341	2.10625989	-0.1098778
0.270157	1.54739048	-0.0144981	537.321258	-50.8086517	1.78682363	-0.1098689
0.280792	1.55066707	-0.0144947	537.334378	-50.5908299	0.82477638	-0.1098374
0.290690	1.55371624	-0.0144960	537.334644	-50.3705851	0.15065675	-0.1097699
0.300728	1.55680877	-0.0144997	537.324268	-50.1253778	-6.96E-02	-0.1096631
0.325010	1.56428923	-0.0145226	537.284524	-49.5293382	-1.7287584	-0.1093675
0.350063	1.57200714	-0.0145645	537.234584	-48.9083486	-3.1229638	-0.1090450
0.375876	1.57995939	-0.0146250	537.197166	-48.3110368	-4.379047	-0.1087791
0.400371	1.58750534	-0.0146973	537.191617	-47.8177513	-5.4398812	-0.1086497
0.425500	1.59524622	-0.0147855	537.211681	-47.3793448	-6.45059	-0.1086239
0.450169	1.60284552	-0.0148850	537.253764	-47.0121792	-7.3749047	-0.1086920
0.475408	1.61062012	-0.0149993	537.318957	-46.7028948	-8.274311	-0.1088547
0.500078	1.61821915	-0.0151229	537.401387	-46.4681331	-9.1171592	-0.1090954
0.525259	1.62597558	-0.0152606	537.507926	-46.302921	-9.9712883	-0.1094374
0.550947	1.63388801	-0.0154131	537.644076	-46.2087106	-10.852545	-0.1098995
0.575937	1.64158508	-0.0155733	537.801782	-46.1745044	-11.730425	-0.1104507
0.600160	1.64904559	-0.0157397	537.974656	-46.1811662	-12.596391	-0.1110644
0.641021	1.6616301	-0.0160459	538.298271	-46.255552	-14.110939	-0.1122310
0.680410	1.67376032	-0.0163711	538.654709	-46.4077208	-15.179358	-0.1134928
0.720761	1.68618535	-0.0167545	538.860851	-46.5252138	-18.60112	-0.1145139
0.760717	1.69848753	-0.0171748	538.989442	-46.5677686	-19.785661	-0.1150627
0.800181	1.71063747	-0.0176113	539.083529	-46.6046113	-20.854481	-0.1154949
0.840463	1.72303859	-0.0180765	539.177201	-46.6686919	-21.841049	-0.1159291
0.880126	1.73524842	-0.0185512	539.297568	-46.7944671	-22.709948	-0.1164538
0.920539	1.74768783	-0.0190667	539.420308	-46.9817839	-26.196832	-0.1173857
0.960213	1.75989721	-0.0196349	539.70959	-47.1234077	-27.986727	-0.1186117
0.999067	1.77185253	-0.0202254	539.500912	-46.5789266	-29.732355	-0.1181028

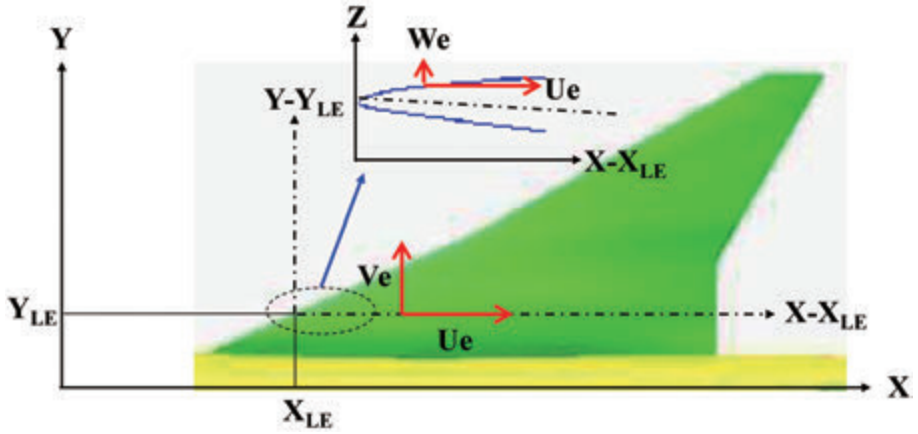

Figure D-1. Definition of each physical quantity

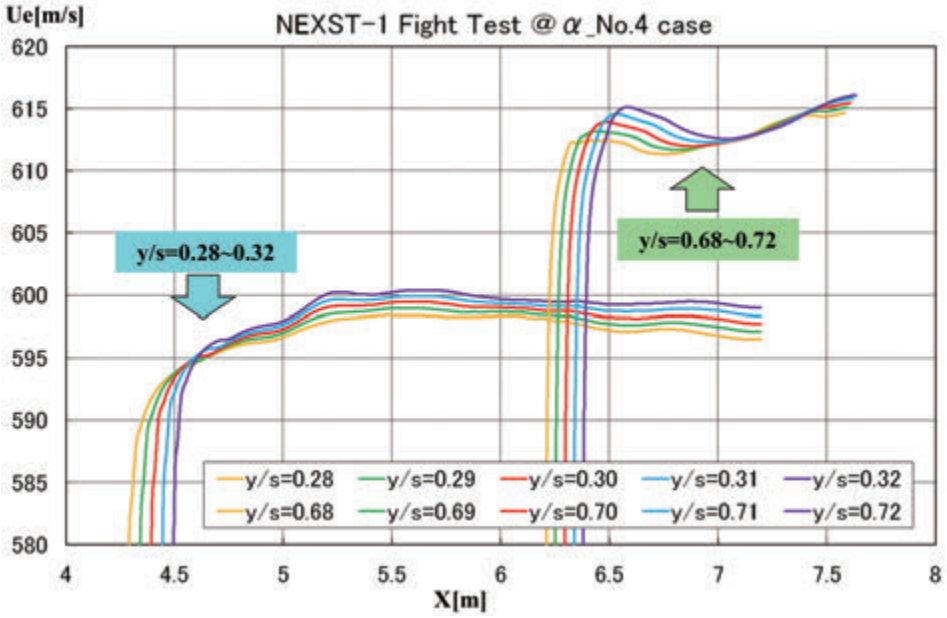

Figure D-2. Edge velocity distributions at α_No.4 of NEXST-1 flight test

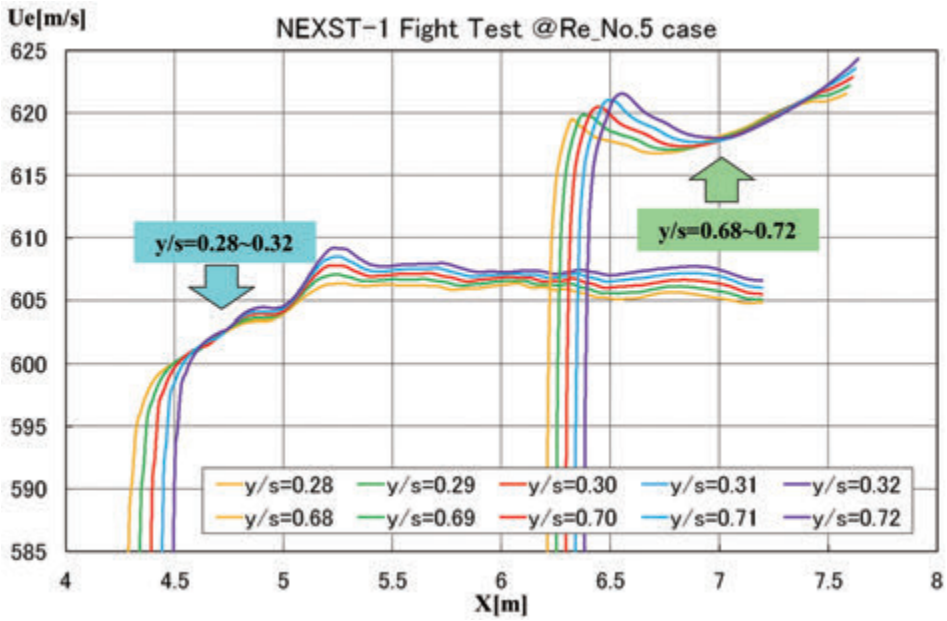

Figure D-3. Edge velocity distributions at Re_No.5 of NEXST-1 flight test

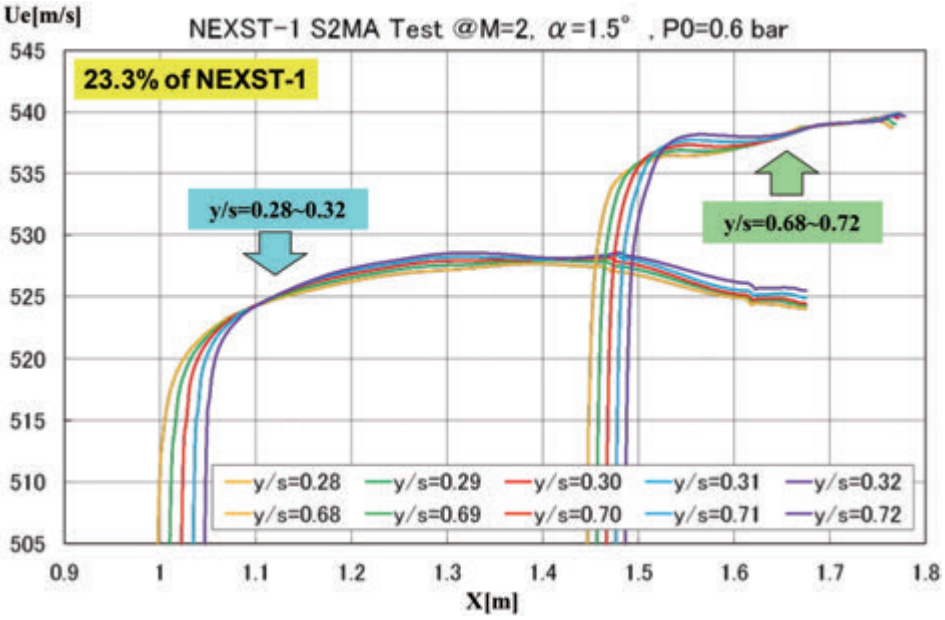

Figure D-4. Edge velocity distributions at P0=0.6 bar of S2MA test

E. Stability results at y/s=0.5 and 0.9 in the case of α_No.4

The comparisons of some chordwise distributions of Mach number (Me), static temperature (Te) at boundary layer edge (BLE) and wall temperature (Tw) at y/s=0.5 and 0.9 are summarized in Fig. E-1(a) at y/s=0.5 and Fig. E-1(b) at y/s=0.9. Several chordwise distributions of boundary layer thickness (indicated "Delta") and displacement thickness ("Delta*") were also summarized in Figs. E-1. Considering that boundary layer edge was defined as the point at U(y = δ) / Ue = 0.995, there was remarkable high correlation between ONERA and JAXA results.

As a typical laminar boundary layer computation result, crossflow velocity profiles plotted in external streamline coordinates are summarized in Fig. E-2(a) at y/s=0.5 and Fig. E-2(b) at y/s=0.9. ONERA's results (solid triangle symbols) are in rather good agreement with JAXA's ones (colored solid lines) at each chordwise locations.

Next, the comparisons of N factor and ψ evolutions computed with envelope strategy are shown in Figs. E-3 and E-4. These figures also include measured transition location ("$X_T$exp") in the flight test which are summarized in Appendix B and special N values at these locations ("N_{TR}"). JAXA's N factors and N_{TR} at y/s=0.9 are in good agreement with ONERA's results, but there was a slight difference at mid-span region (y/s=0.5). This region had a kink in leading edge which may generate a slight distortion of both surface contour and spanwise pressure gradient. Therefore, each 3D-LBL results near this region in each LBL code was very sensitive to such distortion. As for the ψ distributions summarized in Figs. E-4(a) and (b), JAXA's results after x/c>0.1 were not in agreement with ONERA's results. The main reason is the same as that mentioned in Chapter 2: envelope strategy is very sensitive to the selection of the most amplified disturbance.

Figures E-5 and E-6 show similar comparisons of N factors and ψ evolutions computed with fixed β strategy by both parties. The range of several combinations of (β_r , f) was the same as that mentioned in Chapter 2. JAXA's results of both N factors and ψ distributions are in good agreement with ONERA's ones at y/s=0.9. In the same way as for envelope strategy, there is a noticeable difference between ONERA's and JAXA's results at mid-span region (y/s=0.5). The reason is the same as that mentioned above. Fixed β strategy indicates that as CFI was also weak at y/s=0.5 and 0.9, and TSI was the most dominant instability at measured transition locations.

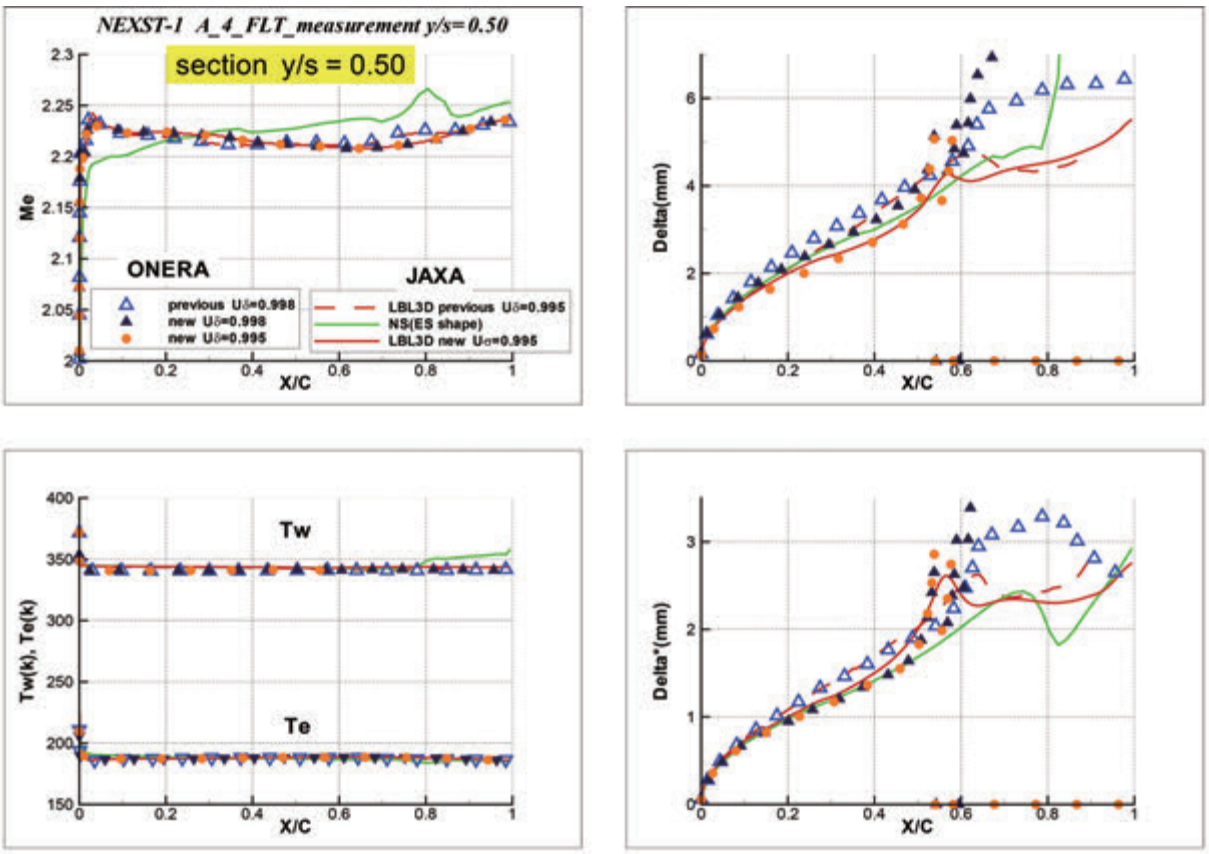

(a) Comparisons of boundary layer thickness at y/s=0.5

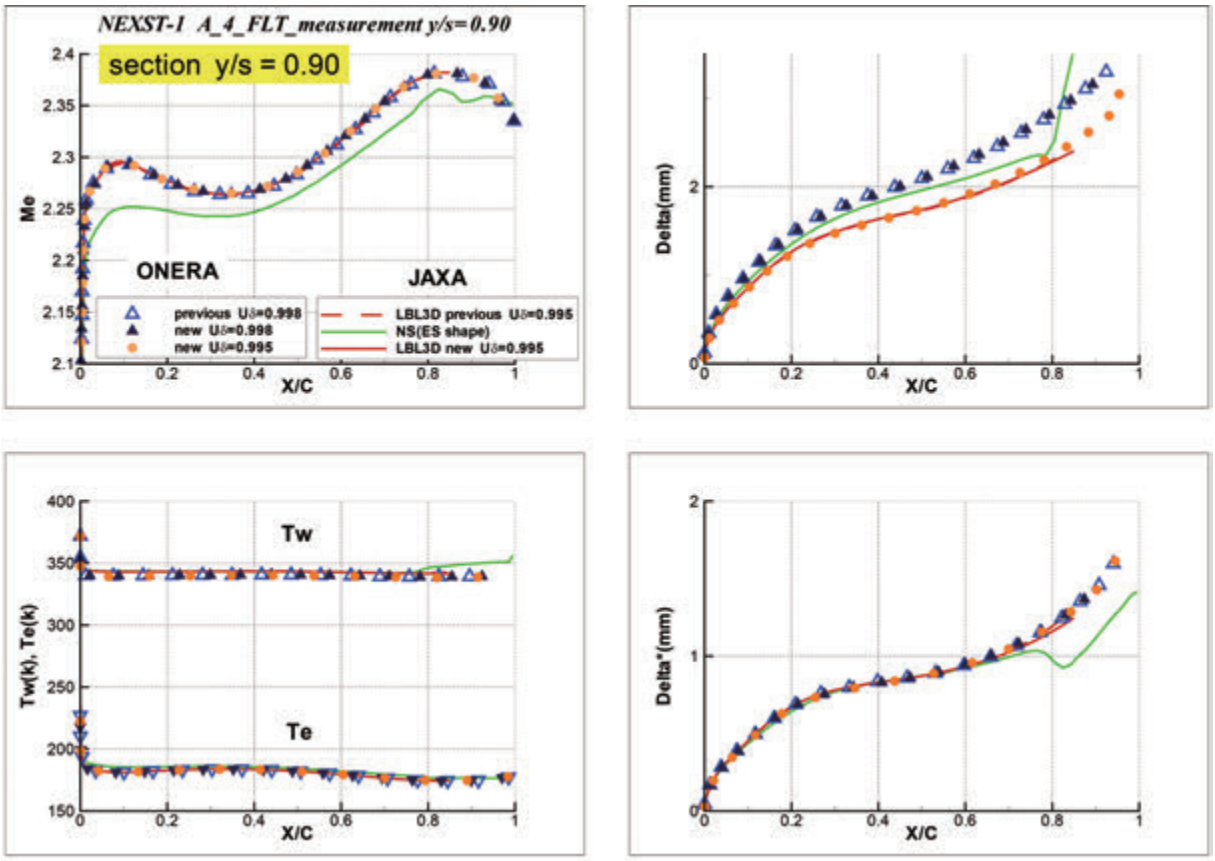

(b) Comparisons of boundary layer thickness at y/s=0.9

Figure E-1. Boundary layer computations at α _No.4

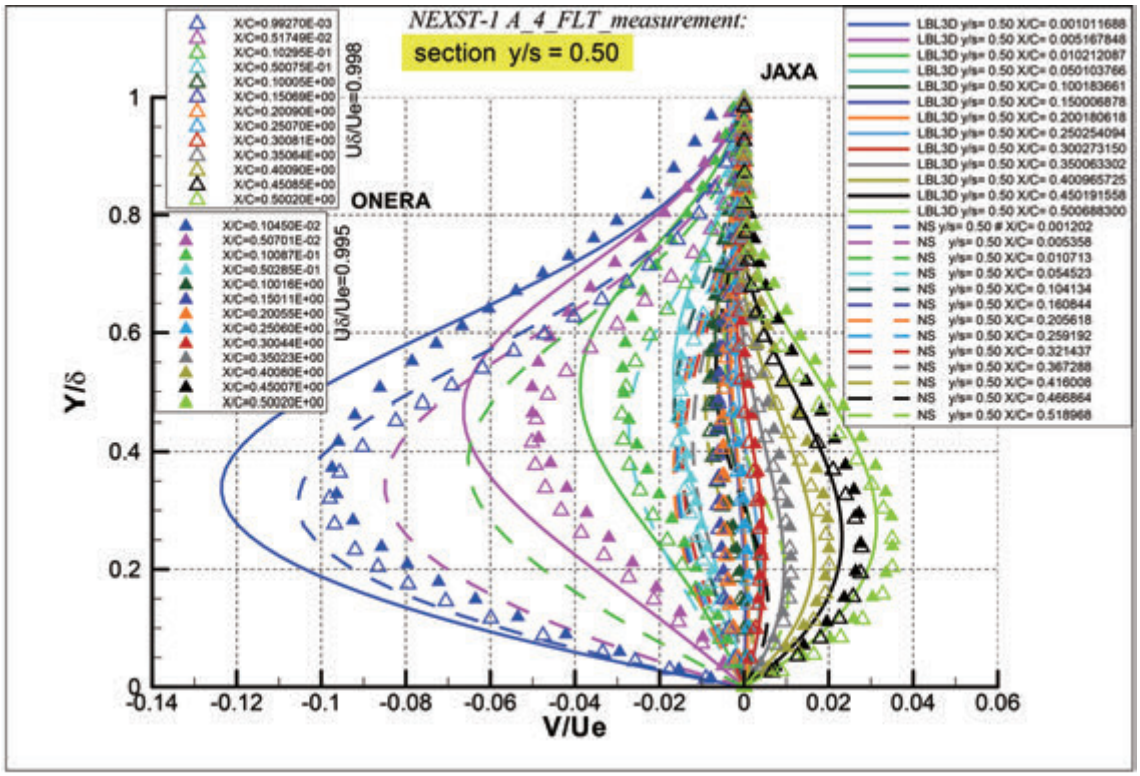

(a) Comparisons of crossflow velocity profiles at y/s=0.5

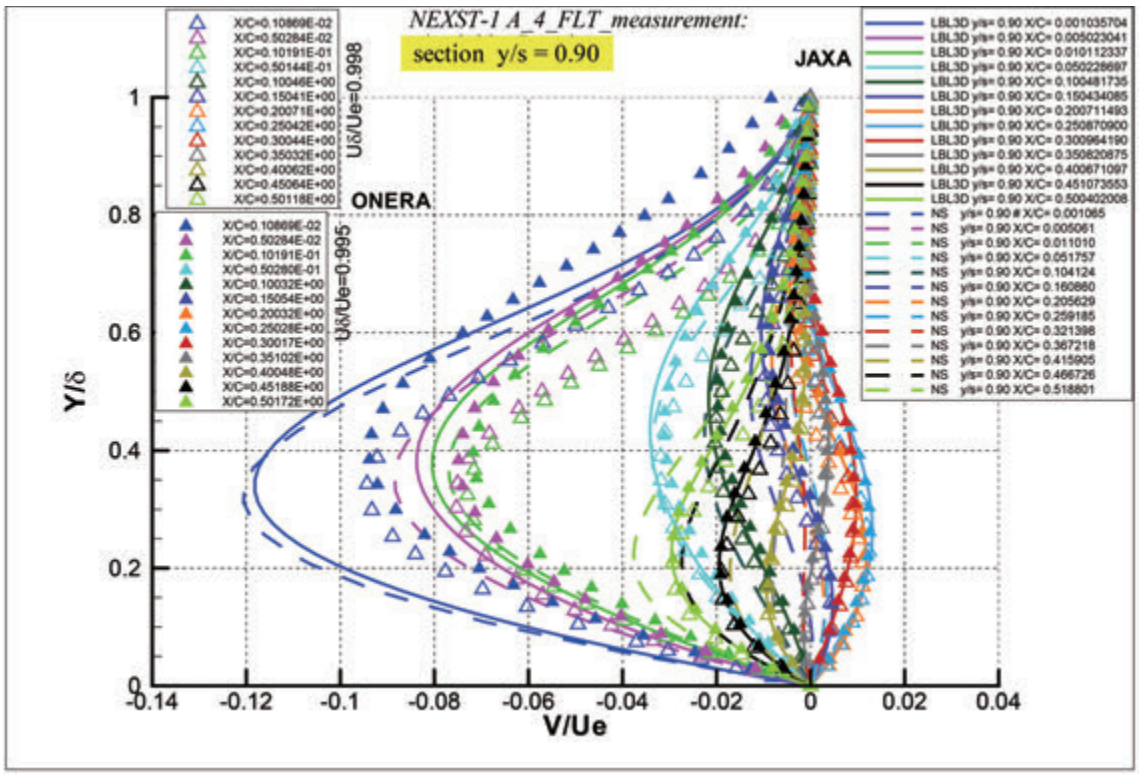

(b) Comparisons of crossflow velocity profiles at y/s=0.9

Figure E-2. Boundary layer computations at α _No.4

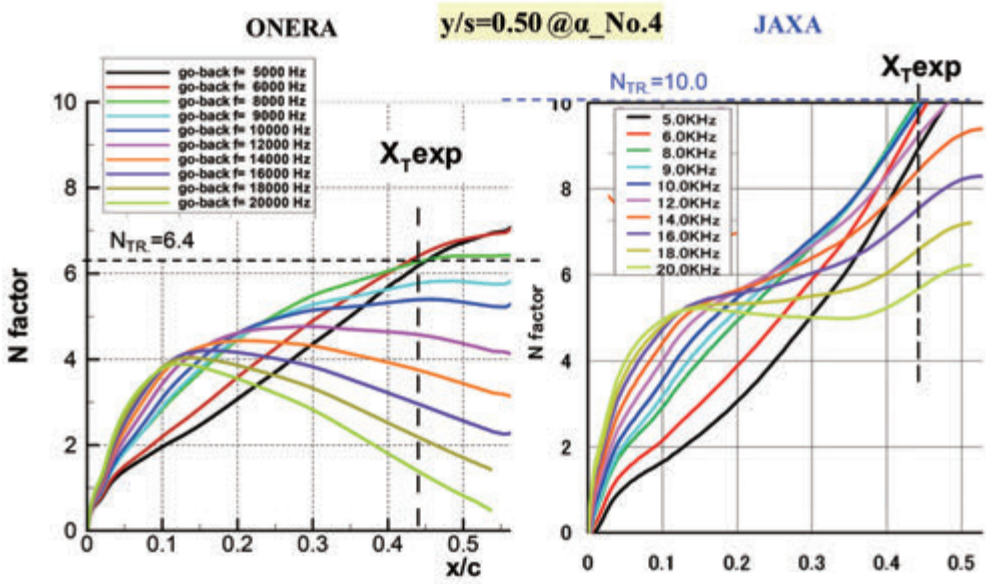

(a) Comparisons of N factors at y/s=0.5

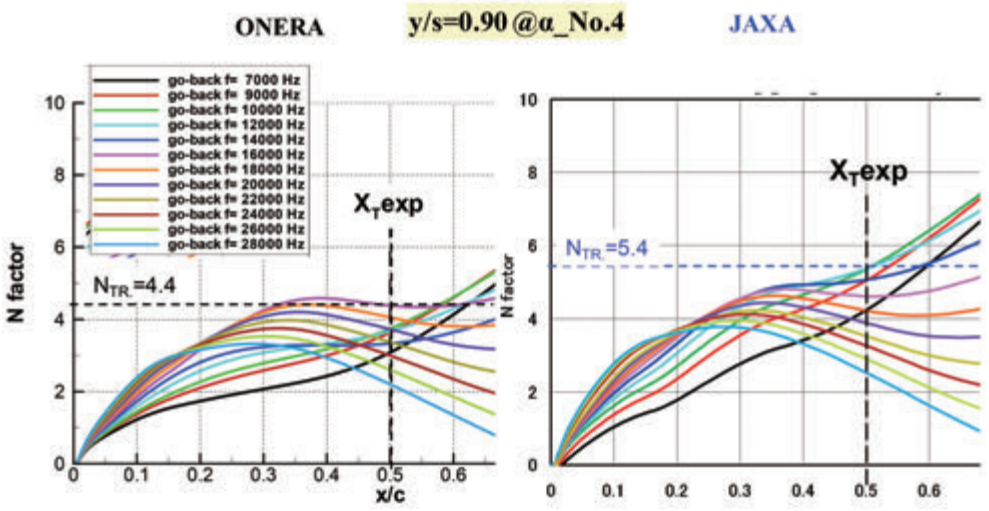

(b) Comparisons of N factors at y/s=0.9

Figure E-3. Stability analysis (envelope strategy) at α _No.4

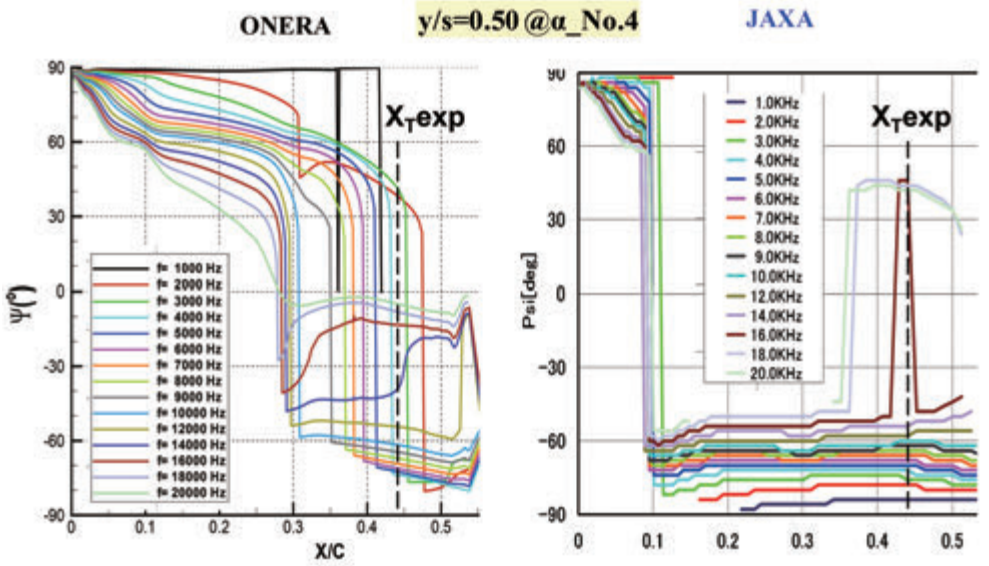

(a) Comparisons of ϕ values at y/s=0.5

Figure E-4. Stability analysis (envelope strategy) at α _No.4

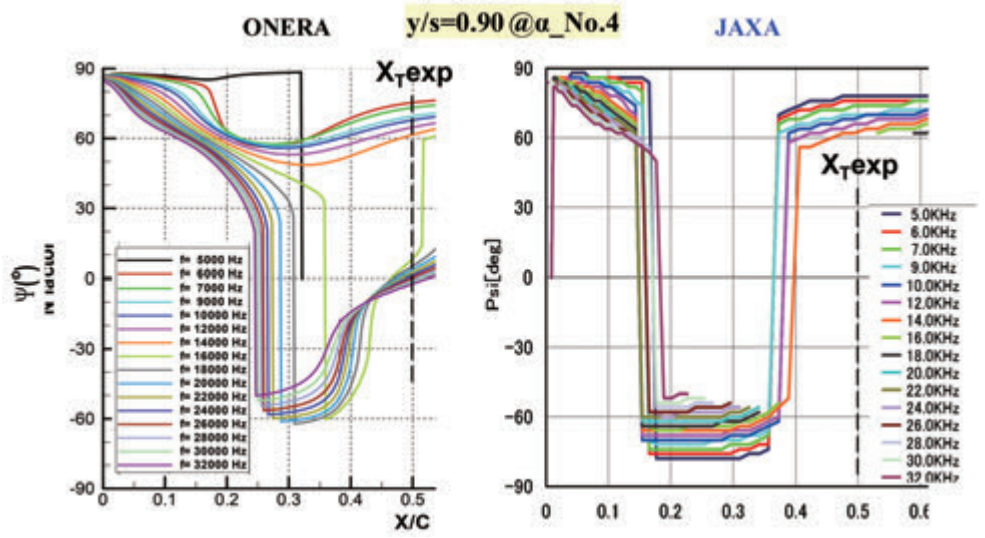

(b) Comparisons of ϕ values at y/s=0.9

Figure E-4. Stability analysis (envelope strategy) at α _No.4

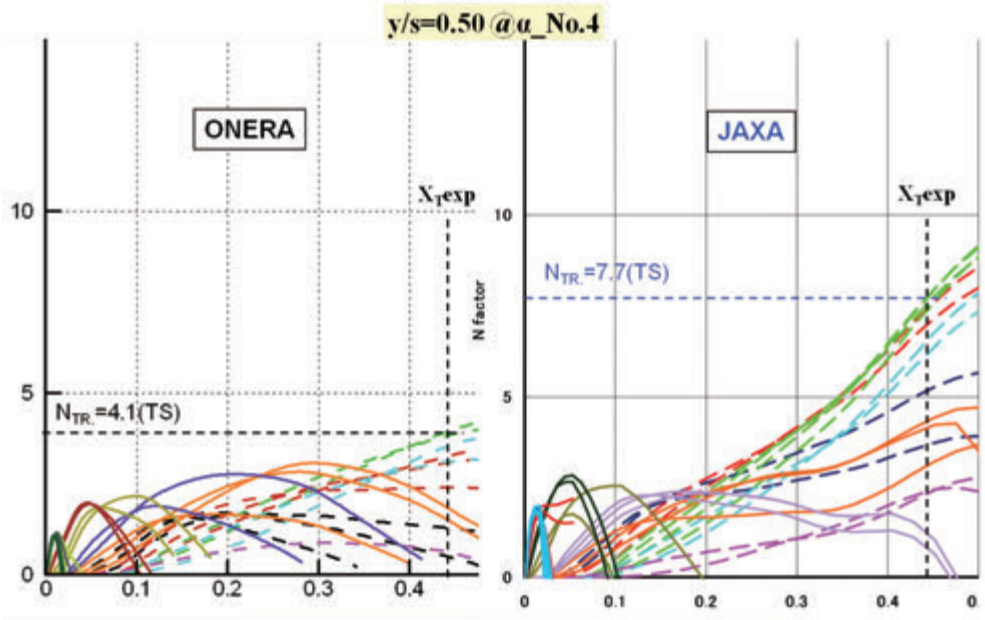

$-400 \le \beta_r[m^{-1}] \le 5000 \quad , \quad 4 \le f[kHz] \le 80$

(a) Comparisons of N factors at y/s=0.5

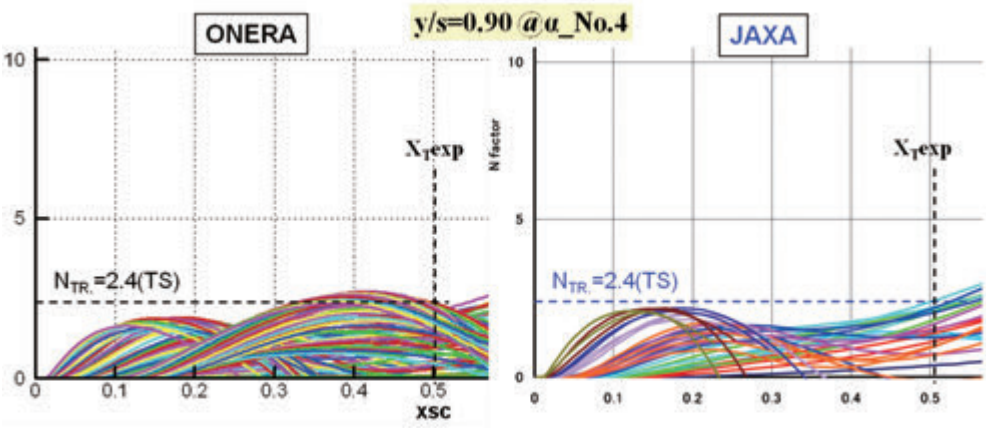

$-200 \le \beta_r[m^{-1}] \le 2000 \quad , \quad 5 \le f[kHz] \le 35$

(b) Comparisons of N factors at y/s=0.9

Figure E-5. Stability analysis (fixed β strategy) at α _No.4

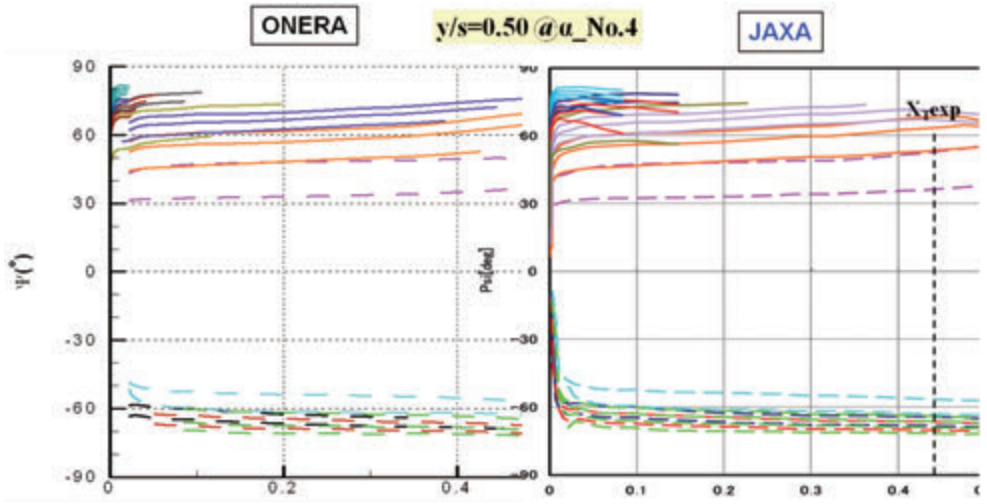

(a) Comparisons of ψ values at y/s=0.5

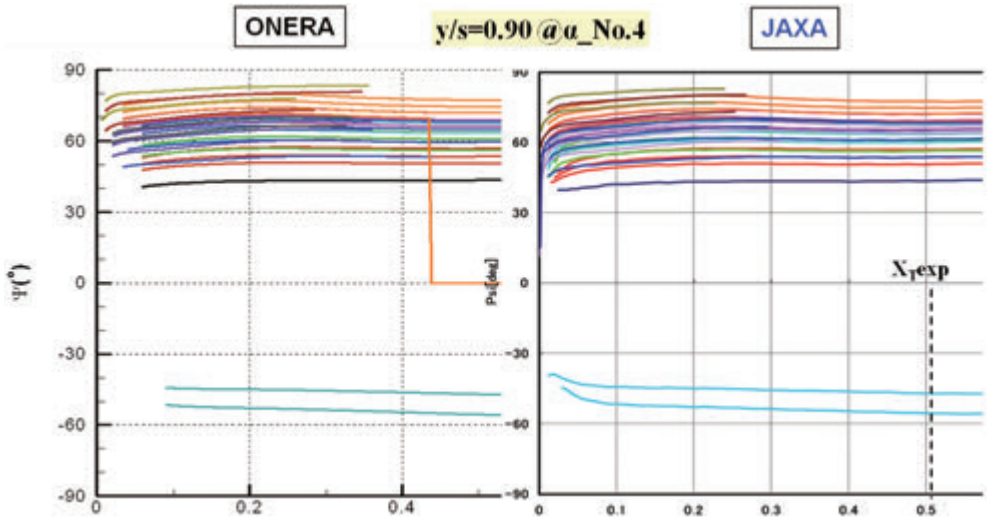

(b) Comparisons of ψ values at y/s=0.9

Figure E-6. Stability analysis (fixed β strategy) at α_No.4

F. Stability results at α_No.2 and α_No.3

Typical stability results at two off-design points of α_No.2 and α_No.3 are summarized in this Appendix.

Figures F-1(a) and (b) show chordwise pressure coefficient (Cp), boundary layer thickness (δ) distributions and crossflow velocity profiles at several chordwise locations at inner and outer wing regions, corresponding to those off-design points. As the angle of attack of the NEXST-1 airplane decreases from the design point, maximum of CF velocity generally increases. According to such situation, N factors with envelope strategy also increase as shown in Figs. F-2.

Figures F-3(a) and (b) show the results computed with fixed β strategy and reveal the nature of the instability responsible for transition. From these figures, CFI was dominant at measured transition location except for tip region (y/s=0.9) at both α_No.2 and α_No.3 cases. Therefore, for the off-design points, the transition line is very close to the leading edge.

Finally, some comparisons of measured transition data and N contours are summarized in Fig. F-4(a) for α_No.2 case and Fig. F-4(b) for α_No.3 case. In both figures, N=10 due to envelope strategy is in good agreement with measured transition locations.

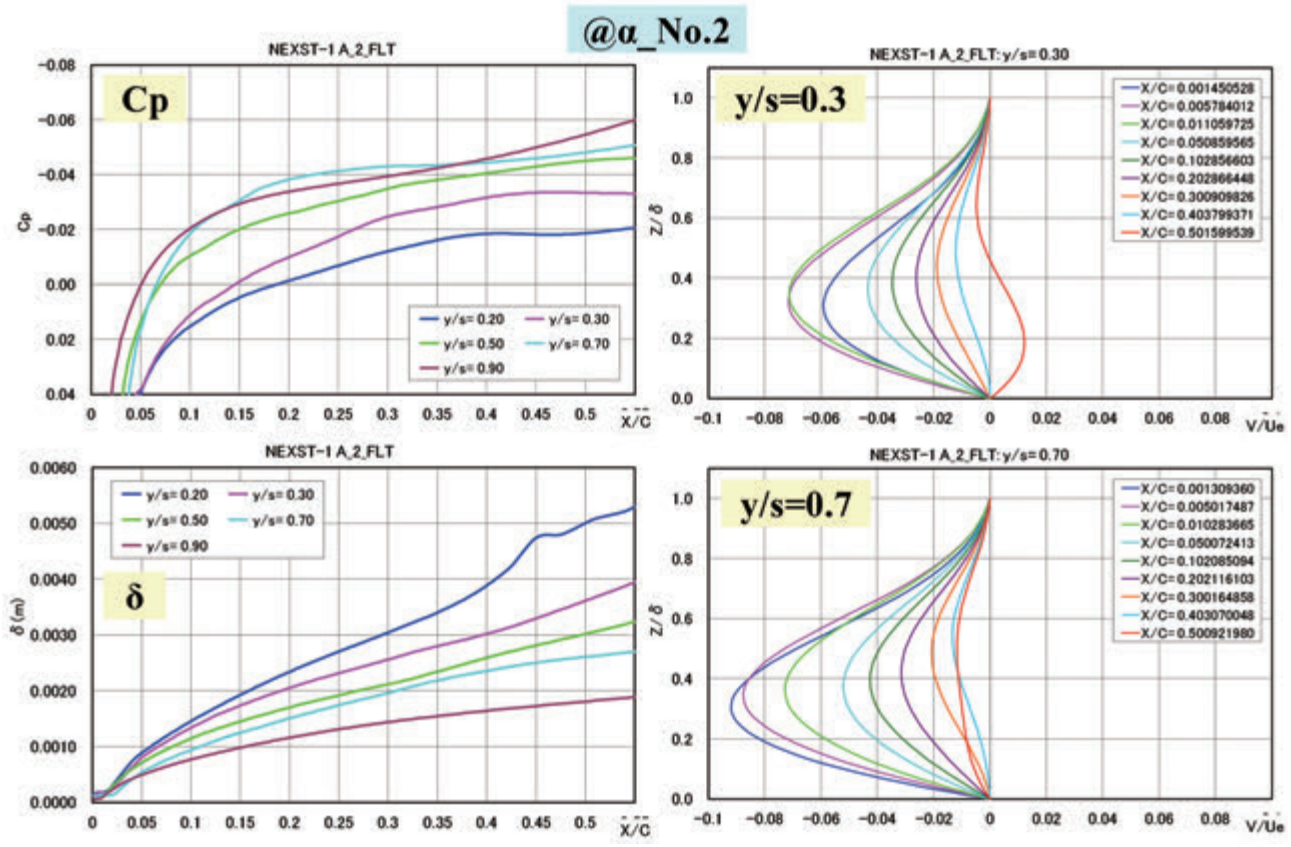

(a) α _No.2 case

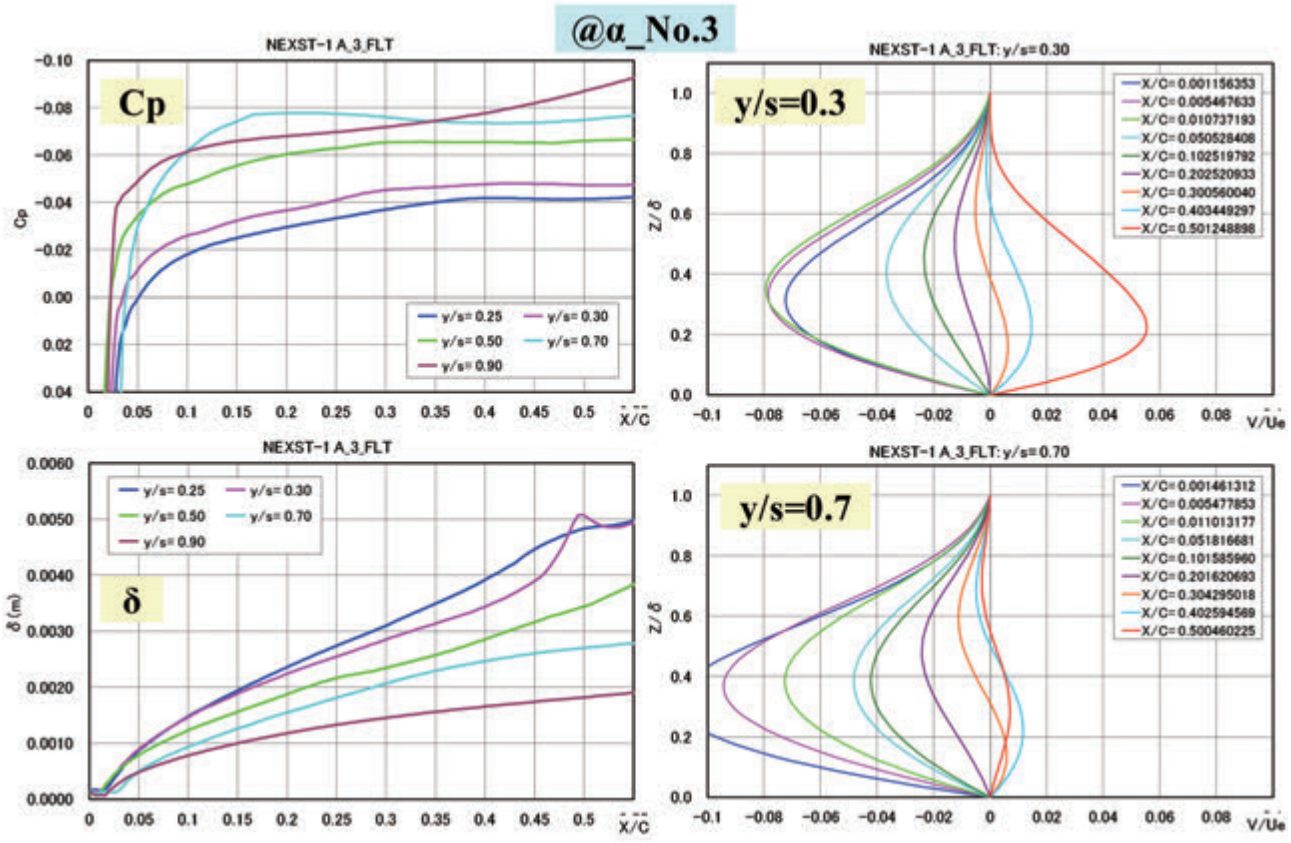

(b) α _No.3 case

Figure F-1. Boundary layer computations at α -sweep cases

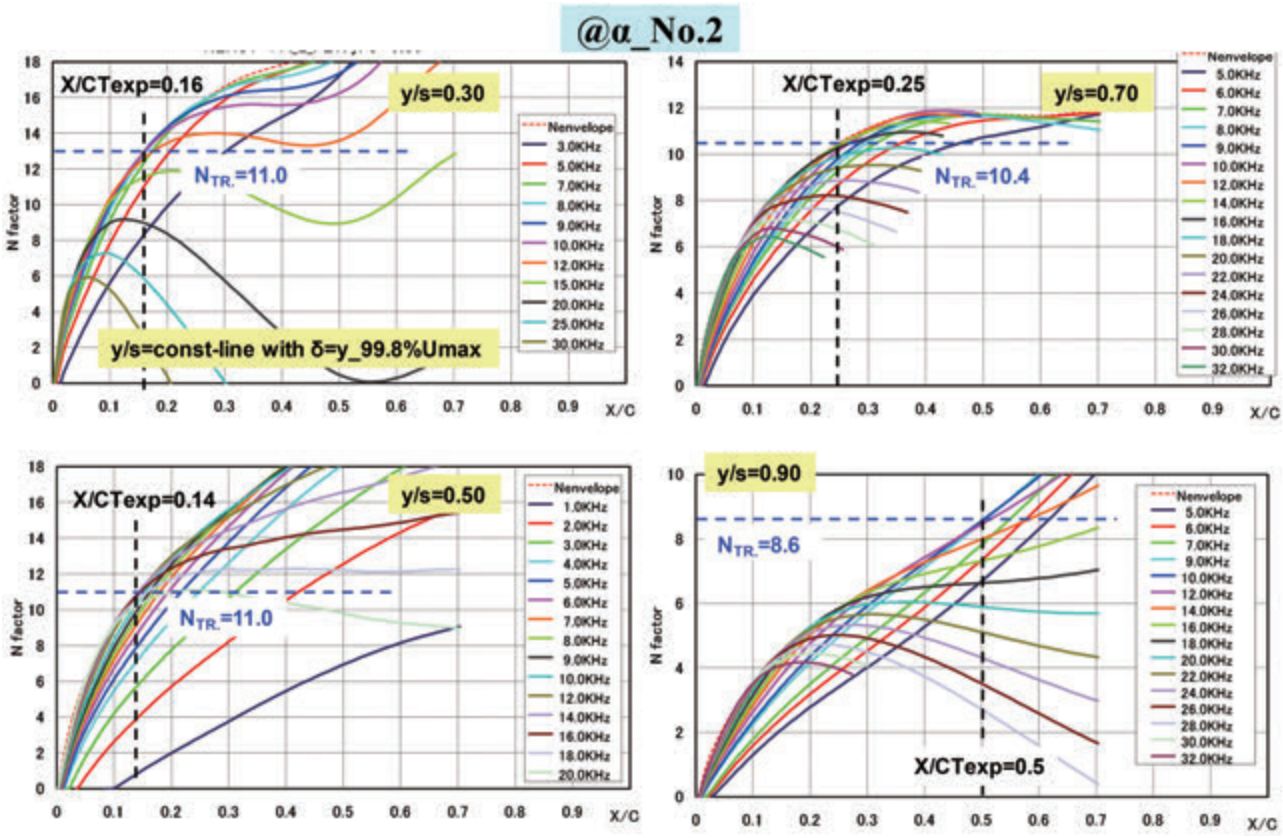

(a) α _No.2 case

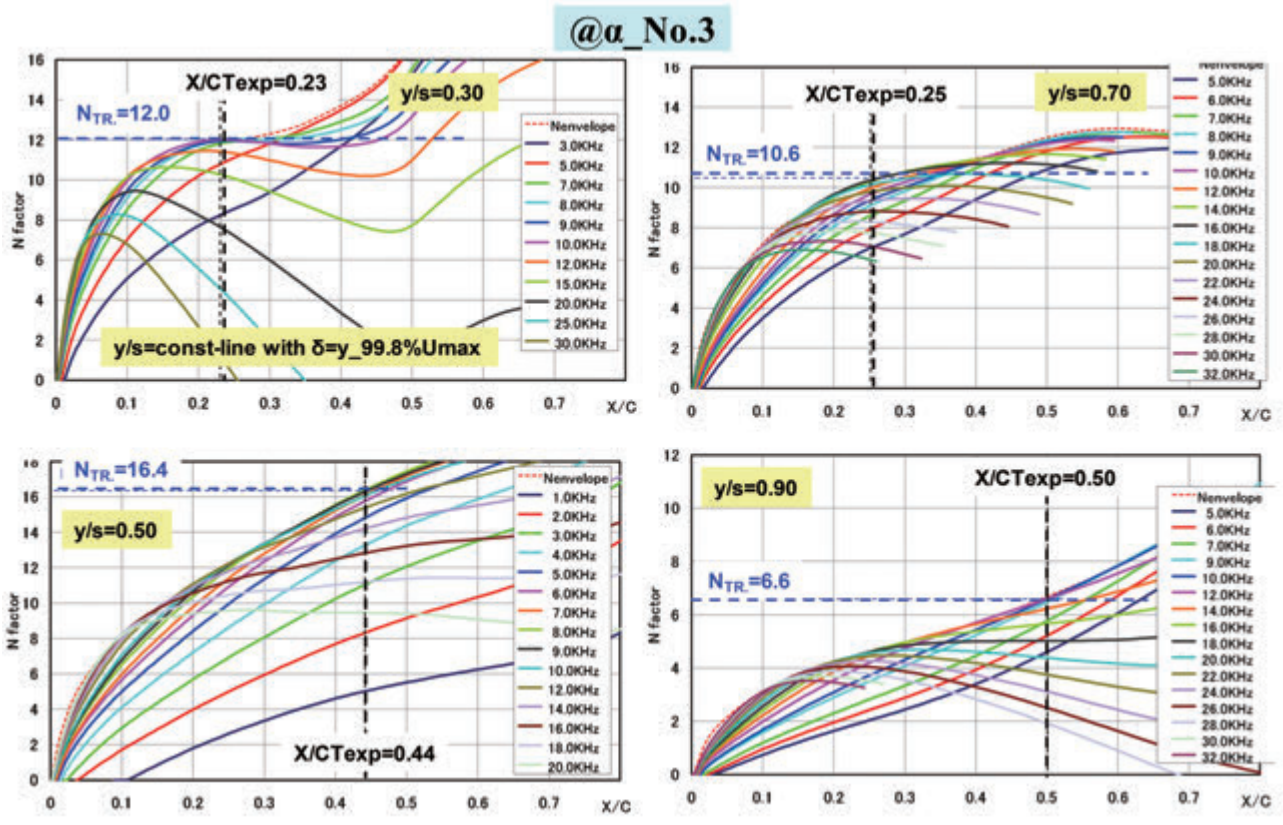

(b) α _No.3 case

Figure F-2. Stability results (envelope strategy) at off-design points

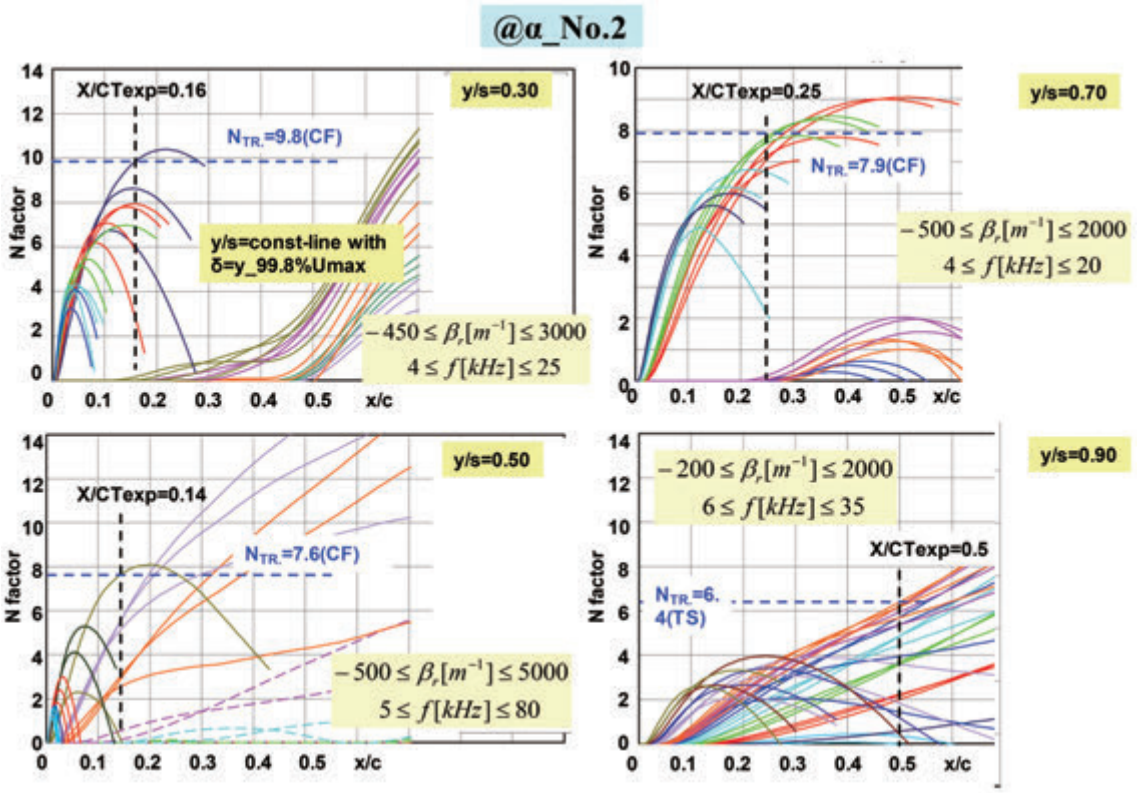

(a) α_No.2 case

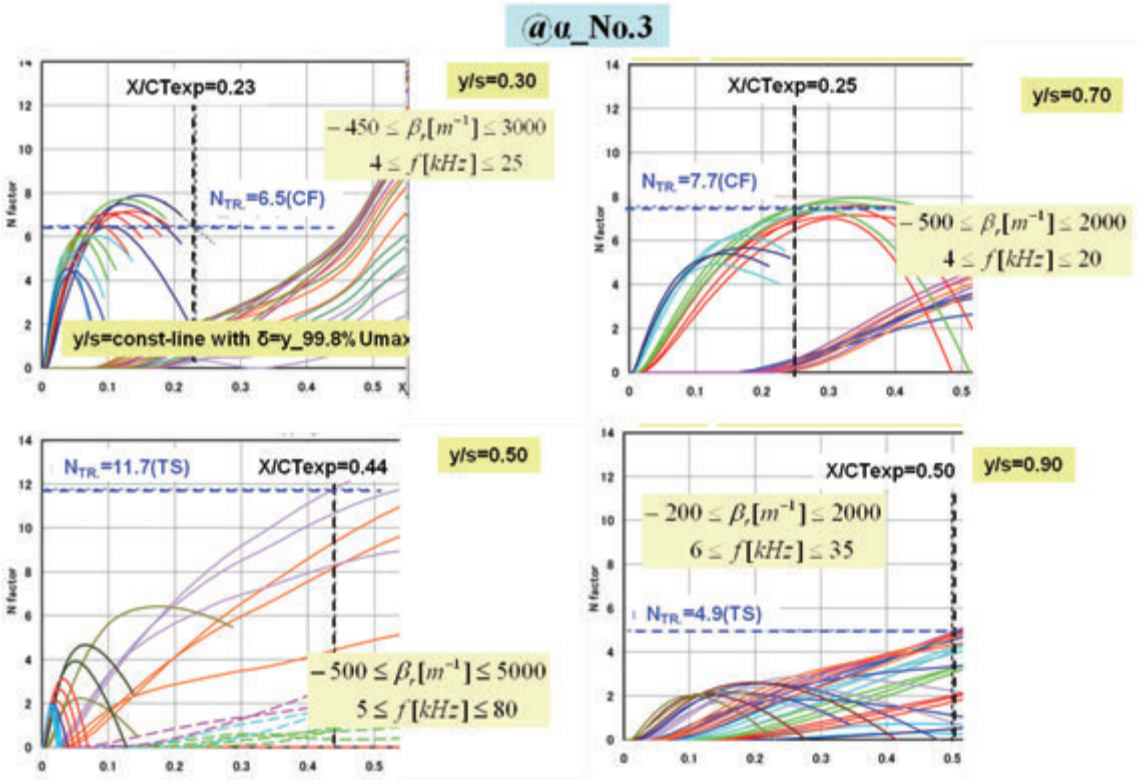

(b) α_No.3 case

Figure F-3. Stability results (fixed β strategy) at off-design points

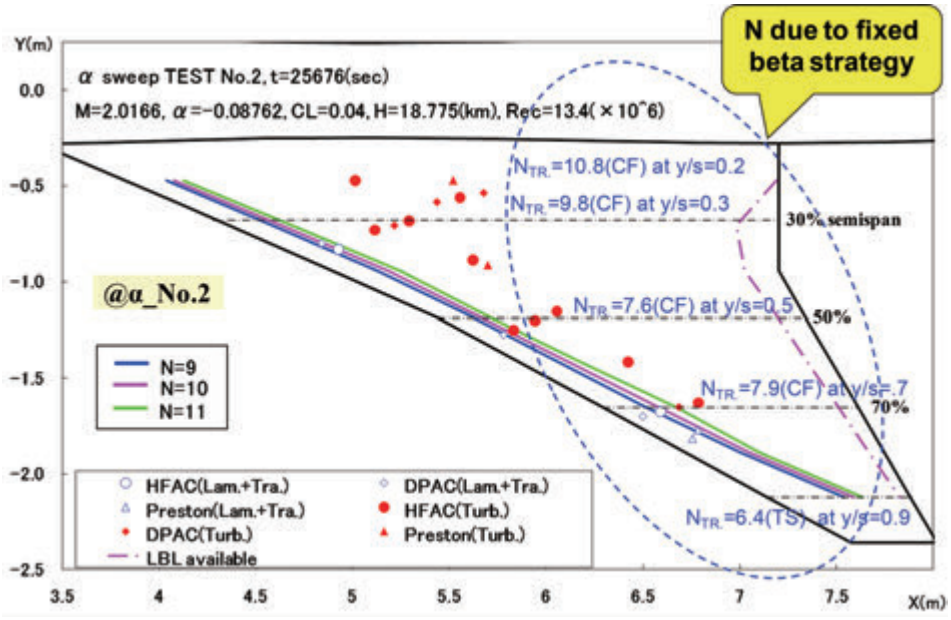

(a) α_No.2 case

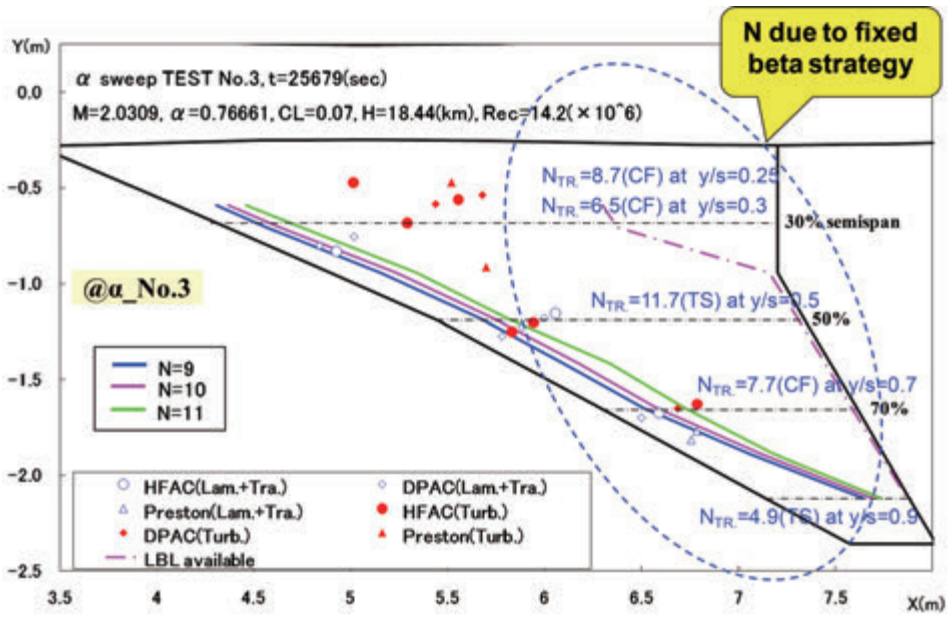

(b) α_No.3 case

Figure F-4. Summary of stability results at off-design points

G. Stability results at y/s=0.5 and 0.9 in the case of Re_No.5

Figures G-1(a) and (b) show the comparisons of crossflow velocity profiles at y/s=0.5 and 0.9 between α_No.4 and Re_No.5. In general, boundary layer theory leads to no Reynolds number effect in the shape of crossflow velocity profiles normalized with boundary layer thickness and edge velocity, that is z/δ vs. V/Ue, and Reynolds number effect only appears in the boundary layer thickness δ distribution. Figure G-1(a) and (b) clearly show such situation.

Stability results computed with both envelope and fixed β strategies at y/s=0.5 and 0.9 in the case of Re_No.5 were summarized in Figs. G-2～G-5. Figures G-2 and G-3 show comparisons of N factors and propagation direction angles (Ψ) corresponding to maximum amplified wave computed with envelope strategy by ONERA and JAXA. There is almost good agreement between them, but Ψ is slightly different. The main reason is the same as the one explained in Chapter 2.

Figures G-4 and G-5 show similar comparisons of N factors and propagation direction angles (Ψ) computed with fixed β strategy. There is almost good agreement between them.

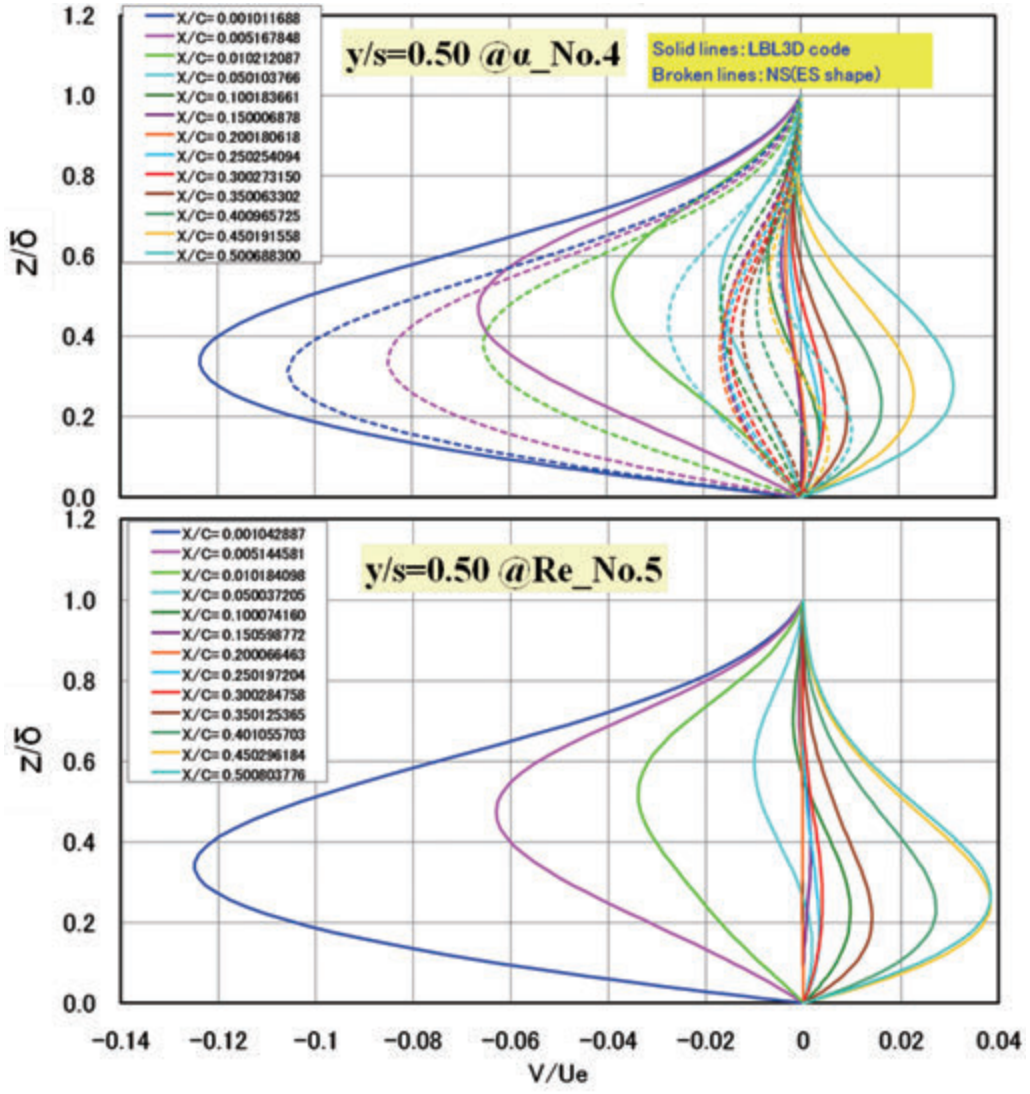

(a) Comparisons of crossflow velocity profiles at y/s=0.5

Figure G-1. Boundary layer computations at Re_No.5

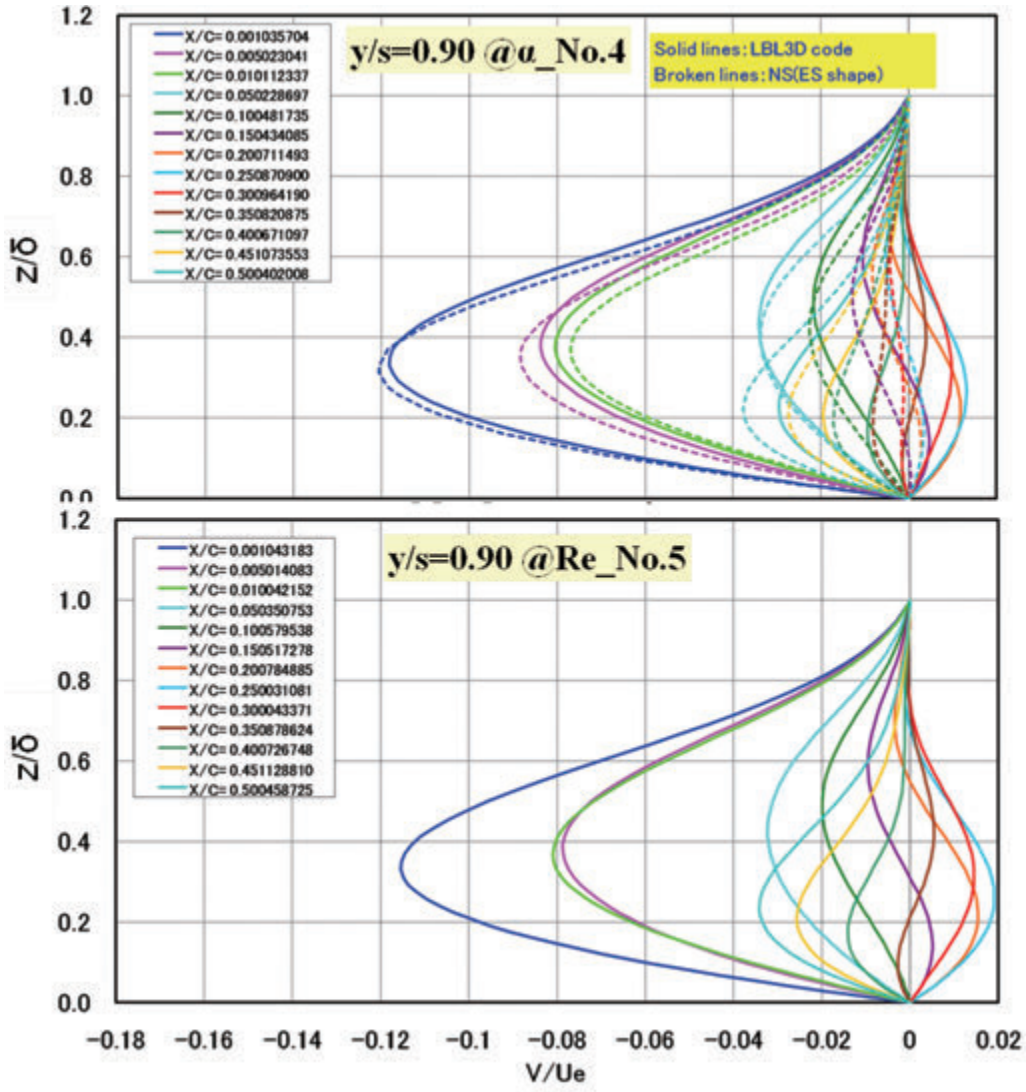

(b) Comparisons of crossflow velocity profiles at y/s=0.9

Figure G-1. Boundary layer computations at Re_No.5

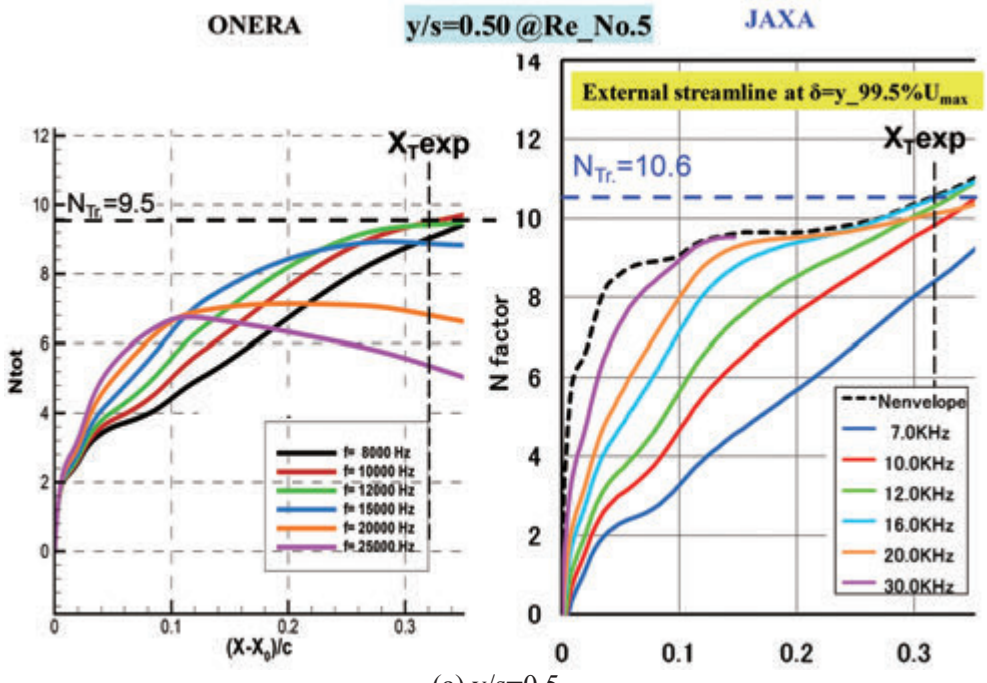

(a) y/s=0.5

Figure G-2. N factors computed with envelope strategy at Re_No.5

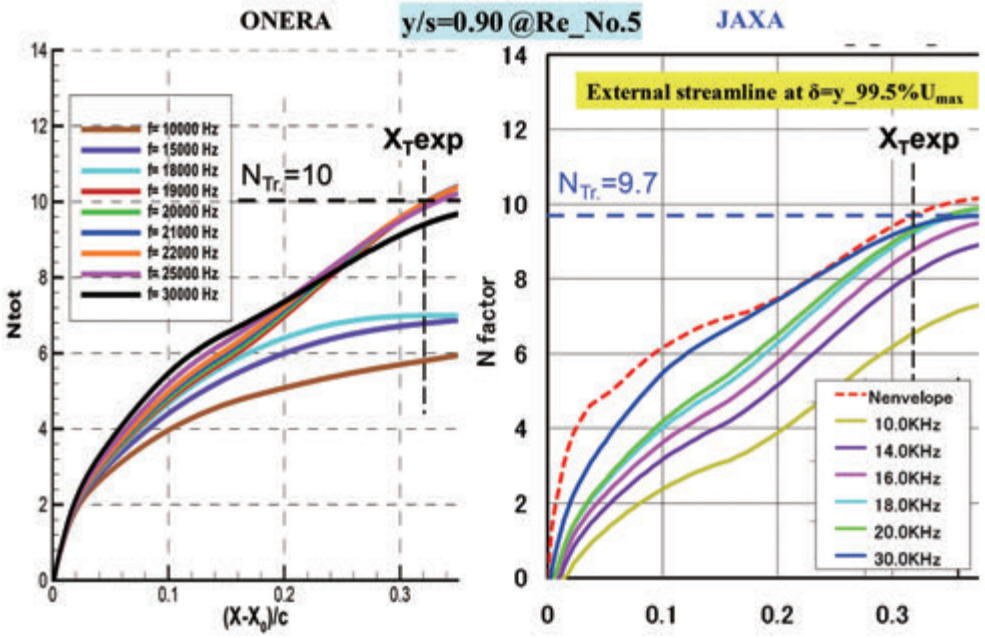

(b) y/s=0.9

Figure G-2. N factors computed with envelope strategy at Re_No.5

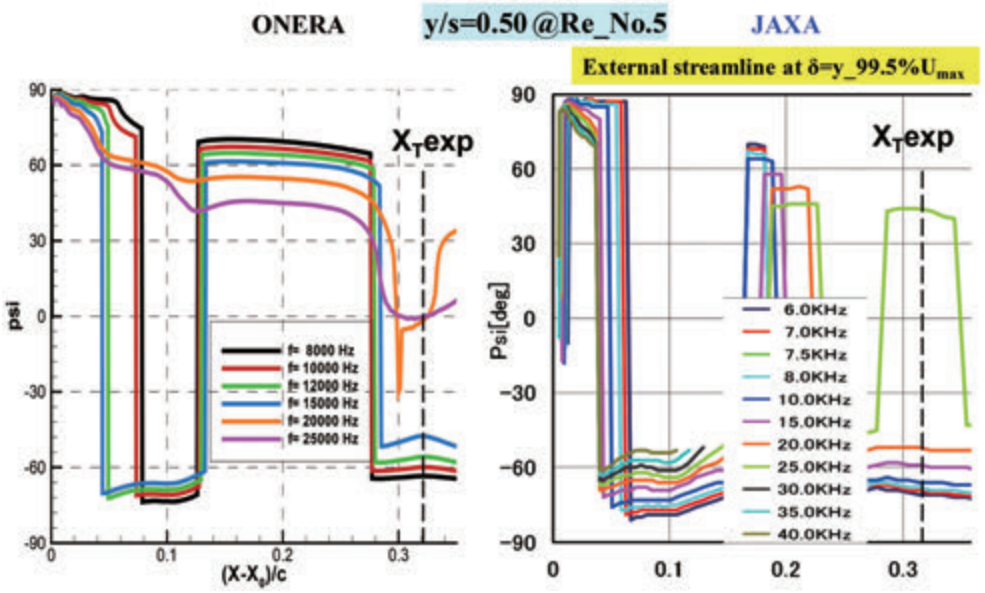

(a) y/s=0.5

Figure G-3. Propagation direction with envelope strategy at Re_No.5

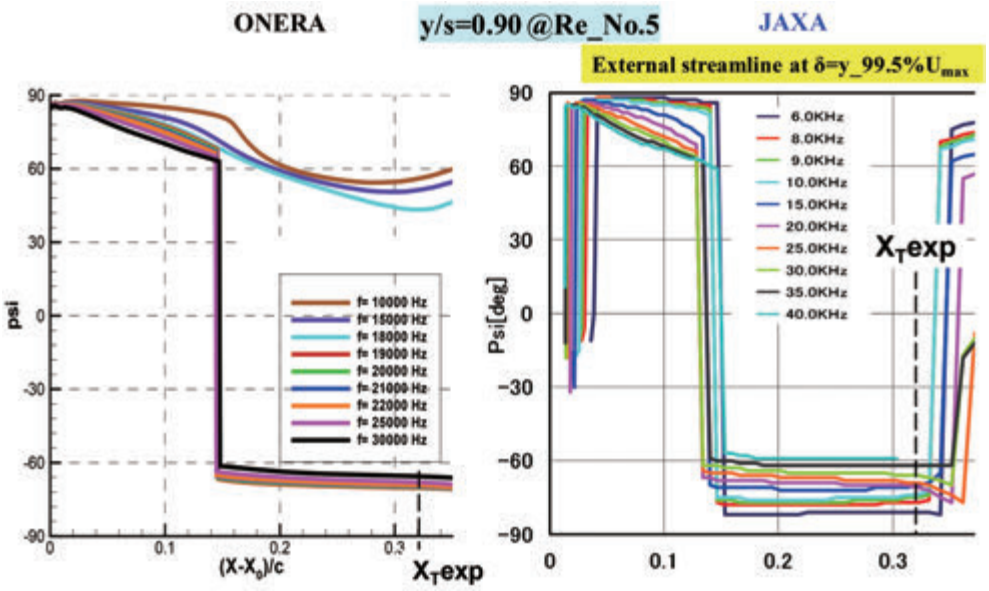

(b) y/s=0.9

Figure G-3. Propagation direction with envelope strategy at Re_No.5

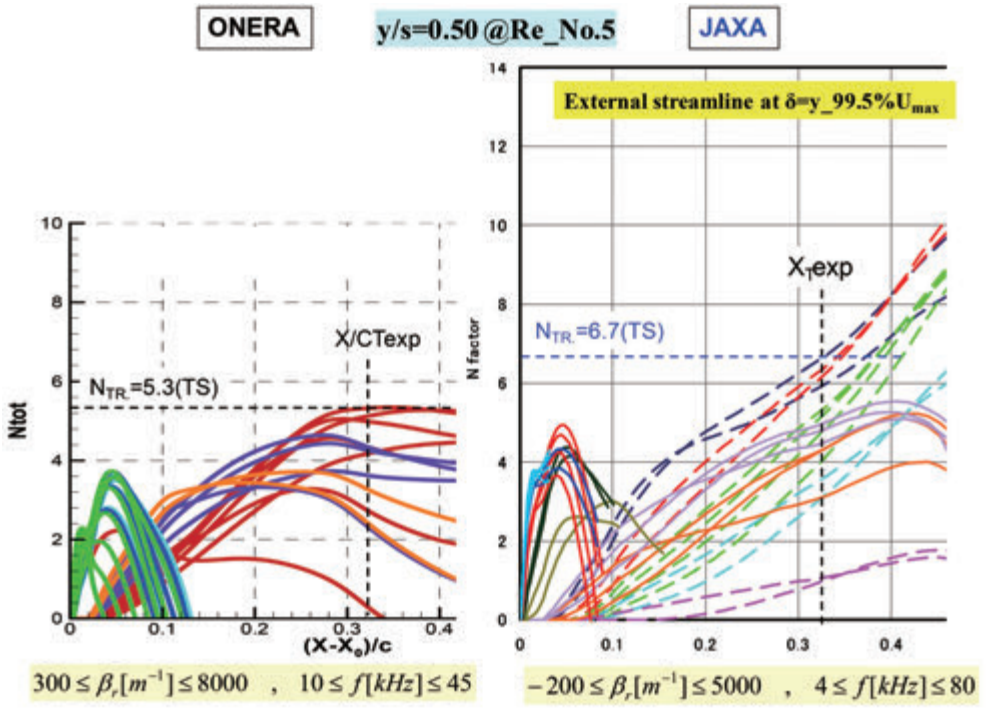

(a) y/s=0.5

Figure G-4. N factors computed with fixed β strategy at Re_No.5

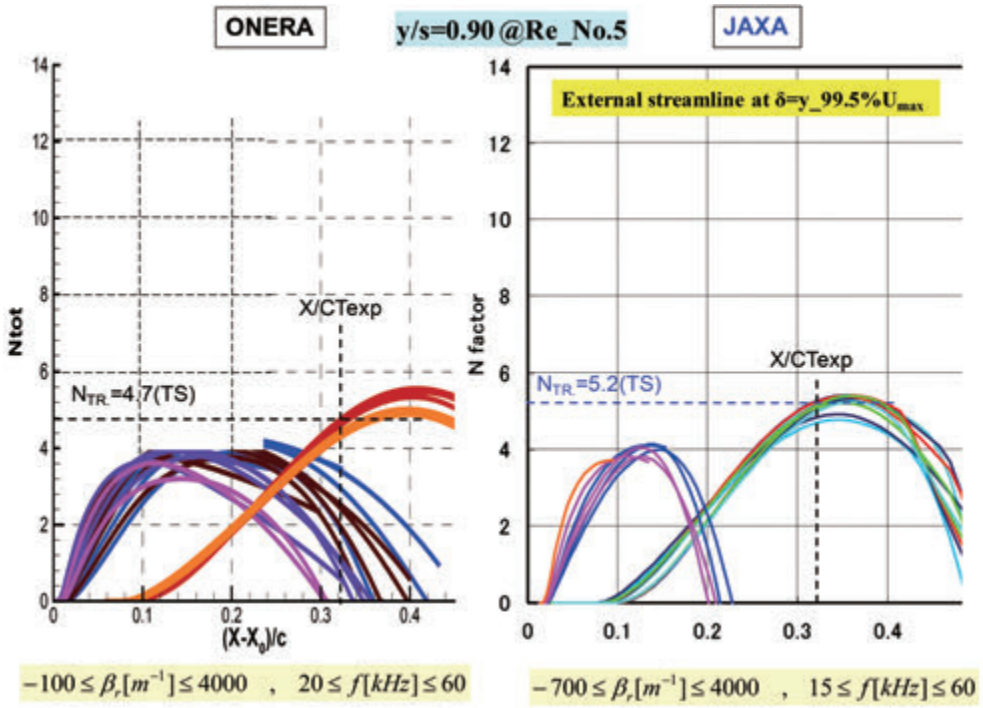

(b) y/s=0.9

Figure G-4. N factors computed with fixed β strategy at Re_No.5

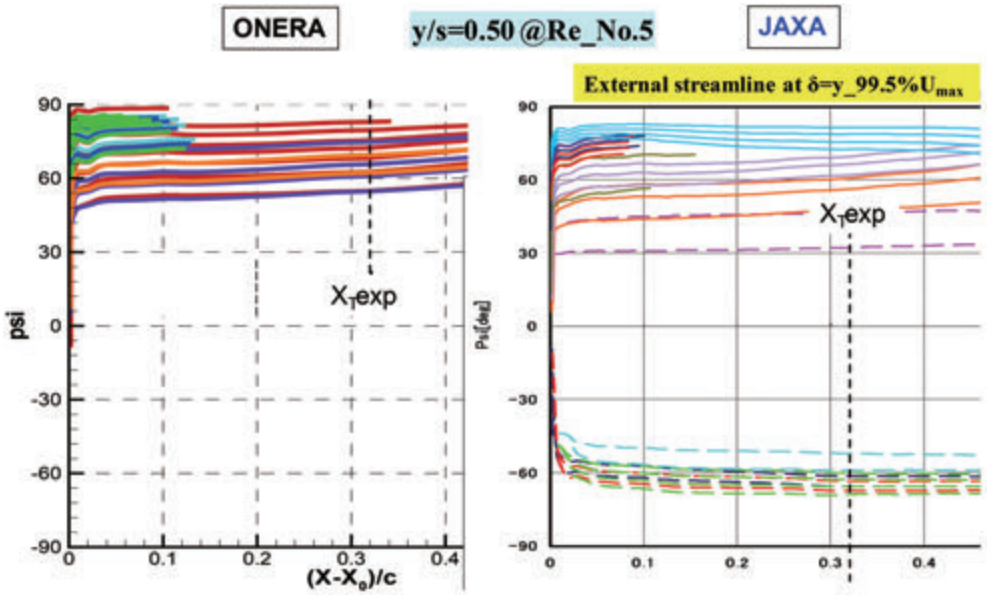

(a) y/s=0.5

Figure G-5. Propagation direction with fixed β strategy at Re_No.5

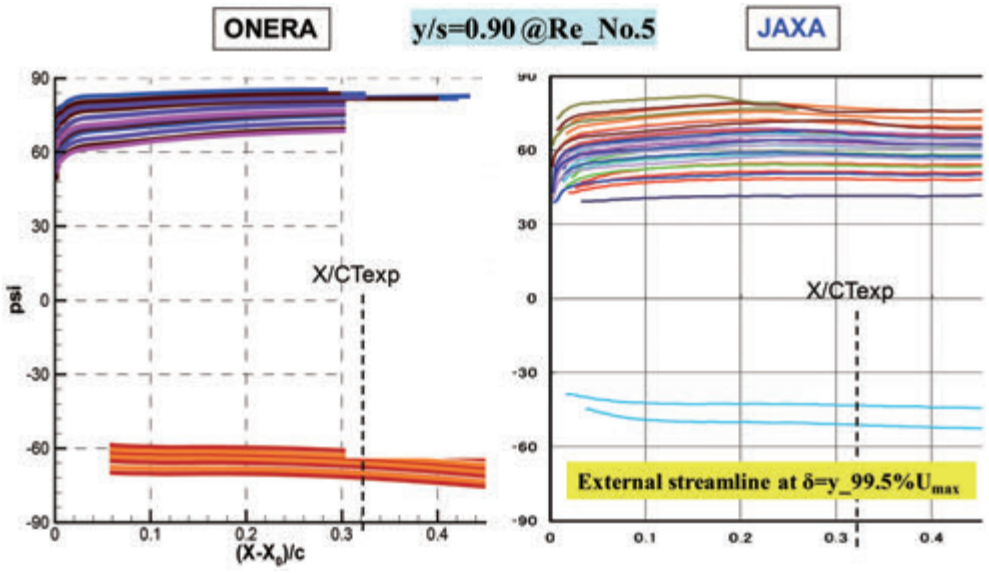

(b) y/s=0.9

Figure G-5. Propagation direction with fixed β strategy at Re_No.5

H. Freestream turbulence level at S2MA measured by JAXA

JAXA conducted transition measurement test of the NEXST-1 configuration at S2MA test facility in 2000. The selection of this facility is the reason why it has lower freestream turbulence level than usual supersonic blow-down type tunnels such as JAXA's supersonic tunnel facility, because of its circuit-driven type tunnel. The turbulence level was already measured and reported by ONERA. In addition, JAXA also independently investigated its freestream turbulence level by using total pressure fluctuation data measured with a pitot probe as illustrated in Fig. H-1. The comparison of JAXA's data and ONERA's data (as indicated in Fig. H-4) is summarized in Fig. H-2. Although JAXA obtained higher turbulence level than ONERA's measured one, relatively lower level possible for meaningful transition measurement test than JAXA's tunnel was confirmed. Figure H-3 explains a procedure to transform from measured total pressure fluctuation to static pressure fluctuation, under a few assumptions of isentropic flow process and normal shock relation.

In general, transition is strongly influenced by freestream turbulence level as well as surface

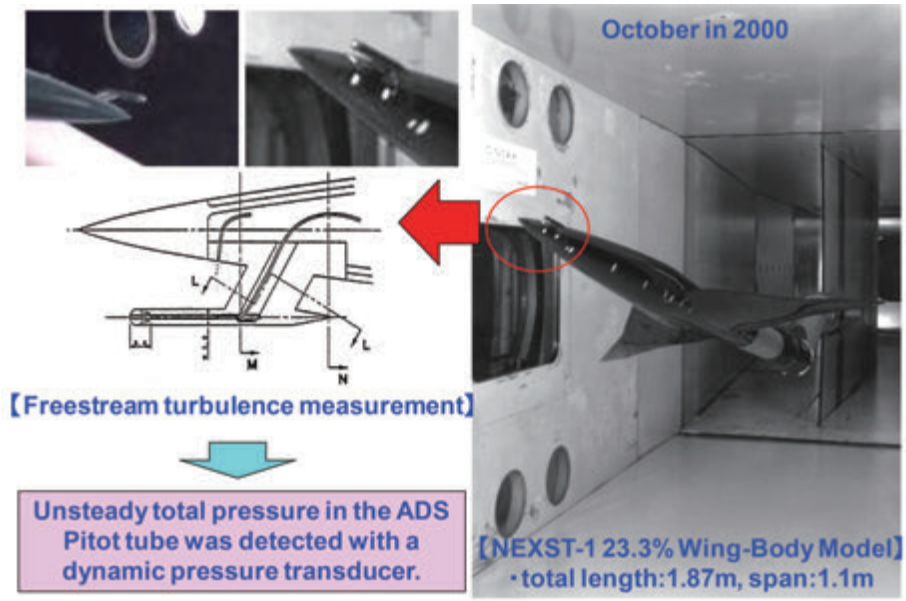

Figure H-1. Measurement technique of freestream turbulence at S2MA

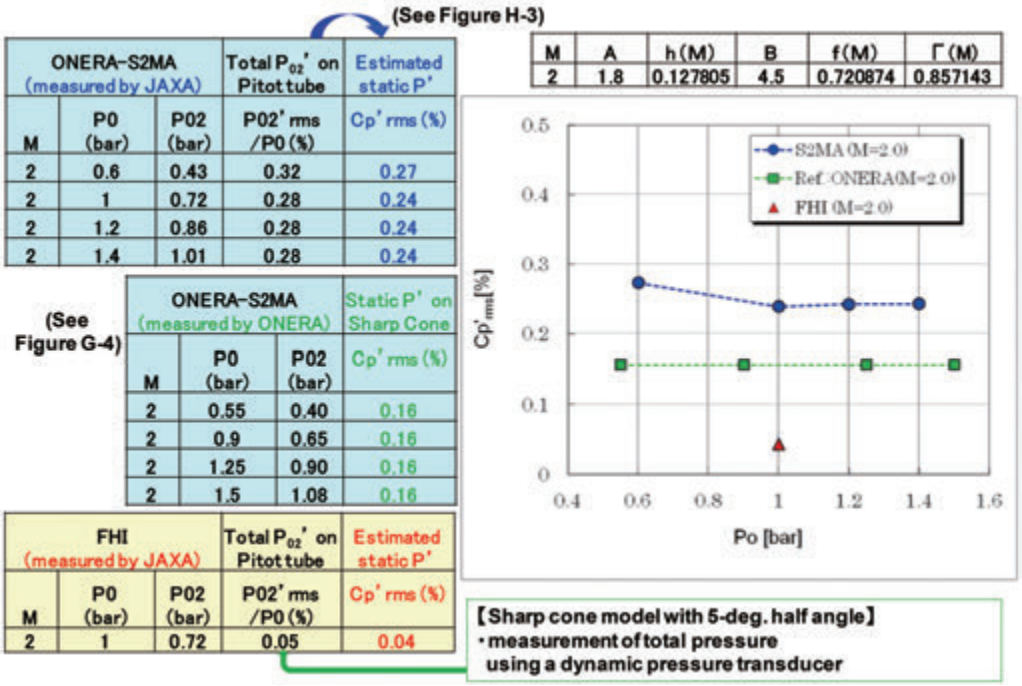

Figure H-2. Comparison of measured data by JAXA and ONERA

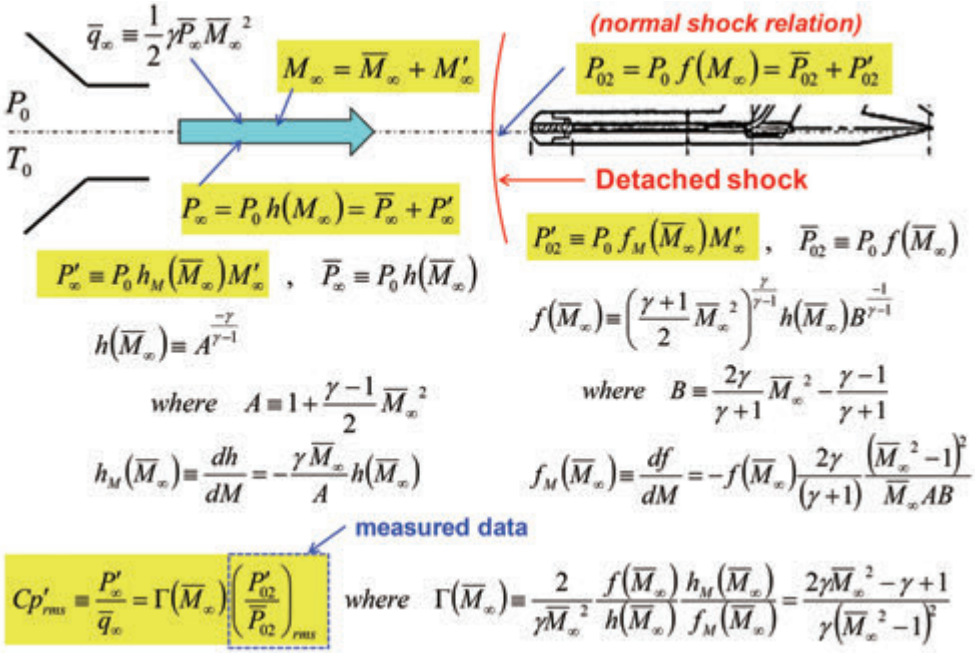

Figure H-3. Relation between static and total pressure fluctuations

roughness. The transition N factor also depends on the level. As already well-known, a relation between that N_T and turbulence level (Tu) was proposed by Mack as described by the relation (1) in Chapter 3 and shown in Fig. H-5. But, this relation was derived under the assumption of incompressible flow condition, that is, low speed flow condition. Unfortunately, a similar effective relation has never derived in supersonic flow condition. Therefore, JAXA tried to make such a relation using both transition data presently obtained at S2MA and previously obtained at another wind tunnel facility of FHI. Here FHI tunnel has remarkably low freestream turbulence level, because it is always operated as in-draft driven type. However, Reynolds number achieved in this tunnel is relatively

- From « Qualification of the supersonic test section of S2MA with a 10° CEAT sharp cone made in Ureol » in French. PV d'Essai ONERA n° 6/1721 (1992)

M	Pi [bar]	Re_{unit}	Tu (10^{-3})	Cp' (10^{-3})
2	0.55	6.80	1.2	1.53
2	0.9	11.06	1.45	1.55
2	1.25	15.20	1.96	1.55
2	1.5	17.80	1.87	1.55

Turbulence intensity may be more importante than noise level

If Tu=0.196%, Nt=6.5 according to Mack relation. Still higher than measurements (Figure H-6 gives Nt≈4.5)

Figure H-4. ONERA measurements in S2MA wind tunnel:noise (p') and turbulence (Tu').

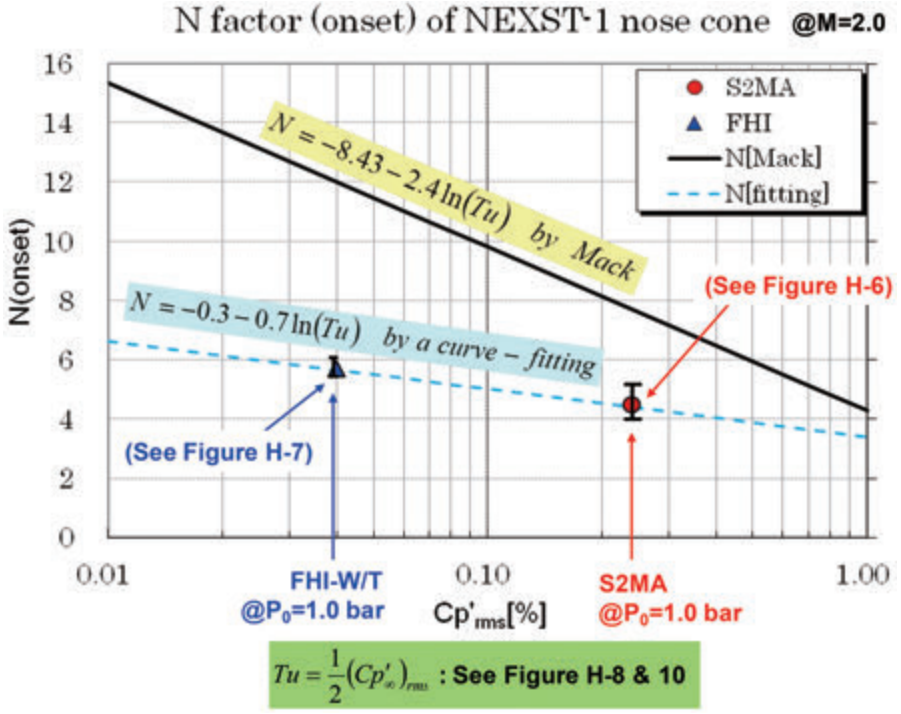

Figure H-5. N factors and pressure fluctuation on the nose cone at W/T tests

low.

JAXA measured transition location of the NEXST-1 nose cone at S2MA and FHI. The summarized results are shown in Figs. H-6 and H-7 respectively. Based on them taking account of measurement error bar, JAXA tried to propose an approximated relation between the N_T and Cp'_{rms} as indicated in Fig. H-5. Here, the relation between freestream turbulence level (Tu) and static pressure fluctuation (Cp'_{rms}) must be estimated to make such a relation. At incompressible case, it is very easy to find out it as shown in Fig. H-10. At compressible case, if Tu is defined as velocity fluctuation only, it is also easy to find the same relation as for the incompressible case as shown in Fig. H-8. But, if Tu is defined as mass fluctuation, it is slightly com-

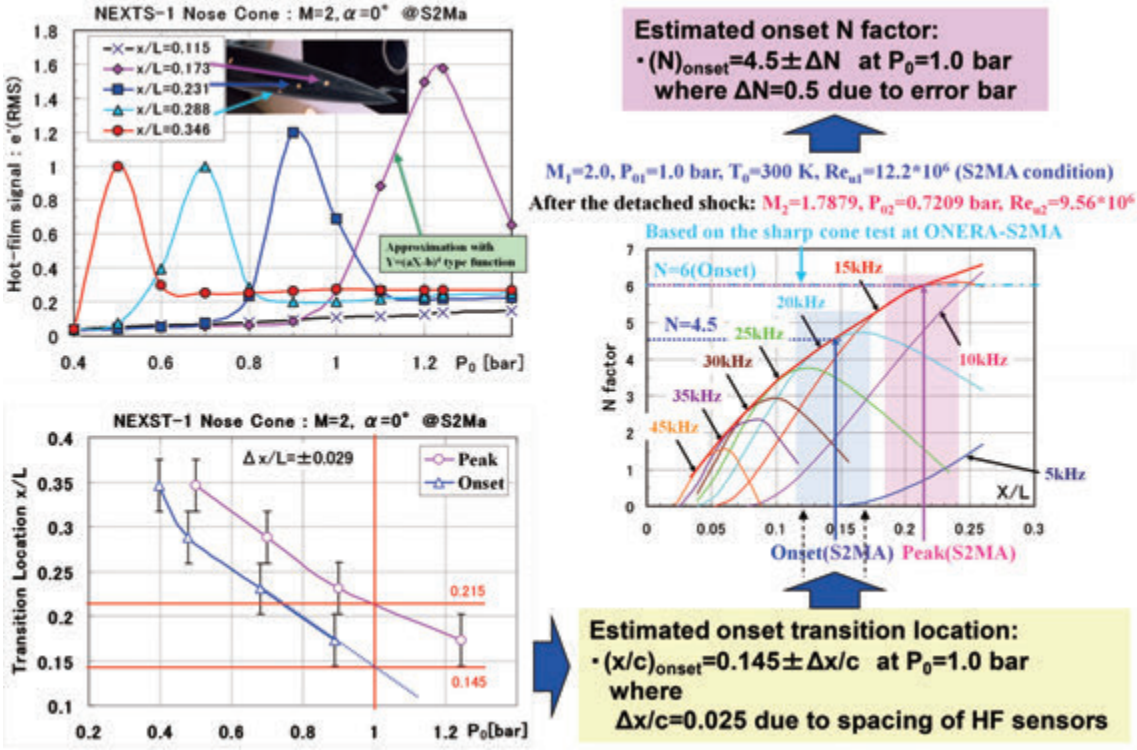

Figure H-6. HF test on NEXST-1 nose cone at S2MA

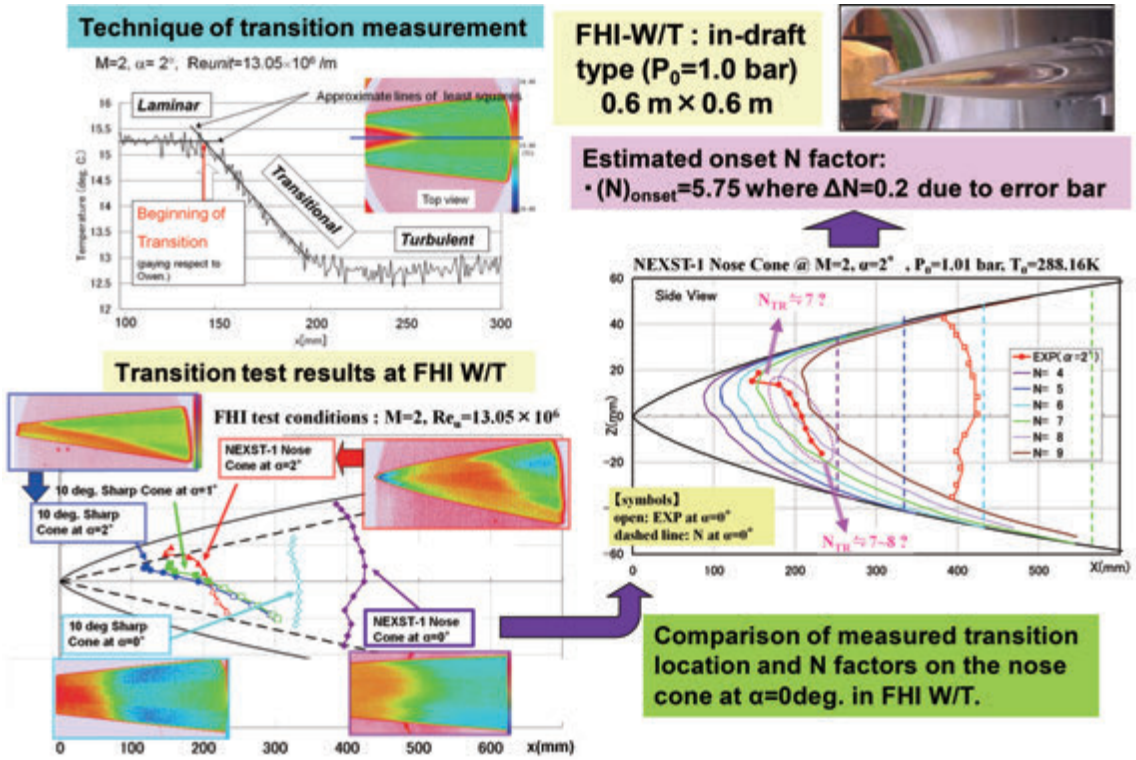

Figure H-7. IR test on NEXST-1 nose cone at FHI

plicated shown in Fig. H-9. M=2 condition generates compressible Tu (defined in Fig. H-9) which becomes three times as incompressible Tu (defined in Fig. H-10).

Finally, compressible Tu based on mass fluctuation has an inherent problem at M=1, because the Tu=0 even though there are any static pressure fluctuations. This relation is mathematically exact, but it is supposed that its relation is only applicable except for near M=1. If the compressible relation $Tu = \frac{1}{2}\left|\overline{M}_\infty^{\,2} - 1\right|(Cp'_\infty)_{rms}$ is used, comparison with Mack relation will be improved. Aa a matter of fact, $(Cp'_\infty)_{rms}$ = 0.25% (S2MA at M=2 measured by JAXA) means Tu=0.375%. Using Mack relation, $N = -8.43 - 2.4\ln(Tu)$, this provides N=4.97. This value is not far from experimental measurements Nt=4.5 of Fig. H6.

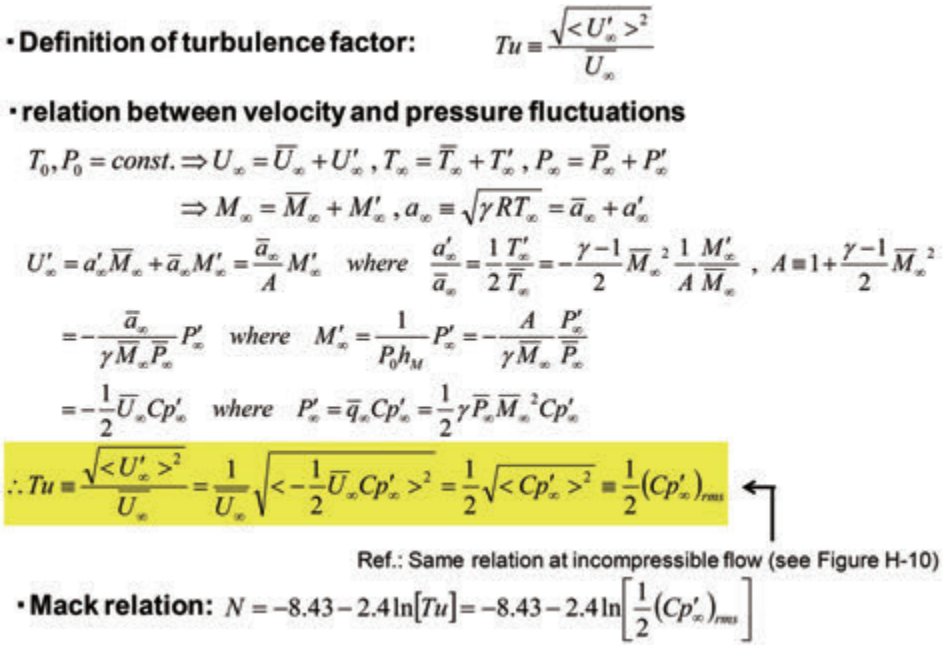

Figure H-8. Consideration of Mack relation

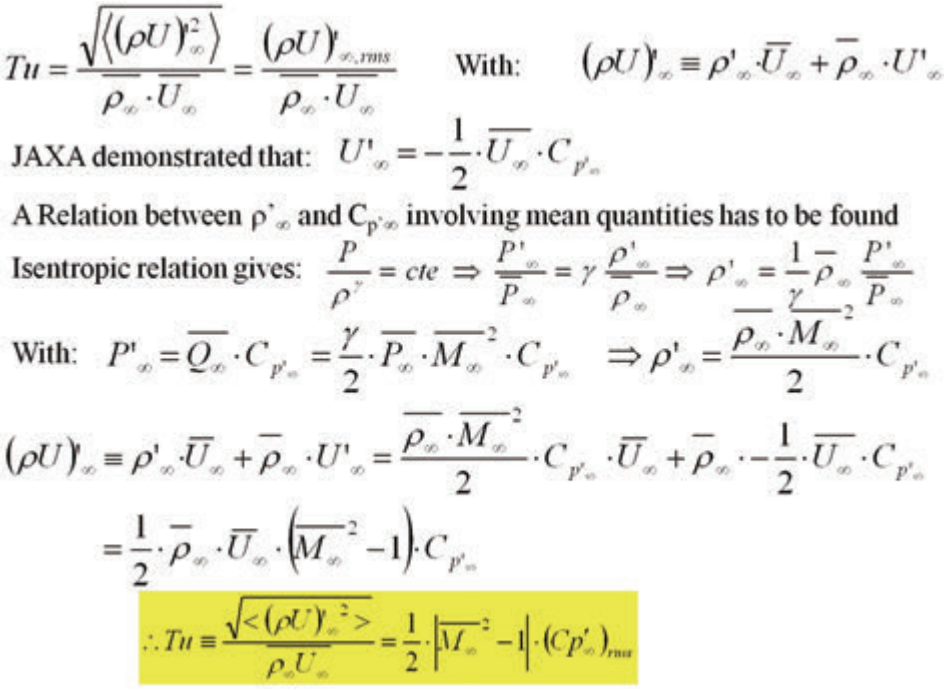

Figure H-9. Taking into account compressibility effects in Tu definition

$$P_\infty + \frac{1}{2}\rho_\infty U_\infty^{\,2} = const. \equiv P_0 \quad where \quad \rho_\infty = const. \quad (\because incompressible)$$

$$P_0 = \overline{P}_\infty + P'_\infty + \frac{1}{2}\rho_\infty\left(\overline{U}_\infty + U'_\infty\right)^2 = \overline{P}_\infty + P'_\infty + \frac{1}{2}\rho_\infty \overline{U}_\infty^{\,2}\left(1+\frac{U'_\infty}{\overline{U}_\infty}\right)^2$$

$$\approx \overline{P}_\infty + P'_\infty + \frac{1}{2}\rho_\infty \overline{U}_\infty^{\,2}\left(1+2\frac{U'_\infty}{\overline{U}_\infty}\right) = \overline{P}_\infty + P'_\infty + \frac{1}{2}\rho_\infty \overline{U}_\infty^{\,2} + \rho_\infty \overline{U}_\infty U'_\infty$$

$$P'_\infty + \rho_\infty \overline{U}_\infty U'_\infty = 0 \quad \Rightarrow \quad P'_\infty = -\rho_\infty \overline{U}_\infty U'_\infty$$

$$Cp'_\infty \equiv \frac{P'_\infty}{\overline{q}_\infty} = \frac{P'_\infty}{\frac{1}{2}\rho_\infty \overline{U}_\infty^{\,2}} = -2\frac{U'_\infty}{\overline{U}_\infty} \quad \Rightarrow \quad U'_\infty = -\frac{1}{2}\overline{U}_\infty Cp'_\infty$$

$$\therefore Tu \equiv \frac{\sqrt{<U'^2_\infty>}}{U_\infty} = \frac{1}{U_\infty}\sqrt{<-\frac{1}{2}\overline{U}_\infty Cp'_\infty>^2} = \frac{1}{2}\sqrt{<Cp'^2_\infty>} \equiv \frac{1}{2}(Cp'_\infty)_{rms}$$

Figure H-10. Incompressible relation between velocity and pressure fluctuation

I. Summary of hot-film test data at S2MA

The whole data measured with multi-element type hot-film (HF) are summarized in this Appendix. Figures I-1(a) and (b) show chordwise output signal of each HF element at inner and outer wing region in the cases of several AOA conditions at P_0=0.6 bar. For high total pressure values P_0=1 and 1.4 bar, Figs. I-2 and I-3 show the same summarized results as for P_0=0.6.

JAXA approximately defined transition location as the location where AC signal reached its maximum value as shown in those figures, except for P_0=1.4 bar.

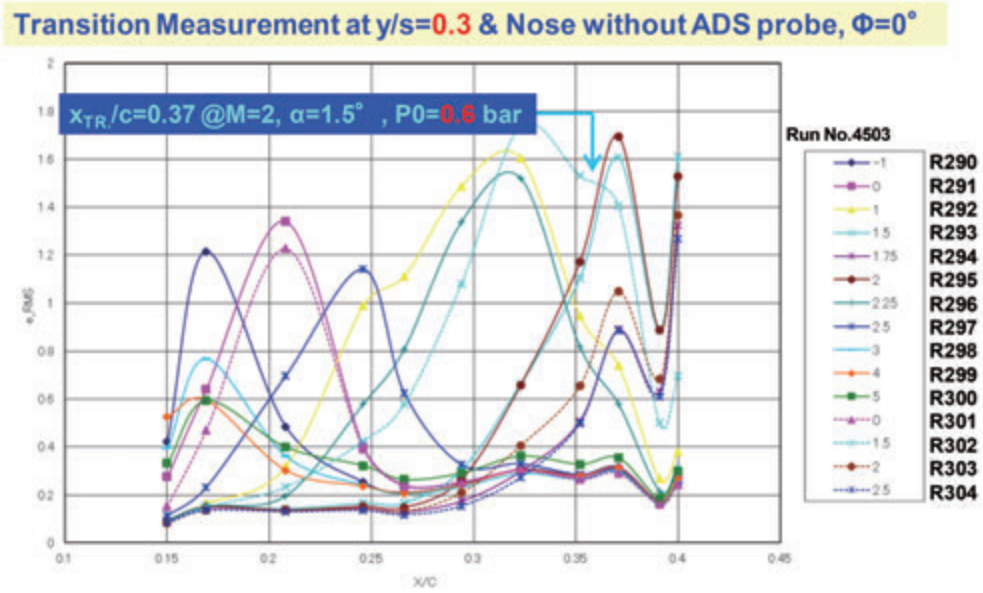

(a) y/s=0.3

Figure I-1. Hot-film test results at P0=0.6 bar at S2MA test

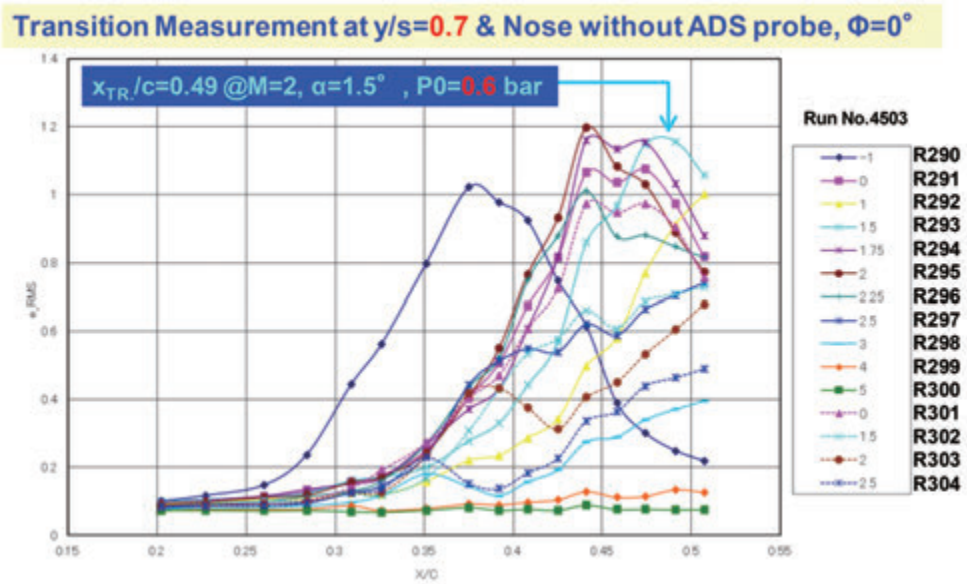

(b) y/s=0.7

Figure I-1. Hot-film test results at P0=0.6 bar at S2MA test

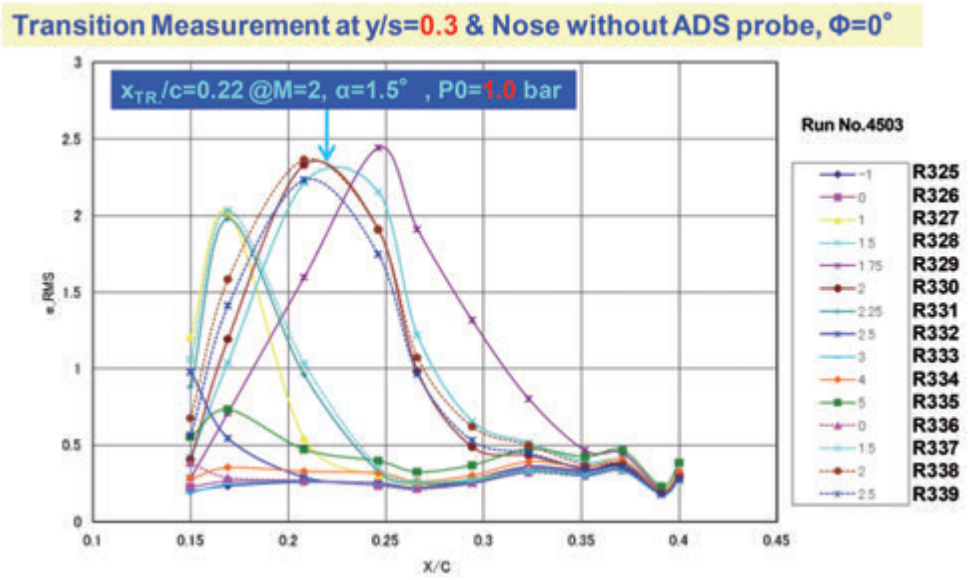

(a) y/s=0.3

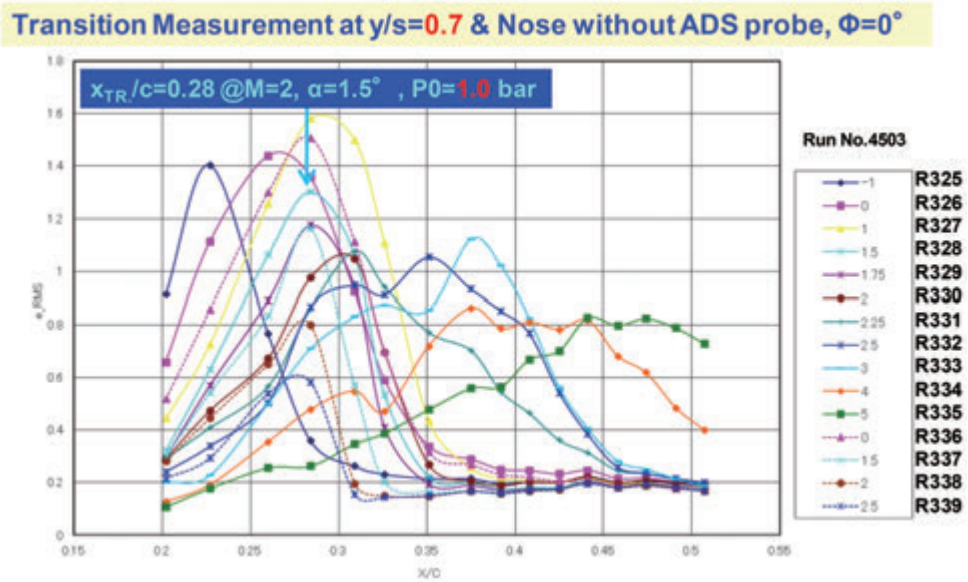

(b) y/s=0.7

Figure I-2. Hot-film test results at P0=1.0 bar at S2MA test

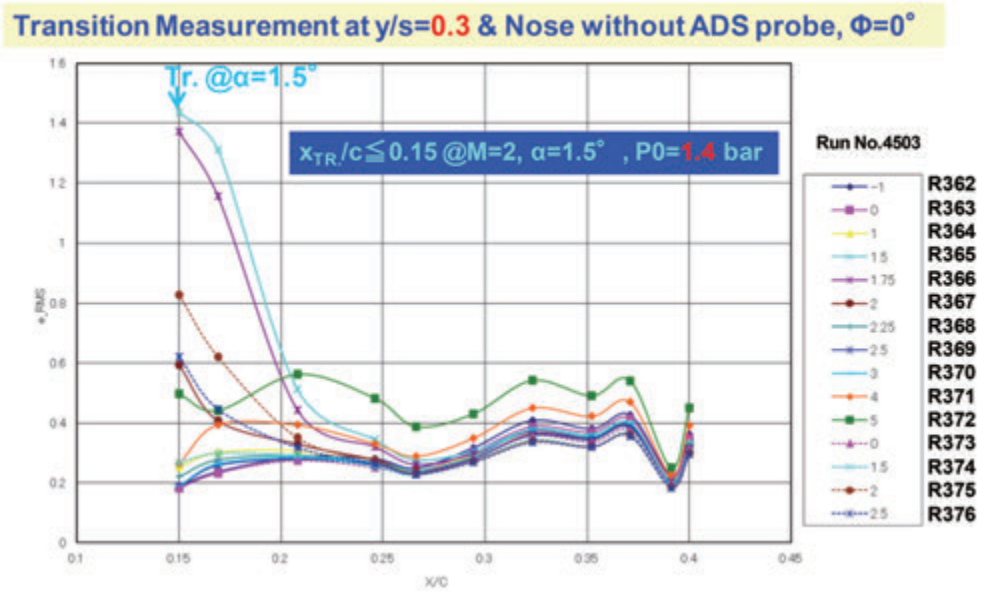

(a) y/s=0.3

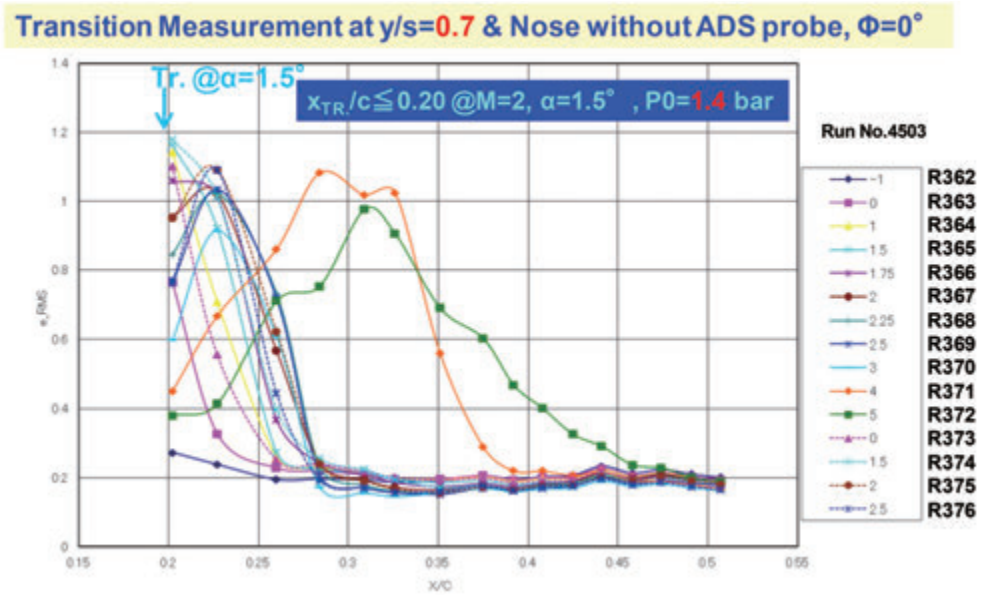

(b) y/s=0.7

Figure I-3. Hot-film test results at P0=1.4 bar at S2MA test

J. Stability results at y/s=0.5 in the case of P_0=0.6 bar

ONERA and JAXA also computed representative boundary layer characteristics at mid-span region (y/s=0.5) in the case of P_0=0.6 bar condition and summarized them in Fig. J-1. Plots corresponds to streamwise velocity profiles, cross-flow velocity profiles, temperature profiles and chordwise thickness distributions (boundary layer thickness δ, displacement thickness δ^*). JAXA's results are in very close agreement with ONERA's results (as mentioned in Chapter 2.)

The evolution of N factors and propagation direction ψ computed with envelope strategy at y/s=0.5 are summarized in Fig. J-2 and J-3 respectively. JAXA's results are in very close agreement with ONERA's ones for each spanwise station mentioned in Chapter 2.

Similar computational results with fixed β strategy at y/s =0.5 are summarized in Fig. J-4 and J-5. Both parties' results were also almost close agreement.

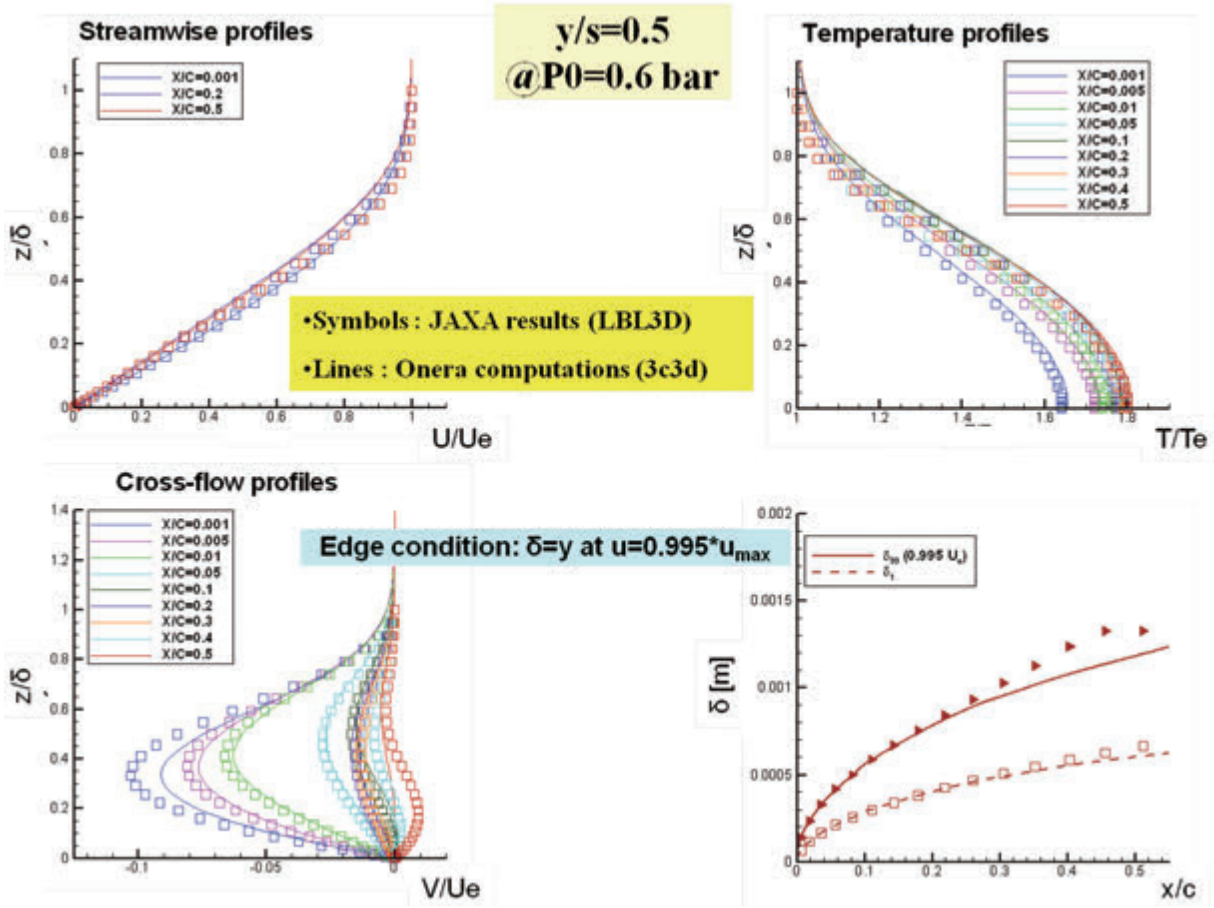

Figure J-1. Boundary layer computations at P0=0.6 bar condition - Mid-span region (y/s=0.5)

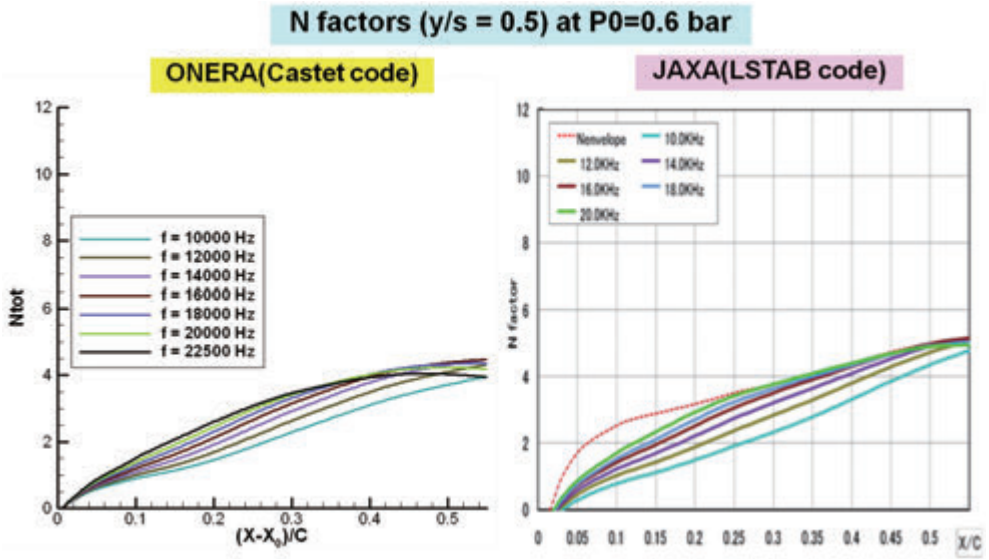

Figure J-2. Comparison of N factor (envelope strategy) at P0=0.6 bar

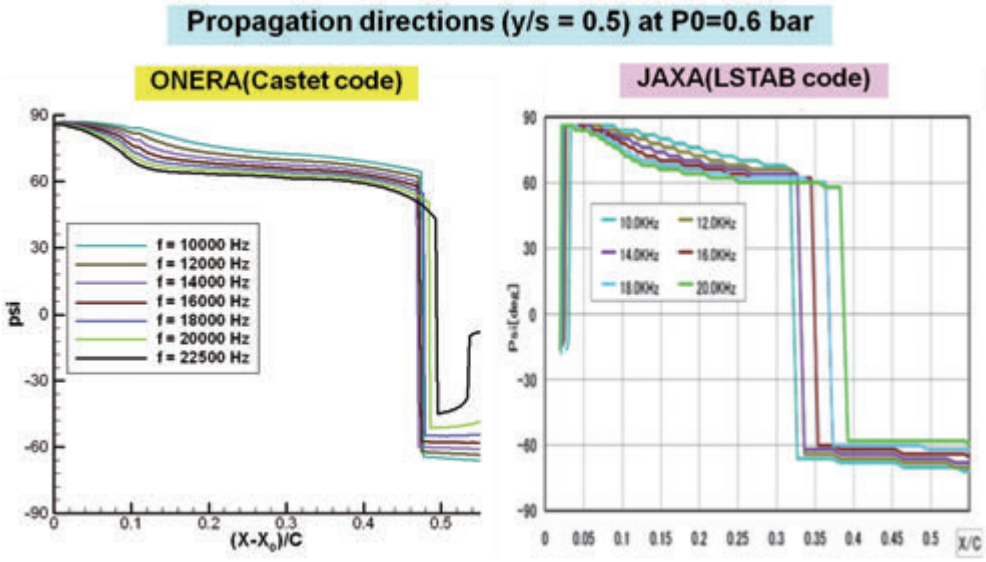

Figure J-3. Comparison of propagation direction (envelope strategy) at P0=0.6 bar

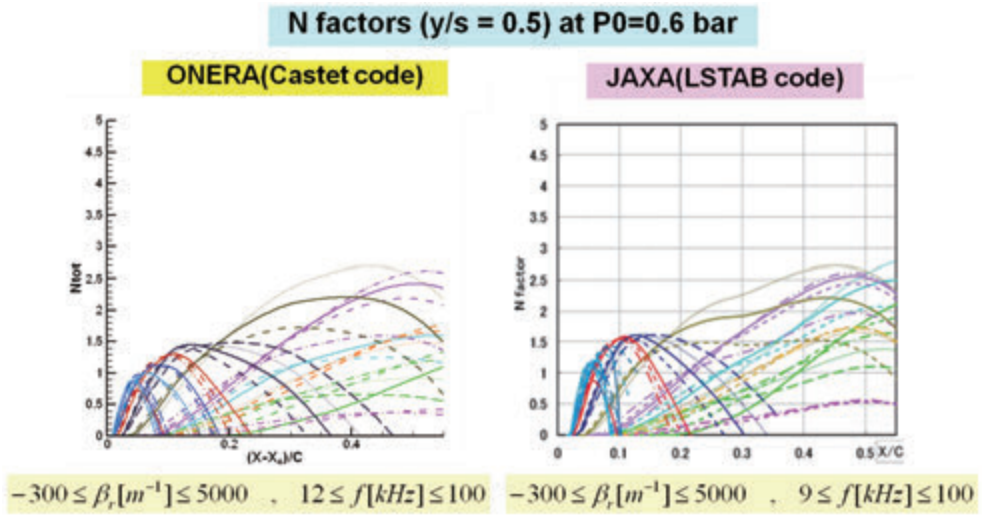

Figure J-4. Comparison of N factor (fixed β strategy) at P0=0.6 bar

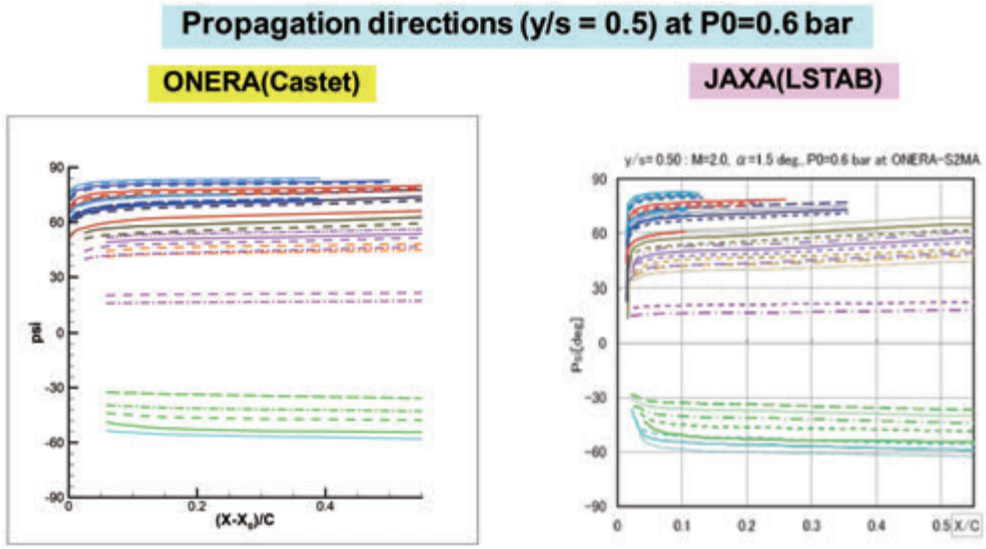

Figure J-5. Comparison of propagation direction (fixed β strategy) at P0=0.6 bar

K. N factors on target Cp distribution computed with envelope and fixed β strategies

JAXA performed lots of stability computations on the target Cp distributions for the NEXST-1 NLF wing design at several Reynolds number conditions as shown in Table K-1. This table is a summary of predicted transition location at y/s=0.3, 0.5 and 0.7 using N=12 for envelope strategy as transition N factor value. Fig. K-1 shows Reynolds number effect on the transition movement predicted with N=12 for envelope strategy.

First of all, as one of trials for analyzing Reynolds number effect on the NLF wing, JAXA investigated Reynolds number influence on numerical transition location predicted with envelope strategy. According to present comparisons of stability results and flight test data, N_{env}=12 as transitional value is used in this study.

Figures K-2(a), (b) and (c) show chordwise N factor evolutions for several Reynolds number conditions at y/s=0.3, 0.5 and 0.7 respectively. Left

Table K-1. Transition location and nature predicted with envelope strategy

NEXST-1 FLT Test		MAC[m]=	2.754	$N_{env,TR}$=		12			
Case No.	Condition	$Re_{\infty u}$[M] (1/m)	Re_{MAC}[M]	y/s=0.3		y/s=0.5		y/s=0.7	
				$(x/c)_{TR}$	Nature	$(x/c)_{TR}$	Nature	$(x/c)_{TR}$	Nature
1	AOA_No.4	5.4	14.9	0.38539	TS	0.47550	TS	0.80000	TS
2	Ps=9KPa	6.6	18.2	0.28908	TS	0.42359	TS	0.80000	TS
3	Ps=9.4KPa	6.9	19.0	0.26820	TS	0.41184	TS	0.80000	TS
4	Ps=9.8KPa	7.2	19.8	0.24058	CF	0.39943	TS	0.80000	TS
5	Ps=10.2KPa	7.5	20.7	0.19507	CF	0.38689	TS	0.80000	TS
6	Ps=10.6KPa	7.8	21.4	0.11145	CF	0.37675	TS	0.80000	TS
7	Ps=11.1KPa	8.1	22.4	0.07438	CF	0.36220	TS	0.80000	TS
8	Ps=11.6KPa	8.5	23.4	0.05852	CF	0.34774	TS	0.80000	TS
9	Ps=12.2KPa	8.9	24.6	0.04731	CF	0.33152	TS	0.80000	TS
10	Ps=13.8KPa	10.1	27.9	0.03065	CF	0.28246	TS	0.78861	TS
11	Ps=14.7KPa	10.8	29.7	0.02598	CF	0.24550	CF	0.70679	TS
12	Ps=15.5KPa	11.4	31.3	0.02304	CF	0.20151	CF	0.64727	TS
13	Ps=16.3KPa	11.9	32.9	0.02050	CF	0.12135	CF	0.57328	TS
14	Ps=17.1KPa	12.5	34.4	0.01862	CF	0.08733	CF	0.48026	TS
15	Ps=18.1KPa	13.3	36.5	0.01643	CF	0.06345	CF	0.19018	CF
16	Ps=19.1KPa	14.0	38.6	0.01487	CF	0.04971	CF	0.12912	CF

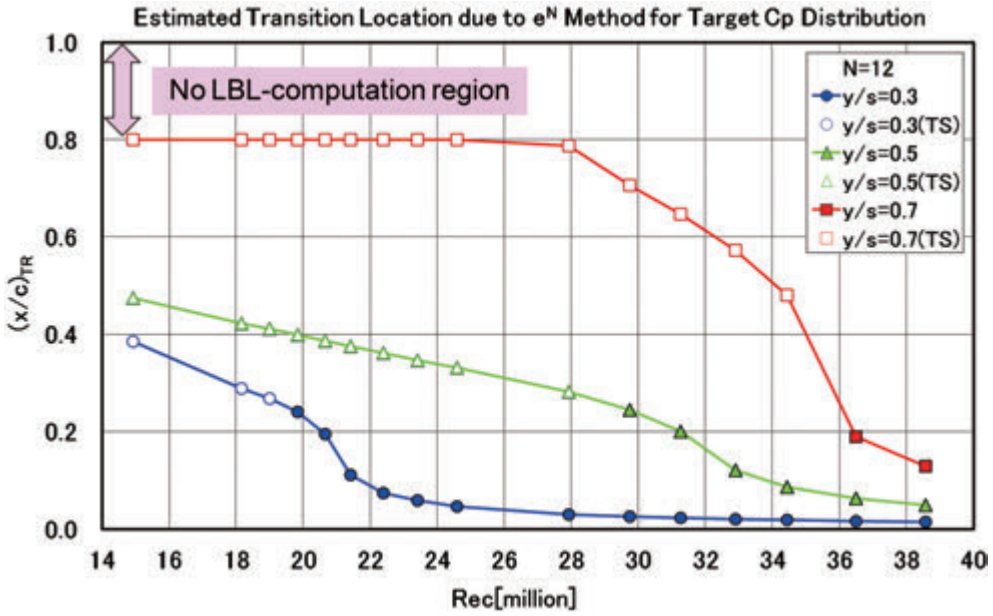

Figure K-1. Re No. trend of transition predicted with Nenv=12

part of the figures corresponds to N evolution computed with envelope strategy and right part shows fixed β strategy computations. "Nature" in the table was estimated from the N evolutions with fixed β strategy at the transition locations predicted with N_{env}=12 as shown in Figs. K-2. Such predicted transition location is plotted in Fig. K-1. This figure indicates general Reynolds number trend on transition movement. But, N factors with envelope strategy include so-called envelope of numerically maximized N values. It means envelope strategy overestimates N values. Therefore, similar analysis for the N evolutions with fixed β strategy should be investigated.

In this study, since JAXA focused on Reynolds number effect on transition characteristics of the NLF wing qualitatively, an N=6 criterion for fixed β strategy was assumed. Present stability results are summarized in Table 7 and Fig. 68 of Chapter 5. As shown in Figs. K-2, N factor evolutions at each Reynolds number condition exhibit two kind of disturbances CFI and TSI. At low Reynolds number conditions, as TSI is dominant, transition location is delayed. But, at a certain Reynolds number (called Re_{II}), the most dominant instability changes from TSI to CFI. This change generates rapid forward movement of transition as shown in Fig. K-2 and Fig. 68. It is considered that such Reynolds number trend on transition movement is qualitatively general. The most important point for the NLF wing design is to increase the Re_{II} beyond the design Reynolds number as illustrated in Fig. 69. There is possibility for improvement of present target Cp distribution by increasing acceleration gradients near leading edge, according to JAXA's patent application[10].

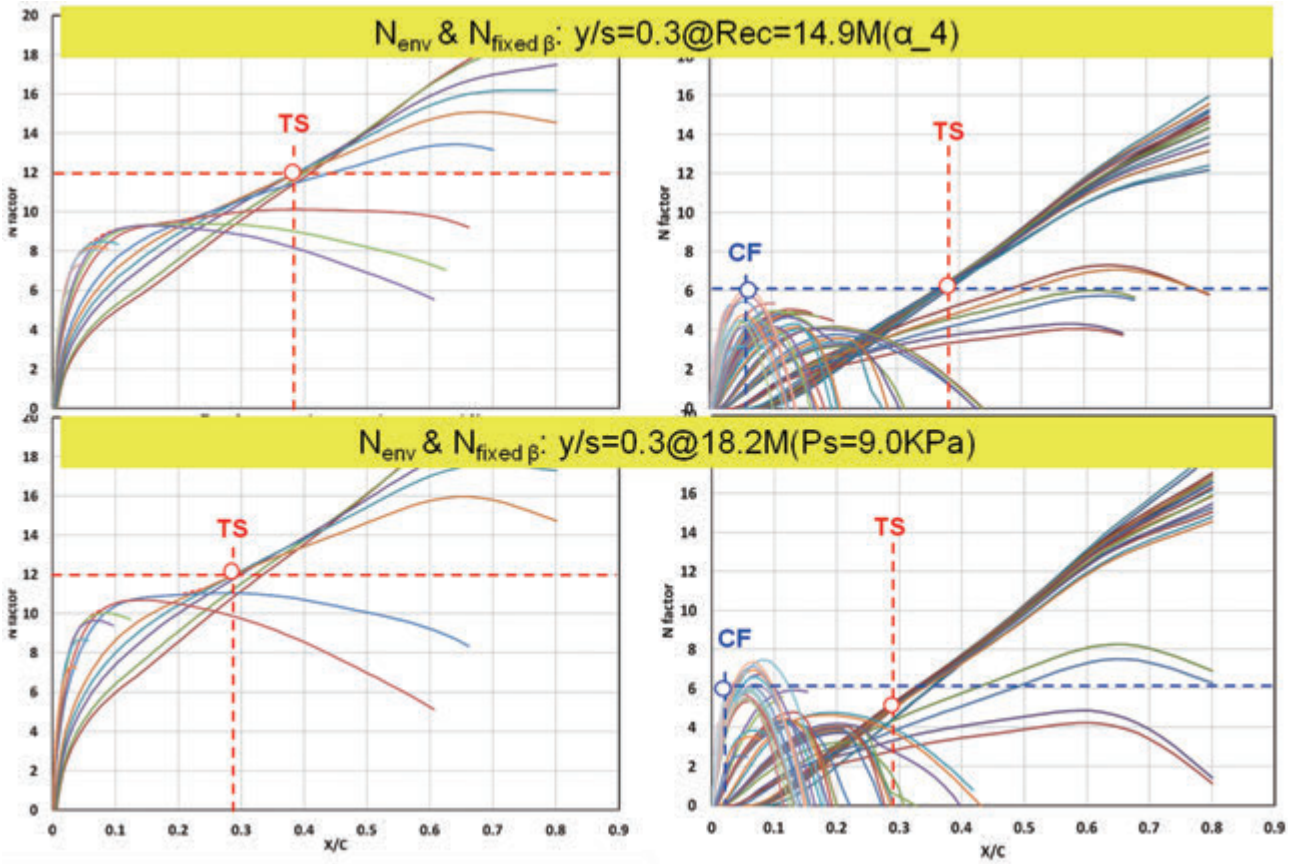

(a) y/s=0.3 (1/8)

Figure K-2. N factors on CpTargect computed with envelope and fixed β strategies

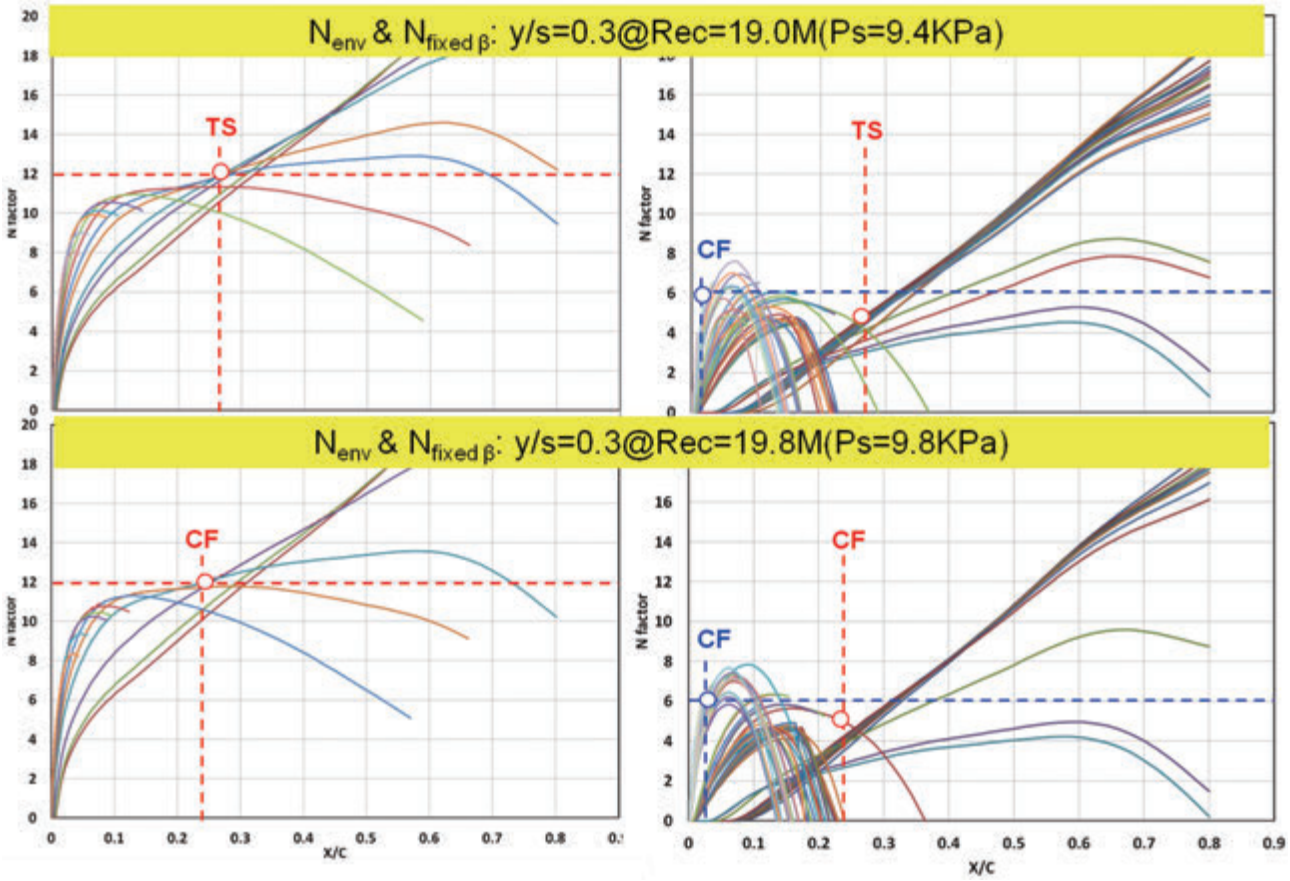

(a) y/s=0.3 (2/8)

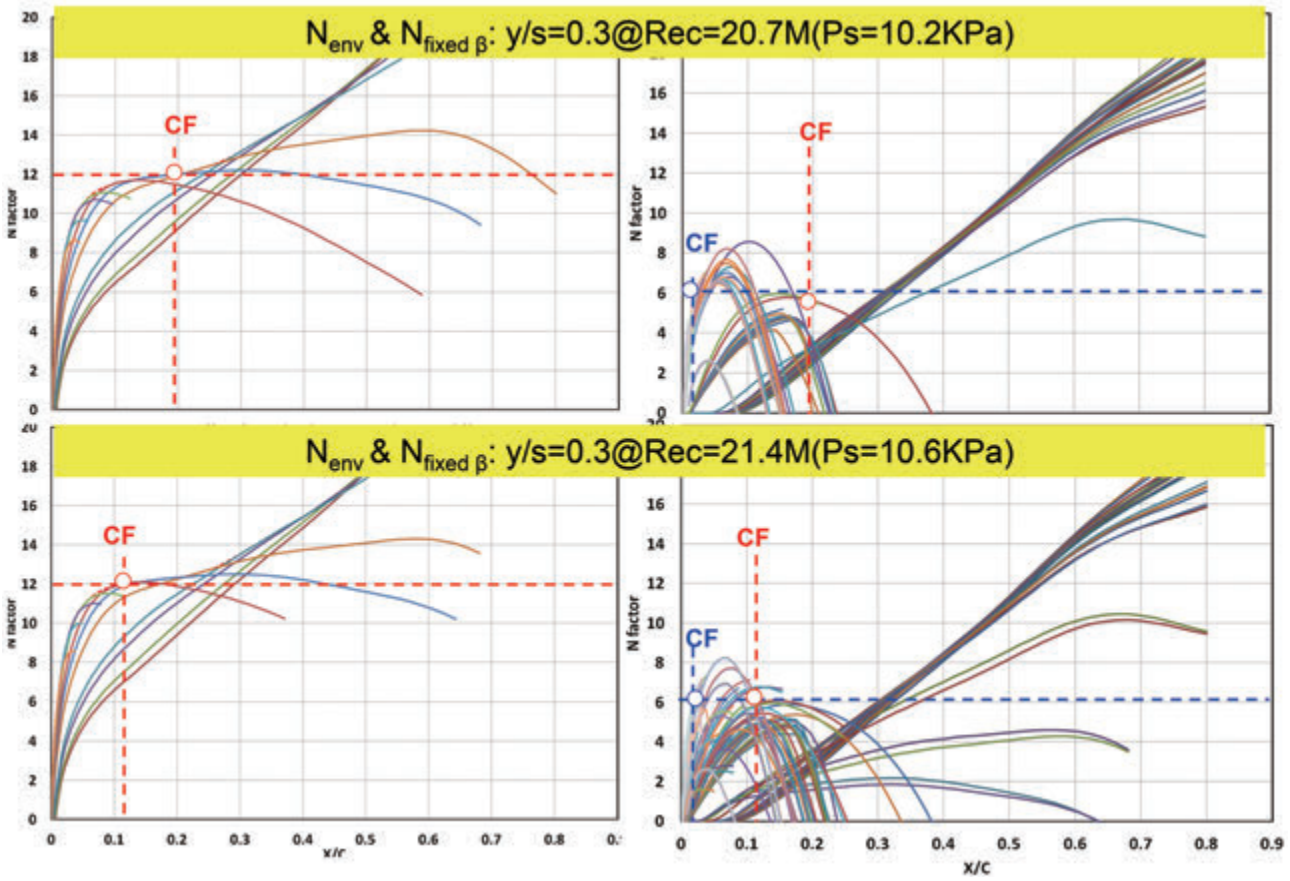

(a) y/s=0.3 (3/8)

Figure K-2. N factors on CpTargect computed with envelope and fixed β strategies

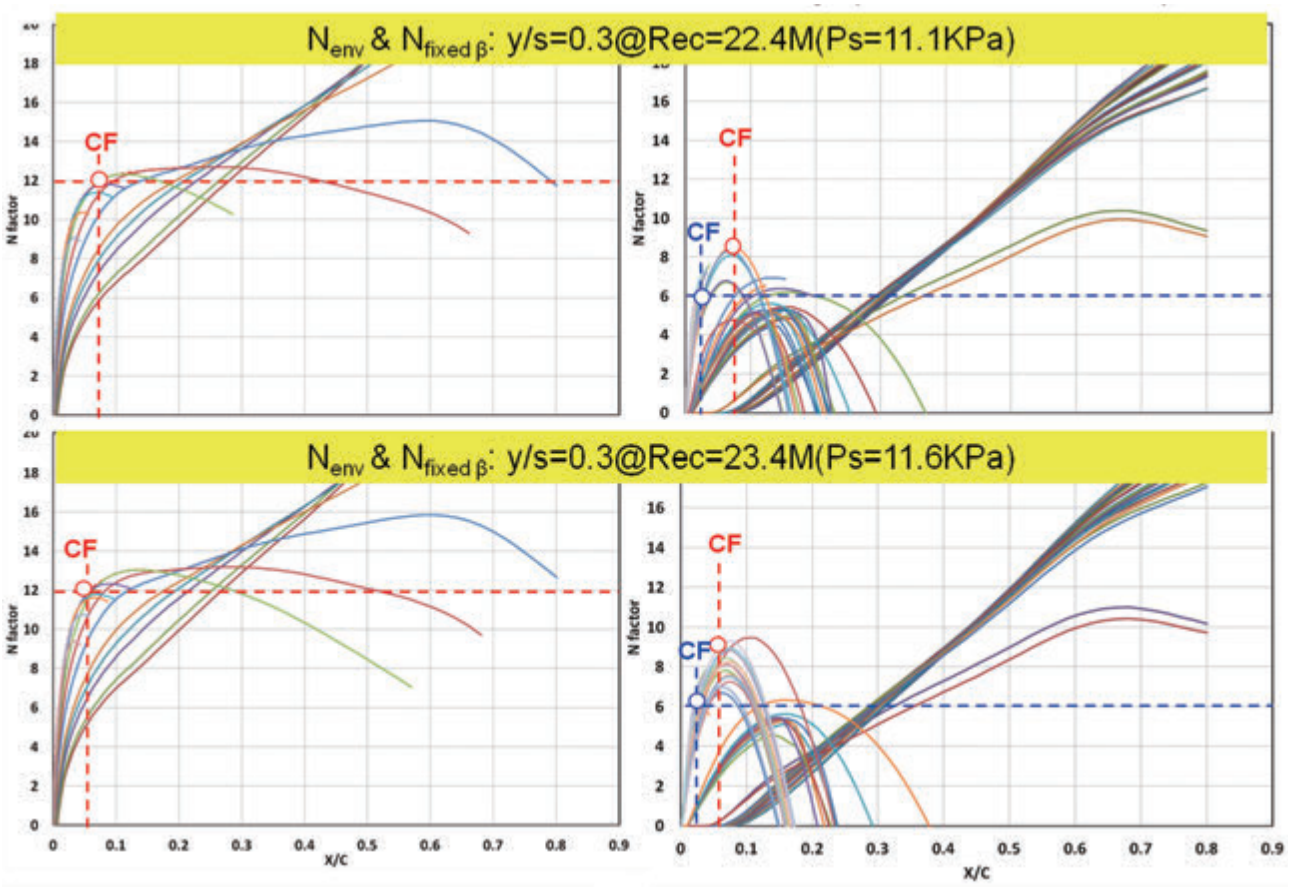

(a) y/s=0.3 (4/8)

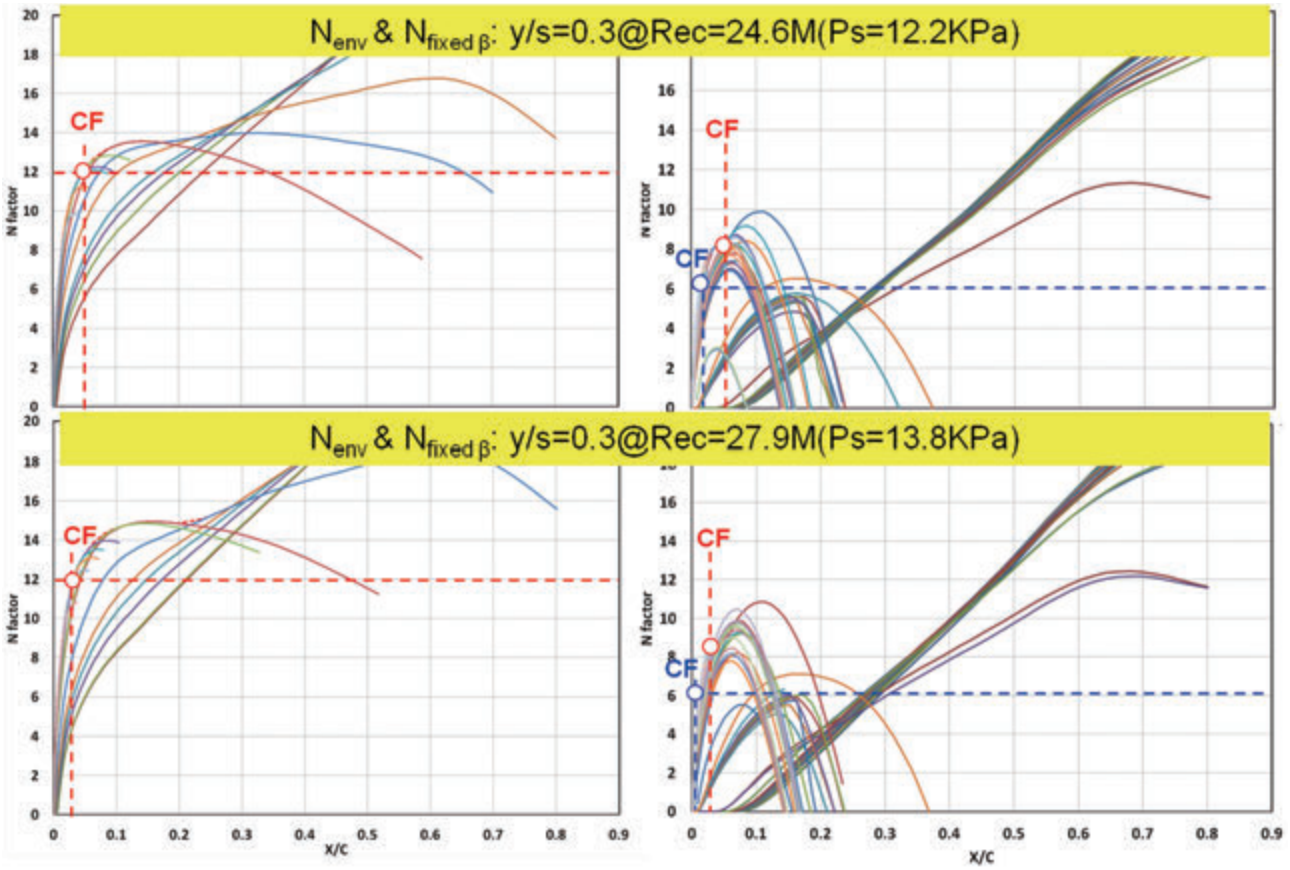

(a) y/s=0.3 (5/8)

Figure K-2. N factors on CpTargect computed with envelope and fixed β strategies

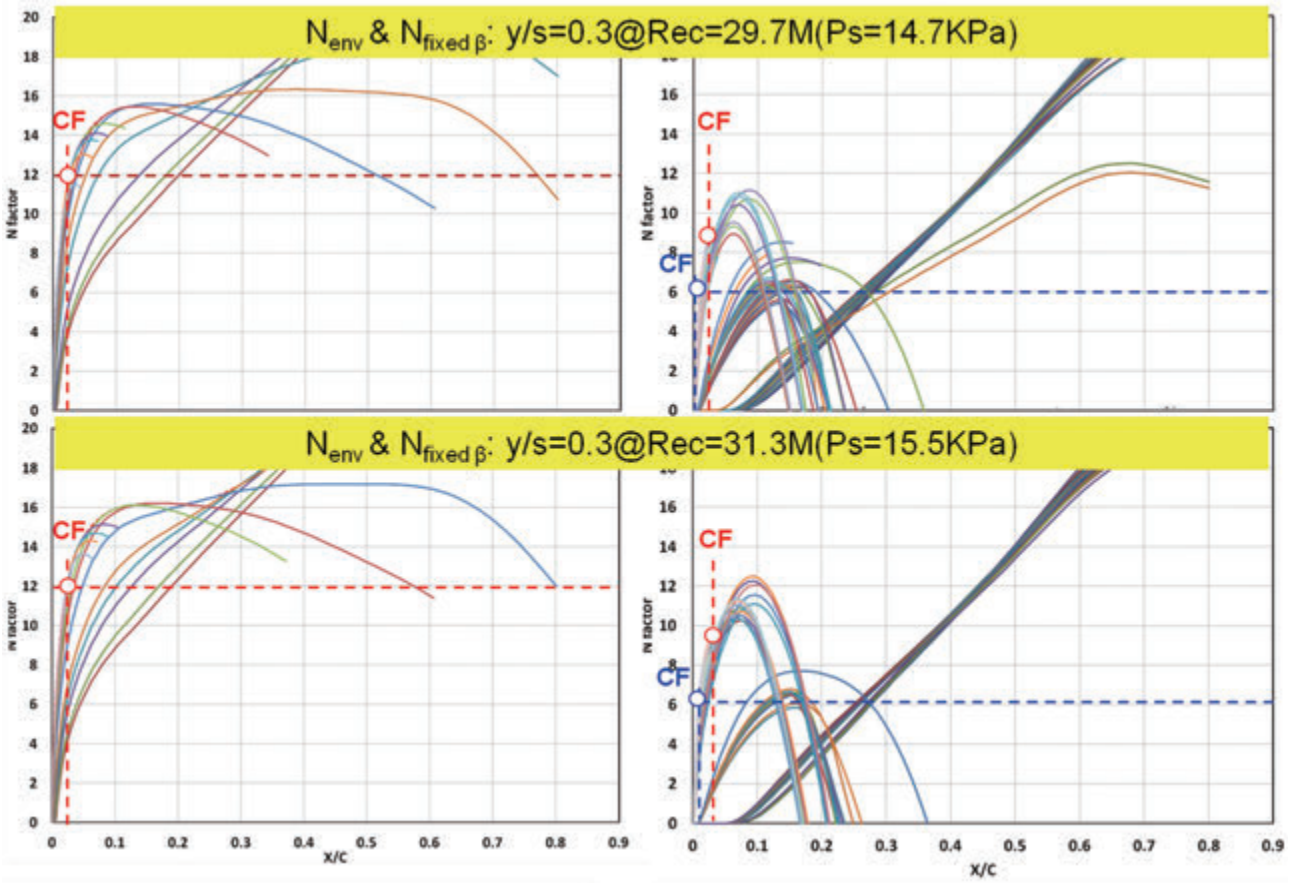

(a) y/s=0.3 (6/8)

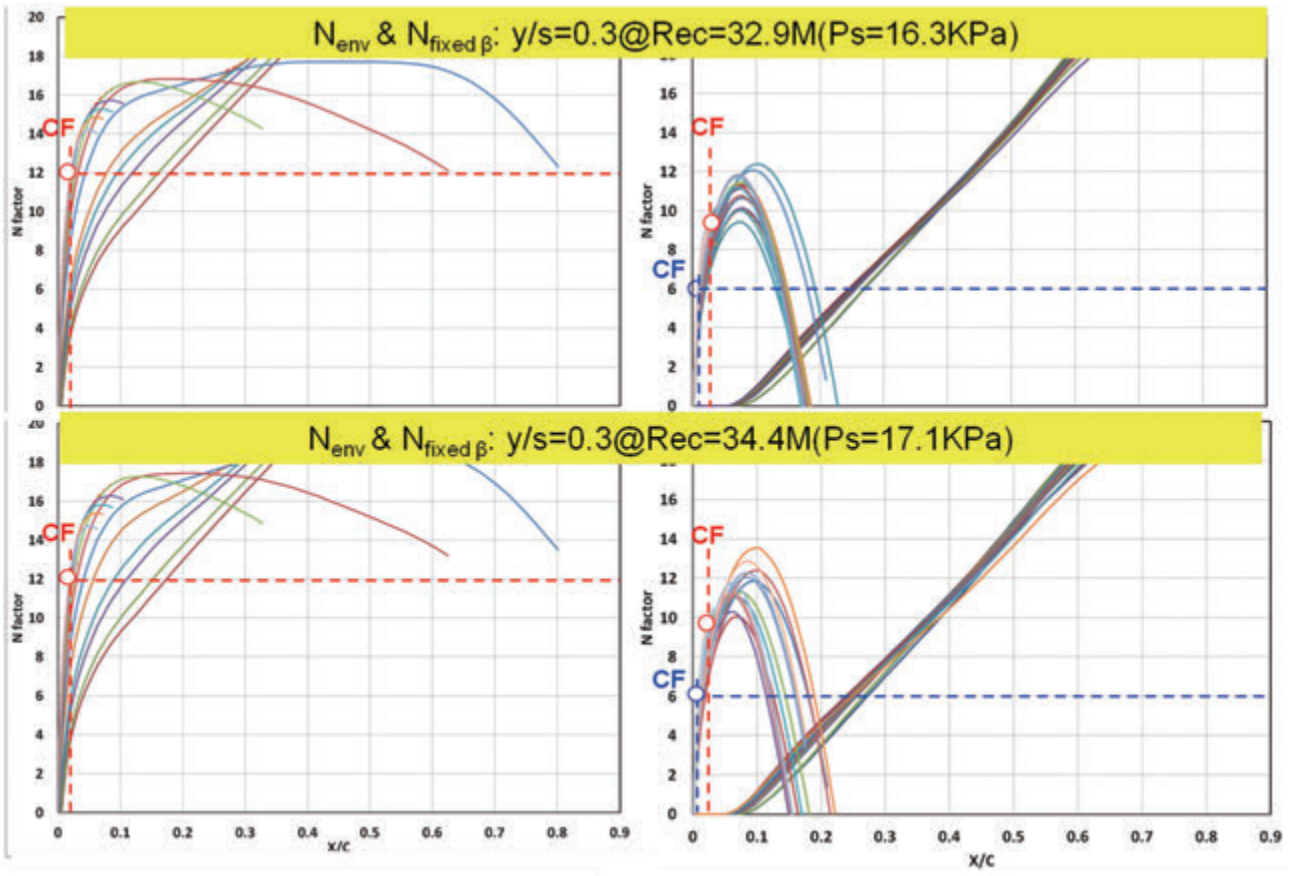

(a) y/s=0.3 (7/8)

Figure K-2. N factors on CpTargect computed with envelope and fixed β strategies

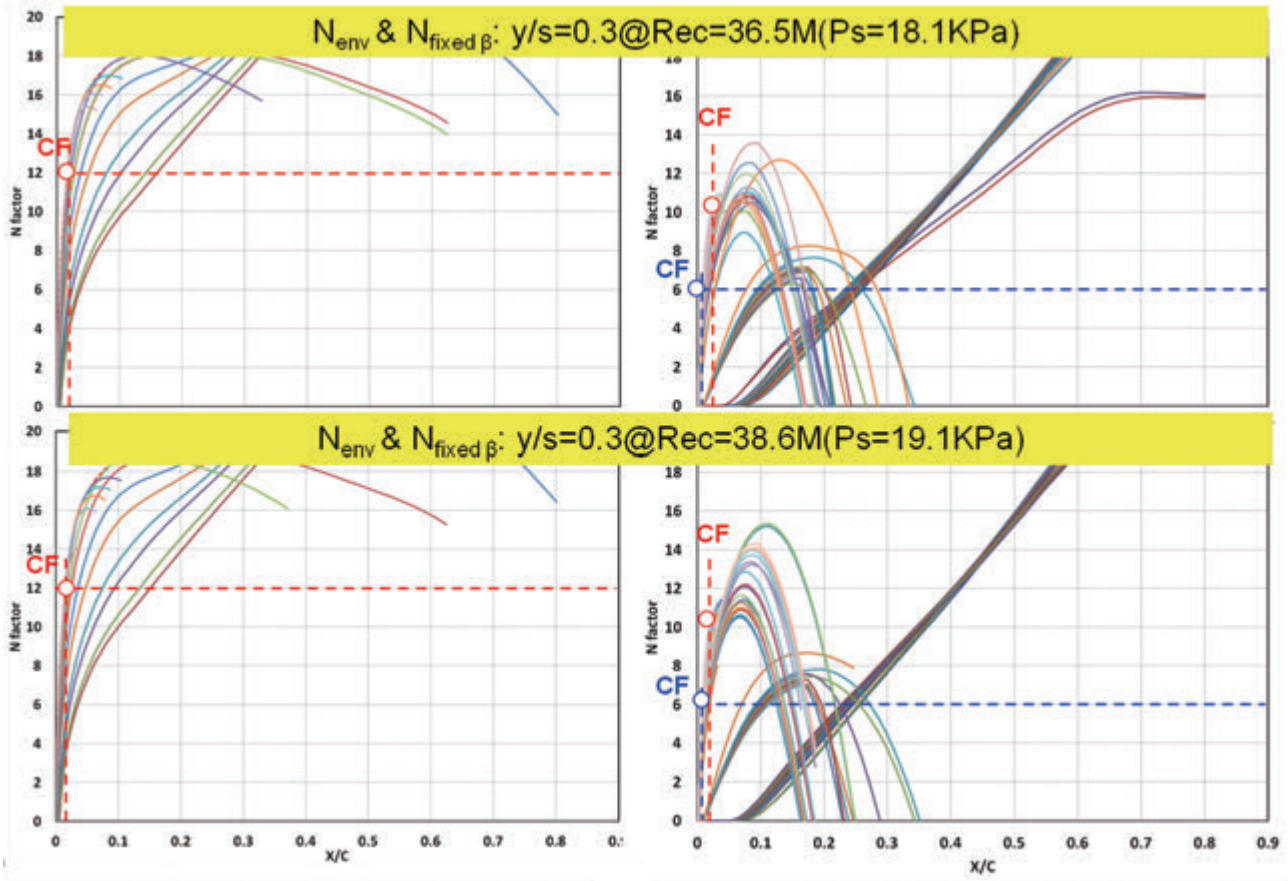

(a) y/s=0.3 (8/8)

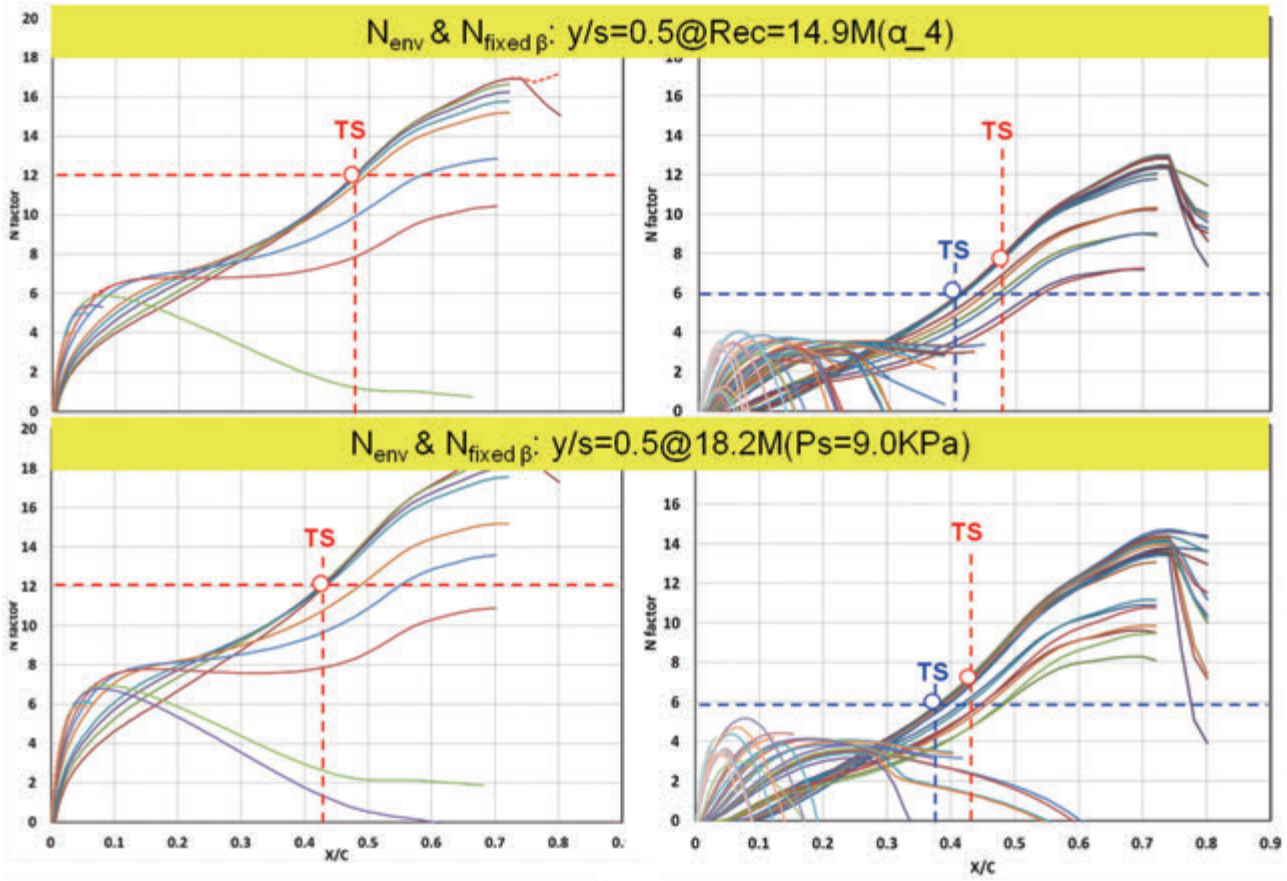

(b) y/s=0.5 (1/8)

Figure K-2. N factors on CpTargect computed with envelope and fixed β strategies

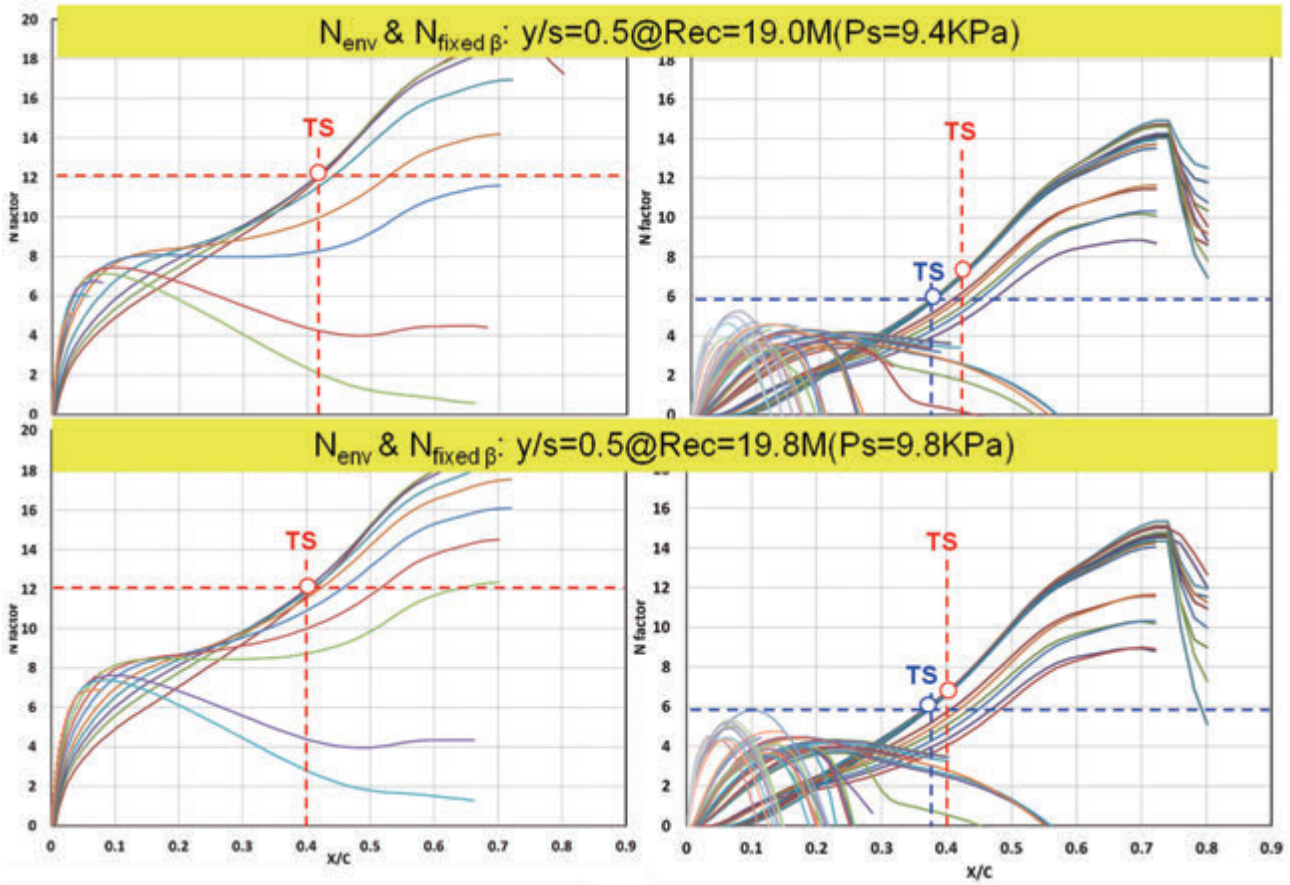

(b) y/s=0.5 (2/8)

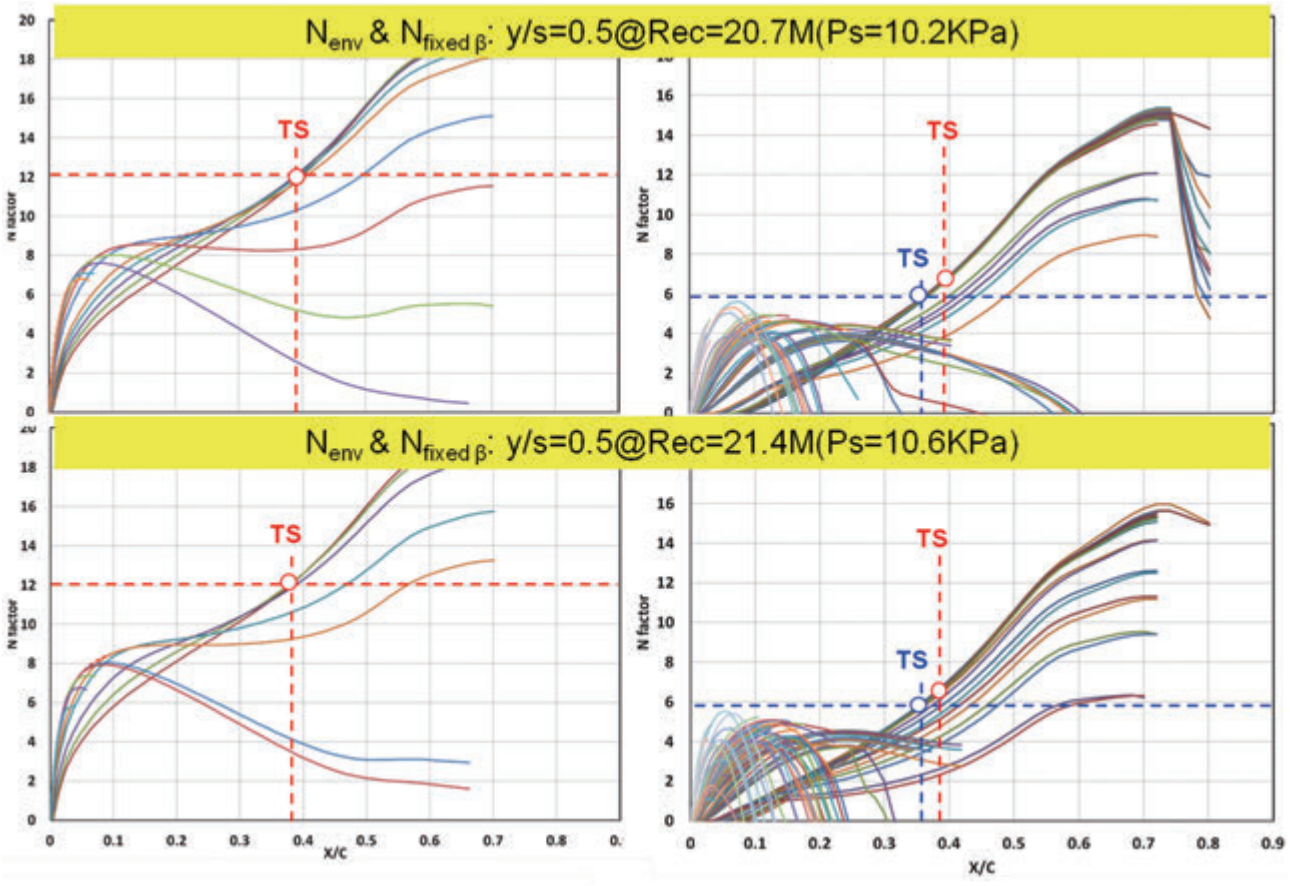

(b) y/s=0.5 (3/8)

Figure K-2. N factors on CpTargect computed with envelope and fixed β strategies

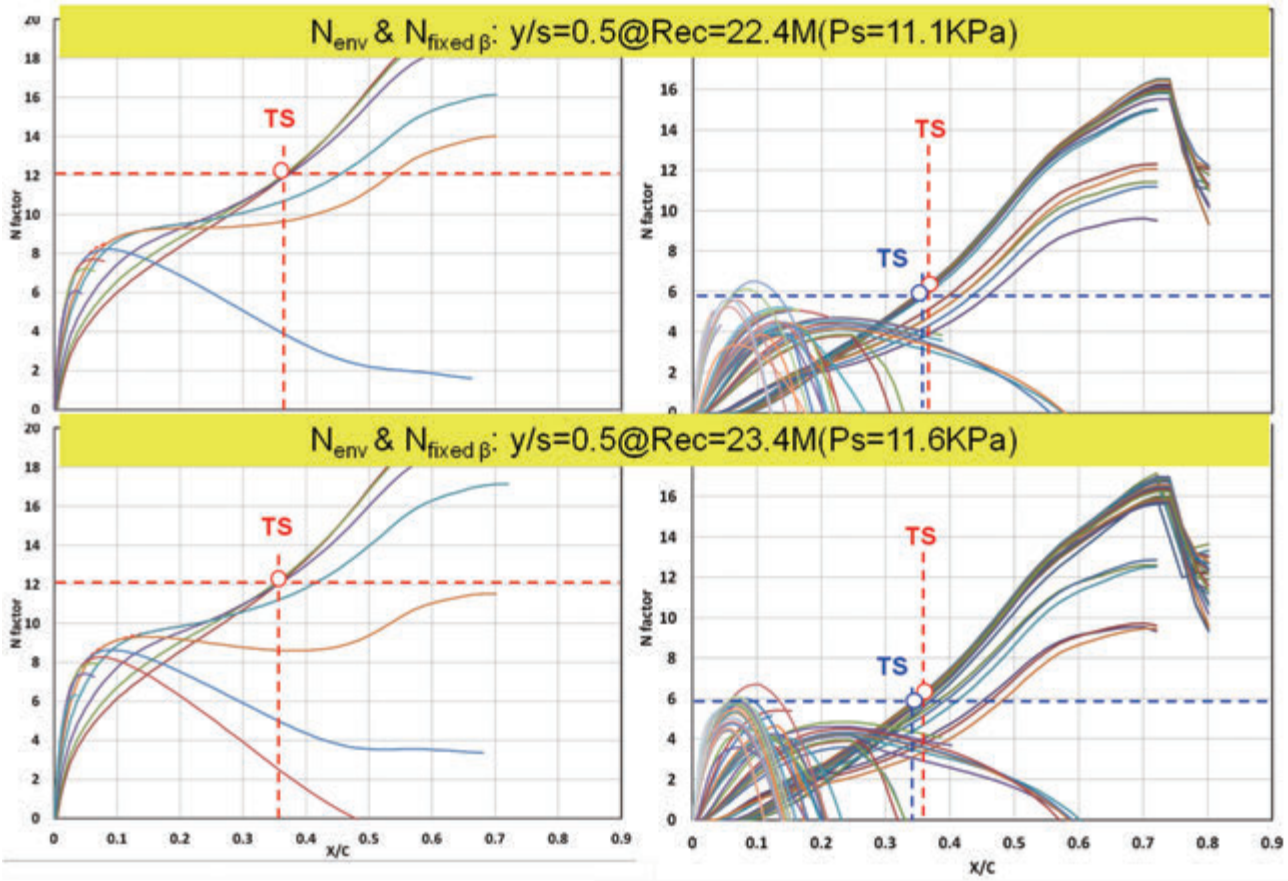

(b) y/s=0.5 (4/8)

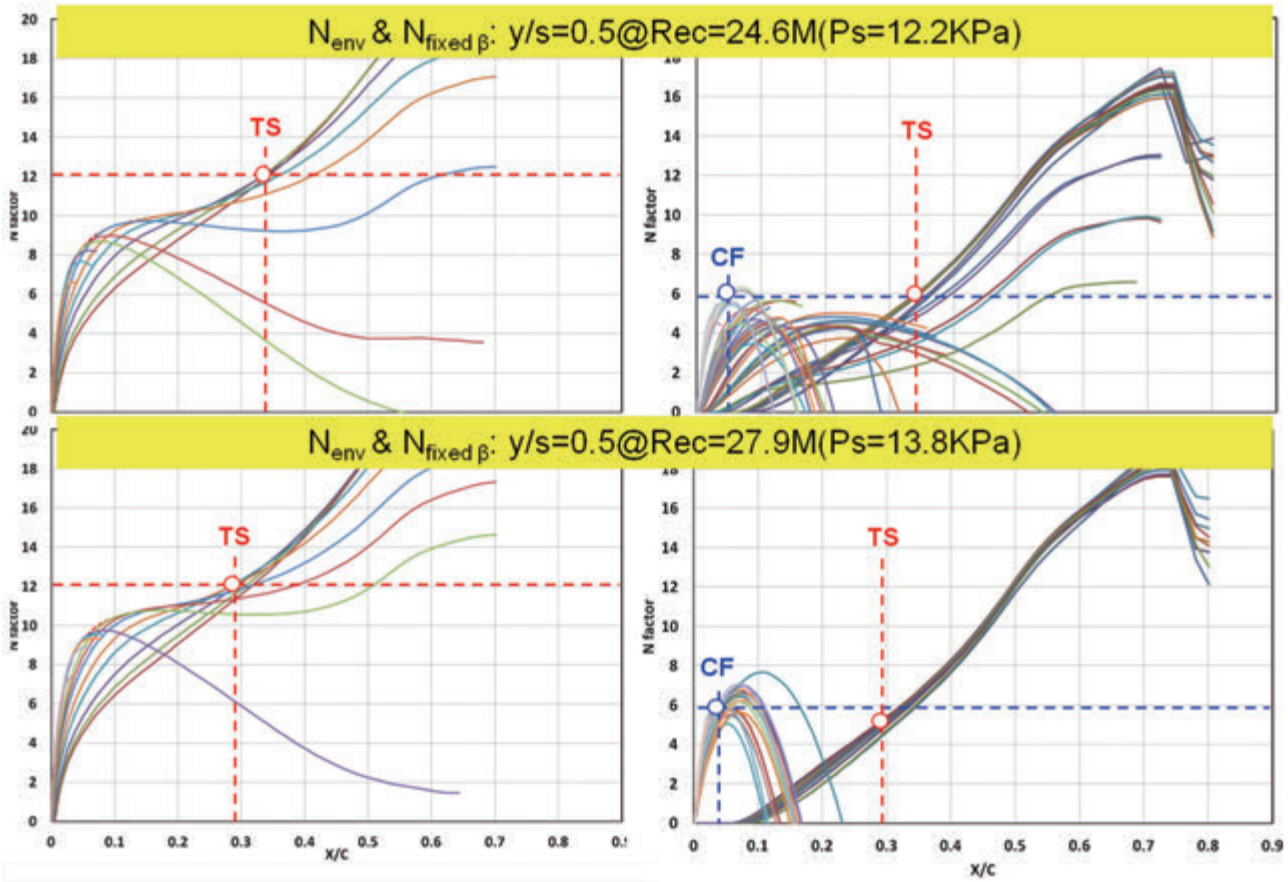

(b) y/s=0.5 (5/8)

Figure K-2. N factors on CpTargect computed with envelope and fixed β strategies

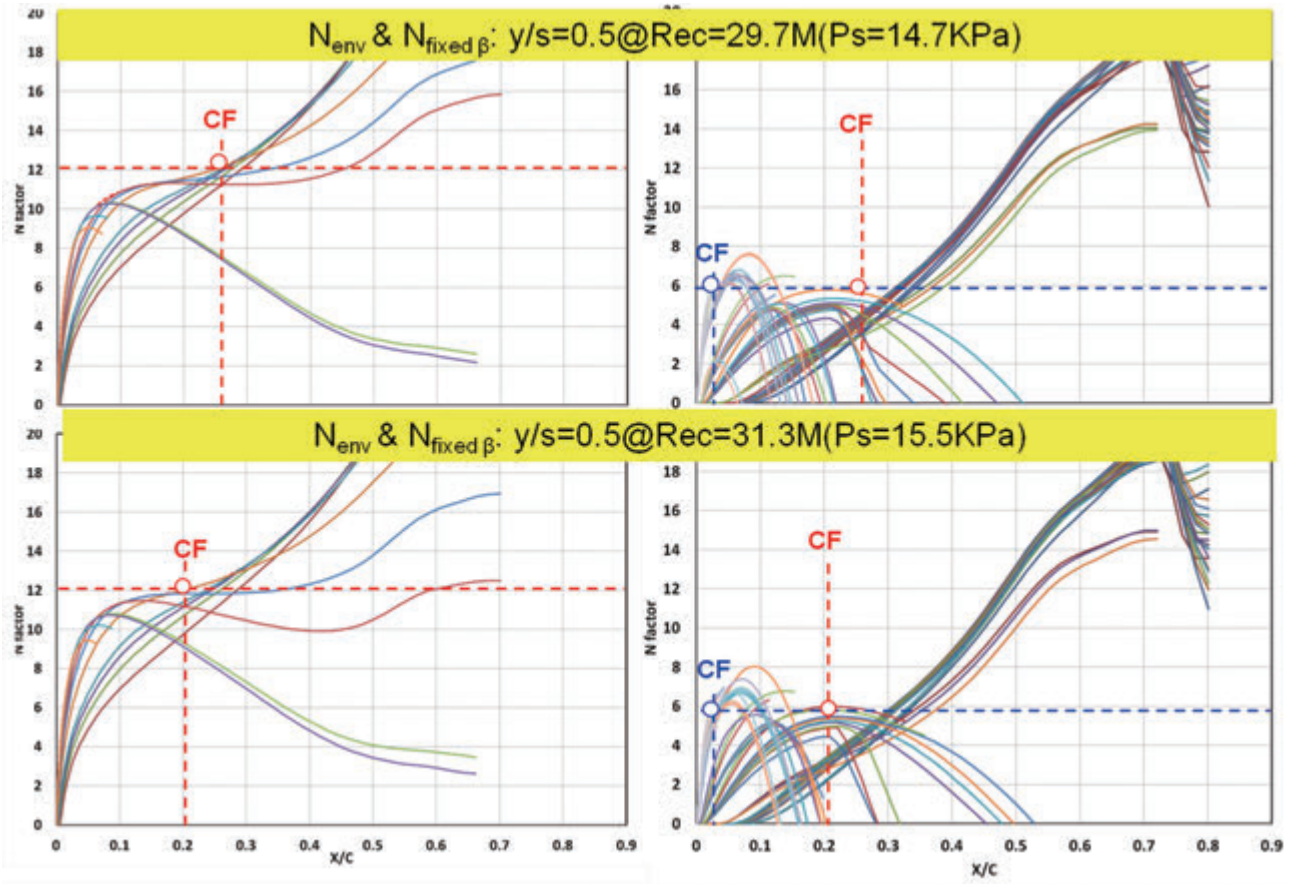

(b) y/s=0.5 (6/8)

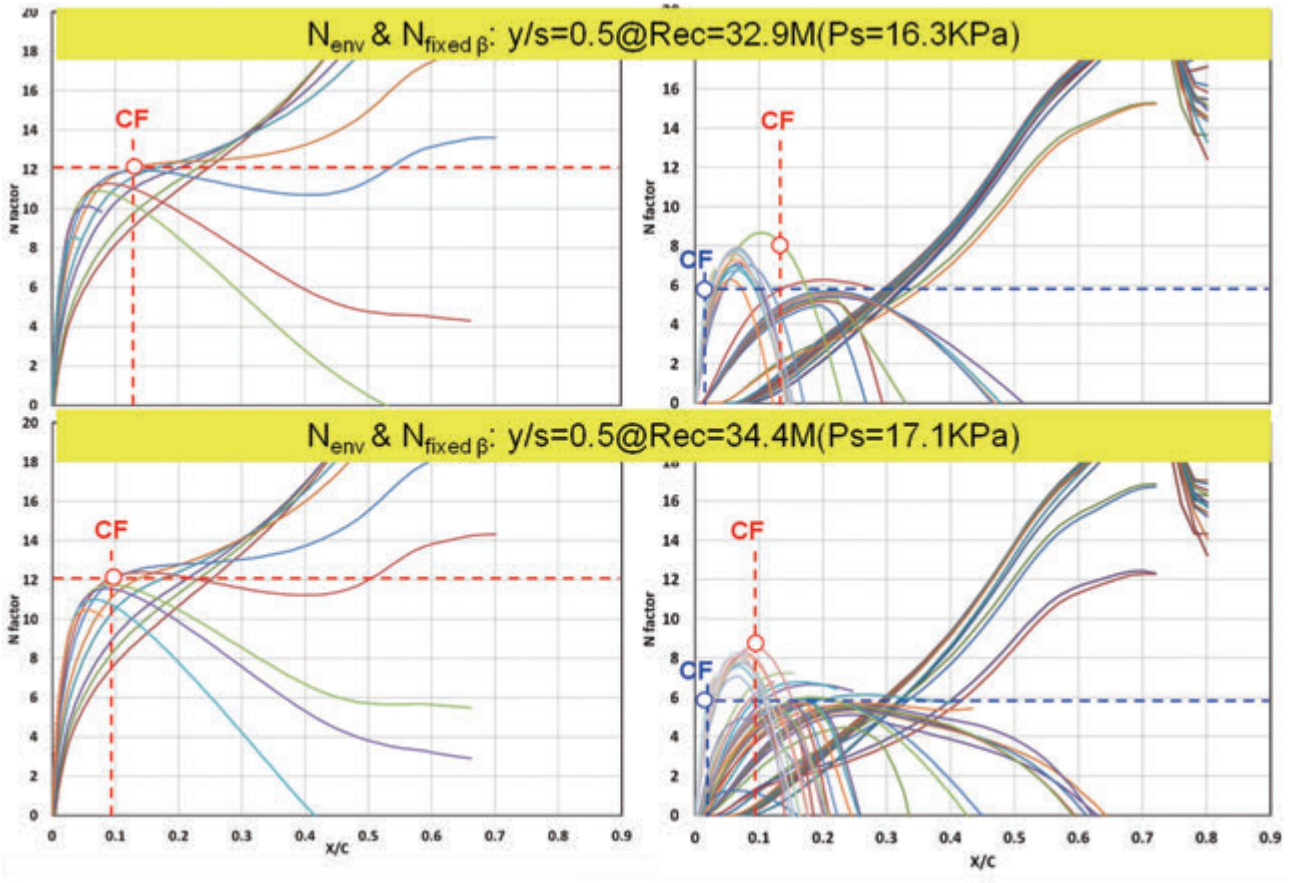

(b) y/s=0.5 (7/8)

Figure K-2. N factors on CpTargect computed with envelope and fixed β strategies

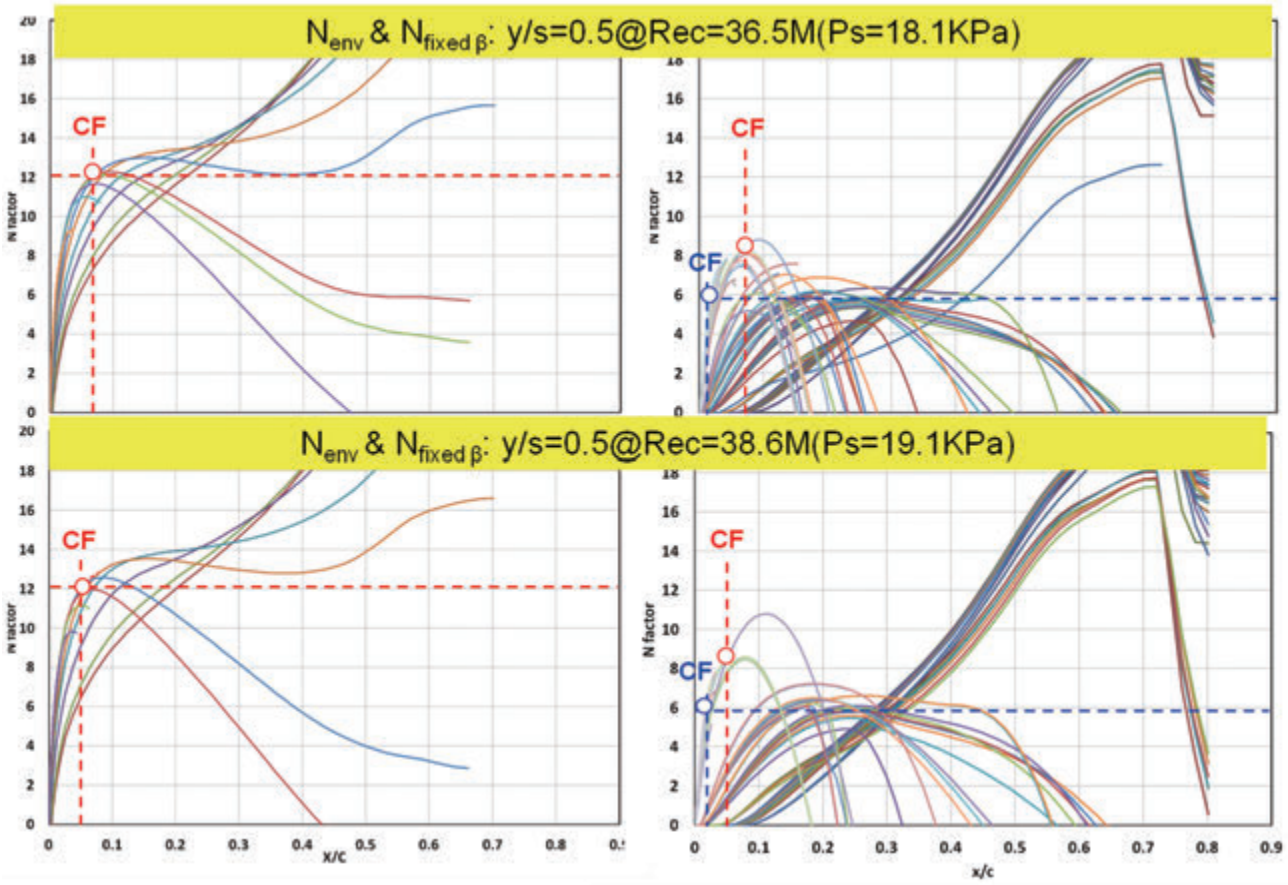

(b) y/s=0.5 (8/8)

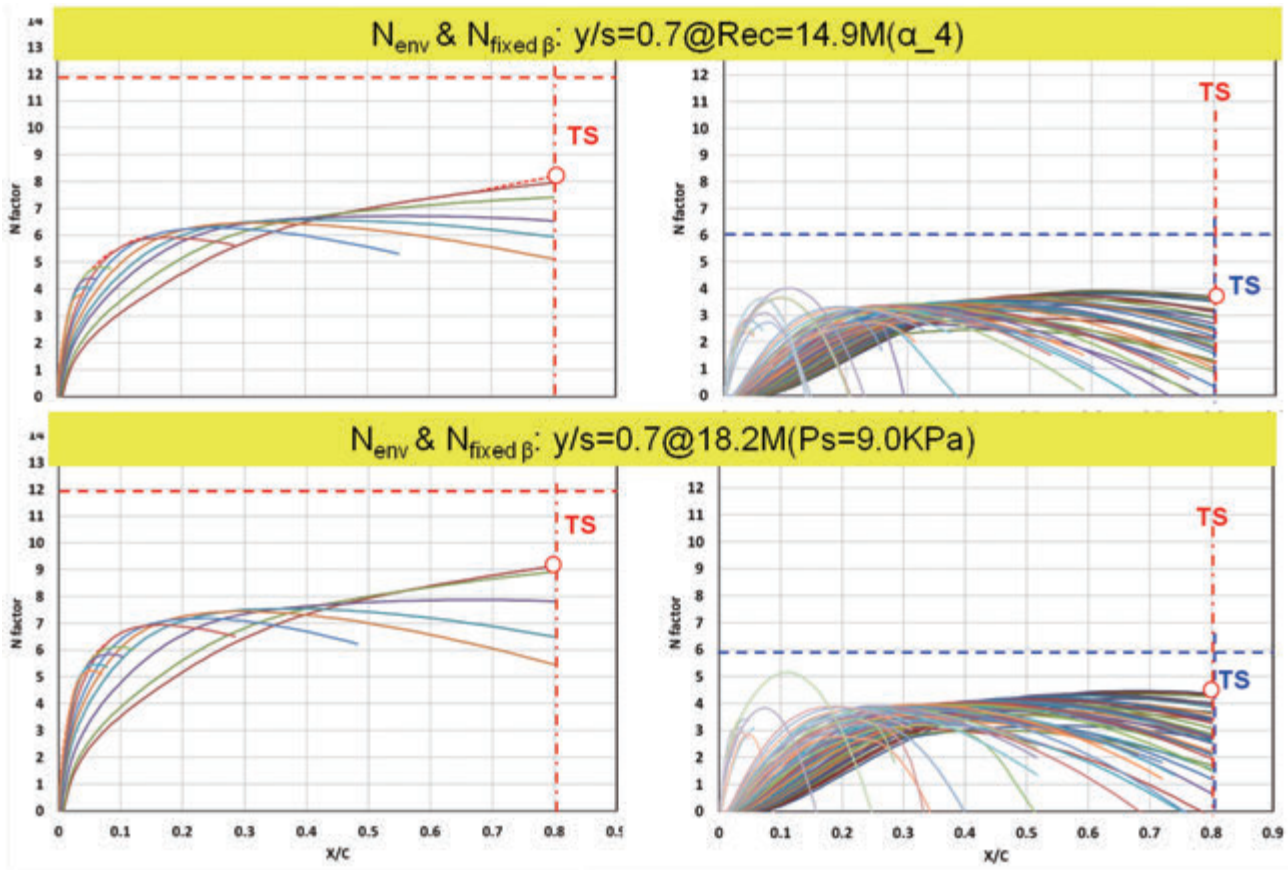

(c) y/s=0.7 (1/8)

Figure K-2. N factors on CpTargect computed with envelope and fixed β strategies

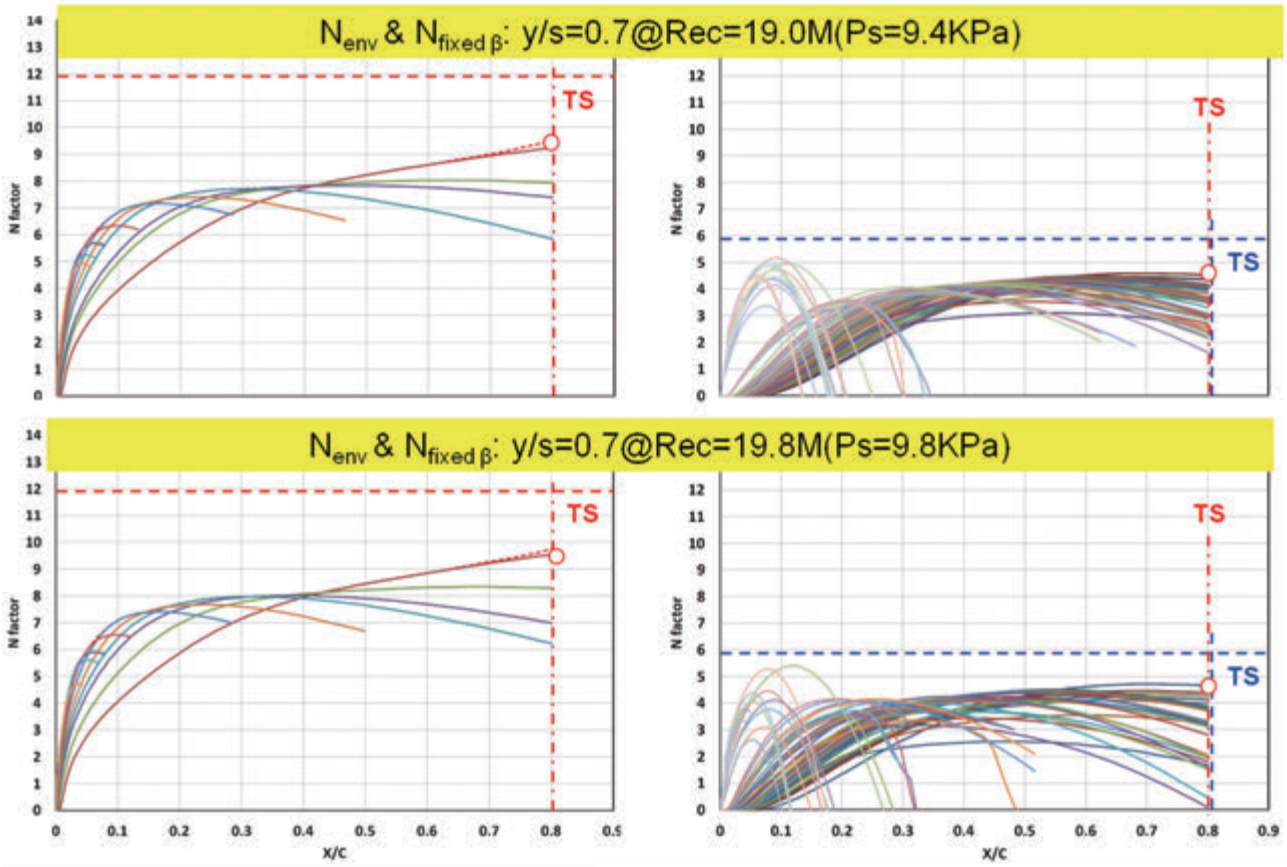

(c) y/s=0.7 (2/8)

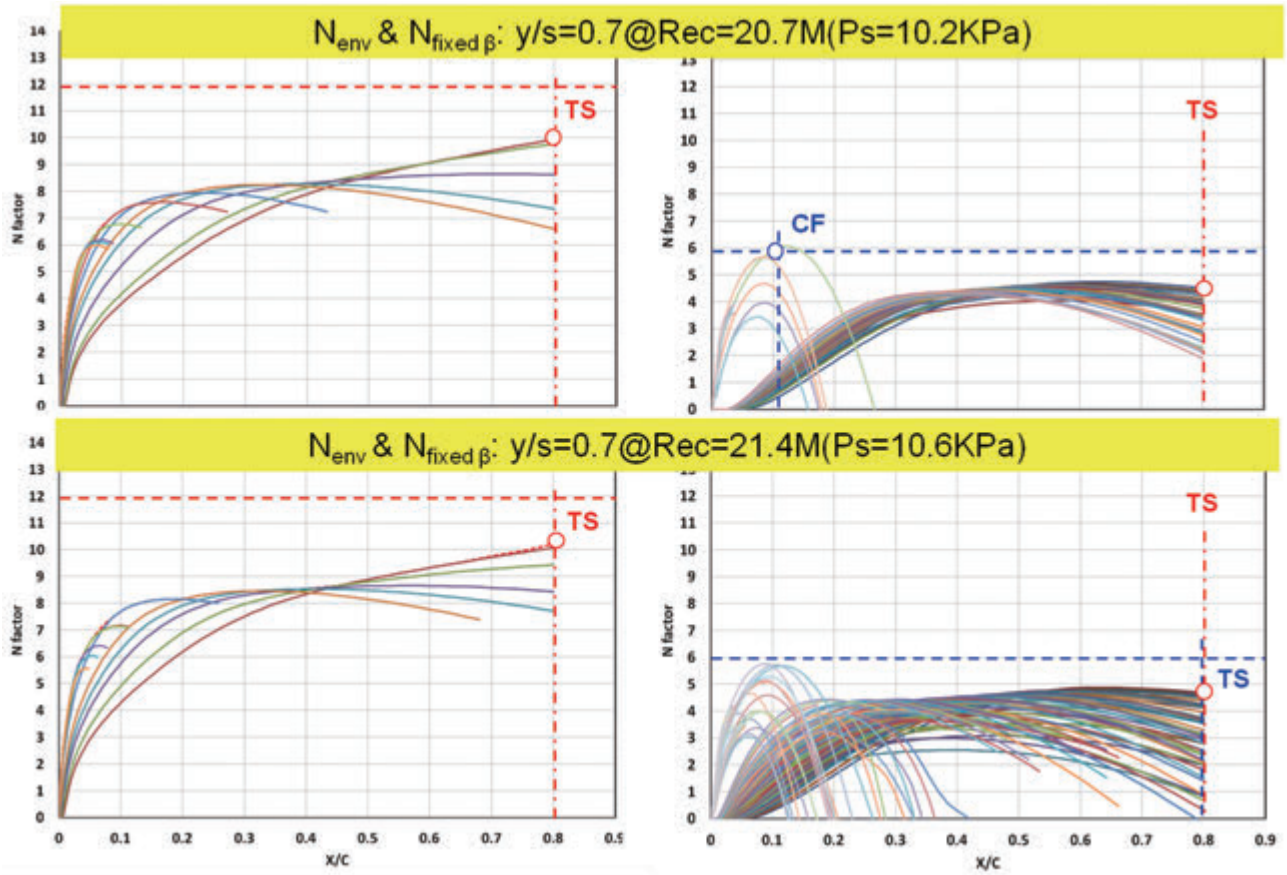

(c) y/s=0.7 (3/8)

Figure K-2. N factors on CpTargect computed with envelope and fixed β strategies

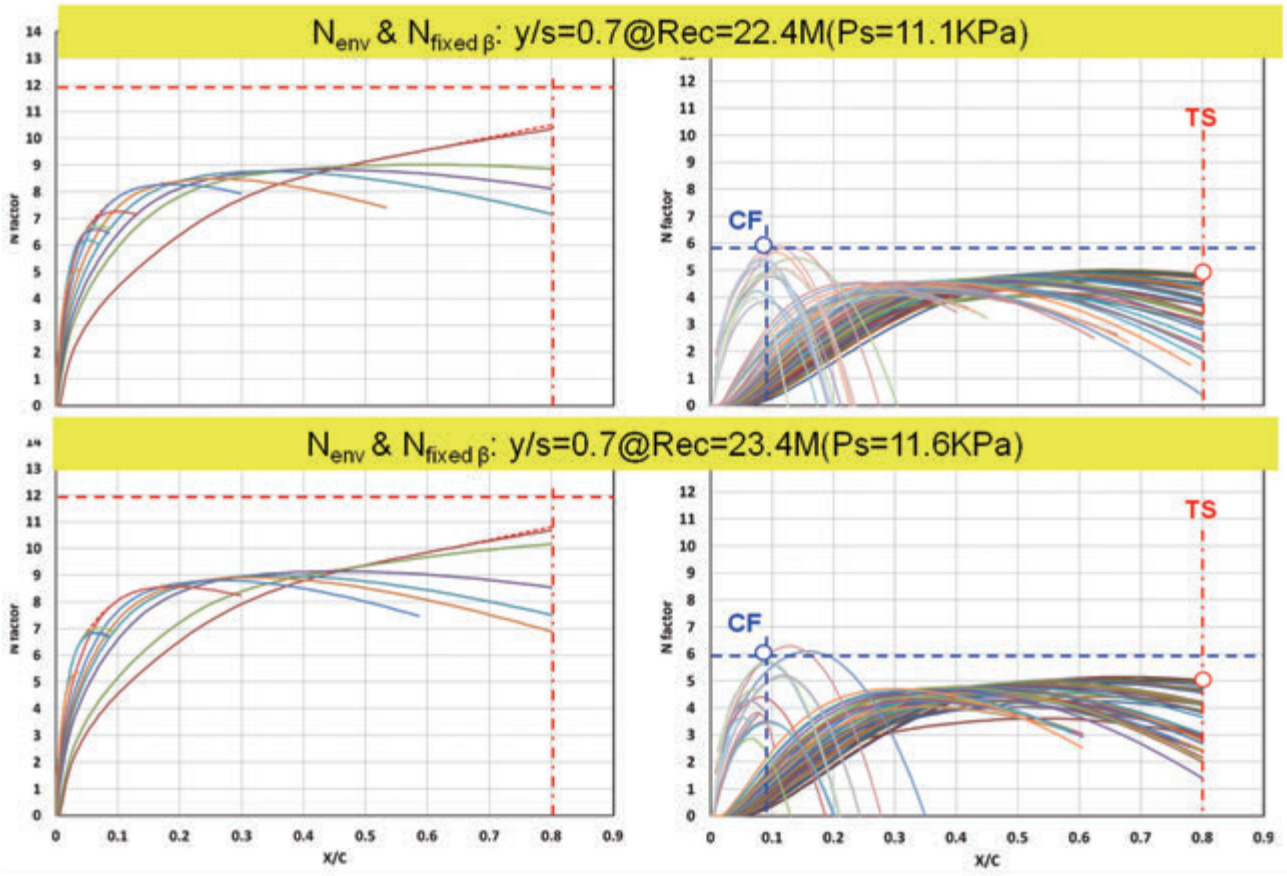

(c) y/s=0.7 (4/8)

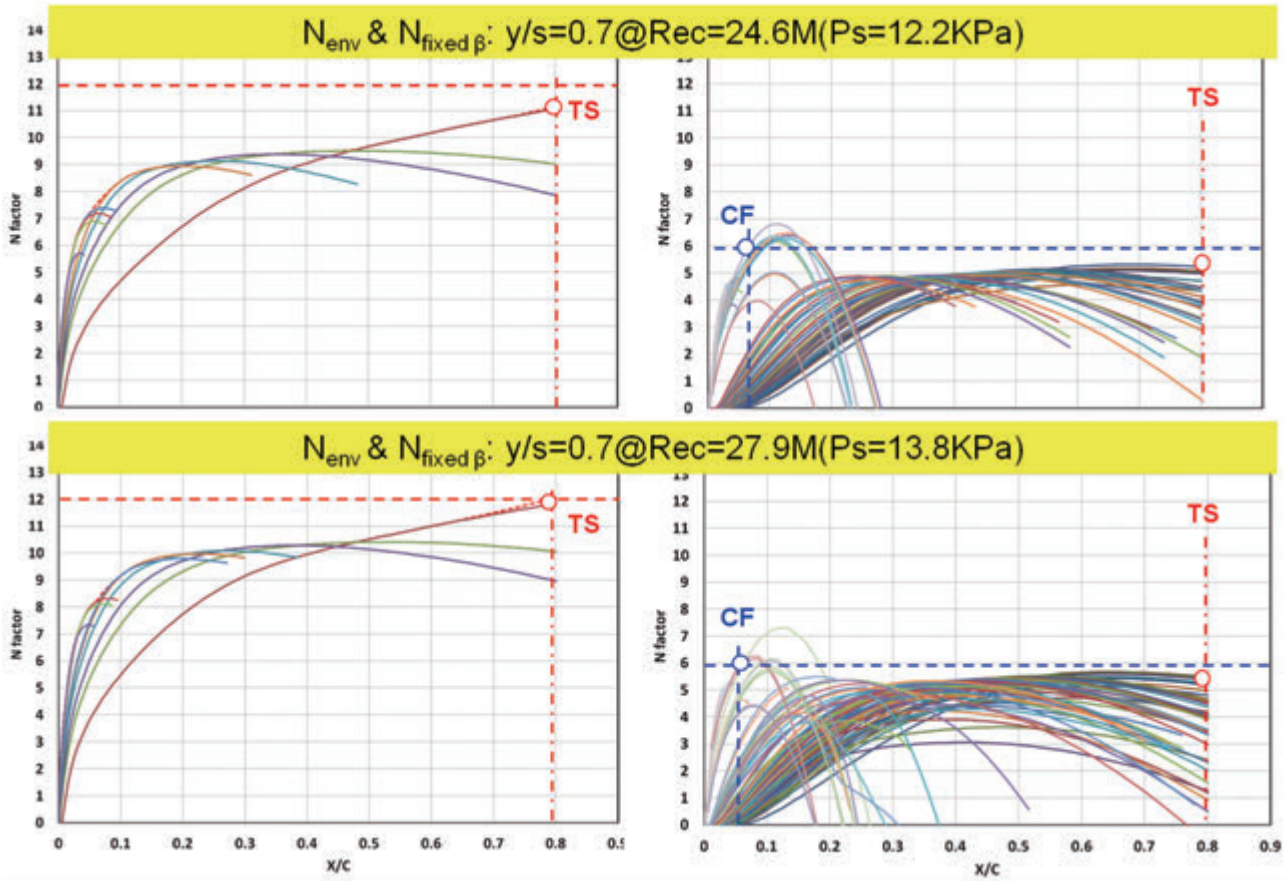

(c) y/s=0.7 (5/8)

Figure K-2. N factors on CpTargect computed with envelope and fixed β strategies

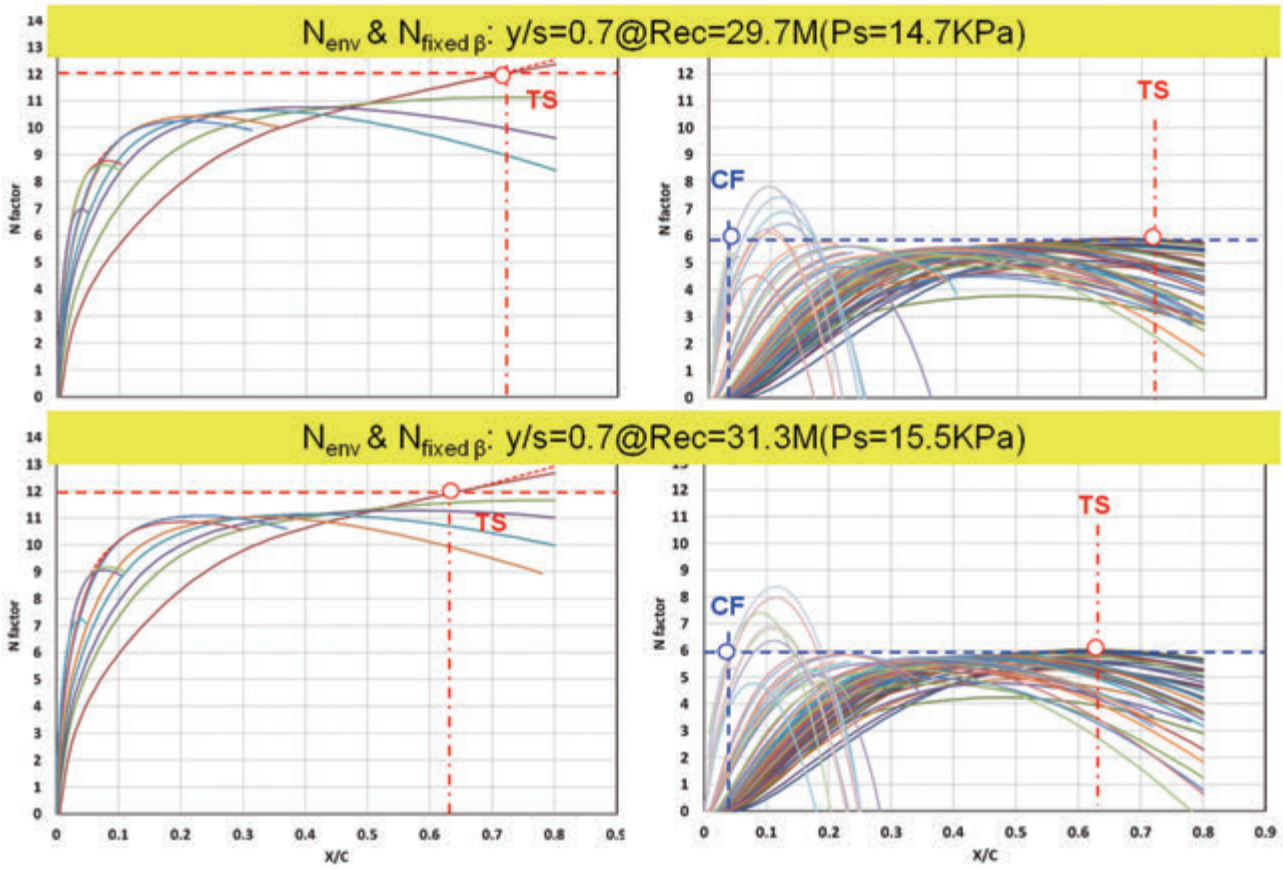

(c) y/s=0.7 (6/8)

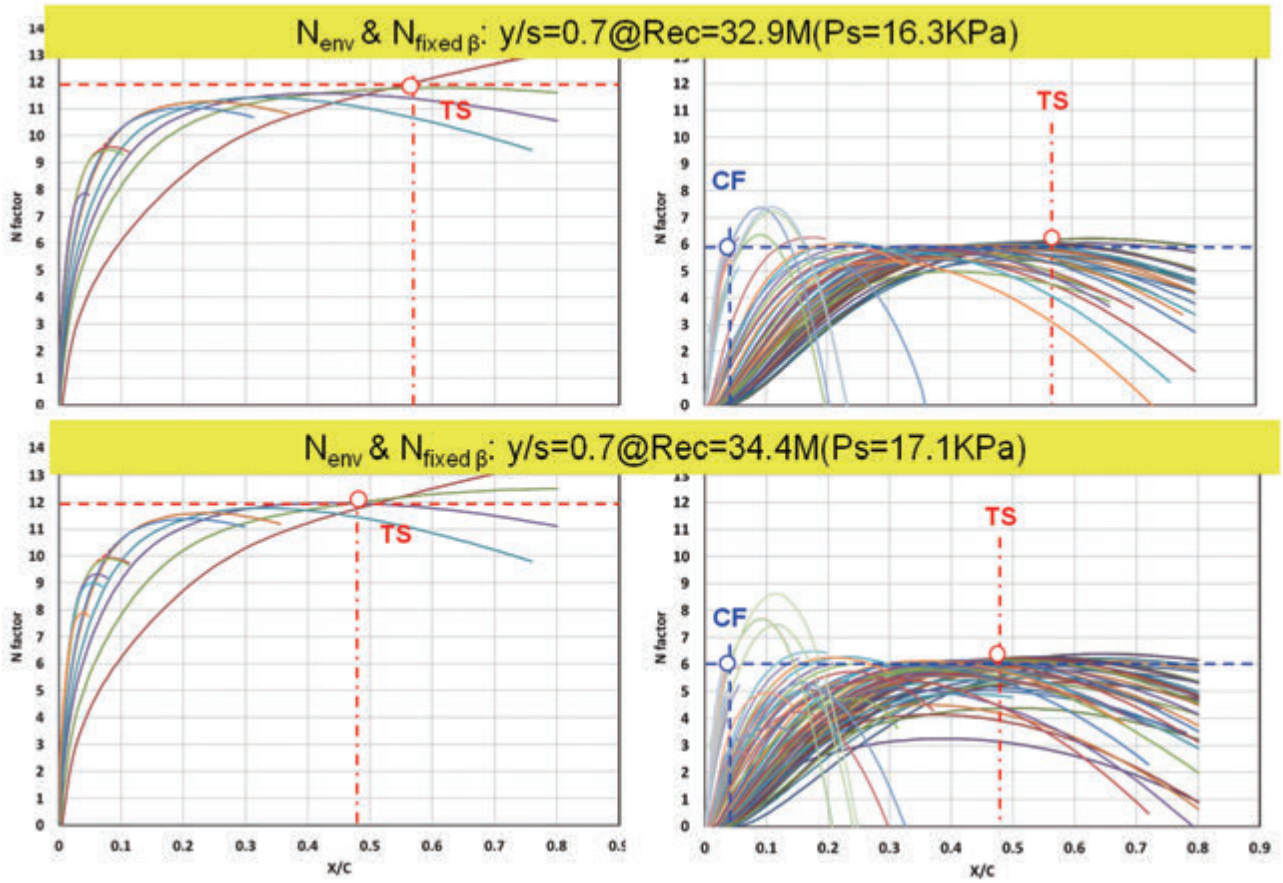

(c) y/s=0.7 (7/8)

Figure K-2. N factors on CpTargect computed with envelope and fixed β strategies

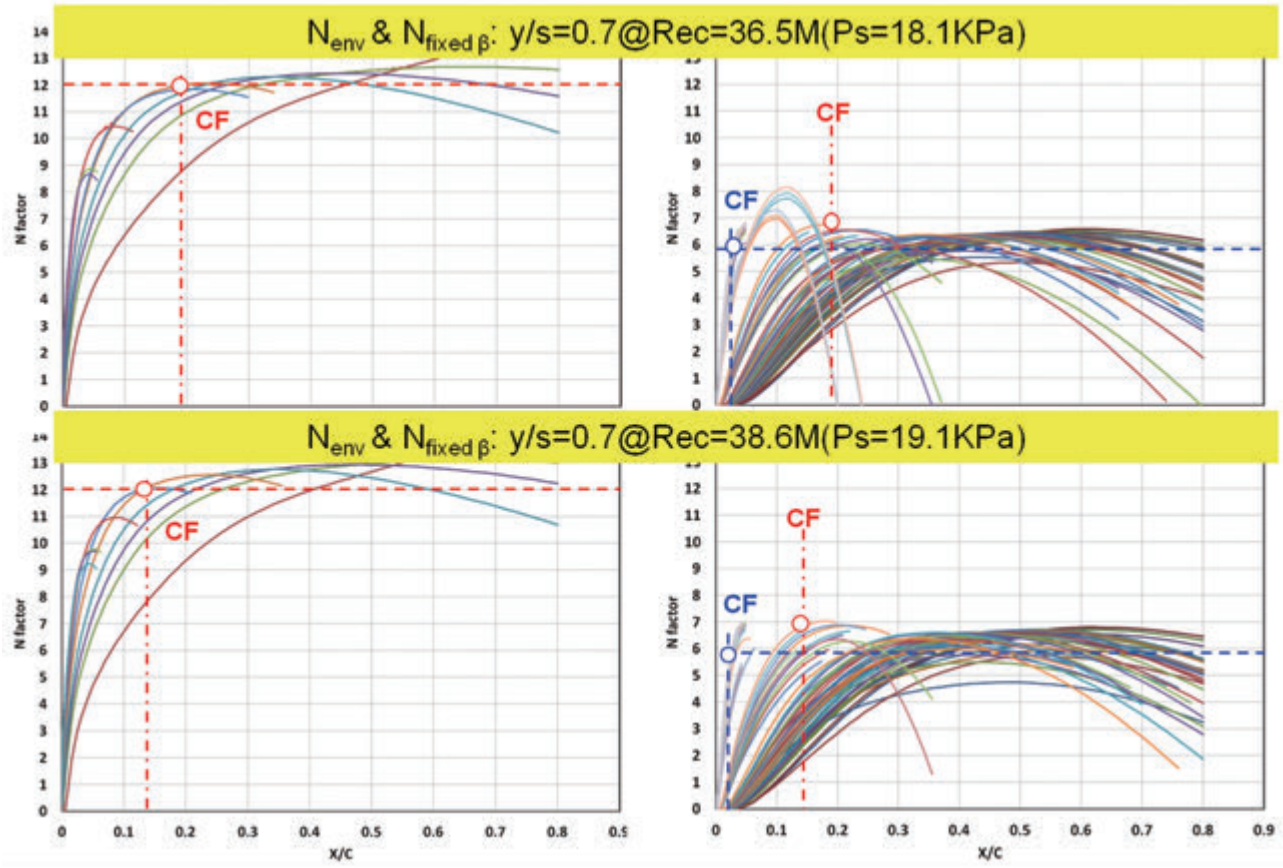

(c) y/s=0.7 (8/8)

Figure K-2. N factors on CpTargect computed with envelope and fixed β strategies